TECHNISCHE UNIVERSITÄT MÜNCHEN

Fakultät für Physik
Lehrstuhl für Experimentalphysik E21

Design, optimization, and implementation of the new neutron radiography facility at FRM-II

Florian Grünauer

Vollständiger Abdruck der von der Fakultät für Physik der Technischen Universität München zur Erlangung des akademischen Grades eines

Doktors der Naturwissenschaften (Dr. rer. nat.)

genehmigten Dissertation.

Vorsitzender: Univ.-Prof. Dr. M. Kleber

Prüfer der Dissertation:

1. Univ.-Prof. Dr. P. Böni

2. Univ.-Prof. Dr. W. Petry

Die Dissertation wurde am 22. 9. 2005 bei der Technischen Universität München eingereicht und durch die Fakultät für Physik am 7. 12. 2005 angenommen.

Abstract (english version)

A neutron radiography and tomography facility was planned and installed at the new research reactor FRM-II in Munich. This paper describes the designing, optimization, construction, and first applications of this facility. Prior to construction, the whole facility was optimized by computational methods. The facility is based on the principle of a pin hole camera. For reduction of background radiation and neutron leakage from regions around the pin hole, a collimator was developed that provides a circular point spread function and a quadratic illuminated area in the detector plane. The radiation shielding for the facility was optimized with regard to weight, cost, volume, and background radiation at the detector position. Different shielding materials and geometries were taken into consideration for this purpose.

With a single pin hole camera high flux at the specimen (low noise level in the projection) and high spatial resolution cannot be achieved simultaneously. A variety of other aperture types and reconstruction algorithms were tested for neutron radiography purposes. Investigations were carried out whether the noise level in projections can be decreased without reduction of resolution.

Abstract (german version)

Eine Neutronen Radiographie- und Tomographie-Anlage wurde geplant und am Forschungsreaktor FRM-II in München aufgebaut. Diese Arbeit beschreibt die Auslegung, die Optimierung und den Aufbau sowie erste Anwendungen der Anlage. Vor dem Aufbau wurde die gesamte Anlage mit rechnerischen Methoden optimiert. Die Anlage basiert auf dem Prinzip der Lochblendenkamera. Zur Reduktion von Untergrundstrahlung und Neutronen-Leckage durch das Blendenmaterial um die Blendenöffnung wurde ein Kollimator entwickelt, mit dem eine kreisförmige Abbildungsfunktion und eine quadratische voll ausgeleuchtete Fläche in der Detektorebene erzielt wird. Die Strahlungs-Abschirmungen für die Anlage wurden optimiert bezüglich Gewicht, Kosten, Platzbedarf und Untergrundstrahlung an der Detektorposition. Verschiedene Abschirm-Materialien und -Geometrien wurden zu diesem Zweck untersucht.

Mit einer Ein-Loch-Blendenkamera kann ein hoher Fluss (und damit ein geringes Rauschen in der Projektion) und eine hohe örtliche Auflösung nicht gleichzeitig erzielt werden. Zahlreiche andere Blenden-Konfigurationen und Rekonstruktions-Algorithmen wurden im Hinblick auf Anwendungen in der Neutronen-Radiographie untersucht. Ziel hierbei war insbesondere die Reduktion des Rauschens in Projektionen ohne Verschlechterung der Auflösung.

Contents

1 Introduction

The first radiography was recorded in 1895 by W. K. Röntgen using a radiation which he called X-rays [1]. Beside the application in medicine Röntgen perceived the wide field of technical applications; in the same year he took a photograph of a weld of zinc plates. The significance of X-rays for the detection of invisible flaws was immediately realized by other research groups, who produced X-ray radiographies in Europe and the USA. It was later found that the attenuation of X-rays increased smoothly with atomic number, indicating that X-rays interact with the orbital electrons around the atomic nucleus. In X-ray radiography a high contrast between elements with highly differing atomic number is achieved. Contrast between close-by elements is rather low.

The first neutron radiography experiments were carried out by H. Kallman in 1935 [2] soon after the discovery of the neutron by Chadwick in 1932 [3]. Neutron radiography is a complementary technique to X-ray radiography: Neutron interaction probabilities are dependent on the nucleus structure. Contrary to X–rays, neutrons are attenuated by some light materials, as e.g. hydrogen, lithium, and boron but penetrate many heavy materials. The major advantage of neutron radiography is its ability to reveal light elements such as hydrogen contained in materials. Even contrast between some close-by elements is rather high. X-ray radiography and neutron radiography are an ideal supplement of each other.

The construction of the new research reactor FRM-II (Forschungsreaktor München) opened the opportunity of a new neutron radiography facility: The high neutron flux yield of the FRM-II provides ideal preconditions for neutron radiography. The FRM-II is a neutron source that is aimed to research purposes in the field of physics, chemistry, biology, geology, archeology, medicine, material sciences, and other fields of neutron applications. The neutron source is an heavy water moderated reactor with a thermal power of 20 MW. The first criticality of the reactor was in March 2004. The reactor core is a compact fuel element containing highly enriched ^{235}U. The neutrons are extracted from the moderator vessel by help of 12 beam tubes. The beam tubes are not directed towards the reactor core, but are arranged in a tangential setup. The effective neutron sources for the experiments are the regions near the entrances of the beam tubes. The tangential arrangement offers the opportunity to get a rather high neutron flux simultaneous with a relative low gamma radiation background. The different beam tubes provide different neutron spectra: fast (1 MeV region), hot (0.1 eV region), thermal (25 meV region), and cold (2.5 meV region). In all experiments that do not use fast neutrons, the latter are regarded as bothering background. The tangential setup of the beam tubes keep the fast neutron component at a minimum. The FRM-II neutron source provides a very high neutron flux for the experiments. A high neutron flux enables for high quality neutron radiographies. Neutron radiography is an interesting application of neutrons in a manifold of scientific and technical fields. Aim of neutron radiography is to reveal inner structures of specimen in a non-destructive way. This is achieved by spatial resolved measurement of neutron transmission through the specimen. Therefore a neutron radiography and tomography facility, called ANTARES (ADVANCED NEUTRON TOMOGRAPHY AND RADIOGRAPHY EXPERIMENTAL SYSTEM) was constructed at FRM-II. This thesis describes the designing, optimization, construction and first applications of this facility. Neutron radiography can be done with fast neutrons as well as with thermal and cold neutrons. Most facilities prefer thermal neutrons because with most specimen a higher contrast can be achieved than with fast neutrons. The advantage of high attenuation in the specimen becomes a disadvantage when observing large specimen from high attenuating material. In this case fast neutrons are to be preferred. Anyway, the ANTARES facility makes use of a cold neutron spectrum. This energy range yields best results for the majority of specimen with respect to their size and their material composition. A cold neutron spectrum provides a high flux in the energy range of Bragg cut-offs, which enables for energy selective radiography [11]. With cold neutrons the phase contrast effect [12] is more distinct than with thermal neutrons with same beam geometry (divergence). Applications where fast neutrons are superior are covered by another experiment (NECTAR) [80][87] at FRM-II.

There are practically no lens systems for neutrons. The basic principle of a neutron radiography facility is therefore that of a pin hole camera. The size of the pin hole (aperture) and the distance between pin hole and specimen defines the spatial resolution of the facility. A small aperture diameter D combined with a big distance L between aperture and specimen enables for a high spatial resolution. From this point of view the ratio L/D should be as big as possible. On the other hand, flux at the specimen is proportional to $(D/L)^2$. A low neutron flux makes long exposure times necessary in order to get a satisfying signal to noise ratio SNR in the projection. Hence the setup of a neutron radiography experiment is always a compromise between high spatial resolution and high SNR. At the ANTARES facility a device for changing the L/D ratio was installed. The L/D ratio can be adjusted to the attenuation of the specimen and to the purpose of the experiment. L/D ratios in the range of 400 up to

16000 can be chosen. There are no 'black' aperture materials for neutron radiation, especially not for the background of epithermal and fast neutrons. The aperture is therefore part of an extended collimator structure. A special inner shape of the collimator was designed, that minimizes the leakage of neutrons through regions outside the desired transmission area. Only neutrons from a quadratic area on the entrance window of the beam tube are transmitted to a quadratic area in the detector plane. Nevertheless the point spread function has the desired shape of a pill-box. The point spread function describes how a point in the specimen is mapped to the detector [21]. The unavoidable gamma background is also minimized by the collimator structures. Despite the quite high L/D ratios a very high neutron flux at position of the specimen is achieved at the ANTARES facility. For a L/D ratio of 400 a flux of about 10^8 $cm^{-2}sec^{-1}$ is obtained. For the big neutron flight path between aperture and specimen an evacuated flight tube is useful. Without the flight tube activation of air and loss of neutron flux would be high. The flight tube was designed to minimum neutron scattering and gamma production. This is important for both beam quality for experiments and for keeping small the radiation shieldings.

Of course, a high neutron flux makes radiation shieldings necessary. The shieldings were optimized with the goals of meeting the radiation protection purposes and keeping low the background radiation for other experiments. Additional optimization criteria were low weight and cost and small extension of the shielding arrangement. Different shielding materials and geometries were tested for this purpose considering attenuation of neutron radiation, gamma radiation and production of gamma radiation (generated gamma radiation) by neutron interaction in the shielding material. The impact of scattered neutrons and generated gamma radiation at the location of the detector was minimized. The shielding should not be a monolithic structure. It is rather a kit of different shielding elements. The influence of the unavoidable gaps between the shielding elements on the dose rate level outside the shielding was tested considering different shapes and widths of gap systems.

The whole radiography facility was optimized computationally. Due to the complex geometry and the necessary energy resolution the Monte Carlo method is the method of choice. Results of methods which make use in discretizations of energy, space, and angular distributions (e.g. discrete ordinates) would yield unpredictable error intervals. Many different very detailed Monte Carlo models of the facility were programmed. The models include all relevant structures as there are the reactor core, the moderator vessel, the cold source and its surrounding, the beam tube, the water pool, the biological shielding, the collimator structures, the shutters, the flight tube, beam limiters, all shieldings of the facility etc. The model for the actual version is shown in Fig. 2.15. The probability of a neutron starting in the reactor core to reach the position of the specimen in the ANTARES facility is in the order of 10^{-10}. The probability to reach the outer margin of the radiation shieldings is even much lower. This makes Monte Carlo calculations very difficult. Many different variance reduction techniques have to be applied and to be adjusted to each other in order to get satisfying results in a reasonable calculation time. However, in this paper the calculation methods are not described but only the results of calculations. Descriptions of the different principles of calculation techniques can be found in [29][15][89][90].

The ANTARES facility enables for investigation of objects up to a size of 1 m x 1 m x 1 m and a weight of 500 kg. Specimens are objects from industry, archeology, geology, etc.. The total 3-D information of the inner structure can be observed by rotation of the object in the beam [4]. Indeed there is another neutron radiography facility at ILL [72] that provides an even higher flux at the specimen, but a high beam divergence ($L/D \approx 100$) limits spatial resolution to values far below that of the ANTARES facility. Considering all beam quality parameters as there are beam divergence, flux at the specimen, contamination of the neutron beam by fast and epithermal neutrons, gamma background in the beam, scattered neutrons from structure elements and gamma production in structure elements, the ANTARES facility is actually the most advanced facility in the world. Some results of the first measurements are shown in this paper.

Whenever a high spatial resolution is desired with a pin hole camera, the diameter of the pin hole has to be chosen small. By this the flux at position of the specimen is decreased considerably. A high flux is desirable in order to obtain a high signal to noise ratio SNR in the projection with short exposure time. From this problem of a pin hole camera the question arises whether an increase of resolution can also be achieved without decreasing the transmission area of the aperture. Several image reconstruction algorithms were tested for this purpose. Blurred projections obtained by apertures with big transmission areas were deconvoluted with the point spread function PSF of the system. The PSF describes how one point in the specimen is mapped to the detector plane. Whenever the signal from the specimen does not exceed the noise level of the detector system (e.g. thermal noise from the CCD chip), choosing a bigger transmission area of the aperture and application of image reconstruction

algorithms can improve the quality of projections considerably. The SNR in the resulting reconstruction exceeds that one of the unprocessed data obtained by an aperture with smaller transmission area without reduction of spatial resolution. The quality of projections and their reconstructions strongly depends on the shape of the PSF. The PSF is shaped by the aperture of the facility. Investigations were carried out whether other aperture shapes than the single pin hole arrangement are advantageous in neutron radiography. Coded masks as used e.g. in X-ray astronomy were tested for this purpose. In contrast to applications in astronomy most specimens in neutron radiography are not 'point like' but extended and fine structured objects. For investigation of such specimen these aperture types are less beneficial: The quality of reconstructions do not exceed the quality of unprocessed projections obtained by a single pin hole mask. However a multiple hole aperture was found that improves the quality of projections when only a very low neutron flux is available. The arrangement of holes is non redundant (non redundant array; NRA). Similar to other coded masks the original idea for reconstructing projections obtained by a NRA mask is a correlation algorithm, which also leads to disappointing results for extended fine textured specimen. Therefore deconvolution techniques were tested in combination with NRA masks. The quality of reconstructions exceeds that of projections obtained by a single pin hole aperture when only a very low neutron flux would be obtained by the single hole aperture. Application of this technique is useful e.g. in phase contrast radiography. The phase contrast effect is only observable when very high L/D ratios are applied. Hence the available neutron flux is decreased considerably. The necessary exposure time in phase contrast radiography is very long (up to several days). Measurements showed that the signal to noise ratio in a phase contrast radiography can be increased by help of a NRA mask in combination with deconvolution techniques without increase of exposure time. Another application is dynamic radiography of not periodic processes with high resolution. In this case the exposure time is limited by the desired time resolution for observation of the dynamic process.

2 Design of the new neutron radiography and tomography facility

2.1 Neutron source FRM-II

The FRM-II is a light water cooled reactor moderated by heavy water. The reactor core is very compact: It consists of a single, cylindrical fuel element with an outer diameter of 243 mm and a height of approx. 700 mm [9]. The fuel material is a dispersion of uranium silicide and aluminum. The uranium is highly enriched (93 % ^{235}U). By this compact core concept a very high ratio of thermal neutron flux to thermal power of the reactor is obtained. The maximum of unperturbed thermal flux is $8 \cdot 10^{14}$ $cm^{-2}s^{-1}$ [9] at a location of some 12 cm outside the fuel element in the moderator tank. The neutrons are extracted from the moderator tank by beam tubes that are directed towards the region with flux maximum (Fig. 2.1). The tangential arrangement of the tubes in relation to the core axis is to avoid direct view from the instruments to the core. This is to achieve a low background radiation of fast neutrons and gamma radiation for the experiments [8].

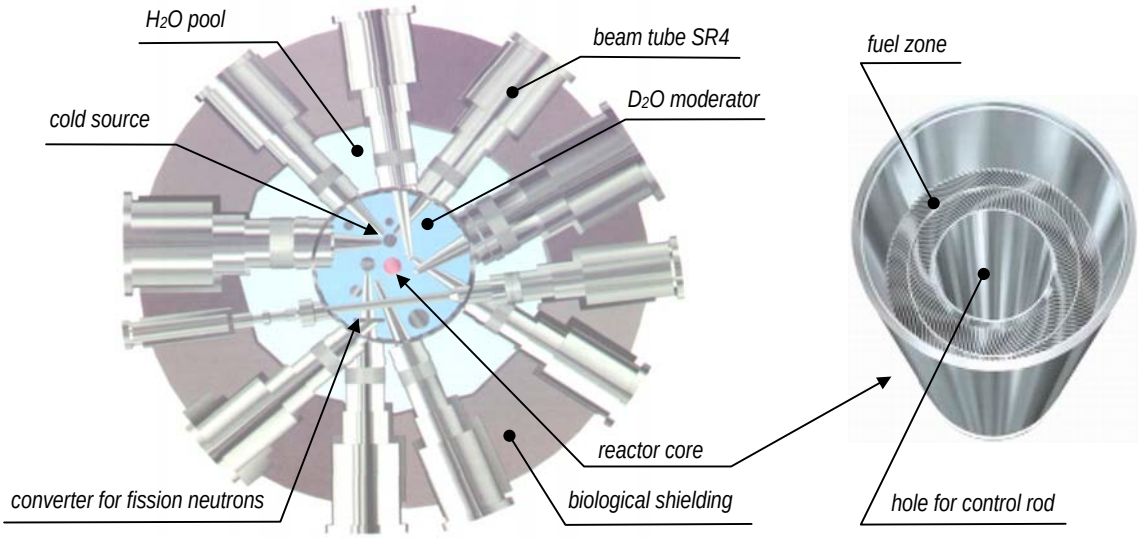

Fig. 2.1: Horizontal section through the reactor pool and the fuel element (SR4: Strahlrohr 4) [10]

2.2 Selection of the beam tube for the neutron radiography station

There are several criteria for the selection of the beam tube used for neutron radiography:

- Energy spectrum of the neutrons
- Size and homogeneity of the neutron beam
- Neutron flux density
- Practical aspects (building layout etc.)

It turns out that with the beam tube SR4B (SR4: Strahlrohr 4) an optimal match of both physical and practical parameters can be achieved. SR4B points to the cold source.

2.2.1 Cold neutron source

2.2.1.1 Neutron energy spectrum

Different neutron spectra are available at the FRM-II facility [8][10]:

- Cold spectrum from a 'cold source', maximum of energy distribution ≈ 3 meV (SR4)
- Thermal spectrum from the heavy water moderator (SR5)
- Hot spectrum from a hot source (SR9)
- Fast spectrum (fission spectrum from an ^{235}U converter plate at beam tube SR10). The fast neutron source consists of a plate of highly enriched uranium, which is installed at the converter experiment of the beam tube SR10. The converter is a plate of highly enriched uranium, which is mounted at the front end of the beam tube. Moderated thermal neutrons from the reactor core cause fission reactions in the plate. The fast fission neutrons are used directly for radiography without further moderation (optional polyethylene filters can be used for modification of the energy spectrum).

The terms 'cold' and 'hot' refer to the mean energy of the energy distribution. A cold neutron spectrum has some advantages for neutron radiography:

- With cold neutrons a high contrast in projections can be obtained, because for most materials the neutron cross section increases with decreasing neutron energy.
- A high flux in the cold energy region enables for energy selective neutron radiography around Bragg cutoffs [11].
- The phase contrast effect is higher for large neutron wavelengths [12].
- Neutron detection efficiency is higher in the cold energy region for most detection reactions.

The advantage of high cross sections with cold neutrons is sometimes also a disadvantage: The penetration depth in material is less than with neutrons of higher energy. Taking radiographs of large objects is therefore sometimes a problem with cold neutrons; the images will have small contrast and long irradiation times will be necessary. There is another neutron radiography station at FRM-II using fast neutrons from the fission source. Therefore there is no necessity of performing radiography of very large specimen with the cold neutron source. Thus the use of cold neutrons can be restricted to cases where they yield superior performance. It was decided to use a cold neutron spectrum for the ANTARES facility.

The cold neutron source is a "moderator vessel inside the moderator vessel". The inner vessel is filled with approximately 16 l of liquid deuterium, which is cooled down to 25 K [10]. A displacement body with no liquid deuterium is included inside the vessel. Its task is to prevent neutron scattering from the outer rim of the liquid deuterium in direction of the beam tubes SR1 and SR2. Neutrons from the outer rim experienced less interactions with the deuterium and have therefore in average higher energies compared to neutrons from the inner part. Neutrons coming from the center of the cold source are closer to the thermal equilibrium with the cold deuterium. The displacement body provides a colder spectrum for the beam tubes SR1 and SR2. The assembly of the displacement body is shown in Fig. 2.3 right hand side. On the assumption that the neutrons are in thermal equilibrium with there environment the neutron energy has a Maxwell distribution with the maximum at $E_{maximum} = k_B T$. A temperature of 25 K thus would result in $E_{maximum}$ =2.15 meV. The volume of the cold source is too small

to obtain the Maxwellian energy distribution of the thermal equilibrium of 25 K, however. Calculations were carried out for the reactor assembly. The simulations show that the maximum of the energy distribution is at about $3\ meV$ at the exit of the beam tube SR4 that is directed to the cold source. Anyway, the maximum is shifted to an energy approximately 10 times less than that in the moderator vessel outside the cold source. The flux in the energy region around $1\ meV$ is more than 10 times higher than with a thermal beam tube. A comparison of the neutron spectrum at beam tube SR4 with the thermal spectrum at beam tube SR5 [13] is displayed in Fig. 2.2.

The spectrum in the detector plane of the neutron radiography facility and the influence of the D_2 filling is discussed in more detail in chapter 2.8.1 'Spectral neutron flux density at position of the specimen'.

The spectral neutron flux density at the beam channel exit at the outer rim of the biological shielding of beam tube SR4 was also calculated by Gaubatz [13] in 1997. These calculations were not aimed to the investigation of details of the radiography facility, however. Besides, since then major changes in the arrangement of the cold source and the beam tubes etc. were carried out (e.g. the displacement body got a modified shape and a bigger volume, see Fig. 2.3). Thus it was advisable to build a new Monte Carlo model of the reactor assembly with special emphasis to spatial resolution in the region of the cold source and the beam tubes headed towards this secondary neutron source. The simulation was done by help of the Monte Carlo code MCNP.

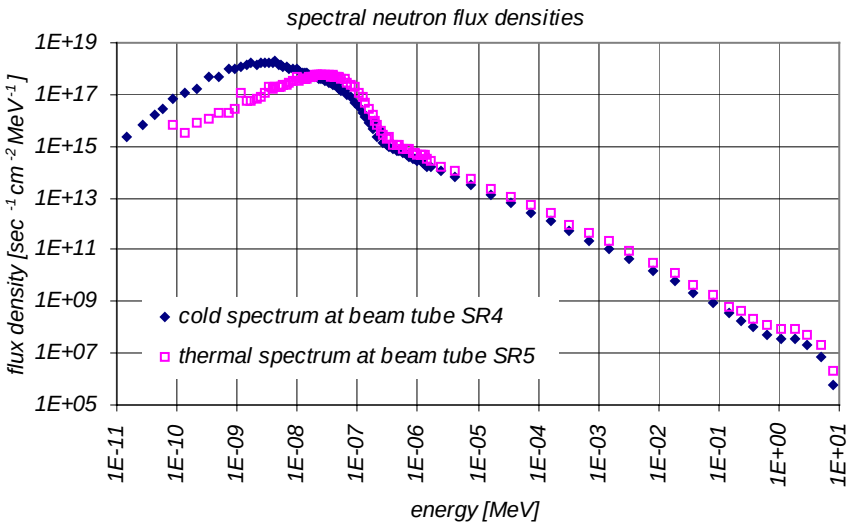

Fig. 2.2: Spectral flux density at the exit of the beam channel through the biological shielding at a beam tube, that is directed to the cold source (SR4), in comparison to the flux density at a thermal beam tube (SR5; data from [13])

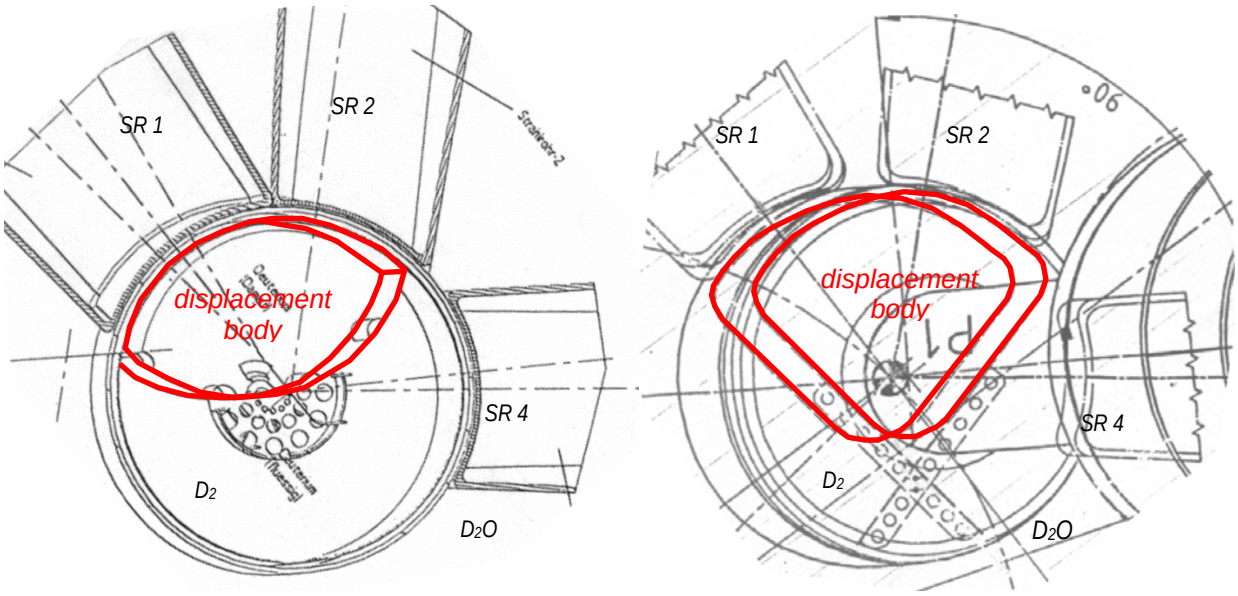

Fig. 2.3: The old geometry of the cold source (left hand side) and the actual geometry (right hand side)

A comparison of the spectral flux densities at the exit of the beam channel at the outer rim of the biological shielding calculated with the new model and the old model from Gaubatz are displayed in Fig. 2.4. The old geometry of the cold source comprises a smaller displacement body. The boundary between displacement volume and liquid D_2 is a cylinder barrel. In the new 'as built' version, a smaller volume of liquid D_2 is located directly in front of the entrance of beam tube SR4. Moderation of neutrons to the temperature of the liquid D_2 is therefore more complete in the old geometry; the spectral flux density is shifted to smaller energies.

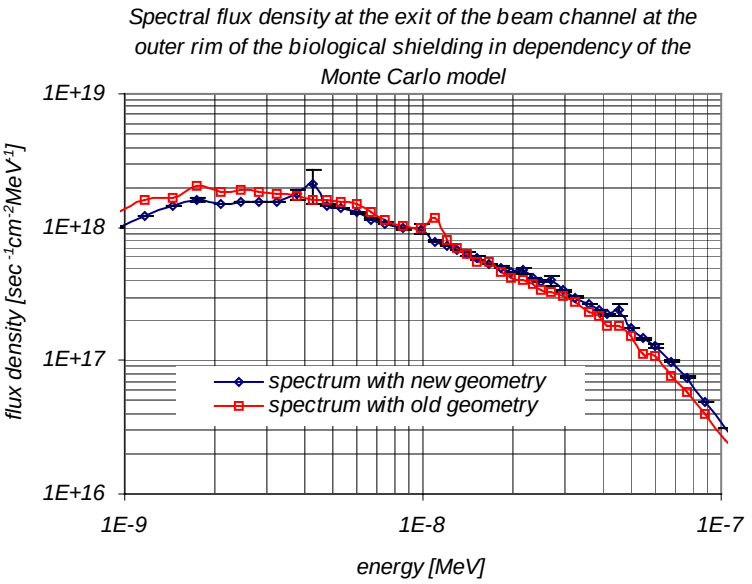

Fig. 2.4: Comparison of the spectral flux densities at the exit of the beam channel through the biological shielding obtained by the old and the new geometry of the cold source.

2.2.1.2 Spatial distribution of neutron flux

A vertical cut through the new 3D Monte Carlo model of the cold source and its surrounding is shown in Fig. 2.6. A horizontal cut along the axis of beam channel SR4B is displayed in Fig. 2.7. The cold source consists of an inner vessel with walls made from AlMg1SiCu and an outer vessel with walls made from zircaloy. The walls of beam tube SR4 consist of AlMg3 (thickness 6 mm). The Monte Carlo model comprises the moderator vessel, the surrounding water pool, a detailed model of the cold source, all beam tubes that are directed to the cold source, and the reactor core. It doesn't consider any of the other beam tubes, because their influences are negligible in this context. The geometry of the fuel element (reactor core) was taken from [13]. The energy distribution of fission neutrons is a Watt spectrum (Fig. 2.5) [13][14][15]:

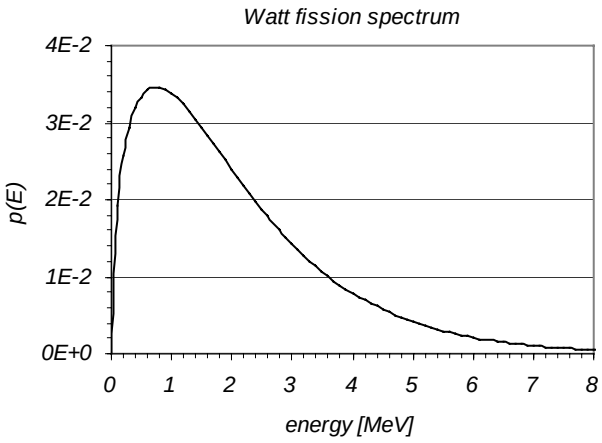

Fig. 2.5: Fission neutron energy distribution (Watt spectrum)

$$p(E) = \exp\left(-\frac{E}{0.998MeV}\right)\sinh\left(\sqrt{2.249MeV^{-1}\cdot E}\right)$$

where E is the neutron energy and $p(E)$ the probability for the emission of a neutron with energy E.

The neutron flux distributions in a horizontal plane at beam axis level of beam tube SR4 (plane as displayed in Fig. 2.7) is shown in Fig. 2.8 to Fig. 2.12 for five different energy groups (from fast to cold energy group).

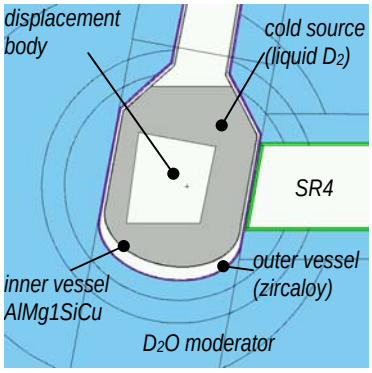

Fig. 2.6: Vertical cut through the Monte Carlo model of the cold source along the axis of beam channel SR4B

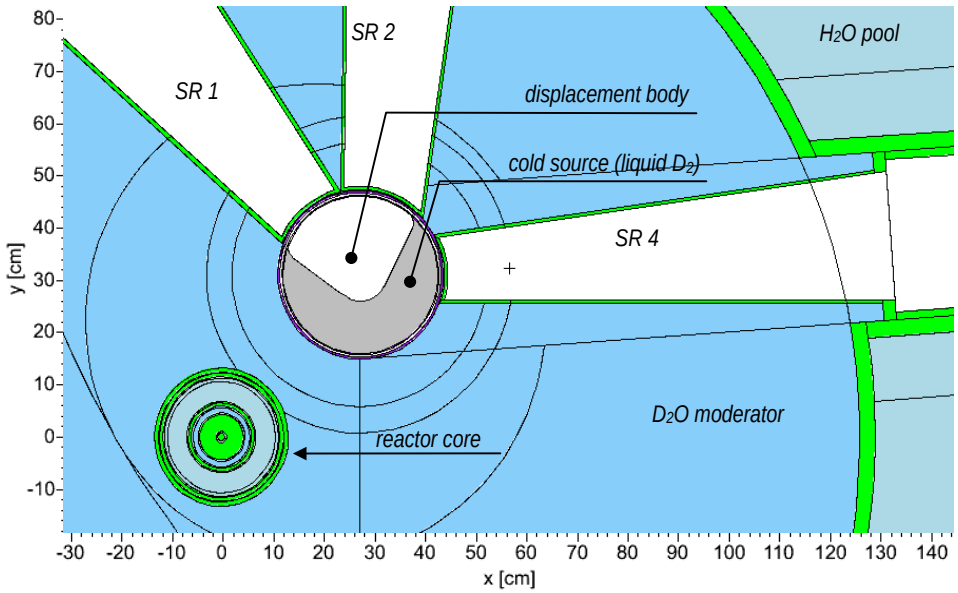

Fig. 2.7: Horizontal cut through the Monte Carlo Model of the moderator vessel, the cold source, and the reactor core

Fast energy range (E > 0.1 MeV)

Fission produces neutrons in the fast energy range. Therefore the maximal flux in the energy range above 0.1 MeV appears in the fuel zones of the reactor core (Fig. 2.8). A small flux depression occurs in the hole for the control rod in the center of the fuel element where no fission takes place. Neutrons are decelerated to lower energy by elastic scattering in the D_2O moderator: Therefore the fast neutron flux decreases with increasing distance to the fuel element. On the average 25 scatter events are necessary for slowing down fast neutrons into the thermal energy range [14]. At the location of the cold source the fast neutron flux is depressed by more than a factor 100 compared to the reactor core, but the effect of fast neutron scattering in the direction of the beam tubes is still clearly visible in Fig. 2.8. This fraction of fast neutrons is the most important component of radiation for the design and dimensioning of the radiation shielding of the experiment as described later.

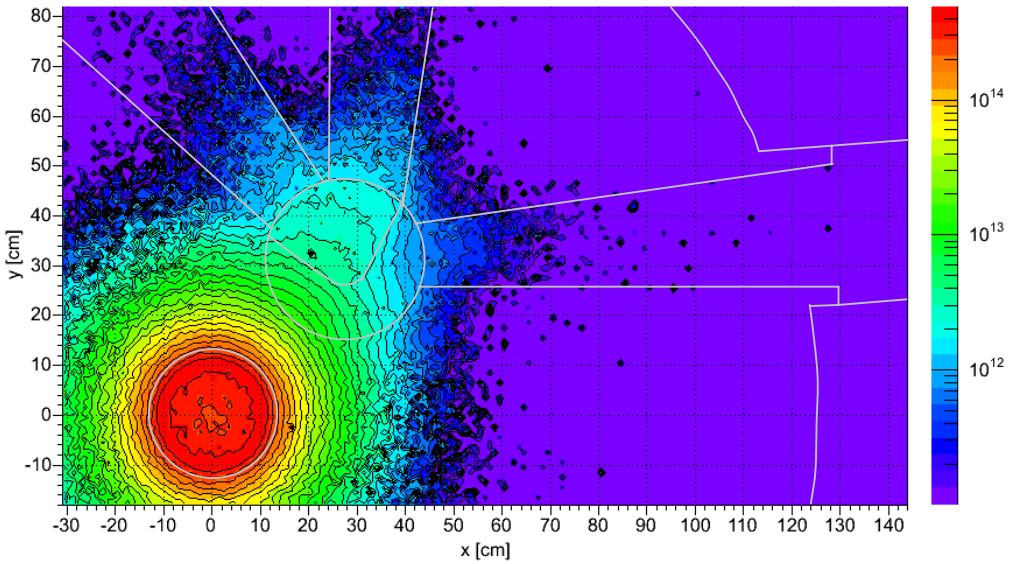

Fig. 2.8: Neutron flux [cm^{-2} sec^{-1}] around the reactor core and the cold source in the 'fast' energy range above 0.1 MeV. All values below 10^{11} cm^{-2} sec^{-1} are displayed in violet.

Epithermal energy range (1 eV < E <0.1 MeV)

The neutron flux density distribution in the epithermal energy range from 1 eV to 0.1 MeV is shown in Fig. 2.9. This flux component decreases considerably slower with the distance from the core than the fast neutron flux. This is because the epithermal energy group is populated by neutrons that are scattered down from higher energy groups. The moderator itself is therefore a secondary source for neutrons in this energy group.

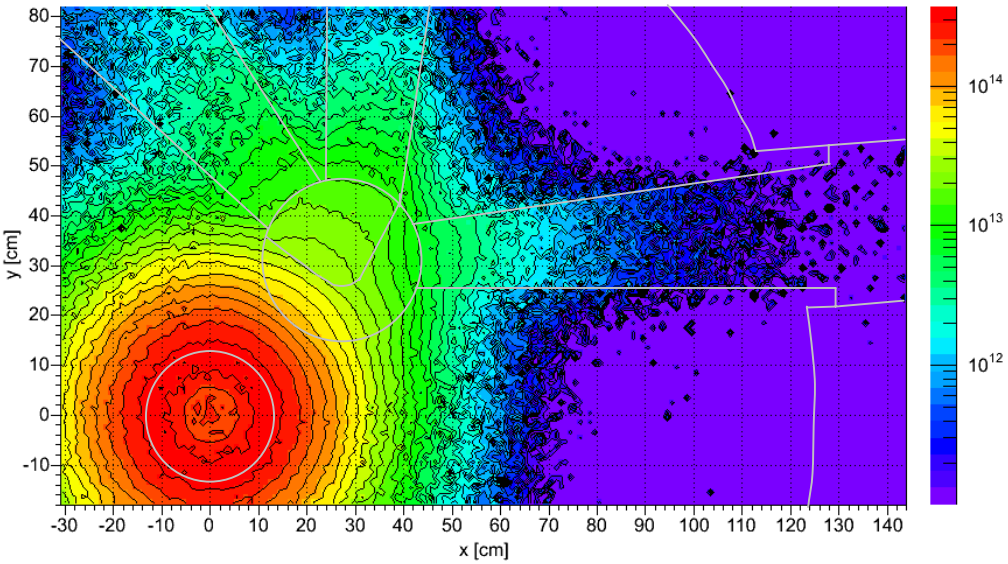

Fig. 2.9: Neutron flux [cm^{-2} sec^{-1}] around the reactor core and the cold source in the 'epithermal' energy range between 1 eV and 0.1 MeV. All values below 10^{11} cm^{-2} sec^{-1} are displayed in violet.

The reactor core is also a source for epithermal neutrons, because of down scattering in the coolant fluid (H_2O) flowing between the fuel plates.

Hot energy range (25 meV < E < 1 eV)

For all energies below 1 eV a clear flux depression appears at the location of the reactor core (Figs. 2.10, 2.11, 2.12). This is because fission events absorb slow neutrons. The flux maximum is outside the fuel element. In the 'hot' energy group from 25 meV to 1 eV the cold source is also a depression for neutrons due to down scattering to lower energies. Inside the cold source the neutron flux is rather inhomogeneous.

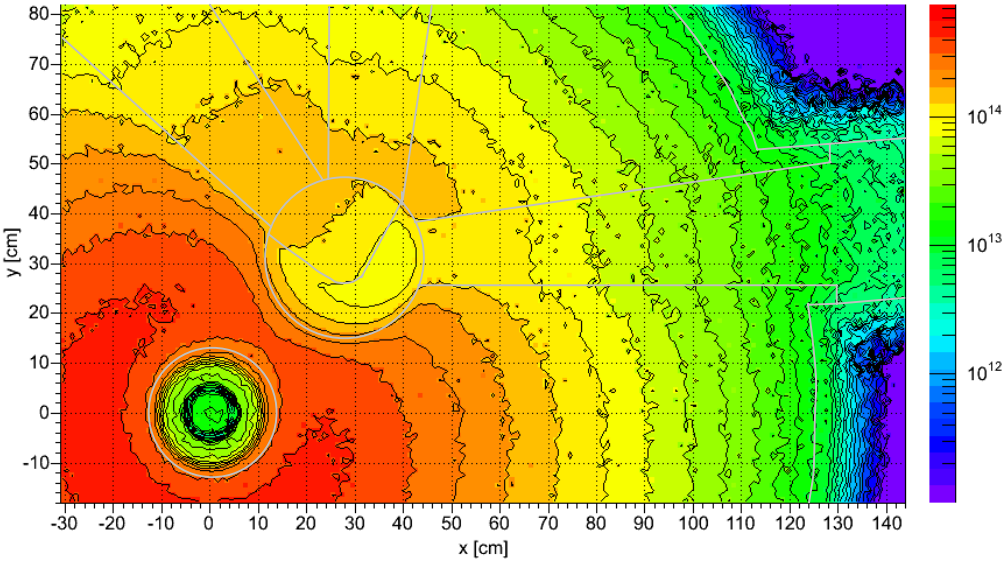

Fig. 2.10: Neutron flux [cm^{-2} sec^{-1}] around the reactor core and the cold source in the 'hot' energy range (25 meV to 1 eV). All values below 10^{11} cm^{-2} sec^{-1} are displayed in violet.

Thermal energy range (2.5 meV < E < 25 meV)

The most important energy group for radiography experiments at the ANTARES facility is that with energies below 25 meV. In the range between 2.5 meV and 25 meV there is an overlap of the energy distributions of neutrons emerging from the cold source and those coming from the moderator vessel. Therefore both regions in the assembly are considerable secondary neutron sources (Fig. 2.11).

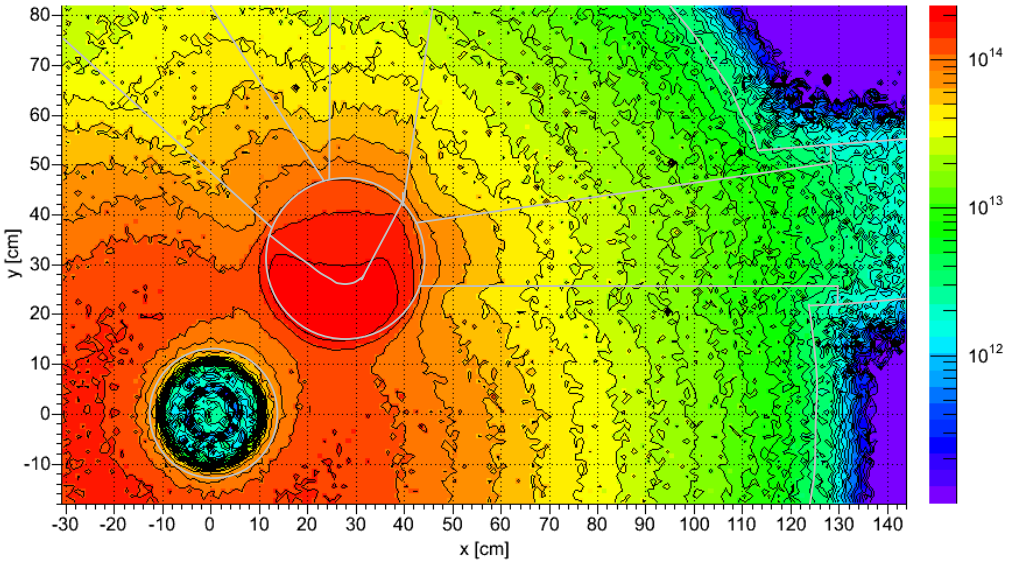

Fig. 2.11: Neutron flux [cm^{-2} sec^{-1}] around the reactor core and the cold source in the 'thermal' energy range (2.5 meV to 25 meV). All values below 10^{11} cm^{-2} sec^{-1} are displayed in violet.

Cold energy range (E < 2.5 meV)

For cold neutrons below 2.5 meV the D_2 volume inside the cold source is the only secondary neutron source (Fig. 2.12). The flux depression inside the cold source is caused by the displacement body. However, the flux distribution at the entrance window of the beam tube SR4 is flat, as desired for radiography experiments.

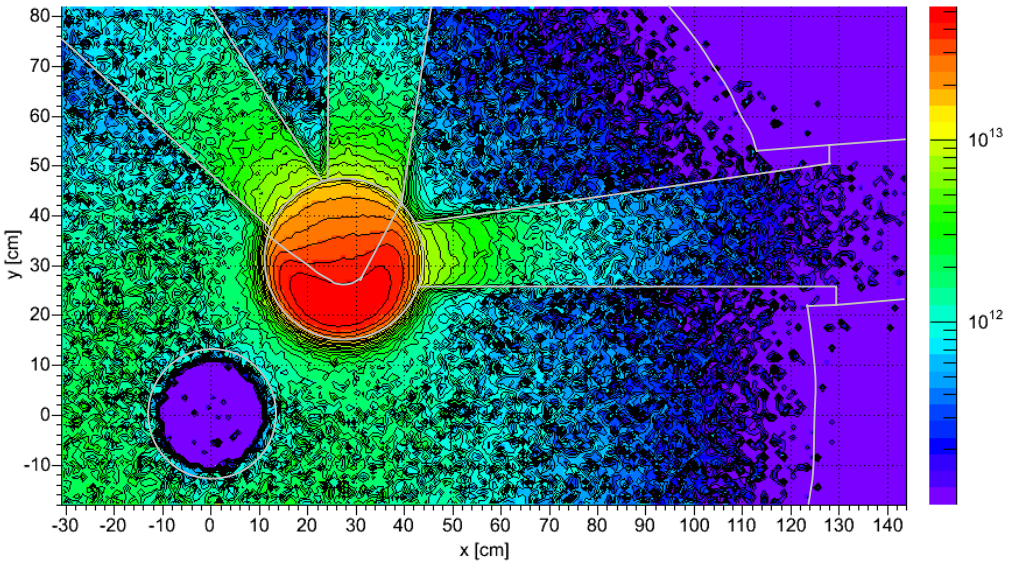

Fig. 2.12: Neutron flux [cm^{-2} sec^{-1}] around the reactor core and the cold source in the 'cold' energy range below 2.5 meV. All values below 10^{11} cm^{-2} sec^{-1} are displayed in violet.

2.2.1.3 Practical aspects

The axis of the beam tube SR4B is heading to a corner of the reactor hall far away from the biological shielding [86]. This big distance enables for a long flight path of neutrons (21 m), which is important for the spatial resolution of the facility. The area at the corner is not used for other experiments, so that a big experimental chamber for the ANTARES facility can be installed. This is important when

investigating big sized specimens like e.g. car engines. From this point of view, the beam tube SR4 seems to be the best choice for the neutron radiography station.

2.2.1.4 Size and homogeneity of the neutron beam

The beam tube SR4 (Fig. 2.13) has an entrance window with an area of 18 cm x 12 cm. The entrance of the beam tube is the effective neutron source for the radiography facility. Beside other parameters, the size of the effective neutron source defines the fully illuminated area in the detector plane. Only this area can be used for radiography.

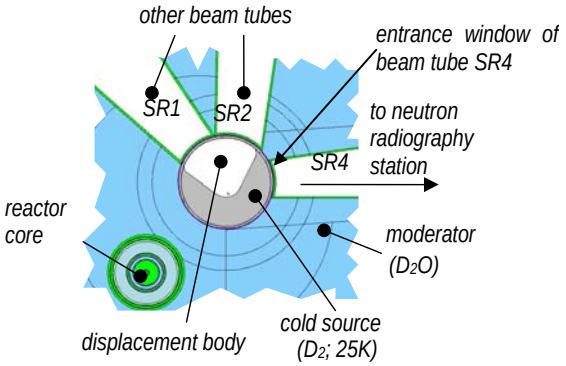

Fig. 2.13: Horizontal cut through the Monte Carlo model of the cold source and its surrounding inside the moderator vessel

The homogeneity of the neutron flux at the entrance window of the beam tube is a crucial parameter for the performance of the radiography facility. An inhomogeneity of the effective neutron source will result in inhomogeneous illumination of the object and the detector, which is disadvantageous for radiography experiments. The influence of inhomogeneities can be corrected to some degree (open beam correction), but this is not without a loss of information in the final images.

Full homogeneity must not be expected at least for the following reasons:

- Flux is non-uniform due to the structure of the cold source itself.
- Flux is non-uniform due to the beam tubes of other experiments (SR1, SR2).

The arrangement of the displacement body in the cold source is asymmetric relative to the axis of beam tube SR4.

In addition, the other beam tubes (SR1, SR2) are arranged in an asymmetric way. As there is no back scattering from the interior of the tubes, these beam tubes will cause a flux depression.

These influences were estimated by calculation of beam profiles in the detector plane of the radiography station for different arrangements of the cold source and its environment inside the moderator vessel:

- Cold source without displacement body and without other beam tubes. The volumes of the tubes are replaced by heavy water.
- Cold source with displacement body but no other beam tubes
- Real arrangement with displacement body and beam tubes.

A circular aperture with 4.3 cm diameter (installed at a distance of 3.7 m from the entrance window of the beam tube) was assumed. The detector plane has a distance of 21 m from the cold source and is perpendicular to the beam axis (see illustration on the right hand side). All structure elements (e.g. flight tube, aluminum widows, etc.) of the final setup are included in this calculation. This corresponds to the actual setup of the instrument. The calculation model of the whole facility is shown in Fig. 2.15.

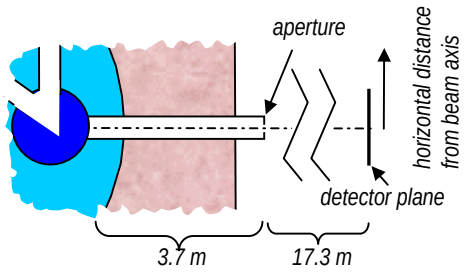

Neutron flux profiles in the energy range below 1 eV in the detector plane are displayed in Fig. 2.14. The profile obtained without displacement body is asymmetric. This is due to different pathlengths of the neutrons through the moderator. The situation is reversed when the displacement body is included: Flux decreases from left to right. The effects caused by both, the displacement body and the neighboring beam tubes, compensate each other, thus yielding a rather flat beam profile. Inhomogeneities are rather low for neutrons in the interesting energy range below 1 eV. For higher energy ranges there are more significant inhomogeneities.

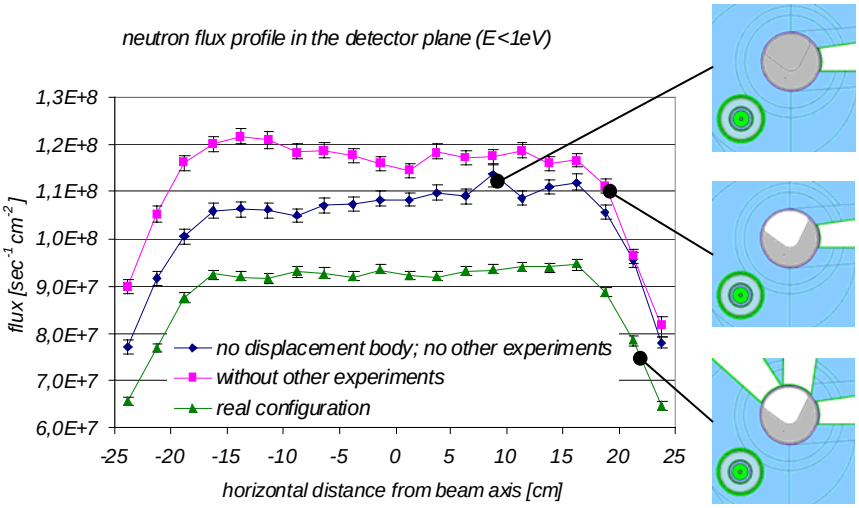

Fig. 2.14: Neutron flux profiles in the energy range below 1 eV in the detector plane for different theoretical arrangements in the moderator vessel.

The total neutron flux at detector position of the ANTARES facility is increased by the displacement body by a factor of about 10 %. The beam tubes of other experiments (SR1 and SR2) cause a flux decrease of about 28 % due to reduction of back scattered neutrons from the inner beam tube volumes.

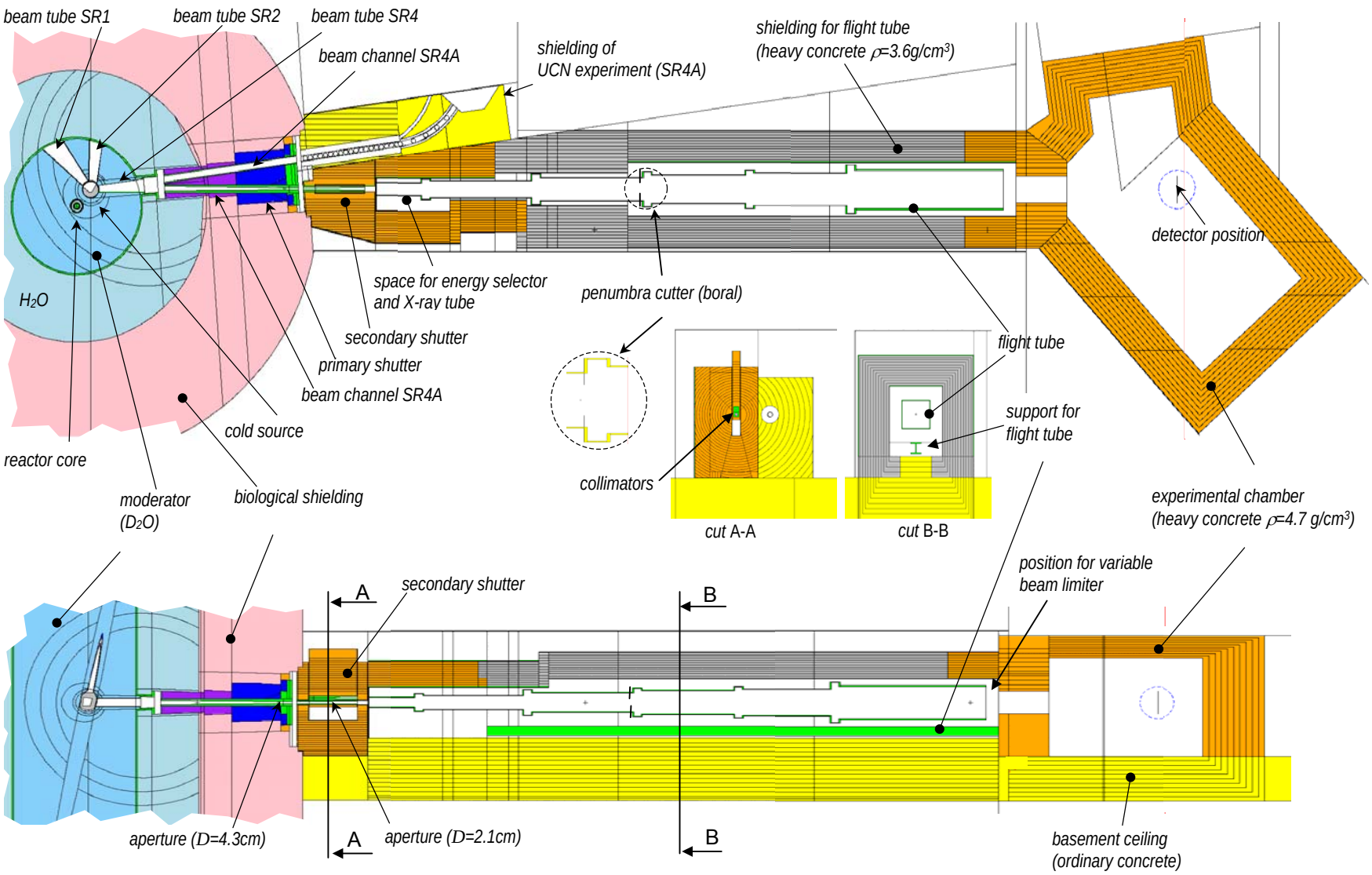

Fig. 2.15: Horizontal cut (top) and vertical cut (bottom) through the Monte Carlo model of the ANTARES facility (as-built version)

2.3 Aperture

Size, location and shape of the aperture define the spatial resolution of the ANTARES facility and the size of the fully illuminated area in the detector plane. For high resolution it is desirable that the information of only one path through the object is projected to one point in the detector plane. This can be achieved with a non-divergent beam, i.e. an exactly parallel neutron beam or a cone beam, fanning-out from one point (pinhole aperture). For extended apertures (divergent beam), the information of neighboring paths through the object overlap in one point of the detector plane, and the resulting projection has a limited spatial resolution. As measure for the beam divergence, the L/D ratio is widely used [16][18], where L is the distance between aperture and object and D is the diameter of the aperture. The overlap of information decreases with increasing L/D ratio. The flux in the object plane decreases with increasing L/D ratio. Therefore choosing the L/D ratio for a facility is always a compromise between high intensity (high signal to noise ratio) and high resolution.

2.3.1 Desired parameters

There is no optimal L/D ratio. The desired L/D ratio strongly depends on the object and the purpose of the investigation. Therefore it was decided for the ANTARES facility not to have a fixed beam divergence, but to use optional a medium L/D ratio for large specimens with high attenuation and a high L/D ratio for small objects and a subtle structure.

The size of the fully illuminated region in the detector plane should be sufficient for most “day-to-day” applications. On the other hand it should not be too big in order to keep background radiation low (scattered neutrons around the detector position). The desired size of the fully illuminated area is about 40 cm x 40 cm [71].

In our case the desired parameters are:

- The L/D ratio must be optional 400 or 800
- The fully illuminated area must have a size of about 40 cm x 40 cm.

2.3.2 Fixed parameters

Parameters given by geometry of the moderator vessel, the biological shielding and the reactor hall are:

- The maximum distance between entrance window of the beam tube (margin of cold source) and the position for the specimen is 21 m ± 1 m. This distance cannot be reduced because of other experiments, which are closer to the biological shielding. Bigger distances are not feasible because of the rear wall of the reactor hall.
- The channel between the cold source and the outer rim of the biological shielding (in 4 m distance to the cold source) is hardly accessible. The cross section of the channel is 12 cm x 12 cm.
- No structure elements may be mounted inside the beam tube within the moderator vessel and the water reservoir. Minimum accessible distance to the entrance window of the beam tube is therefore 1.3 m. Structures at closer distances could affect the reactivity of the reactor and would be in the sight of view of the neighbor experiment (Ultra Cold Neutron source at beam channel SR4A).
- The entrance window of the beam tube at the margin of the cold source has a size of 18 cm x 12 cm (height x width). That is the effective secondary neutron source for the facility

2.3.3 Shape of aperture

Without a diaphragm, the beam channel in the biological shielding would act like an aperture. The illuminated field in the detector plane would become unsatisfactory with respect to size and homogeneity of illumination. A relative small area of the detector (12 cm x 12 cm) would be fully illuminated; the remaining area would be in the penumbra (Fig. 2.16 bottom). Therefore, an aperture is essential for the ANTARES facility. Several different aperture and collimator types were considered. For calculation of the obtained neutron flux distributions in the detector plane, aperture and collimator materials were assumed to be ideal, i.e. each neutron that enters the material is absorbed immediately.

Sometimes parallel collimators (honey comb collimators) are used in radiography [20]. A parallel collimator with a length of 2.72 m and 6 x 6 channels, each of size 2 cm x 2 cm, was calculated. The small field size (Fig. 2.17) in the detector plane is prohibitive for a series of planned experiments with large specimens. Even if the cross section of channels is doubled, the resulting width of fully illuminated area is not satisfying (Fig. 2.18). An additional bothering effect of this collimator type is that the point spread function PSF (see chapter 3.3 'Image degradation in neutron radiography', [21]) in the detector plane is not shift invariant, hence resolution is not constant over the whole fully illuminated area. This type of aperture/collimator has therefore no advantages when applied in the given geometry.

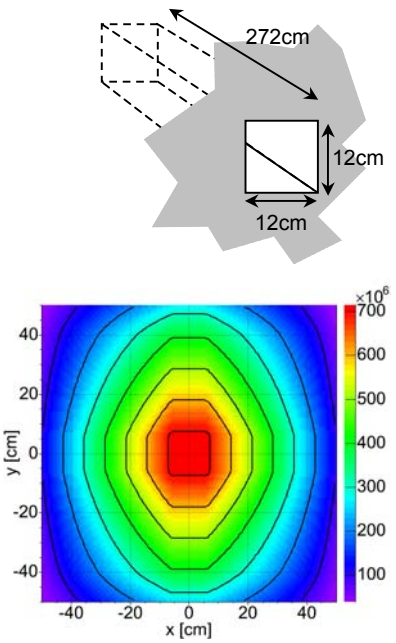

Fig. 2.16: Top: Channel in the biological shielding without aperture.
Bottom: Neutron flux [cm^{-2}sec^{-1}] in the detector plane if no aperture is used; collimation by the channel in the biological shielding.

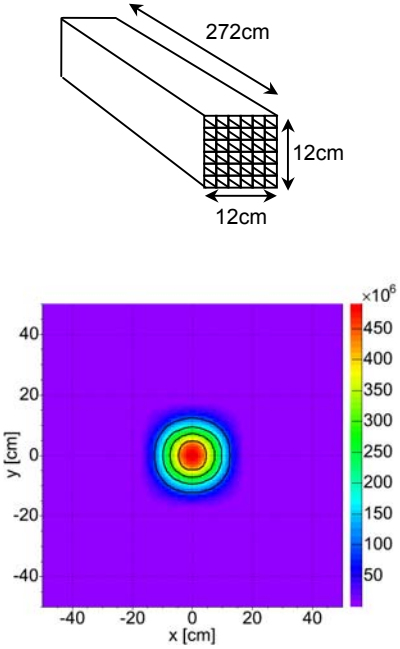

Fig. 2.17: Top: Parallel collimator with 6x6 channels inside the channel in the biological shielding.
Bottom: Neutron flux [cm^{-2}sec^{-1}] in the detector plane for a parallel collimator with 6x6 channels.

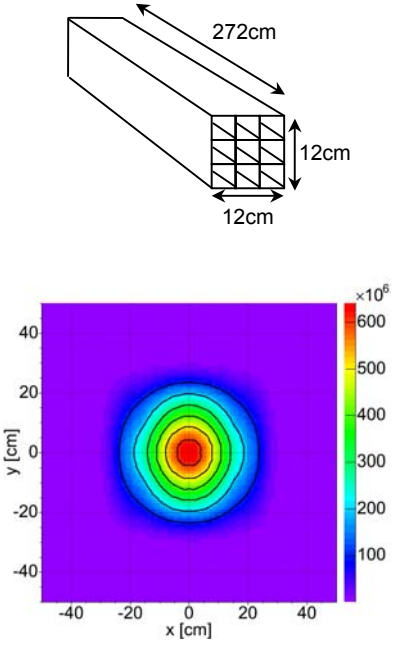

Fig. 2.18: Top: Parallel collimator with 3x3 channels inside the channel in the biological shielding.
Bottom: Neutron flux [cm^{-2}sec^{-1}] in the detector plane for a parallel collimator with 3x3 channels.

As the secondary source of the facility has a rectangular shape and the desired shape of the fully illuminated region in the detector plane is quadratic, apertures with rectangular and quadratic transmission area were considered. The advantage of such designs is that a corresponding collimator has only planar surfaces, hence machining is easier and cheaper than for other collimator types as described below. A quadratic aperture of 14.5 cm^2 transmission area (Fig. 2.19 top), located at a distance of 3.7 m from the cold source, creates a fully illuminated region in the detector plane as shown in Fig. 2.19 bottom. The desired width is close to the desired one, but the height is too big. Having a neutron beam of bigger size than the detector causes background radiation in the facility. This is not desired because of degradations in projections and the necessity of bigger radiation shieldings. An additional disadvantage of quadratic apertures is that the resolution in projections is not constant but depends on direction: In the diagonal it is worse than in horizontal and vertical direction. For some detector systems, as e.g. the ANTARES standard detector system (described in chapter 2.9.1 'ANTARES detector system'), this would not be bothering, because the detector itself provides less resolution in the diagonal (due to quadratic shape of pixels). For other detection methods without pixel structure, e.g. a Gd layer in combination with X-ray film [16], this effect is really bothering.

In principle the fully illuminated area can be shaped exactly to the desired size by a rectangular aperture as shown in Fig. 2.21, but none of the disadvantages that occur with quadratic apertures are resolved: The penumbra region in vertical direction is enlarged and the spatial dependency of resolution is worse.

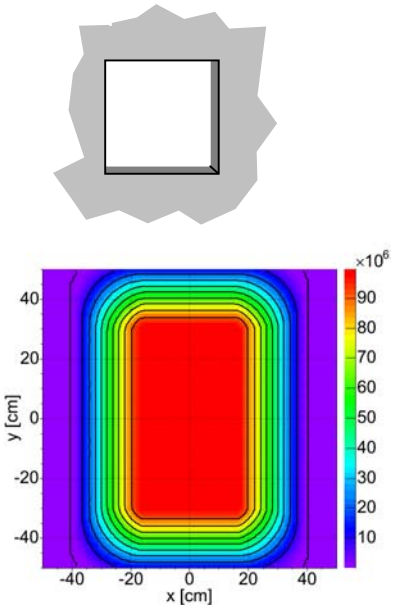

Fig. 2.19: Top: Quadratic aperture.
Bottom: Neutron flux [cm^{-2}sec^{-1}] in the detector plane for the quadratic aperture.

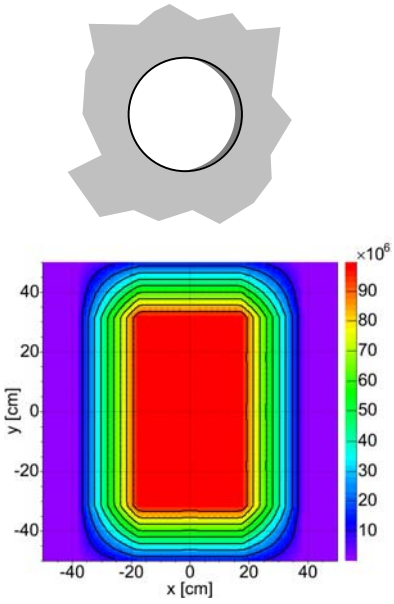

Fig. 2.20: Top: circular aperture.
Bottom: Neutron flux [cm^{-2}sec^{-1}] in the detector plane for the circular aperture.

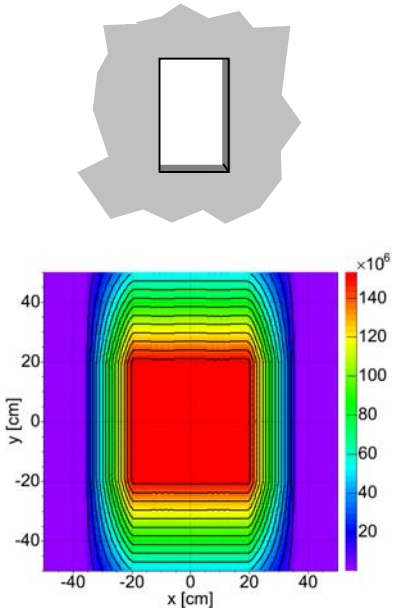

Fig. 2.21: Top: Rectangular aperture, that shapes the fully illuminated area in the detector plane to a square.
Bottom: Neutron flux [cm^{-2}sec^{-1}] in the detector plane for this aperture.

A circular aperture (Fig. 2.20 top) with same transmission area as the quadratic aperture described above (Fig. 2.19) provides the same size of the fully illuminated area without the disadvantage of directional dependency of resolution. The problem of large beam height in the detector plane can not be resolved by the aperture but only by limitation of the source area: The effective source is limited to an effective size of 12 cm x 12 cm by a collimator as described below. By this, fully illuminated areas that are close to the desired one can be obtained by circular apertures. The area obtained by an aperture with diameter 4.3 cm at a distance of 3.7 m from the cold source is shown in Fig. 2.22. An aperture with diameter 2.1 cm, located at a distance of 430 cm from the cold source, provides a fully illuminated area as shown in Fig. 2.23. In both cases the fully illuminated areas are close to the desired one.

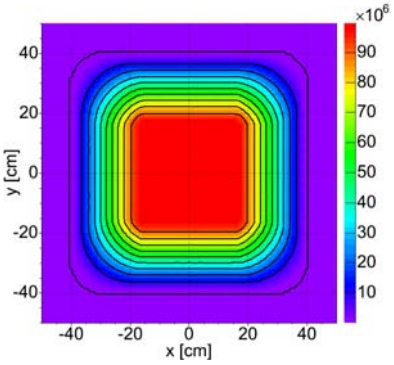

Fig. 2.22: Neutron flux [cm^{-2}sec^{-1}] in the detector plane for a circular aperture with diameter 4.3 cm located at 370 cm distance to the source. The source area is limited to 12 cm x 12 cm.

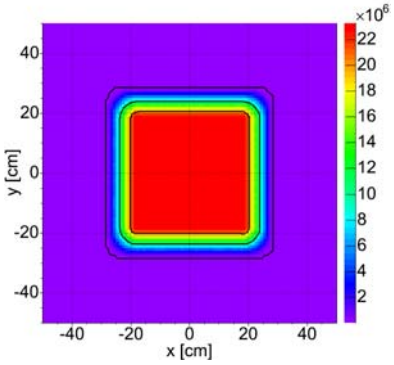

Fig. 2.23: Neutron flux [cm^{-2}sec^{-1}] in the detector plane for a circular aperture with diameter 2.1 cm located at 430 cm distance to the source. The source area is limited to 12 cm x 12 cm.

2.3.4 Location of aperture

Considering only the beam divergence and intensity, there is no preference in choosing the location of the aperture because the intensity in the object plane is proportional to D^2/L^2, i.e. for each aperture position, an aperture diameter can be found that keeps beam divergence and intensity constant. However, there are several issues for a deliberate choice of the location:

- Radiation shieldings can be kept small when all undesired radiation components are removed as close to the source as possible (these components are neutrons that do not cross the transmitting area of the aperture and gamma radiation).

- The unwanted background intensity of scattered neutrons and generated gamma radiation from neutron absorption in the aperture and collimator material is reduced in the detector plane for big distances between aperture and detector (geometry effect).
- The size of the fully illuminated area strongly depends on the location and the size of the aperture
- Close to the aperture position it must be possible to install an aperture exchanging device, in order to set the L/D ratio to the desired value.

The first two points are in favor of locating the aperture as close to the cold source as possible (i.e. at a big distance to the detector). The last point requires a position outside of the biological shielding, because access to the channel part inside the biological shielding is limited. The width of fully illuminated area W_f in the detector plane is given by Eq. 2.1, where W_s is the width of source, X_{ap} is the distance between source and aperture, D is the diameter of aperture and L is the distance between aperture and detector plane (in literature L often indicates the distance between aperture and specimen). The quantities are displayed in Fig. 2.24.

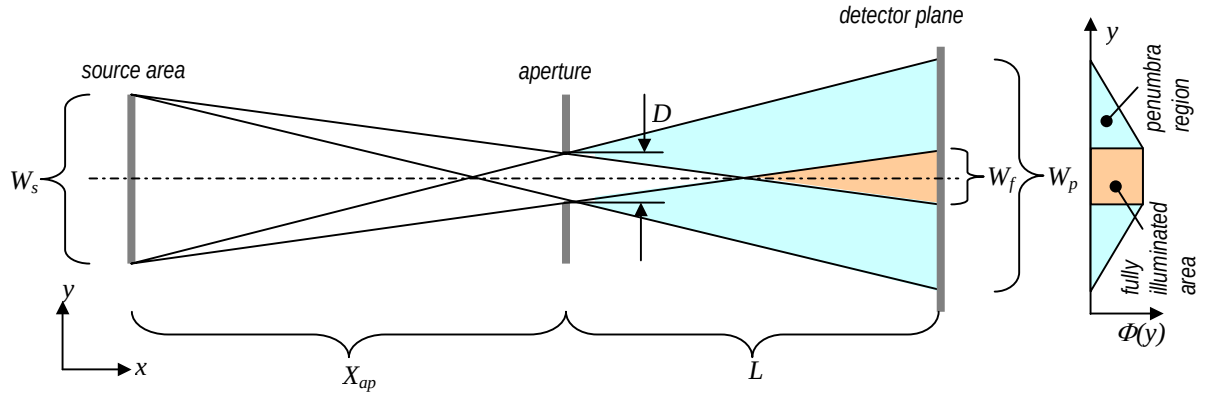

Fig. 2.24: Construction of fully illuminated area and penumbra region in the detector plane

$$W_f = \frac{-D + W_s}{X_{ap}}\left(X_{ap} + L\right) - W_s \qquad (2.1)$$

Eq. 2.1 shows that the size of the fully illuminated area W_f does not depend directly on the L/D ratio. For a fixed L/D ratio, the size of the fully illuminated area can therefore be chosen by positioning the aperture. The aperture diameter must be adjusted for each aperture location in order to keep the L/D ratio constant. Fig. 2.25 shows the width of fully illuminated area W_f in dependence of aperture location for the desired L/D ratios at the ANTARES facility.

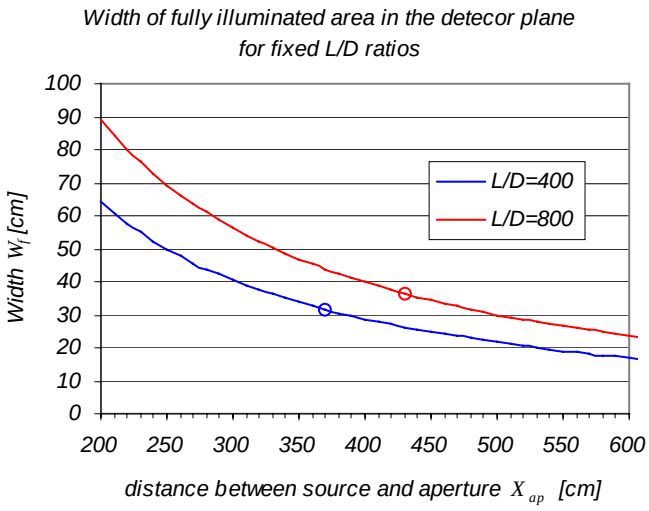

Fig. 2.25: Width of fully illuminated area W_f in the detector plane in dependency of aperture location for given L/D ratios.

Aperture position for L/D=800:

Full utilization of the scintillator screen is achieved for X_{ap}=4 m (detector size = fully illuminated area). Unfortunately at this position the aperture exchanging device cannot be installed because of the biological shielding. The aperture for L/D=800 therefore was installed at a distance of 4.3 m from the cold source. At this distance the fully illuminated area in the detector plane has a width of 36.4 cm; the diameter of the aperture is 2.09 cm.

Aperture position for L/D=400:

Full utilization of the scintillator screen is achieved for X_{ap}=3 m. Again practical restrictions make it impossible to mount the aperture at this location: For such small distances from the cold source, the aperture would hamper neutron paths for the L/D=800 geometry. Therefore a distance of 3.7 m was chosen (see appendix A.2 'Optimal adjustment of the L/D=800 and L/D=400 collimators'). For this position the fully illuminated area in the detector plane has a width and a height of 31.6 cm; the diameter of the aperture is 4.33 cm. The location is inside the biological shielding where no aperture exchanging device can be installed. This time this is no problem, because the 4.33 cm aperture can remain at its position when the L/D=800 aperture at a distance of 4.3 m from the cold source is in use.

2.3.5 Collimators

There exist no ideal 'black' absorbers as aperture material as it has been assumed in the preceding chapters (in the following the ideal circular apertures for the L/D=800 ratio and the L/D=400 ratio, as described above, are called 'desired apertures'). Good attenuation (especially of epithermal and fast neutrons) can only be achieved by extended layers of shielding materials. Therefore a collimator is necessary to shape the beam in the same manner, as the desired aperture would do. The collimator defines the point spread function PSF which defines the resolution of the facility. In the case of the ANTARES facility a pill-box function (Fig. 3.9 left hand side) is desired, hence contributions from outside the desired transmission area must be as low as possible. For this purpose the path lengths of undesired radiation components through collimator material have to be maximized. Undesired radiation components are:

- Cold and thermal neutrons propagating on paths that do not lead directly from the source area through the transmitting area of the desired aperture.
- All fast and epithermal neutrons.
- Gamma radiation.

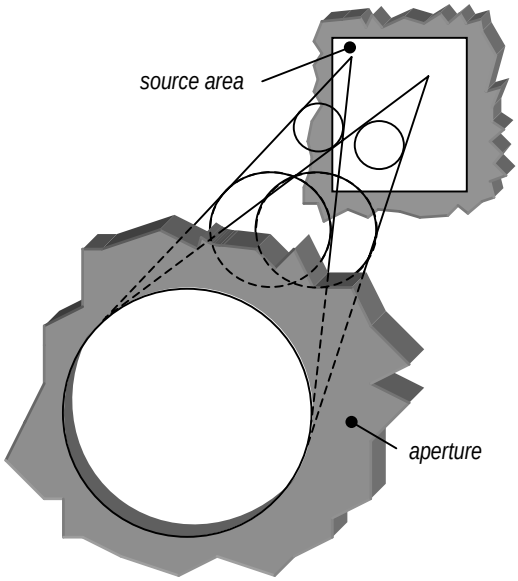

Fig. 2.26: Flight paths emerging from one point on the source area and passing through the transmitting area of the desired aperture are confined by elliptical cones. View from the aperture to the source area

All materials, which are exposed to the neutron beam become sources of scattered neutrons and - depending on the material - sources of secondary gamma radiation. As scattered neutrons do not emerge from the source plane, they broaden the point spread function, i.e. the resolution becomes worse. Besides, scattered neutrons and generated gamma radiation require additional shielding. Undesired radiation components should be attenuated as close to the cold source as possible. For this purpose the collimator is mounted within the channel through the biological shielding. It should confine the desired part of the beam as tightly as possible: All neutron paths spreading out from the source area and passing the transmission area of the desired aperture must not be attenuated by the collimator material, and all paths not traversing the transmission area should traverse as early as possible as much collimator material as possible. Obviously, having a rectangular source and a circular aperture, no simple geometry of the collimator can fulfill all requirements [23]. A simple geometry would be a cone shape collimator [24], a collimator with rectangular cross section, or any other arrangement, which can be easily machined.

2.3.5.1 Inner collimator

The inner collimator is the part of the collimator setup between the source area and the aperture. Its purposes are:

- Definition of the resolution for the facility (shaping the PSF)
- Suppression of undesired radiation components inside the biological shielding.
- Limitation of the effective source area to the desired size of 12 cm x 12 cm.

The penumbra region cannot be limited by this part of the collimator. For each point on the source area, only the neutron paths in direction of the transmitting area of the aperture are desired. These paths are within the inner volume of an elliptical cone as shown in Fig. 2.26. The volume that includes all desired paths from the whole source area is the set union of all cones, which have their apex in the desired source area (12 cm x 12 cm).

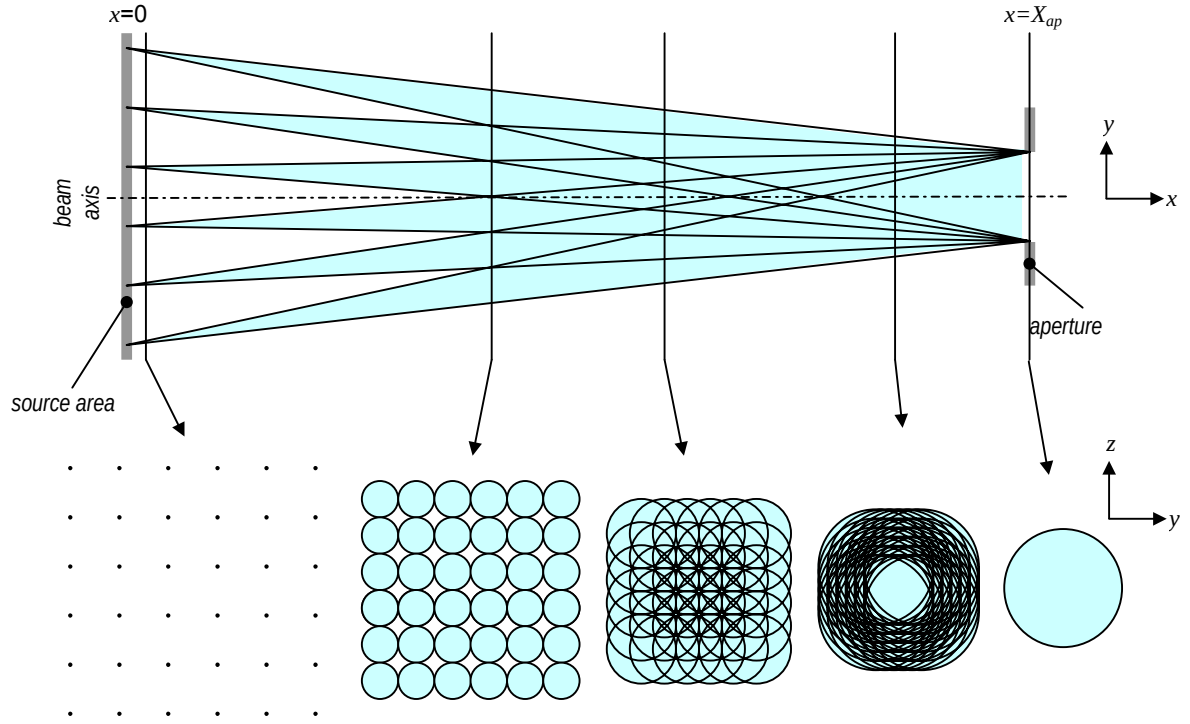

Fig. 2.27: Top: Horizontal cross section through the cones emerging from 6 source points between source area and aperture.
Bottom: Vertical cross section through the cones emerging from all 36 source points at different distances from the source area.

A schematic overview for 6x6 source points is shown in Fig. 2.27: The top of Fig. 2.27 shows a horizontal cut through the cones emerging from 6 source points that are located in the plane of the drawing. Cuts perpendicular to the beam axis through the 36 cones from all considered source points are displayed in the suite at the bottom of Fig. 2.27: In the source area, all desired paths are confined by a quadratic cross section. Between source area and aperture, the corners of the quadratic cross section become circle segments. The radii of the circles increase with increasing distance to the source area, hence the circle segments become more and more dominant when approaching the aperture. At location of the aperture the confining cross section is a circle corresponding to the transmission area of the aperture.

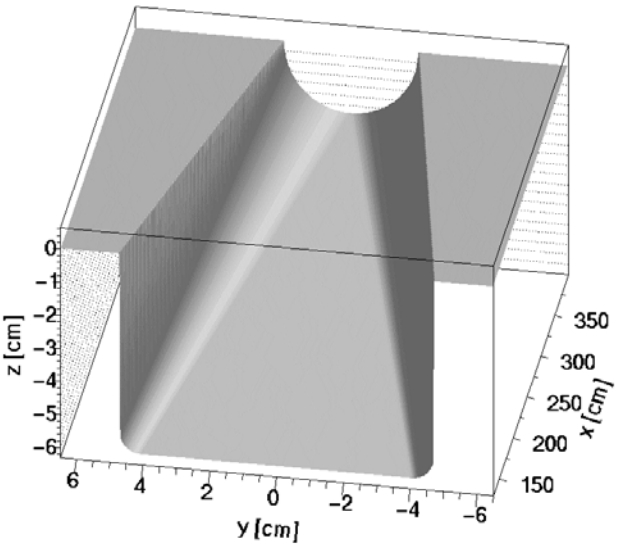

Fig. 2.28: Lower half of the surface, that confines all desired neutron paths between source area and aperture. The volume inside the surface corresponds to the transmitting volume of an optimal ‚beam adjusted' collimator

Under consideration of all source points, the confining shape for all desired neutron paths looks like the surface displayed in Fig. 2.28 (here only the lower half of the surface is plotted). The volume that is confined by this surface corresponds to the inner transmitting volume of an optimal 'beam adjusted' collimator, that attenuates undesired radiation components as close to the source as possible and that maximizes path lengths through collimator material of undesired radiation components. The narrowest part of the collimator has the location and

the diameter of the desired aperture. For machining such a collimator a mathematical description of the inner shape is necessary. This is given in appendix A.1 'Collimator geometry'.

2.3.5.2 Outer collimator

The outer collimator is the part of the collimator behind the aperture (in beam direction). It fulfills the same purposes as the inner collimator except of limiting the source area. In addition, the size of the penumbra region of the neutron beam can be reduced by the outer collimator.

The distance between margins of the penumbra region W_p without using an outer collimator is given by Eq. 2.2:

$$W_p = \frac{D + W_s}{X_{ap}}\left(X_{ap} + L\right) - W_s \qquad (2.2)$$

For a circular source area and a circular aperture the resulting fully illuminated area would have a circular shape. In this case a collimator that cuts the penumbra region therefore must have the shape of a cone that connects the aperture rim with the margin of the fully illuminate area. The desired slope of the cone can be found as shown in Fig. 2.29 (red line).

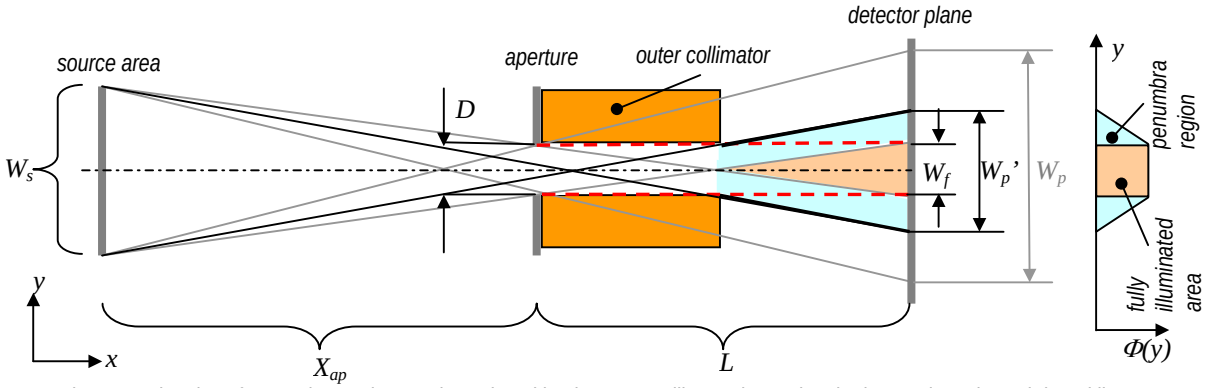

Fig. 2.29: The size of penumbra region can be reduced by the outer collimator by cutting the beam along the red dotted line

For a quadratic source area and a circular aperture (as in the case of the ANTARES facility), the shape of the outer collimator is more complicated: It looks similar to the shape of the inner collimator. Derivation of the shape is analog to that for the inner collimator (appendix A.1), but the source width W_s is replaced by the width of fully illuminated area W_f (Eq. 2.1) and X_{ap} is replaced by L.

Complete suppression of the penumbra region could only be achieved with an outer collimator extended from the aperture to the detector plane. That is not feasible in reality. But even with smaller extensions, a considerable reduction of the penumbra region can be obtained. In the case of the ANTARES facility the total length along the beam line where a collimator can be mounted is 3.9 m. This is the length of the channel inside the biological shielding and the channel in the aperture exchanging device (see chapter 2.3.6 'Changing the L/D ratio'). Beam profiles obtained by the beam adjusted inner collimator and by the combination of inner and outer collimator are displayed in Fig. 2.30. The profiles are calculated for a distance of 1.5 m behind the end of the outer collimator (in beam direction). The steeper gradient at the flanks of the beam when using the combination of inner and outer collimator are clearly visible. The smaller penumbra region enables for keeping radiation shieldings and the cross section of the flight tube small as shown in the chapter 2.10.5.3 'Radiation shielding for the flight tube'.

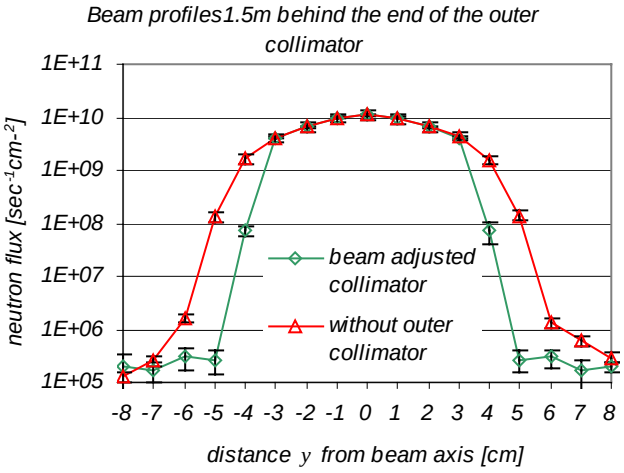

Fig. 2.30: Beam profiles 1.5 m behind the end (in beam direction) of the outer collimator. The red curve shows the profile obtained by using only the inner collimator and the green curve shows the profile obtained by using inner and outer collimator. The collimator material is steel.

2.3.5.3 Collimator materials

Good attenuation of cold and thermal neutrons can be achieved by use of Cd or Gd. For higher neutron energies, materials with bigger attenuation can be found, hence a collimator made only of Cd or Gd is not the optimal solution for reduction of high energetic neutron background radiation. Materials with a high content of hydrogen sometimes are supposed to improve the collimation [20][25]. Polymers are solid state materials with high hydrogen content, e.g. polyethylene (CH_2). These plastic materials suffer from embrittlement on a short time scale when irradiated with high neutron flux (the tensile strength of pure polyethylene is reduced to about 80 % of the initial value by irradiation with a dose of 10^7 Gy [27]). In addition, the attenuation of gamma radiation by polymers is rather low. A collimator made from pure polymers is therefore less advisable. Due to its high density of resonances, a high attenuation of fast neutrons can be achieved by iron. Besides, iron also attenuates gamma radiation quite well.

As shown in chapter 2.10.3 'Shielding materials', high attenuation of fast and epithermal neutrons is achieved by a combination of inelastic scattering (e.g. in iron) and elastic scattering (e.g. in hydrogen). Therefore a 'sandwich structure' of steel and polyethylene has to be considered for the collimator. The problem of embrittlement is lessened to some degree, because the polyethylene layer is located behind the iron layer (in beam direction), hence polyethylene is not exposed to the full neutron beam.

Beside many other collimator configurations, four versions were tested for the ANTARES facility:

- A collimator consisting of pure iron (Fig. 2.32 top).
- A collimator made of iron with a cadmium aperture at the smallest part. The thickness of the cadmium layer is 1 mm (Fig. 2.32 middle).
- A sandwich structure of iron, cadmium and polyethylene. The inner collimator consists of iron and the outer collimator consists of polyethylene. At the throat of the collimator (at the transition between inner and outer collimator) a cadmium aperture is included (like in the version above; thickness 1 mm). Length of the iron part is 243 cm and length of the polyethylene part is 138 cm (Fig. 2.32 bottom).

For comparison a cone shaped collimator consisting of iron was considered. Its shape does not hamper any neutrons moving directly from the desired source area to the transmitting area of the aperture. Hence its inner cross section circumscribes the inner cross section of the beam adjusted collimator as shown in Fig. 2.31.

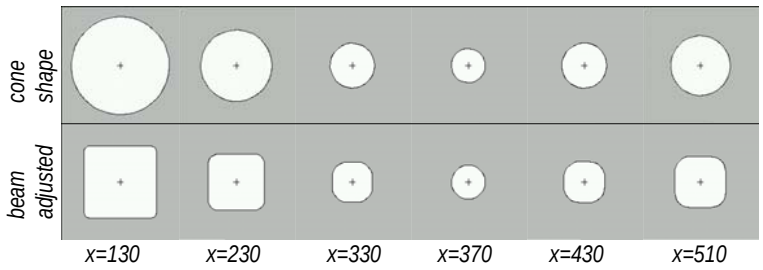

Fig. 2.31: Vertical cross sections through the cone shape collimator (top) and the beam adjusted collimator (bottom) at different distances to the entrance window of the beam tube. The inner cross section of the cone shape collimator circumscribes the inner cross section of the beam adjusted collimator.

Horizontal cuts through the different collimator versions are displayed in Fig. 2.32. In this illustration the length in x-direction is compressed by a factor of six. Hence the angles between collimator walls and beam axis (dotted line) are much smaller in reality. The narrowest part of the collimator (location of desired aperture) is at a distance of 370 cm to the entrance window of the beam tube and the diameter is 4.3 cm corresponding to the desired L/D=400 aperture for the ANTARES facility. All collimator versions are composed of two parts: One part inside the biological shielding and the other part inside the aperture exchanging device adjacent to the biological shielding. The length inside the biological shielding is 2.6 m, the length inside the aperture exchanging device is 121 cm. Between the two parts there is a gap of 9 cm length at the transition between biological shielding and the aperture exchanging device (Fig. 2.32).

For comparison of collimation quality, the neutron and gamma flux in a 12 cm x 12 cm area located 50 cm behind the end of the outer collimator (in beam direction) was calculated. The results are compared to a beam adjusted collimator, consisting of ideal black material (i.e. all radiation is absorbed immediately when entering the collimator material and no gamma radiation is generated). In Fig. 2.33 neutron flux in different energy groups, achieved by the different collimator versions consisting of 'real' materials, are compared to the ideal case. The poorest attenuation of neutron background is obtained by the cone shaped collimator. Neutron transmission is 144 % compared to the ideal collimator. The weak collimation quality is caused by a much larger entrance field than the desired one of this collimator and by the smaller path lengths through the collimator material. All other collimator versions yield results very close to the ideal collimator. The cadmium aperture does not reduce leakage of neutrons significantly (leakage in this context means the additional radiation compared to the radiation level obtained by the ideal collimator). The share of thermal neutrons is very small even without Cd aperture, hence the advantage of the Cd aperture is rather low. Best result is obtained by the 'sandwich structure' made of iron and polyethylene. However, the difference to the pure iron collimator is not worth mentioning (it is below 1 %). Due to the big path lengths of leakage neutrons in the beam adjusted collimator, leakage is very low for all considered materials. Hence choosing the right shape is of more importance than the choice of the material. The fraction of scattered neutrons from collimator material is decreasing with increasing distance to the collimator. As the distance between the end of the outer collimator and the specimen is some 15 m, the amount of undesired neutron radiation for the experiment is even smaller than displayed here.

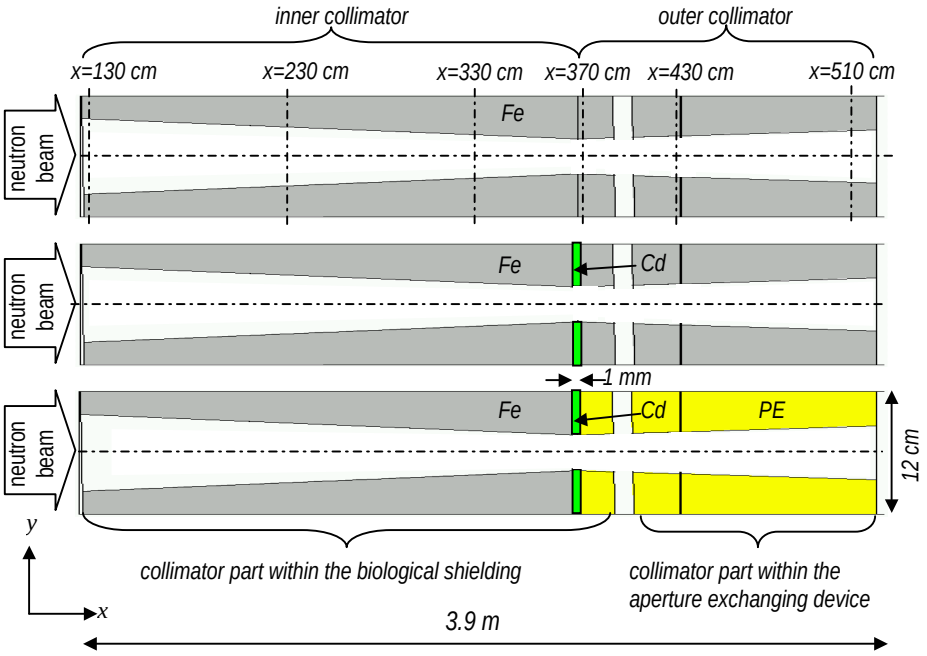

Fig. 2.32: Horizontal cross sections through the different collimator arrangements.
Top: collimator consisting of pure iron.
Middle: collimator consisting of iron and a cadmium aperture at its narrowest part.
Bottom: 'sandwich structure' of iron, cadmium and polyethylene.
In this illustration the length in x-direction is compressed by a factor of 6.

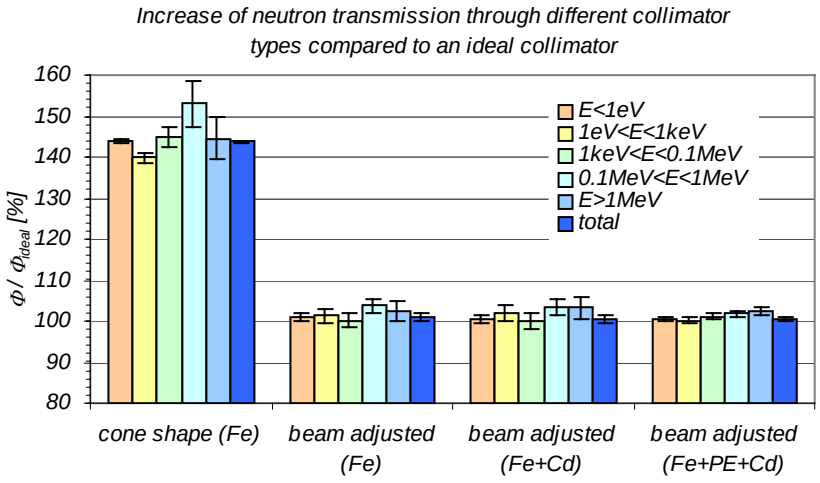

Fig. 2.33: Increase of transmission of neutron radiation for different collimator types in comparison to the ideal 'black' beam adjusted collimator.

The ratios of primary gamma flux behind the different collimator types compared to the ideal case are shown in Fig. 2.34. The cone collimator shows worst results for the same reasons as described above for neutron radiation. Contrary to neutron radiation, significant differences between the beam adjusted

collimators are observable. The 'sandwich structure' made from iron and polyethylene causes a considerable higher gamma background radiation than the other beam adjusted collimators. The leakage is six times higher than for the pure iron collimator (due to the low gamma attenuation in polyethylene), i.e. this collimator type increases the gamma-neutron ratio and is therefore not beneficial for the ANTARES facility. The beam adjusted pure iron collimator is therefore the best solution for the ANTARES facility. Besides, polyethylene has the disadvantage of being flammable. In the reactor hall of FRM-II, flammable materials have to be avoided and if unavoidable they have to be encapsulated (e.g. in aluminum casings). Hence the usage of polyethylene is problematic, anyway.

The generation of gamma radiation in the collimator material is not considered here because the contribution to the gamma background at the position of the specimen is negligible [23] as shown below in chapter 2.5 'Flight tube'. Generated gamma radiation emerges isotropic from the collimator. The lower part of the collimator for the L/D=400 geometry is shown in Fig. 2.35. This collimator is mounted inside the biological shielding.

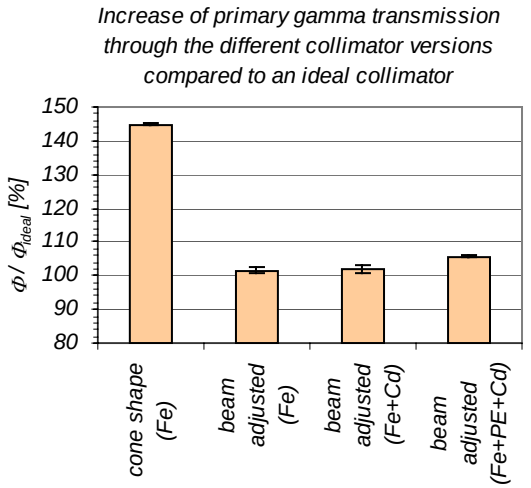

Fig. 2.34: Increase of transmission of primary gamma radiation for different collimator types in comparison to the ideal 'black' beam adjusted collimator.

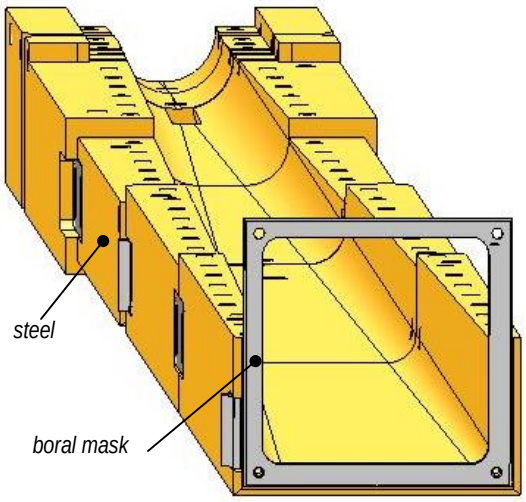

Fig. 2.35: Lower collimator part inside the biological shielding.

In order to reduce activation of iron, boral masks (borated aluminum; 4.3 Wt.% B, [28]) cover all front areas of collimators (in the biological shielding as well as in the collimator exchanging device). A knock down to an upper and a lower collimator part is necessary for machining the collimators. To avoid a continuous gap, the horizontal separation plane between upper and lower part is located at different heights at different locations of the collimator (Fig. 2.35).

2.3.6 Changing the L/D ratio

The collimator part inside the biological shielding is fixed and cannot be exchanged easily for modification of the L/D ratio. An horizontal cut through the arrangement is shown in Fig. 2.36. The L/D ratio is changed by inserting another collimator part into the beam outside the biological shielding (Fig. 2.37). On the one hand, no desired neutron path for the new L/D ratio should be hampered by the fixed part of the collimator. The collimator with the bigger cross section (L/D=400) has to be mounted

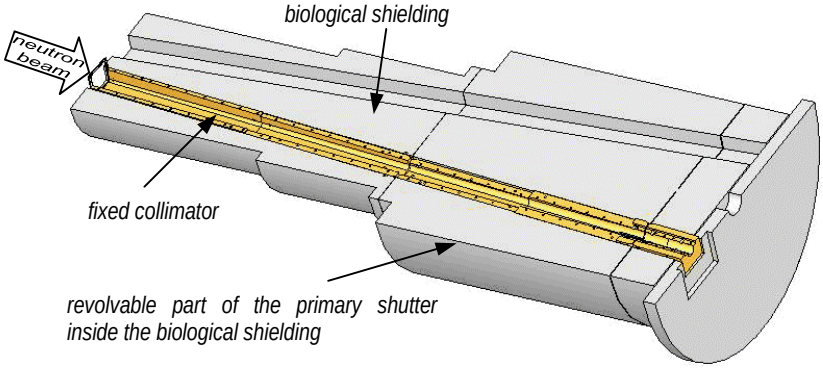

Fig. 2.36: Fixed part of the L/D=400 collimator mounted inside the biological shielding

therefore inside the biological shielding and the collimator with smaller cross section (L/D =800) must be installed in the aperture exchanging device adjacent to the biological shielding. On the other hand, the fixed collimator part for the L/D =400 ratio should confine the desired neutron paths for the L/D =800 geometry as close as possible for reduction of background radiation. For both reasons, the location of the narrowest part of the L/D =400 collimator (location of desired aperture) and its diameter cannot be chosen arbitrarily. There is an optimal solution: When the narrowest part of the L/D =400 collimator is located at a distance of 370 cm from the cold source, the collimator shape is very close to the desired one for the L/D =800 collimator and no desired neutron paths for the L/D =800 geometry are hampered by the fixed L/D =400 collimator part. The derivation is shown in the appendix A.2 'Optimal adjustment of the L/D=800 and L/D=400 collimators'.

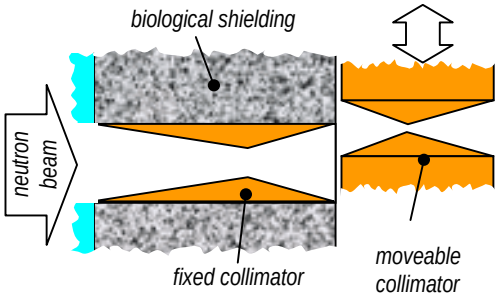

Fig. 2.37: The L/D ratio is changed by moving the L/D=800 collimator into the beam.

Beside an aperture changing device, a secondary shutter is necessary for the ANTARES facility. Both functions are combined in one device. The setup of this device is shown in chapter 2.4.2 'Secondary shutter'.

2.3.7 Point spread functions

The most important measure for quality of collimators is the achieved point spread function PSF for the neutron beam. For the desired ideal apertures, the PSF is a pill-box function. The diameter d_{PSF} of the PSF can be found by:

$$d_{PSF} = D \cdot x_{spec-de} / x_{ap-spec} \quad (2.3)$$

where $x_{ap\text{-}spec}$ is the distance between aperture and specimen and $x_{spec\text{-}de}$ is the distance between specimen and detector.

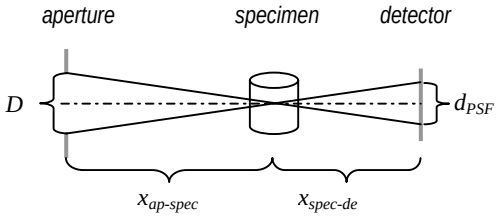

Fig. 2.38: Construction of the diameter of the PSF

At the ANTARES facility the diameters of the $PSFs$ for a specimen located 0.5 m in front of the detector (in beam direction) are 0.65 mm for the L/D =800 arrangement and 1.3 mm for the L/D =400 arrangement.

Before machining the collimators, it was tested by Monte Carlo calculation if there are major deviations from the ideal case (e.g due to transmission through collimator material).

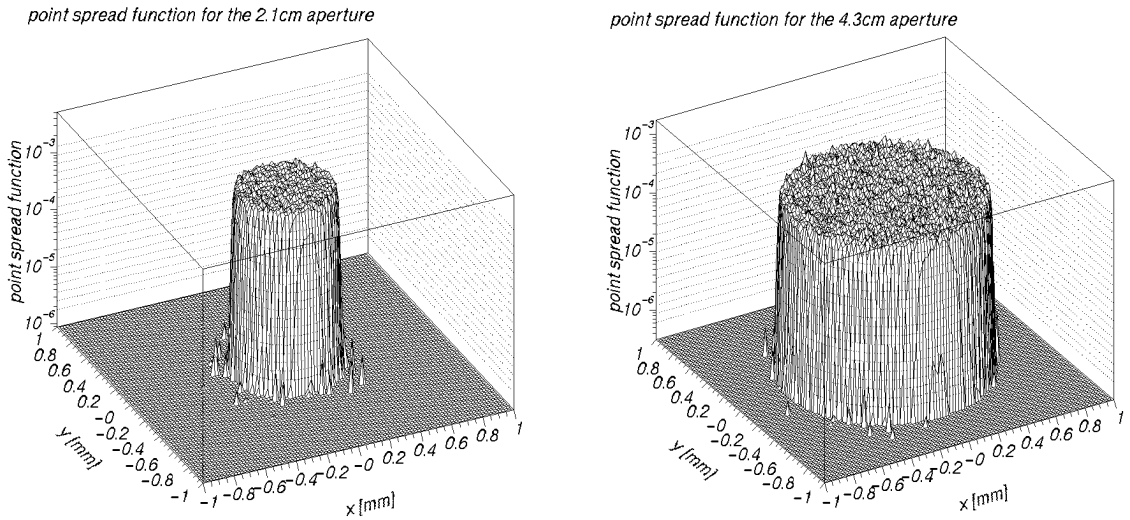

Fig. 2.39: Point spread function for the L/D=800 collimator arrangement (left hand side) and for the L/D =400 arrangement (right hand side). The specimen is positioned 0.5 m before the detector (in beam direction).

These calculations consider not only transmission through collimator material, but the whole facility in its final version from the reactor core to the experimental chamber. All structures that can cause a broadening of the *PSF* are considered, like e.g. aluminum windows of the flight tube. The results for both collimator arrangements (L/D =800 and L/D =400) and a specimen positioned 0.5 m before the detector are shown in Fig. 2.39. No major deviations from the ideal case are to be observed.

2.4 Shutters

2.4.1 Primary shutter

There is a shutter inside the biological shielding for interruption of the neutron beam during reactor operation. It consists of a revolvable drum with two channels surrounded by heavy concrete. By rotating this drum, its channels are moved out of the neutron beam. The neutron beam is stopped by the heavy concrete in the drum. Radiation transport through the shutter and the surrounding gap systems is described in [29]. In the case of SR4 this 'primary' shutter is not applicable when the UCN (ultra cold neutron) experiment is in operation. For generation of the ultra cold neutrons it is necessary to bring frozen D_2 close to the cold source. This is done by a pipe traversing the biological shielding and the primary shutter [30]. This pipe disables any movement of the shutter.

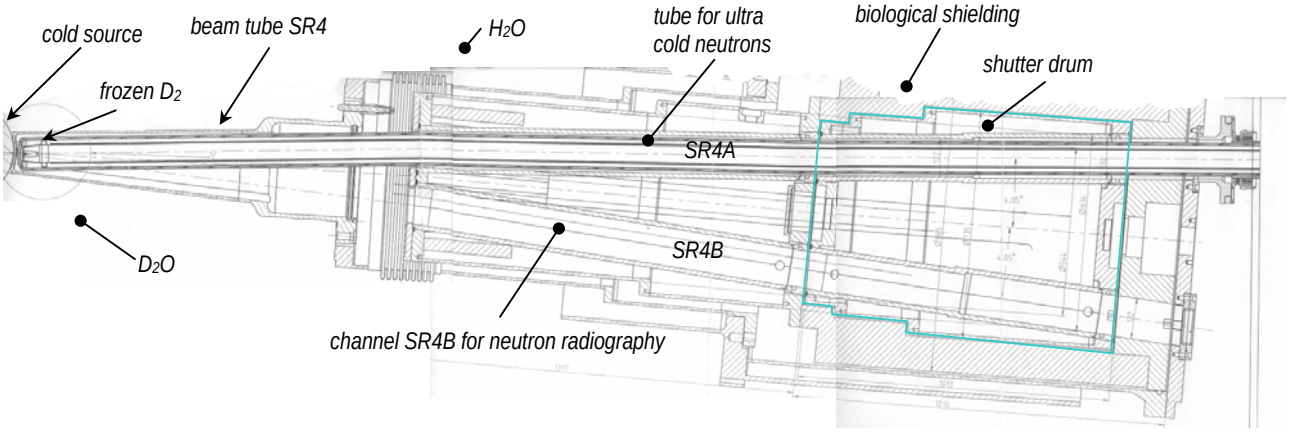

Fig. 2.40: The pipe for the UCN experiment blocks the primary shutter.

2.4.2 Secondary shutter

A 'secondary' shutter is necessary to interrupt the neutron beam when the primary shutter is blocked by the UCN-experiment. It consists of a moveable heavy concrete block that is moved vertically into the beam [84]. The major advantage of this concept compared to a rotating shutter drum is, that the shutter can be closed faster and that it can be closed by gravity in emergency situations. The secondary shutter takes over simultaneously the function of the aperture exchanging device. For this purpose two collimators are mounted at the bottom of the heavy concrete block (Fig. 2.41):

- The collimator for the L/D =800 geometry
- An extended outer collimator for the L/D =400 geometry

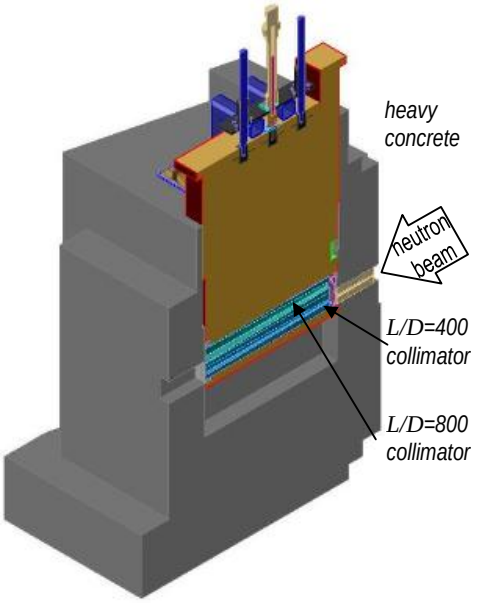

Fig. 2.41: Vertical cut through the secondary shutter and the collimator exchanging device

2.4.3 Fast shutter and filters

In some cases it is desirable to shut the neutron beam for a very short time. This is especially the case during tomography measurements. The rotation of the specimen to the next angular position and data read out from the detector usually needs a few seconds. Measurements with up to 400 angle positions

cause avoidable activation (in some cases the net neutron exposure time is only about 70 % of total exposure time, the rest of the time is needed for data read out, rotation of the specimen, etc.). The time period between two angle positions is too short for the secondary shutter that needs about 20 sec for closing and opening the beam. An additional fast moving shutter is therefore used. Its mass must be kept low for this purpose. High attenuation of epithermal and fast neutron flux cannot be achieved by a low mass shutter but activation of the specimen can be reduced considerably. As fast shutter a layer of boron carbide (thickness 1 cm) is used. The neutron spectra after 1 cm of boron carbide powder and 2 mm of cadmium is shown in Fig. 2.42. The boron carbide powder reduces the total neutron flux to 2.0 %. The cadmium filter attenuates neutron flux to 6.6 %. Due to its higher attenuation, a layer of boron carbide powder (1 cm thickness, bulk density ρ=1.8 g/cm^3) encapsulated in an aluminum casing (1 mm wall thickness) was installed as fast shutter adjacent to the secondary shutter. It is moved into the beam by compressed air. Beside the minimization of activation of specimen the fast shutter can be used as filter when only epithermal neutrons are desired for radiography. This is the case when specimens with very high neutron attenuation are investigated for which high exposure times are necessary. Thermal and cold neutrons bypassing the specimen limit the exposure time due to detector overflow. Fig. 2.42 shows that a cadmium filter is superior for this purpose, because it cuts the low energy region much steeper than the boron carbide filter does and its attenuation in the epithermal region is lower. Additional to the boron based fast shutter, a cadmium filter (thickness 2 mm) that can be moved into the beam is therefore installed.

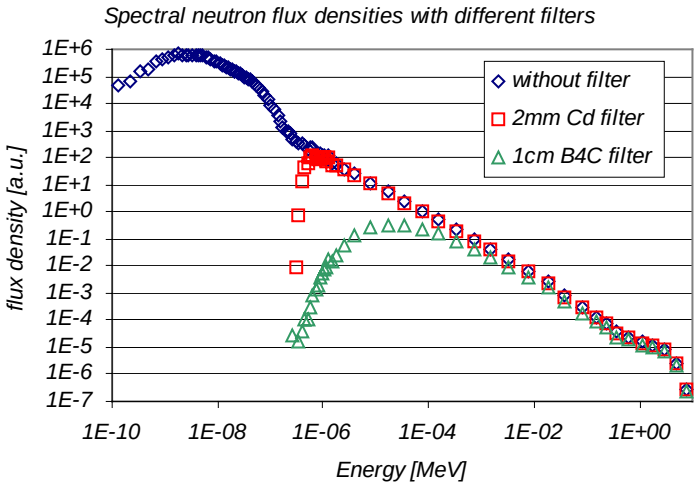

Fig. 2.42: Neutron spectra without filter, with 2 mm of Cd as filter and with 1 cm of boron carbide powder as fast shutter.

From the point of view of an experimenter, flux after the cadmium filter is less interesting than the decrease η of signal in the detector due to the filter (in this context, the signal is the number of detected neutrons per time). As neutron detection is dependent on neutron energy, signal and flux are not reduced to the same amount by the filter. For the ANTARES detector system (chapter 2.9.1) that uses the ^{6}Li(n,α)^{3}H reaction for neutron detection, η is given by:

$$\eta = \frac{\int_0^\infty \phi(E) \cdot e^{-\Sigma_{Cd}(E)\cdot d} \cdot \Sigma_{^6Li}(E) dE}{\int_0^\infty \phi(E) \cdot \Sigma_{^6Li}(E) dE} \qquad (2.4)$$

where $\phi(E)$ is the neutron flux at energy E before the filter, $\Sigma_{Cd}(E)$ the total macroscopic cross section of cadmium for energy E, d the thickness of the cadmium plate and $\Sigma_{^6Li}(E)$ the ^{6}Li(n,α)^{3}H cross section at energy E. With regard to the ANTARES neutron spectrum the signal is reduced to η=0.190% using a 2 mm Cd-plate (for a 1 mm Cd-plate the signal would be decreased to η=0.219%).

2.5 Flight tube

The distance between secondary shutter and entrance of the experimental chamber is 12.5 m. Within this distance neutron scattering and absorption in air reduce the total neutron flux by 52 % when using the cold neutron spectrum of beam tube SR4. For a thermal energy distribution of neutrons, reduction would be 47 %. The loss of neutron pay flux is extremely bothering because it worsens the signal to noise ratio significantly. The background radiation is raised by interactions of the neutron beam with air. In addition, the activation of air (especially activation of argon ^{40}Ar(n,γ)^{41}Ar [31]) will deliver an unwanted, prohibitive contribution to activated gases in the reactor hall. ^{41}Ar decays with a half time of 1.83 h [32]. The neutron attenuation due to absorption and scattering in air for the cold spectrum of beam tube SR4B and the thermal spectrum of SR5 is shown in Fig. 2.43 left hand side. Neutron attenuation in air depends on the energy distribution of the incident beam. Neutrons with lower

energies are more probably scattered or absorbed than those with higher energies. Neutron flux at 1 meV is even reduced to 20 %. The result is a beam hardening in air. A shift of the neutron spectrum towards higher energies is disadvantageous for the radiography experiment. The decrease of unscattered neutron flux in dependency of neutron energy is shown in Fig. 2.44.

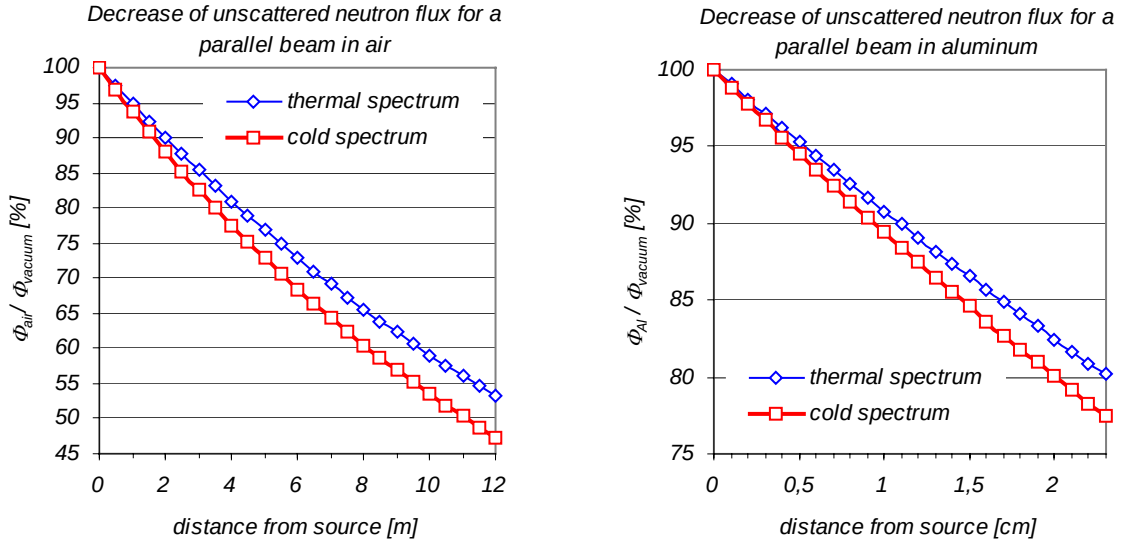

Fig. 2.43: Loss of neutrons in air (left hand side) and in aluminum (right hand side). The cold neutron spectrum is that of the ANTARES facility, as thermal spectrum that of beam tube SR5 was used.

It is useful to evacuate the volume between the secondary shutter and the experimental chamber. The vacuum has to be enclosed by a flight tube. As structure material of the flight tube aluminum is preferable, because it combines both high mechanical strength and low activation potential under neutron irradiation. Aluminum is activated by the reaction $^{27}Al(n,\gamma)^{28}Al$ [31]; the cross section is rather low: microscopic thermal activation cross section: σ=0.23 barn [32]; ^{28}Al decays with a half life time of $t_{1/2}$=2.246 min [32]. The windows of beam entrance and exit are of special interest: The beam attenuation should be kept at a minimum in order not to compensate the benefit of the flight tube. Again, aluminum is the material of choice. A 2 mm Al-plate is sufficient to withstand the pressure of atmosphere [33]. The beam is attenuated by both the entrance and the exit window not more than 4.4 %. Fig. 2.43 right hand side shows the attenuation of a parallel beam by an aluminum layer as a function of layer thickness. The flight tube at the ANTARES facility can be evacuated down to 10^{-1} mbar resulting in a decrease of particle density of air of 4 orders of magnitude. An evacuation below this residual pressure would only rise cost but would not improve the transmission more than marginally.

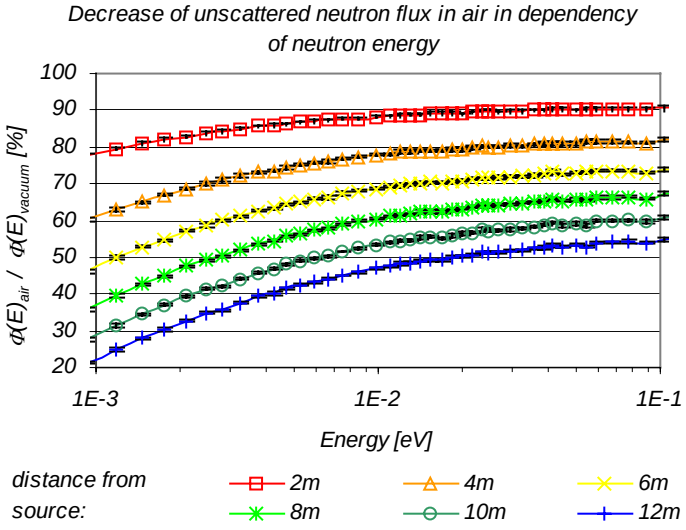

Fig. 2.44: Loss of neutrons in air in dependency of neutron energy for a parallel beam

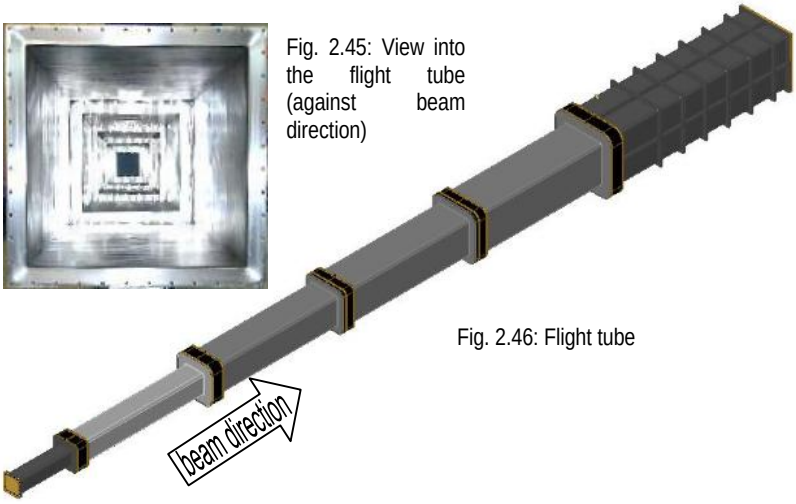

Fig. 2.45: View into the flight tube (against beam direction)

Fig. 2.46: Flight tube

The horizontal cut through the Monte Carlo model of the final version of the facility in Fig. 2.47 shows the arrangement of the flight tube inside the facility. The neutron flux around the flight tube in the red marked area in Fig. 2.47 is shown in Fig. 2.48. The data refers to application of the L/D=400 collimator/aperture setup and a reactor power of 20 MW. The level of scattered neutrons inside the shielding is about four orders of magnitude below the direct beam. Local maxima of flux of scattered neutrons appear at distances of 1060 cm from the cold source and 1250 cm: At these positions flanges between flight tube segments are located. Although the structure of the flight tube does not touch the direct beam, an increase of scattered neutron flux is observable here. The narrowing of the neutron beam at a distance of 1060 cm from the cold source is caused by a boral plate that cuts into the penumbra region. This plate is necessary for keeping the radiation shielding thickness small as described in chapter 2.10.5.3 'Shielding for the flight tube'.

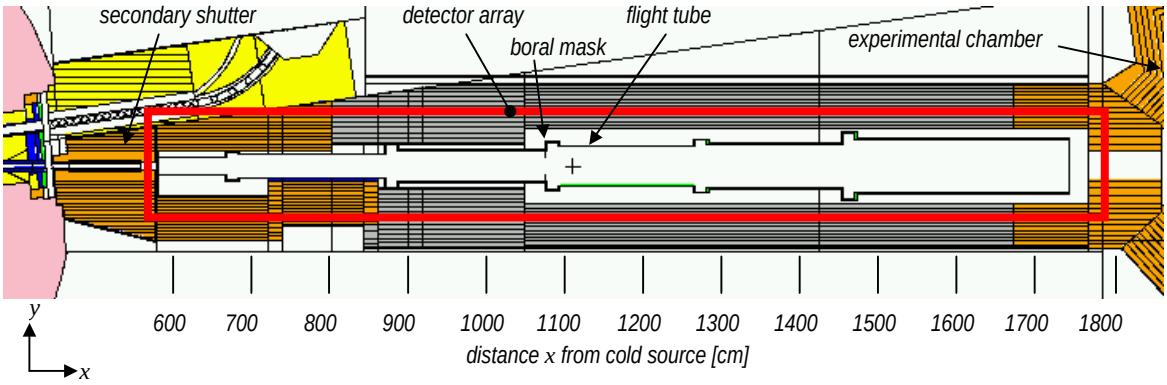

Fig. 2.47: Horizontal cut at level of the beam axis through the Monte Carlo model of the flight tube and its surrounding.

The flux of generated gamma radiation around the flight tube is shown in Fig. 2.49. Three local maxima can be recognized: The first one at the end of the secondary shutter at a distance of 560 cm from the cold source. This maximum is caused by gamma production in the collimator material. The second maximum at a distance of 1060 cm from the cold source is caused by the boral plate, which cuts into the penumbra region. The third maximum appears at a distance of 1800 cm to the cold source, where the fully illuminated part of the neutron beam enters the experimental chamber and the penumbra region and scattered neutrons impinge on the radiation shielding around the entrance window to the experimental chamber. The fast decrease of flux from the secondary shutter and the boral plate for increasing distance shows that the contribution of both structure elements to background radiation inside the experimental chamber is negligible.

The flux distribution of primary gamma radiation is similar to that of neutrons as it is also shaped by the collimators (Fig. 2.50). For distances of more than 1060 cm from the cold source, the γ-field spreads wider than the neutron beam, as the boral plate attenuates mainly thermal and cold neutrons but no gamma radiation. The flux of primary gamma radiation is at all positions about 50 % of the neutron flux.

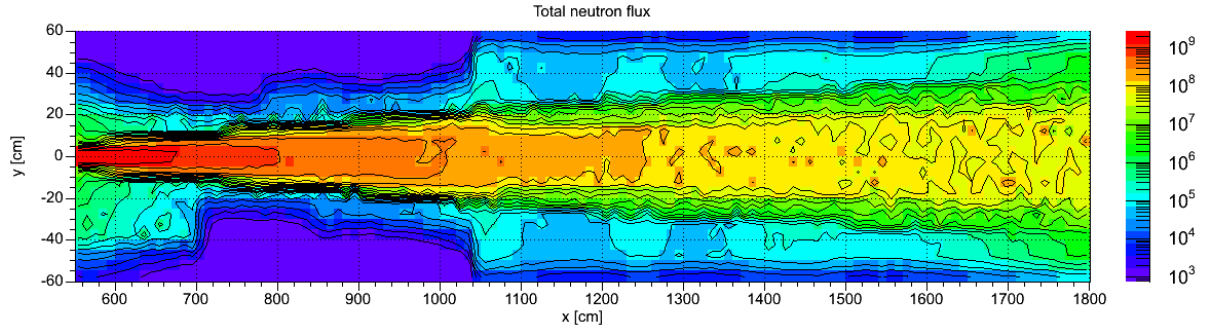

Fig. 2.48: Neutron flux [cm^{-2}sec^{-1}] in a horizontal plane through the flight tube (red bordered area in Fig. 2.47). For this calculation the final version of the facility was used.

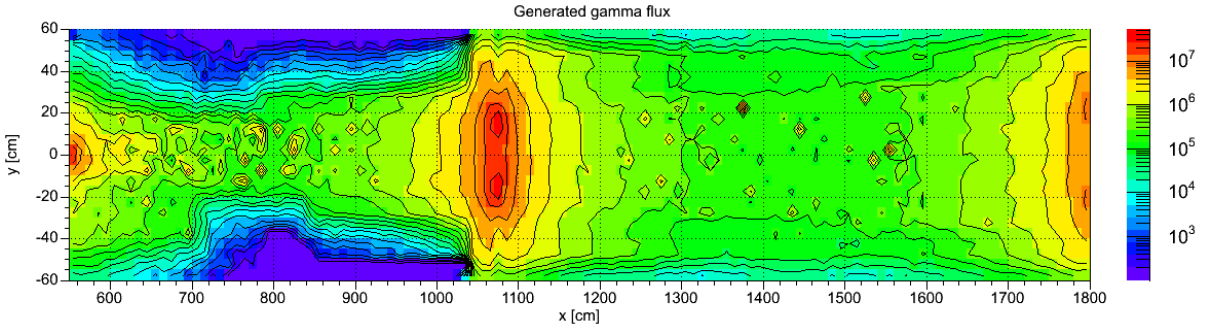

Fig. 2.49: Flux of generated gamma radiation [cm^{-2}sec^{-1}] in a horizontal plane through the flight tube (red bordered area in Fig. 2.47). For this calculation the final version of the facility was used.

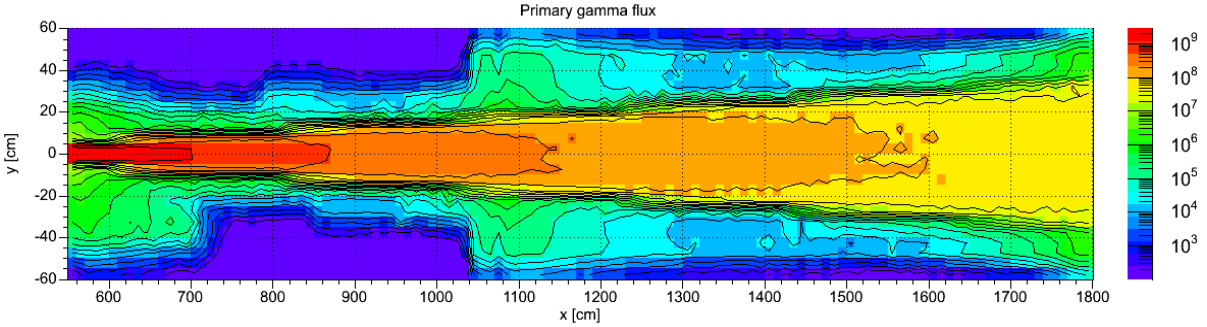

Fig. 2.50: Flux of primary gamma radiation [cm^{-2}sec^{-1}] in a horizontal plane through the flight tube (red bordered area in Fig. 2.47). For this calculation the final version of the facility was used.

2.6 Beam limiter

At the end of the flight tube (in beam direction) at the entrance to the experimental chamber a beam limiter was installed. It consists of four boral (borated aluminum [28]) plates (each of thickness 6 mm) that can be driven independently into the neutron beam. By this the beam size at the position of the specimen can be adjusted to the desired area around the specimen. Background radiation of cold and thermal neutrons and activation in the experimental chamber can be reduced by this device.

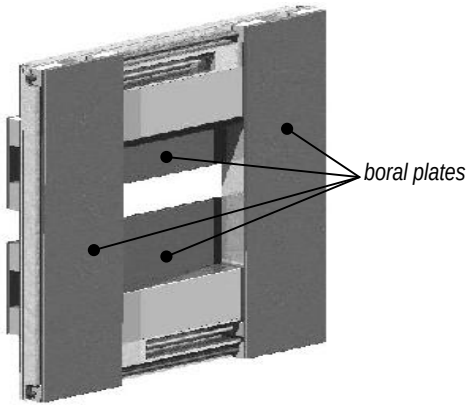

Fig. 2.51: Beam limiter

2.7 Experimental chamber

The experimental chamber is a room, which houses specimens and the detector system at the ANTARES facility.

The layout of the experimental chamber has to meet the following requirements:

- The background level of scattered neutrons inside the chamber should be negligible compared to the intensity of the direct beam
- Production of secondary gamma radiation inside the chamber should be as low as possible
- Activation of structure material must be low in order to reduce background gamma radiation and to ensure save access for experimenters to the chamber soon after irradiation.
- Neutron and gamma radiation outside the chamber must be reduced to a save level with regard to radiation protection standards and in order to minimize background radiation for other experiments.

Scattered neutrons from inside the experimental chamber are detected by the scintillator likewise as unscattered neutrons from the direct beam. As scattered neutrons contribute no information about the object, they are bothering when observing weak signals from objects with high neutron attenuation. The projection is degraded by scattered neutrons in terms of a nearly homogeneous noise level in the signal.

Gamma radiation contributes also to an unwanted background in the scintillator (the cross section for gamma radiation is some orders of magnitude smaller than for neutrons, but it is not zero). In addition gamma radiation produces free charge clouds in the CCD chip of the camera. The result are “white spots” in the projection (known as “salt and pepper noise”). Therefore it is necessary to reduce neutron scattering and gamma production in the experimental chamber as much as possible. Several layouts for the experimental chamber were examined by Monte Carlo simulation with regard to background radiation at the detector position. Radiation background outside the experimental chamber is discussed in the chapter 2.10.5.4 ‘Radiation shielding for the experimental chamber’.

A horizontal cut through the Monte Carlo model of the experimental chamber at the height level of the beam axis is shown in Fig. 2.52a. The spatial flux distributions in this horizontal plane are shown for different setups of the experimental chamber in the following diagrams. The section of the plane for which the flux is displayed in the diagrams is shown in Fig. 2.52b. The walls of the experimental chamber consist of heavy concrete (mass density ρ=4.7 g/cm^3, see chapter 2.10.3.3 ‘Concrete as shielding material’, concrete type B). The scintillator of the detector system is located at x=2100 cm (x is the distance from the cold source) and y=0 (y is the horizontal distance from the beam axis). The CCD camera is outside the direct beam at approximately x=2100 cm and y=-50 cm. Due to the small distance between scintillator and CCD camera, the level of scattered background radiation is nearly the same for both positions. Therefore only the radiation level at the position of the CCD-camera (“CCD position”) is discussed below. A comparison of neutron and gamma fluxes at the detector position is shown in Fig. 2.59. All presented data refer to the application of the L/D=400 collimator/aperture setup and a reactor power of 20 MW.

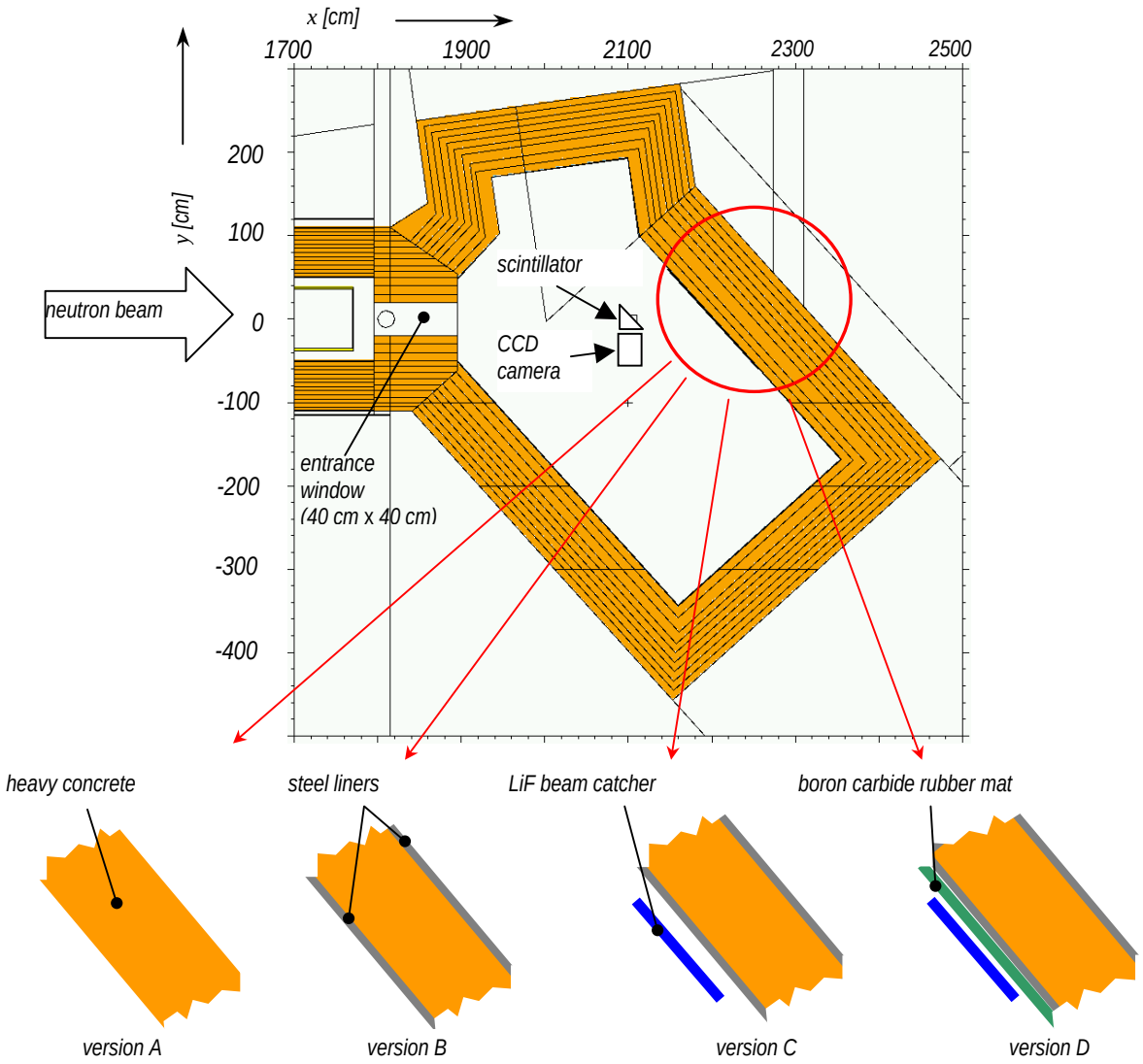

Fig. 2.52a: Horizontal cut through the Monte Carlo model of the experimental chamber at beam axis level (top) and four different versions of the setup (bottom). These versions are (from left to right): experimental chamber with heavy concrete walls (version A), heavy concrete walls with steel liners (version B), additional beam catcher (version C) and walls covered by boron carbide rubber mats (version D).

Version A

In version A of the experimental chamber there is no beam catcher and the walls are not covered by steel liners. The direct neutron beam impinges on the heavy concrete of the rear wall of the chamber. The resulting flux distribution of scattered neutrons and generated gamma radiation is shown in Fig. 2.53.

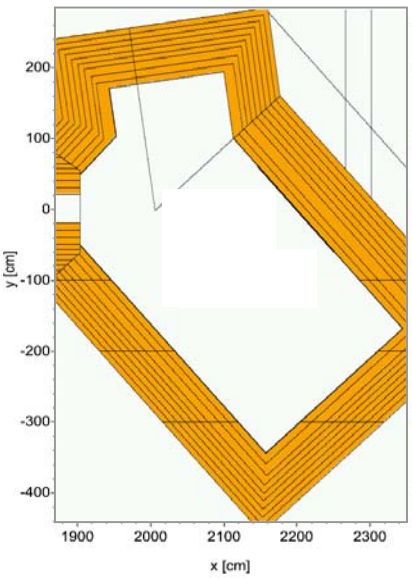

Fig. 2.52b: Section of the horizontal plane shown in Fig. 2.52a for which the spatial flux distributions are displayed in the following diagrams.

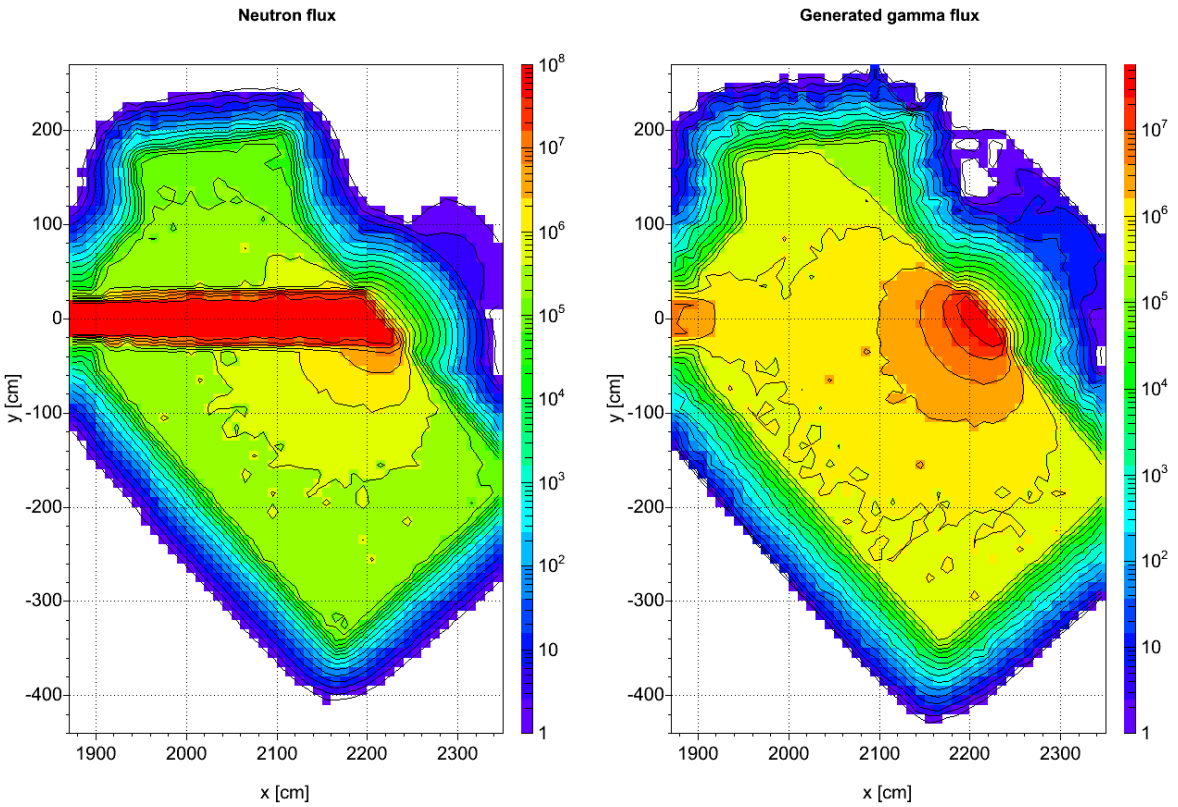

Fig. 2.53: Version A: Total neutron flux [$sec^{-1}cm^{-2}$] (left hand side) and flux of generated gamma radiation [$sec^{-1}cm^{-2}$] (right hand side) in a horizontal plane at level of beam axis through the experimental chamber without steel liners and without beam catcher (version A). The walls consist of heavy concrete (ρ=4.7 g/cm^3).

The area where the direct beam impinges the wall of the chamber (around x=2220 cm; y=0 cm) is a considerable source of scattered neutrons. At CCD position a scattered neutron flux level of $7.2 \cdot 10^5$ $cm^{-2}sec^{-1}$ is obtained (0.8 % of the intensity of the direct beam). 80.6 % of these neutrons are in the “cold and thermal” energy region below 1 eV. Scattered neutrons in these energy regions are most disturbing because they are detected in the scintillator with higher efficiency compared to neutrons in higher energy regions.

The highest intensity of generated gamma radiation occurs also around the area where the neutron beam hits the wall of the chamber. At the CCD position the flux of generated gamma radiation is $1.7 \cdot 10^6$ $cm^{-2}sec^{-1}$. Besides the high generated background in the experimental chamber, version A has some practical disadvantages: In the case of contamination by activated powders or liquids, the rough surface of the heavy concrete walls is difficult to clean. Liquids may even infiltrate the concrete. In addition, the mechanical strength of heavy concrete is limited. For these reasons it makes sense to encapsulate the heavy concrete.

Version B

In version B the heavy concrete walls are encapsulated by steel liners (6 mm thickness). The disadvantageous practical aspects of version A are avoided. Width of gaps between single shielding elements can be kept small, as surfaces of steel liners are more precise than surfaces of heavy concrete elements. In addition, the problem that parts of the heavy concrete may crumble off (e.g. during assembly of the facility) is resolved. However, considering background radiation inside the experimental chamber the situation is worse in version B: Scattered neutron flux is increased by 46 % and generated gamma flux by 22 % compared to version A.

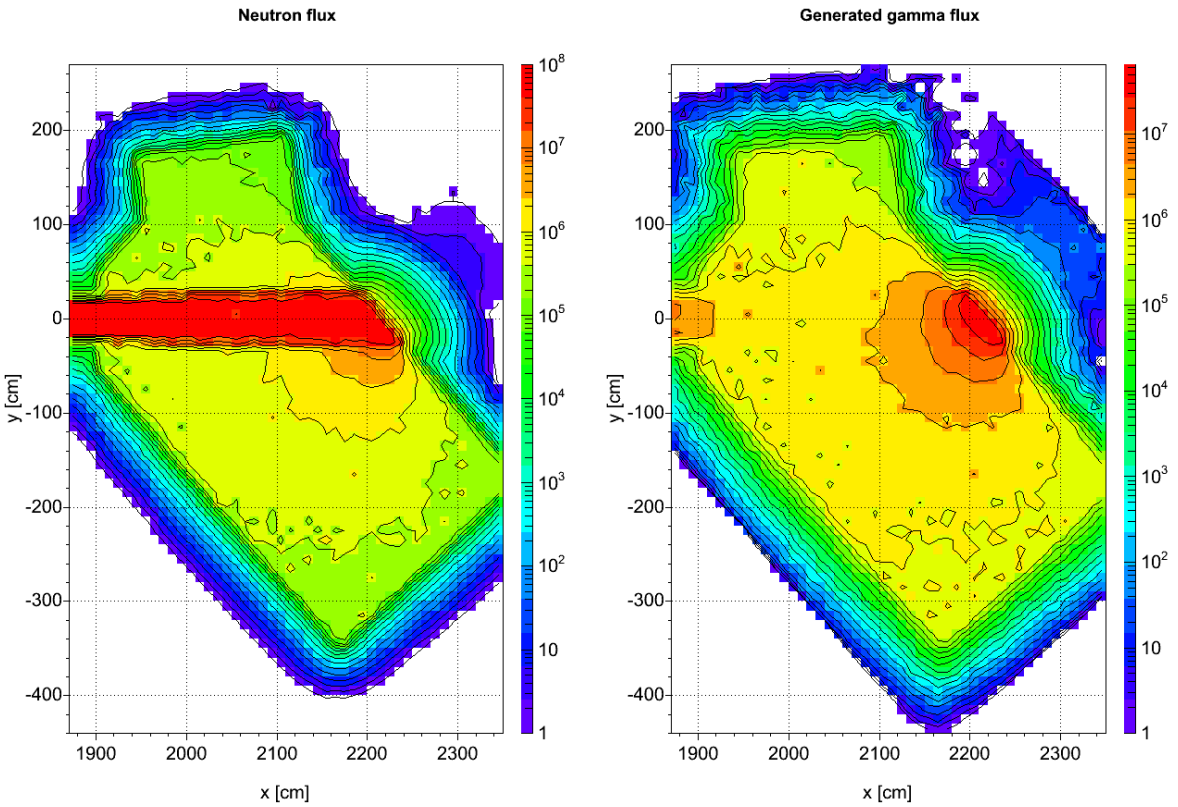

Fig. 2.54: Total neutron flux [$sec^{-1}cm^{-2}$] (left hand side) and generated gamma flux [$sec^{-1}cm^{-2}$] (right hand side) in a horizontal plane at beam axis level through the experimental chamber with steel liners and without beam catcher (version B). The walls consist of heavy concrete (ρ=4.7 g/cm^3).

Version C

In order to reduce neutron scattering and gamma production inside the experimental chamber a beam catcher has to be applied. For neutron absorption, ^{6}Li is the isotope of choice because no gamma radiation is generated along with neutron absorption (the neutron is absorbed by the reaction $^6Li(n,\alpha)^3H$). Natural Li contains only 6 % of ^{6}Li; therefore a material with enriched ^{6}Li content has to be preferred. As some broken LiF plates (ρ=2.64 g/cm^3; Li^6 enrichment: 90%) from scrap of an experiment at ILL [72] were available, it was tested by calculation if this material is of use for the beam catcher. Due to the small size of the shards, the only possibility was to grind the material and to encapsulate the powder (in an aluminum case). The bulk density of the powder is some 70% of the ceramics density. The beam catcher is mounted directly on the steel liner of the heavy concrete wall and covers the whole area where the direct beam impinges the wall. The neutron and generated gamma flux distributions in the experimental chamber for this arrangement are shown in Fig. 2.56. Compared to version B the neutron flux at the CCD position is decreased to 14 % ($1.5 \cdot 10^5$ $cm^{-2}sec^{-1}$). The generated gamma radiation is reduced by a factor of 34 ($6.1 \cdot 10^4$ $cm^{-2}sec^{-1}$). The most intensive source for generated gamma radiation is now the beam entrance of the experimental chamber. This type of beam catcher is very effective in the case of the ANTARES facility therefore.

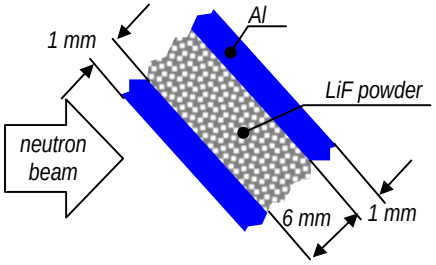

Fig. 2.55: Schematic cut through the beam catcher

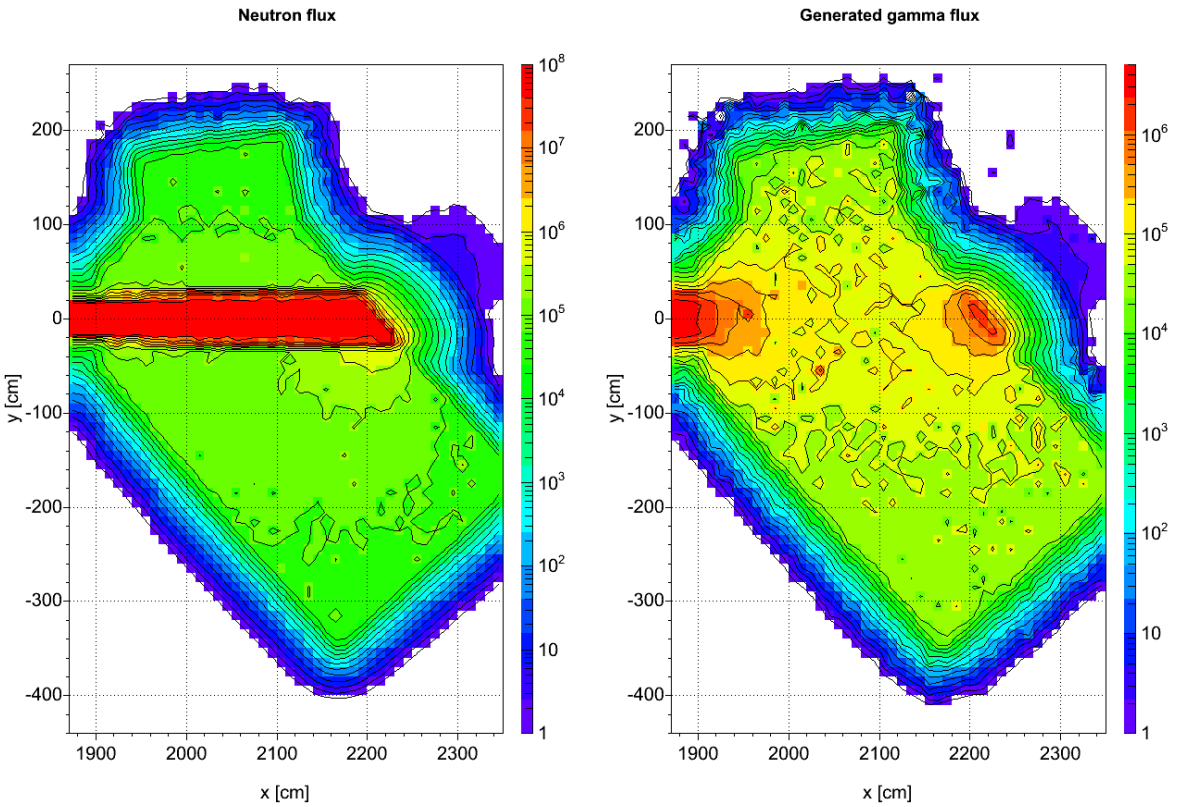

Fig. 2.56: Total neutron flux [$sec^{-1}cm^{-2}$] (left hand side) and generated gamma flux [$sec^{-1}cm^{-2}$] (right hand side) in a horizontal plane at beam axis level through the experimental chamber with steel liners and with beam catcher (version C). The walls consist of heavy concrete (ρ=4.7 g/cm^3).

Version D

In version D all steel liners in the experimental chamber are covered by boron carbide rubber mats (thickness 5 mm). The resulting flux distributions for neutrons and generated gamma radiation are shown in Fig. 2.57. The neutron flux at CCD position is reduced by a factor of 1.5 to $1.0 \cdot 10^5$ $cm^{-2}sec^{-1}$ in comparison to version C. The flux of generated gamma radiation is even increased slightly by 13 % to $6.9 \cdot 10^5$ $cm^{-2}sec^{-1}$ by the reaction $^{10}B(n,\alpha)^7Li$. ^7Li decays under emission of gamma radiation with an energy of 0.4774 MeV [40]. 81 % of the level of generated gamma radiation at position of the CCD chip is in the energy region below 0.5 MeV. A lead shielding of 1 mm thickness would attenuate 0.5 MeV gamma radiation to 16 %; for lower energies, attenuation is even higher. Therefore a thin lead shielding around the CCD camera can reduce the background in the CCD chip considerably. However, a significant reduction of background radiation is not obtained by the rubber mats themselves, but they are essential to avoid activation of the steel liners. Version D is the realized setup for the experimental chamber.

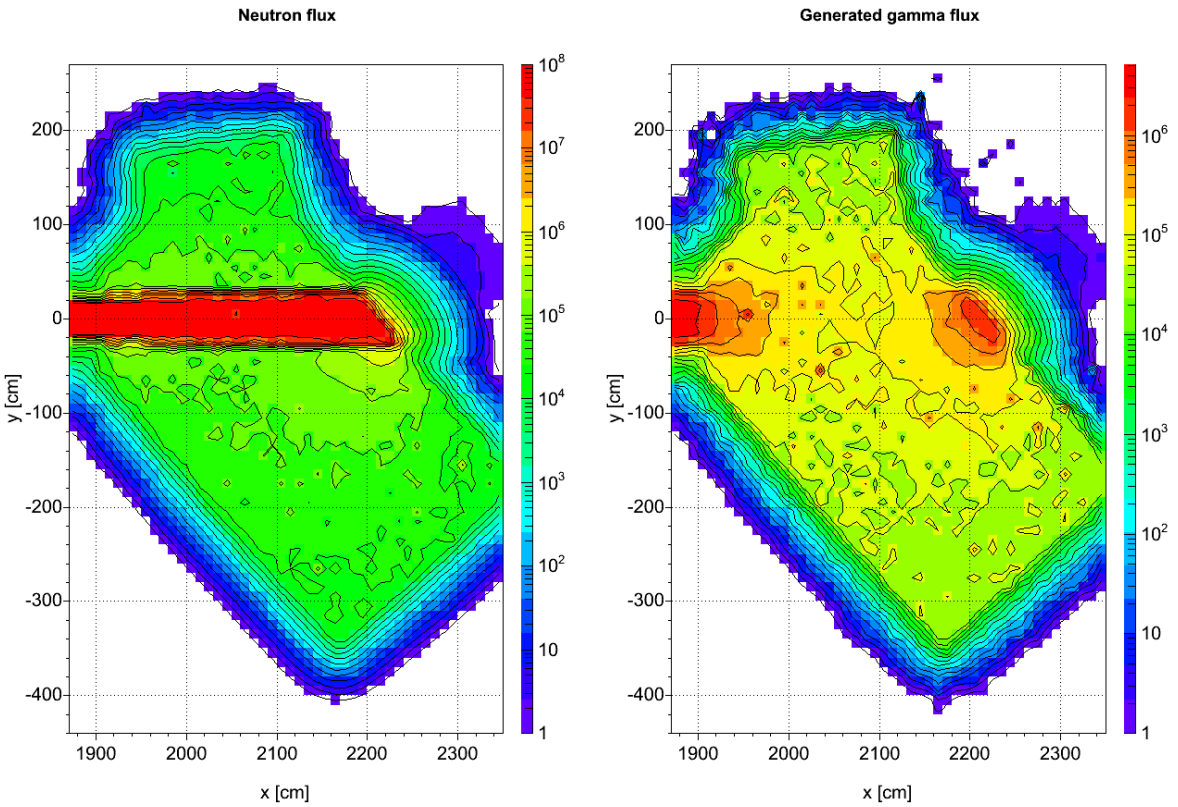

Fig. 2.57: Total neutron flux [$sec^{-1}cm^{-2}$] (left hand side) and generated gamma flux [$sec^{-1}cm^{-2}$] (right hand side) in a horizontal plane at beam axis level through the experimental chamber with steel liners covered by boron carbide rubber mats and a LiF beam catcher (version D). The walls consist of heavy concrete (ρ=4.7 g/cm^3).

The flux distributions of primary gamma radiation are very similar for all examined configurations. Therefore only the distribution for version D is shown in Fig. 2.58. The scattered primary gamma flux at CCD position is more than 5 times higher compared to generated gamma radiation in version D.

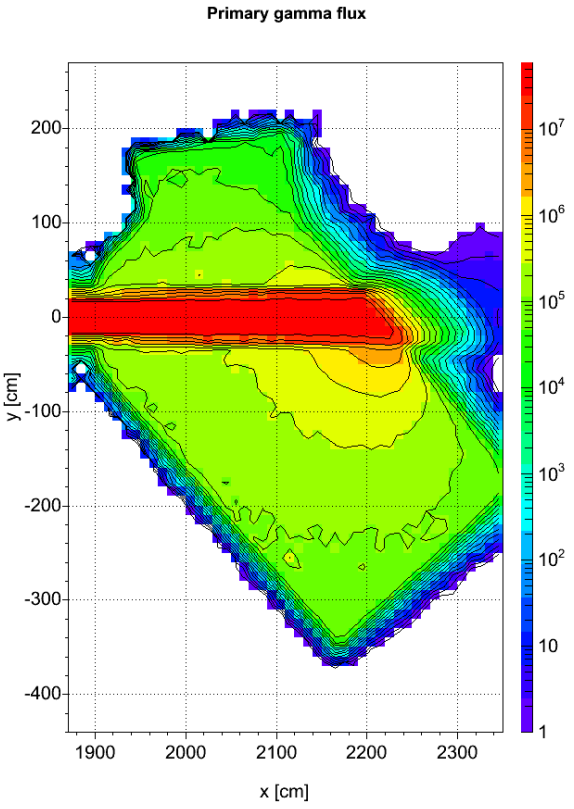

Fig. 2.58: Flux of primary gamma radiation [$sec^{-1}cm^{-2}$] in a horizontal plane at beam axis level through the experimental chamber with steel liners covered by boron carbide rubber mats and a LiF beam catcher (version D). The walls consist of heavy concrete (ρ=4.7 g/cm^3).

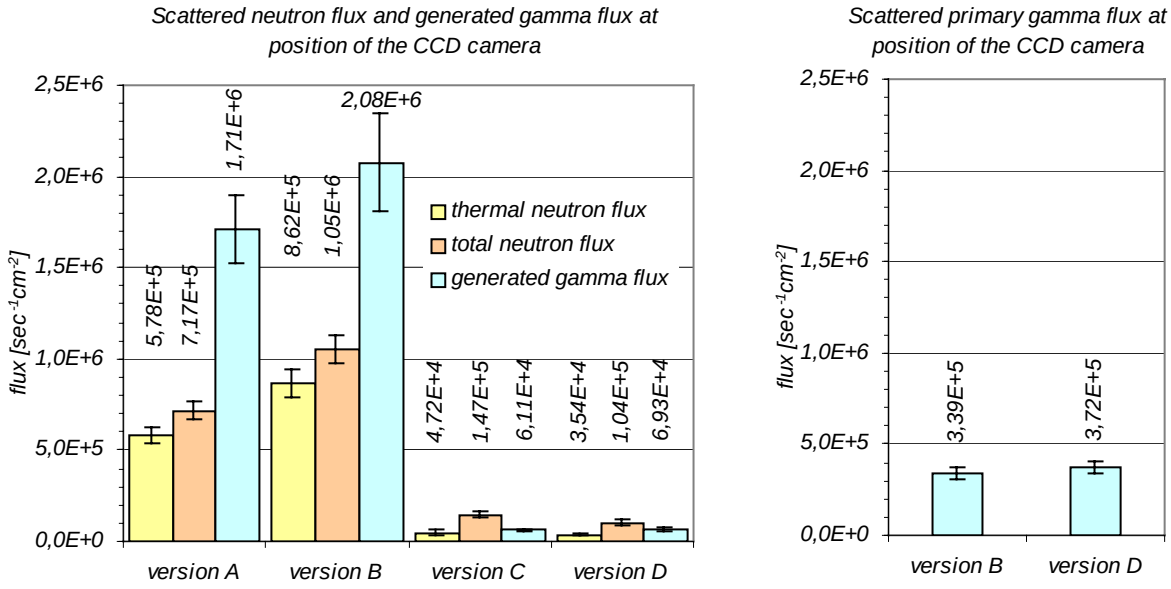

Fig. 2.59: Comparison of background radiation levels at position of the CCD camera for the different versions of the experimental chamber. The flux of scattered neutrons and generated gamma radiation is shown on the left hand side. The flux of primary gamma radiation is shown on the right hand side. As the flux of primary gamma radiation is very similar for all versions of the experimental chamber, only the values for version B and version D are shown here. The error bars indicate the statistic confidence intervals of the Monte Carlo simulations.

2.8 Beam parameters

The most interesting beam parameters in the detector plane are shown in Tab. 2.1. The exact values of the L/D ratios obtained by the collimators are 795.2 and 402.4. All flux data correspond to a reactor power of 20 MW. Total neutron flux for the L/D=795.2 ratio was verified by a gold foil activation measurement (see chapter 2.8.2 'Measurement of total flux and Cd ratio at position of the specimen'). The background of fast and epithermal neutrons was estimated by activation of a gold foil in a Cd case. From both gold foil measurements, the Cd ratio can be concluded. The Cd ratio is the ratio of activity induced by the neutron beam in a bare gold foil to that induced when the foil is covered with Cd [16]. The spectral neutron flux density in the cold and thermal energy region was verified by a time of flight (TOF) measurement (see chapter 2.8.1 'Spectral neutron flux density at position of the specimen').

As measure for the gamma background radiation in a neutron beam, the neutron/gamma ratio is widely used. The neutron/gamma ratio is defined as the ratio of neutron flux to gamma dose rate [16]. For the ANTARES facility it is given in Tab. 2.1. Results of measurements and calculations are discussed in the following chapters.

Parameter	*Calculation*	*Measurement*
width of fully illuminated area (L/D =402,4)	31,7 cm	
width of fully illuminated area (L/D =795,2)	36,4 cm	
height of fully illuminated area (L/D =402,4)	31,7 cm	
height of fully illuminated area (L/D =795,2)	36,4 cm	
fully illuminated area (L/D =402,4)	1,00E+3 cm^2	
fully illuminated area (L/D =795,2)	1,32E+3 cm^2	
neutron flux (L/D =402,4) [1]	9,36E+7 $cm^{-2}s^{-1}$ ± <1% [2]	
neutron flux (L/D =795,2) [1]	2,48E+7 $cm^{-2}s^{-1}$ ± <1% [2]	2,56E+7 $cm^{-2}s^{-1}$ ± 20%
neutron flux after Cd filter (L/D 795,2) [1]	1,64E+6 $cm^{-2}s^{-1}$ ± <1% [2]	2,00E+6 $cm^{-2}s^{-1}$ ± 25%
Cd ratio	1,51E+1 ± <1% [2]	1,28E+1 ± 32%
gamma flux (L/D =402,4) [1]	4,15E+7 $cm^{-2}s^{-1}$ ± <1% [2]	
gamma dose rate (L/D =402,4) [1]	6,92E-1 Sv/h ± <1% [2]	
neutron/gamma ratio	1,35E+8 $cm^{-2}s^{-1}Sv^{-1}h$ ± <1% [2]	

[1] reactor power 20 MW

[2] statistical error from Monte Carlo simulation

Tab. 2.1: Calculated and measured beam parameters in the detector plane

2.8.1 Spectral neutron flux density at position of the specimen

2.8.1.1 Calculation

For practical reasons the level of liquid D_2 cannot always be kept at a constant level. In the following the impact of the D_2 level on the neutron spectrum at position of the specimen is investigated. The spectral flux density at the location of the specimen inside the experimental chamber was calculated for different levels of liquid D_2 in the cold source. For the calculations the model of the final version of the ANTARES facility was used and the L/D =400 collimator/aperture setup was applied.

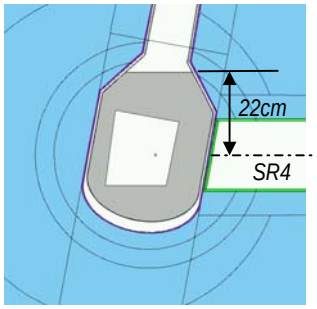

Fig. 2.60: Vertical cut through the Monte Carlo model of the cold source with a liquid level of 22 cm above the axis of beam tube SR4.

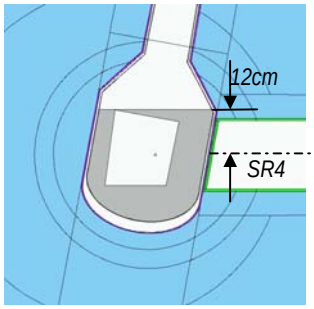

Fig. 2.61: Vertical cut through the Monte Carlo model of the cold source with a liquid level of 12 cm above the axis of beam tube SR4.

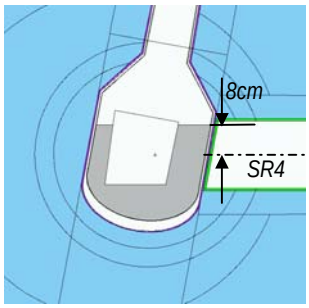

Fig. 2.62: Vertical cut through the Monte Carlo model of the cold source with a liquid level of 8 cm above the axis of beam tube SR4.

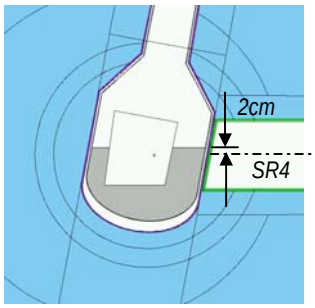

Fig. 2.63: Vertical cut through the Monte Carlo model of the cold source with a liquid level of 2 cm above the axis of beam tube SR4.

The standard level of liquid D_2 in the cold source is 22 cm above the beam axis of SR4 (corresponding to 16 l total volume of liquid D_2) as shown in Fig. 2.60. The spectral flux density at the location of the specimen is shown in Fig. 2.64 (green diamonds). For levels down to 8 cm above the beam tube axis of SR4 the influence is rather low. A small decrease in neutron flux in the energy region below 10 meV and a slight increase in the energy region above 10 meV is observable due to the lower amount of moderator volume. For a liquid level of 8 cm, the entrance window of the beam tube is not covered completely by liquid D_2. The rather small influence on the spectrum at the position of the specimen is caused by the collimator that cuts the projection of the source area to the desired size. The effective source area (12 cm x 12 cm, centered on the beam tube axis) is still covered by liquid D_2.

Calculated spectral flux densities in the detector plane in dependency of the liquid level in the cold source compared to measured data

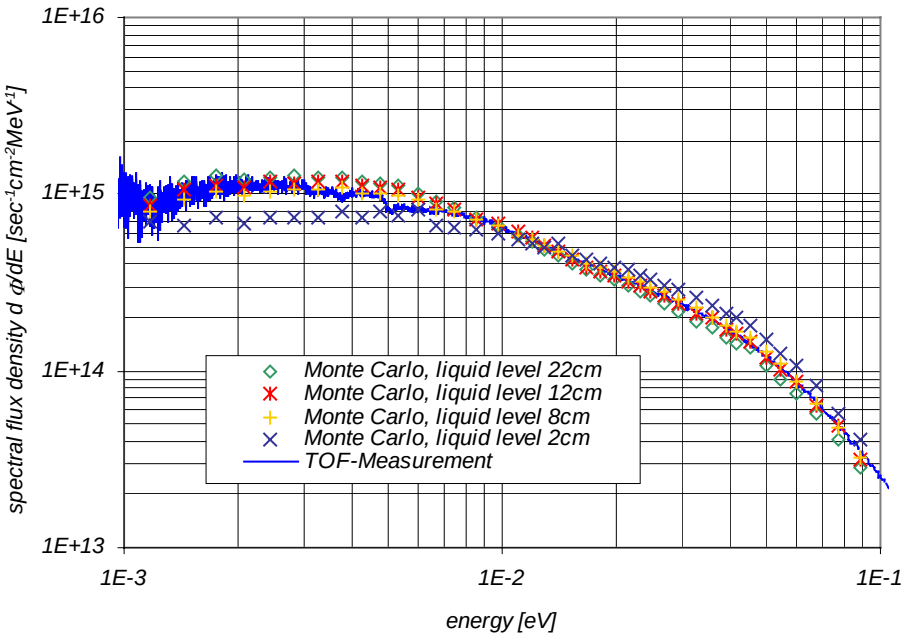

Fig. 2.64: Spectral flux densities at position of the specimen inside the experimental chamber of the ANTARES facility for different liquid levels in the cold source.

For comparison measured data is included in Fig. 2.64 (blue line). The total volume of liquid D_2 was 11.56 l during the measurement. The corresponding liquid level is about 10 cm above the beam axis. The measured data are in good agreement with the calculated data for 8 cm and 12 cm. Only one major deviation is observable between 5 meV and

6 meV. This is caused by the Bragg cut-off of aluminum. The neutrons have to cross several aluminum windows (e.g. entrance window of the beam tube and windows of the flight tube) before they reach the specimen. The Bragg cut-off is not considered in the calculations.

2.8.1.2 Measurement

Neutron spectra at the position of the specimen were verified by help of the time of flight method (TOF). The setup for the measurement consists of a chopper, a flight path, and a neutron detector.

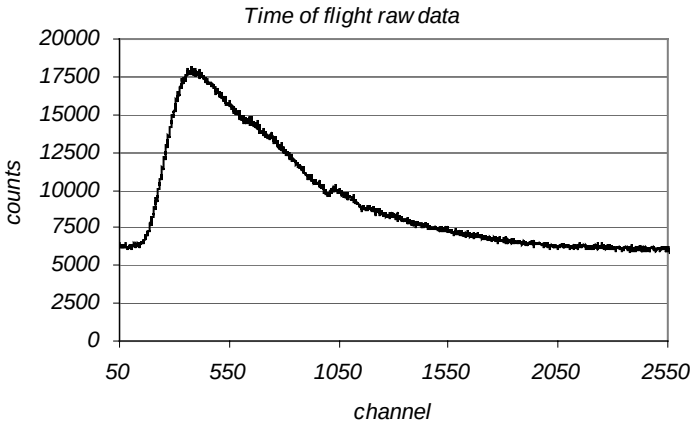

Fig. 2.65: Raw data of the time of flight measurement

The chopper is a single gap wheel (Ø 40 cm), which rotates at a speed of 4740 rpm. The wheel is coated with a Gd-layer in order to make it nearly opaque for cold and thermal neutrons. The gap has a width of 1 mm and is located on the wheel at a radius of 15 cm. The flight path between the chopper wheel and the detector has a length of 96 cm. Neutron detection is done by a ^{3}He counter tube. The underlying detection process is the ^{3}He(n,p)^{3}H reaction. The counter tube is shielded against background neutrons by means of a 5 mm layer of borated rubber. The flight path itself is shielded by a Cd-case.

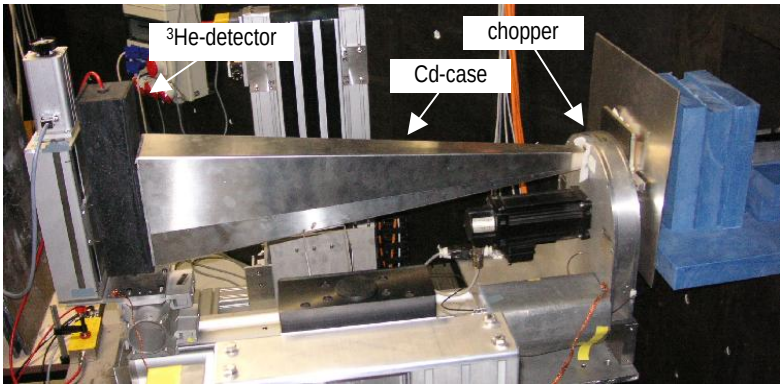

Fig. 2.66: Setup for time of flight measurement

The counts of the ^{3}He tube are collected in a multi-channel analyser. The registration of counts in the analyser is triggered by a photo sensor, which registers the wheel's phase. Each channel corresponds to a time interval of 1 µs. Fast and epithermal neutrons cause a high background. These neutrons traverse the chopper wheel and the Cd-case nearly without attenuation, but are still detected by the ^{3}He-tube. An additional shielding had to be applied. This shielding was made up from paraffin blocks with a thickness of 60 cm (Figs. 2.67, 2.68). The duct is a channel through the blocks with a cross section of 2 cm x 2 cm. Further reduction of the background radiation was achieved by a collimator. It consists of a block of borated polyethylene with a duct of 1 mm diameter. The length of the collimator is 40 cm. However, the background level was still rather high. Fig. 2.65 shows an example for raw data from the multi-channel analyser. The constant background level is at about 6000 counts. The signal itself surmounts the background by some 11500 counts at the maximum.

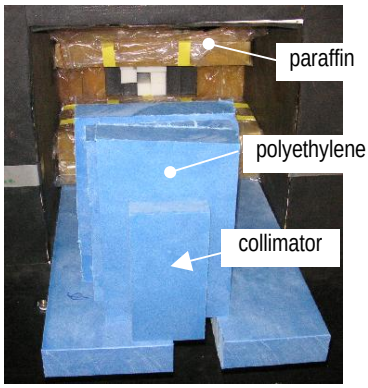

Fig. 2.67: Shielding for background reduction for time of flight measurement

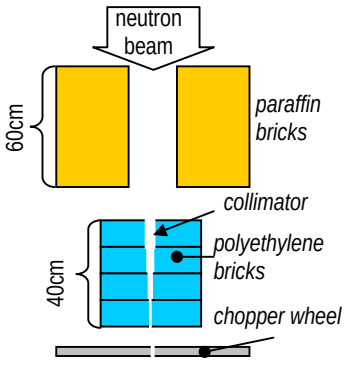

Fig. 2.68: Schematic overview of the shielding for background reduction (horizontal cut)

2.8.2 Measurement of total flux and Cd ratio at position of the specimen

The total flux at the position of the specimen inside the experimental chamber was measured by activation of gold foils. Gold captures neutrons by the reaction $^{197}Au(n,\gamma)^{198}Au$. The ^{198}Au nucleus is a β^--emitter (half-life time 2.69 d). The resulting nucleus from the β^--decay is an excited ^{198}Hg nucleus that emits γ -radiation with an energy of 411.8 keV [40]. Activity of the gold foil can be determined by measurement of this γ -radiation in a detector after neutron exposure. This measurement was carried out by help of a Ge-detector. From the activity of the gold foil, the total neutron flux can be concluded (the analysis of the measured data is described in the appendix A.3 “Analysis of Au-foil measurement”). The result of the measurement for the L/D=800 geometry is a neutron flux at position of the specimen of Φ_{total}=2.56 10^7 $sec^{-1}cm^{-2}$ ± 20%. This is in good agreement with the calculation which predicts a neutron flux of Φ_{total} =2.48 10^7 $sec^{-1}cm^{-2}$ ± 1% (the error is the statistical error of the Monte Carlo calculation).

The contamination of the neutron beam by epithermal and fast neutrons was measured by a gold foil confined in a cadmium casing. Cadmium shows a steep increase of neutron absorption cross section for energies below 0.6 eV, hence only activation by epithermal and fast neutrons is considered in this case. The ratio of total flux and flux after a cadmium filter is called Cd-ratio. The result of the measurement for the filtered flux is $2.00 \cdot 10^6$ $sec^{-1}cm^{-2}$ ± 25 %. The deviation from the result of calculation ($1.64 \cdot 10^6$ $sec^{-1}cm^{-2}$ ± 1 %) is bigger than for the total flux, but still within the confidence interval. The gold foils with and without the Cd-case were exposed simultaneously and had the same irradiation time (90 min). Therefore the statistical error of the counting of the Cd-covered foil is higher than that of the pure gold foil. Due to the lower count rate in the detector, uncertainty of activation is bigger. The resulting Cd ratio is 12.8 ± 32 % (calculation: 15.1 ± 1 %).

2.8.3 Spatial resolution of the facility

Different measures exist for the resolution of optical systems, depending on the purpose of the instrument. E.g. in astronomy the smallest angle under which two sources can be separated is widely used [34]. By this measure only the resolution limit of the system is given. For separation of the sources a minimum of intensity must be recognizable between the maxima caused by the sources. If this minimum value is close to the values of the maxima, the sources can hardly be separated. Hence high resolution in a signal is obtained when the modulation (see chapter 2.8.3.2 ‘Modulation transfer function’) between minima and maxima is not decreased too much by the optical system. The most general measure for resolution is the modulation transfer function that can be derived from the point spread function PSF [21]. The point spread function PSF defines the mapping of one point of the specimen in the projection. In an ideal case the PSF would be a delta function. In reality there are several reasons why a point in the specimen is mapped to an extended area in the measured data set. The most important contribution to blurring in neutron radiography is caused by the extended aperture, i.e. the geometry of the neutron beam. As described in the chapter 2.3 ‘Aperture’ the collimators at the ANTARES facility are designed to shape the PSF of the neutron beam ($PSF_{neutron}$) to a pill-box function. The accordance between predicted shape of $PSF_{neutron}$ and the real shape was verified by measurements.

2.8.3.1 Measurement of the point spread function

The projection of a specimen corresponds to the correlation of the 'ideal' image I_{ideal} (projection obtained by a neutron point source) with the $PSF_{neutron}$ (see also chapter 3.3 'Image degradation in neutron radiography'). For a specimen that is known in every detail, the $PSF_{neutron}$ could be found by deconvolution of the measured data with I_{ideal}. But there is another contribution to image degradation PSF_{de} from the detector system (the measurement was performed with the ANTARES standard detector system; see chapter 2.9.1 'ANTARES detector system'): The lens system of the CCD camera maps not exactly one point from the scintillator to one pixel on the CCD chip. In general, *PSFs* of lens systems have the shape of a Gauss function [21]. The combined PSF in a projection is therefore the correlation of $PSF_{neutron}$ and PSF_{de}. I.e. the measured data I_{proj} is the correlation of the ideal image with $PSF_{neutron}$ and PSF_{de} .

$$I_{proj} = I_{ideal} \otimes PSF_{neutron} \otimes PSF_{de} \qquad (2.5)$$

For a given neutron beam geometry the contribution $PSF_{neutron}$ is dependent on the distance between specimen and detector as shown in Eq. 2.3 (see chapter 2.3.7 'Point spread functions'). The radius of the pill-box decreases for decreasing distance between specimen and scintillator. In contrary, the PSF_{de} of the detector system is constant, i.e. for decreasing distance between specimen and scintillator, PSF_{de} becomes more and more dominant. When the distance is as small that the extension of $PSF_{neutron}$ is smaller than the area of one pixel, $PSF_{neutron}$ behaves like a delta function (in this context a pixel is the region of the scintillator that is mapped to one pixel on the CCD chip by an ideal optical system). For the setup used for the measurement this is the case for distances between specimen and scintillator of less than 5 cm. The blur in the projection is then only caused by the detector:

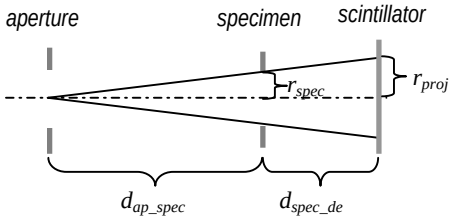

Fig. 2.69: Determination of the radius r_{proj} in the ideal projection I_{ideal}.

$$I_{proj} = I_{ideal} \otimes PSF_{de} \qquad (2.6)$$

In this case PSF_{de} can be determined by deconvolution of the measured data I_{proj} with I_{ideal}. For the measurement the pixel size in the scintillator was 126 µm x 126 µm. As reference specimen, a cadmium plate with a circular hole of 250 µm radius (r_{spec}) was used. The ideal projection of this specimen is a circle with radius:

$$r_{proj} = r_{spec} \cdot (d_{ap\_spec} + d_{spec\_de}) / d_{ap\_spec} \qquad (2.7)$$

where d_{ap_spec} is the distance between aperture and specimen and d_{spec_de} is the distance between specimen and detector (Fig. 2.69). The PSF_{de} derived from the measurement according to Eq. 2.6 is shown in Fig. 2.70. For deconvolution a Wiener filter was used (see chapter 3.4.2 'Wiener filter'). PSF_{de} can be described by a Gauss function:

$$PSF_{de}(r) = \exp\left(-(r / 2.4 \cdot ps)^2\right) \qquad (2.8)$$

where r is the distance from the center of PSF_{de} and ps is the pixel size (of course PSF_{de} depends on the distance of the CCD camera to the scintillator screen and the lens system, therefore Eq. 2.8 is only valid for exactly the setup used for this measurement). The knowledge of PSF_{de} enables for determining $PSF_{neutron}$ according to Eq. 2.5. Signals from the specimen located 221 cm and 157 cm before the scintillator are shown in Fig. 2.71. Deconvolutions were performed by a Wiener filter. The results are shown in Fig. 2.72. The *PSFs* have the shape of the anticipated pill-box functions (The small ring surrounding the PSF is an artifact due to the deconvolution algorithm). The radius of the $PSF_{neutron}$ is 9 pixels (=1.14 mm) for a distance of 157 cm between specimen and scintillator screen

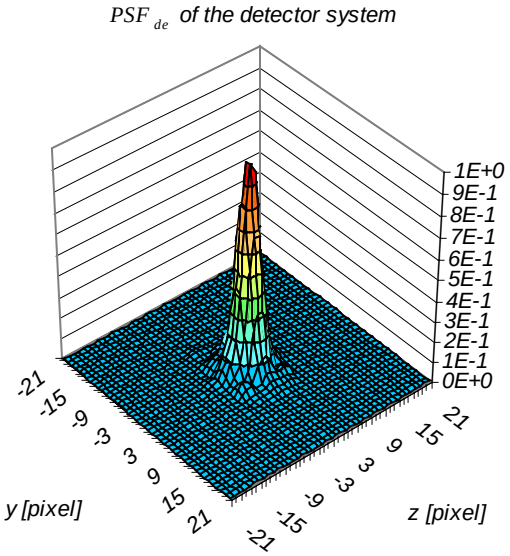

Fig. 2.70: Point spread function of the ANTARES standard detector system PSF_{de}

and the radius for a distance of 221 cm is 14 pixels (=1.78 mm). These values are in good agreement with the theoretical values obtained by Eq. 2.3 (1.09 mm resp. 1.60 mm) within the scope of pixel size.

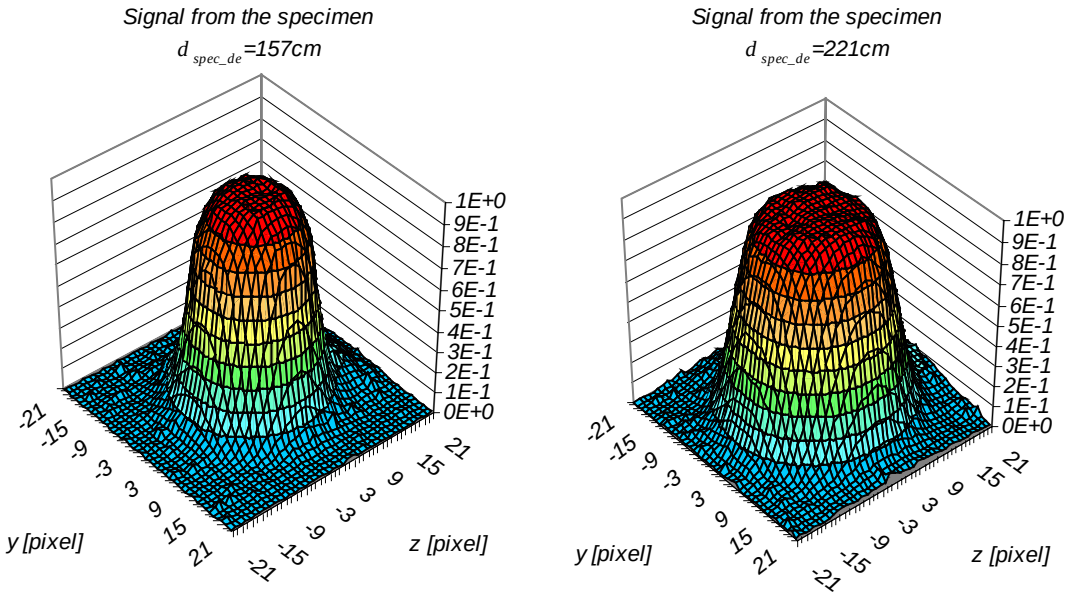

Fig. 2.71: Measured signal from the specimen (hole with diameter 0.5 mm in a Cd-plate) for a distance between specimen and detector of 157 cm (left hand side) and 221 cm (right hand side)

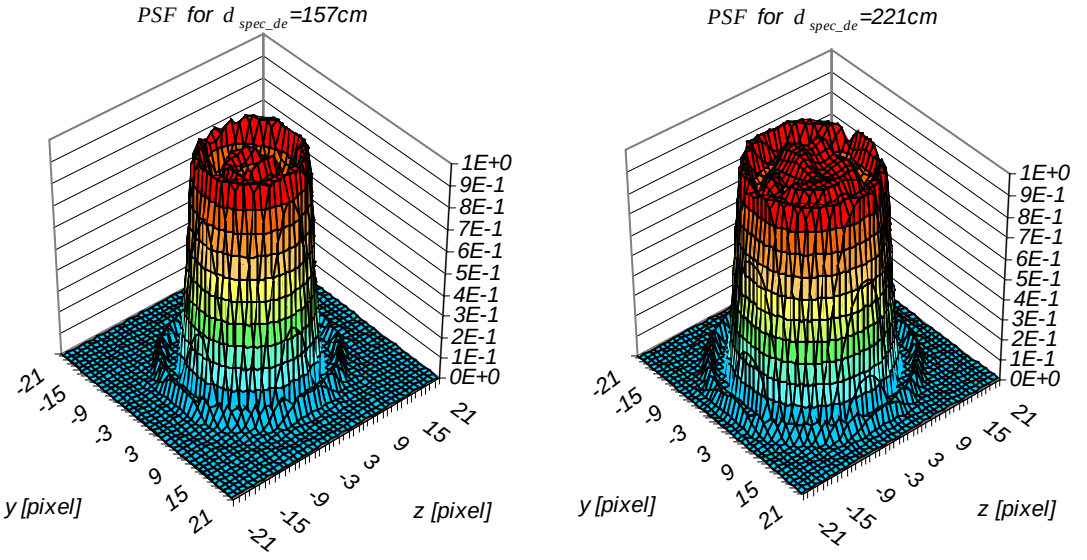

Fig. 2.72: Point spread functions $PSF_{neutron}$ from neutron beam geometry for a distance between specimen and detector of 157 cm (left hand side) and 221 cm (right hand side)

The radius of $PSF_{neutron}$ for the ANTARES facility can be calculated therefore according to Eq. 2.3 (see chapter 2.3.7 'Point spread functions'). Radii obtained by the two different collimator geometries are displayed in Fig. 2.73 in dependency of the distance between specimen and detector.

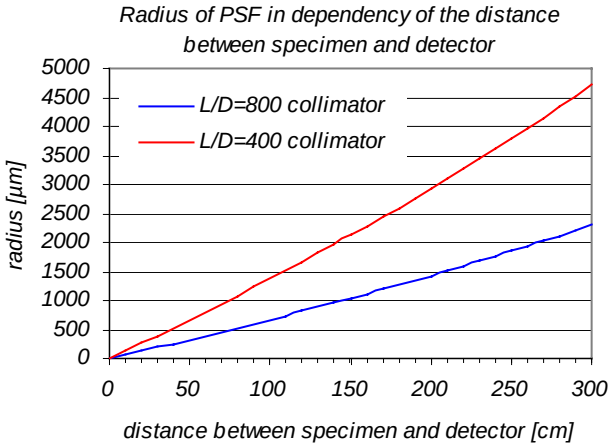

Fig. 2.73: Radius of the point spread function from neutron beam geometry ($PSF_{neutron}$) in dependency of the distance between specimen and detector

In the literature it is often proposed to derive the point spread function of an optical system from the edge spread function. The edge spread function is the line profile perpendicular to a projection of the rim of an absorber plate. The derivation of the edge spread function is a cut through the PSF. The disadvantage of this method is that only one dimension of the PSF is obtained. This is not bothering when the PSF is rotational symmetric; here the aim of the measurement was to verify the PSF and the collimator quality; point symmetry must not be presupposed for this purpose.

2.8.3.2 Modulation transfer function

For testing the resolution of the facility by calculation, a grid with varying lattice spacing was used as specimen. It consists of cylindrical bars filled by an ideal 'black' absorber. The specimen was placed at a distance of 221 cm before the detector and the L/D=800 collimator was applied, hence the PSF for this arrangement is the same as shown in Fig. 2.72 right hand side. The grid and its arrangement is shown in Figs. 2.74a and 2.74b. The spacing between the bars of the grid and the diameter of the bars increases from left to right when the grid is observed from the direction of the detector (against the neutron beam direction). In the projection of the grid each spacing and the bordering bars correspond to a certain frequency f:

$$f = 2\pi / \left(d_{spacing} + d_{bar} \right) \quad (2.9)$$

where $d_{spacing}$ is the size of the projected spacing and d_{bar} is the projected diamater of the bordering bars.

Small spacings and small diameters of the bars correspond to high frequencies and vice versa. Hence, with a projection of the grid it can be tested how a certain frequency is mapped in a projection. In an ideal projection, where the PSF is a delta function, the signal of this specimen divided by the open beam image (signal without specimen) would consist only of ones and zeros. The real, blurred signal is shown in Fig. 2.75. In the signal neither one nor zero is reached. Certain lattice spacings (i.e. certain frequencies) are not resolved at all, modulation is zero. The modulation m in a signal is [21]:

$$m = \frac{I_{\max} - I_{\min}}{I_{\max} + I_{\min}} \quad (2.10)$$

where I_{max} is the intensity at a maximum and I_{min} the intensity at a minimum.

The problem that structures with certain frequencies cannot be resolved occurs due to the extended pill-box shape of the PSF. In chapter 3.5.5 'Apodization', it is described whether this problem can be resolved by other shapes of the PSF.

The modulation transfer function MTF describes how the modulation of a structure is decreased by blurring due to the extended PSF as function of the frequency of the structure. Hence, the MTF is the most general measure for resolution. In principle one dimension of the MTF can be derived from the projection (Fig. 2.75) of the grid (Figs. 2.74a, 2.74b). In order to get the complete MTF many projections of the grid under different rotation angles would be necessary.

However, when the PSF of an optical system is known as in the case of the ANTARES facility, the MTF can be derived directly from the PSF. Projections of a grid as shown in Figs. 2.74a and 2.74b are not necessary in this case.

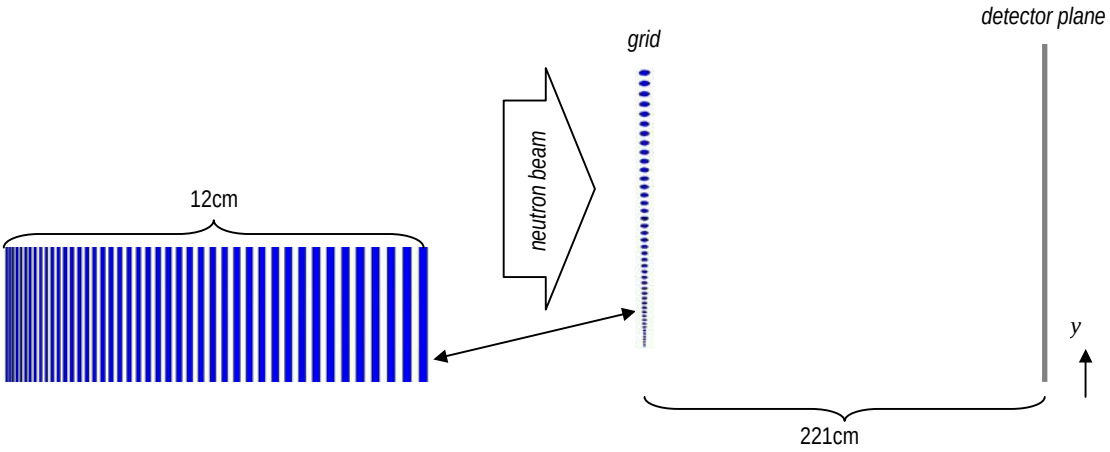

Fig. 2.74a: Vertical cut through the grid for estimation of the resolution of the ANTARES facility.

Fig. 2.74b: Horizontal cut through the grid (top) and vertical cut through the arrangement for estimation of the resolution of the ANTARES facility.

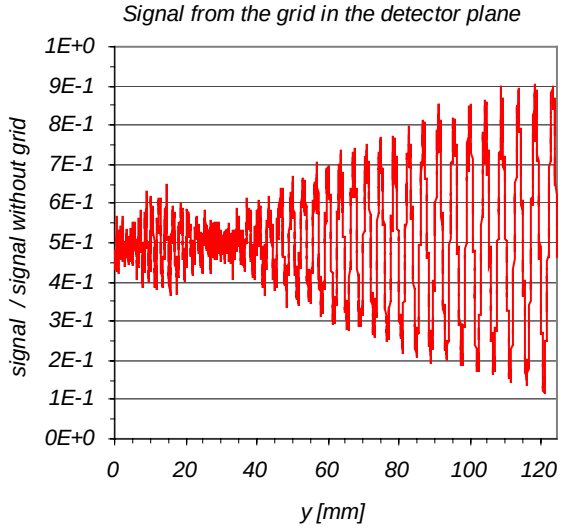

Fig. 2.75: Signal of the absorber grid as specimen in the detector plane divided by the signal without grid. The distance between grid and detector is 221 cm. For the projection the L/D =800 collimator was used.

The *MTF* is the absolute value of the *PSF* in the Fourier domain [21].

$$MTF(u,v) = \left|FT\left(PSF(x,y)\right)\right| = \left|\int_{-\infty-\infty}^{+\infty+\infty} PSF(x,y)\cdot e^{i\cdot 2\pi(u\cdot x+v\cdot y)}\,dxdy\right| \qquad (2.11)$$

The *MTF* for a distance of 221 cm between specimen and detector and application of the *L/D*=800 collimator is shown in Fig. 2.76. The profile has the shape of the absolute value of a sine cardinal function. As the *PSF* is rotational symmetric, the *MTF* is rotational symmetric, too. Hence the value of the *MTF* at location (*u*,*v*) in the Fourier domain depends only on the distance $\sqrt{u^2+v^2}$ to the origin in Fourier space.

The values of the *MTFs* for the ANTARES facility in dependency of the distance between specimen and detector are displayed in Fig. 2.77 for application of the *L/D*=800 collimator and in Fig. 2.78 for the *L/D*=400 collimator.

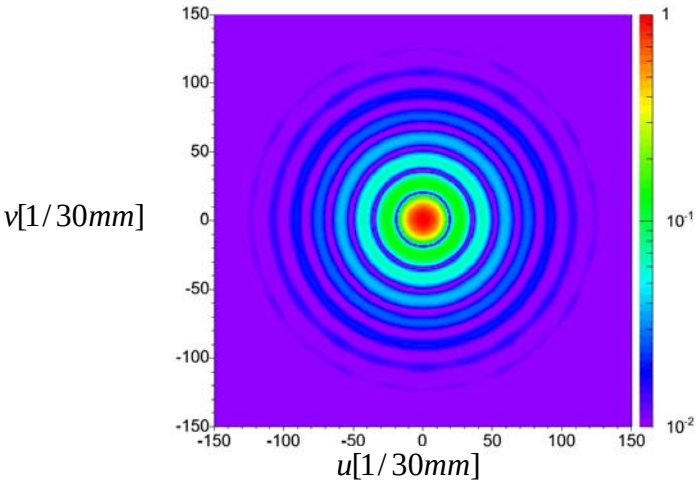

Fig. 2.76: Modulation transfer function (*MTF*) for the point spread function of the neutron beam obtained by the *L/D*=800 collimator and a distance between specimen and detector of 221 cm (the point spread function is shown in Fig. 2.72 right hand side)

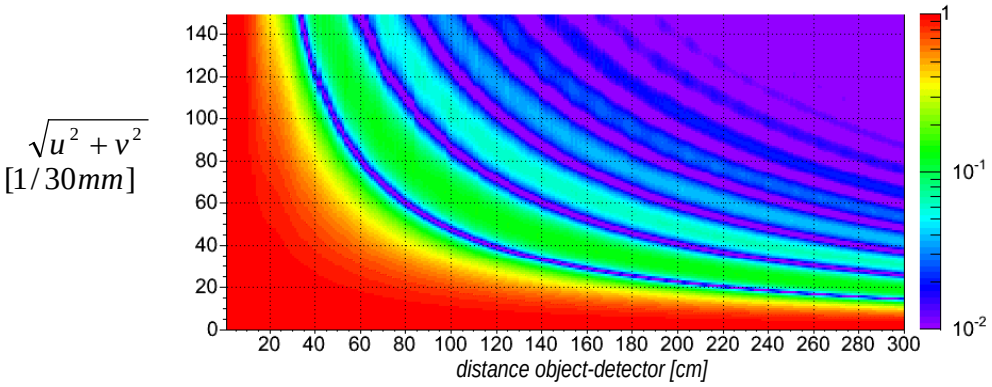

Fig. 2.77: Modulation transfer function in dependency of the distance from the origin in the Fourier domain and in dependency of the distance between specimen and detector for the *L/D* =800 collimator.

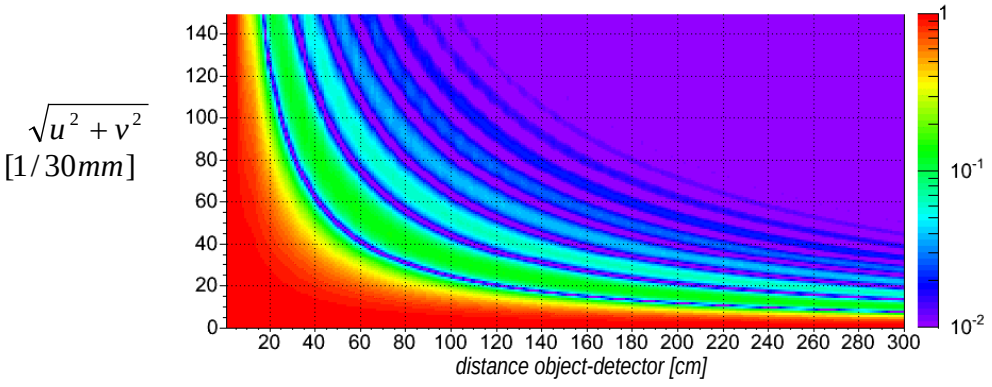

Fig. 2.78: Modulation transfer function in dependency of the distance from the origin in the Fourier domain and in dependency of the distance between specimen and detector for the *L/D* =400 collimator.

2.9 Neutron detection

2.9.1 ANTARES detector system

Neutrons are detected by help of a scintillator [35]. It consists of a thin layer of a powder mixture of lithium fluoride and zinc sulfide that is activated with Au, Al, and Cu [73] arranged on an aluminum plate. ^{6}Li captures neutrons by the reaction $^{6}Li(n,\alpha)^{3}H$. The gross kinetic energy of the reaction products (α and ^{3}H) is 4.78 MeV. Especially the α-particle ionizes due to its double charge the scintillator material. By recombination of electrons and nuclei in zinc sulfide, visible light is emerged [35] (on the average $1.75 \cdot 10^{5}$ photons per captured neutron). The Au, Al, and Cu content in the scintillator material is used to shift the spectrum of the emitted light to the desired wavelength region (green light; the maximum of the emission spectrum is at 540 nm). The gain of light in ZnS+LiF scintillators is higher compared to other commercial available scintillators e.g. ZnS+B and Gd_2O_2S scintillators [36]. A part of these photons is recorded by a CCD camera (highest sensitivity for green light). As the CCD-chip would suffer damage from the intense neutron beam, the camera is located outside the direct beam. The photons are reflected to the CCD camera by a mirror. A schematic overview of the detector system is shown in Fig. 2.79 and the real setup in Fig. 2.80. In principle the spatial resolution of this system is only limited by the range of α-particles in the scintillator material (some 10 µm). However, as shown in the chapter 2.8.3.1 'Measurement of the point spread function' the actual spatial resolution is worse due to the lens system. It could be improved by installation of a more sophisticated optical system. The main advantage of this system is that measured data can be read out nearly just in time. A disadvantage is that only about 20 % of neutrons are detected in the scintillator screen, 80 % of neutrons traverse the scintillator without interaction. Increasing the thickness of the scintillator is not useful as the material is semipermeable for visible light. Increasing thickness would decrease the number of photons reaching the CCD chip. This detector system is used for day-to-day radiography and tomography purposes at the ANTARES facility and is called 'ANTARES standard detector system' in the following. Other detection systems that could be used for special purposes are e.g. image plates [37]. Their advantage is higher neutron

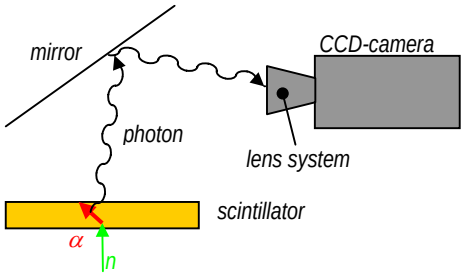

Fig. 2.79: Schematic overview of the ANTARES standard detector system

Fig. 2.80: ANTARES standard detector system

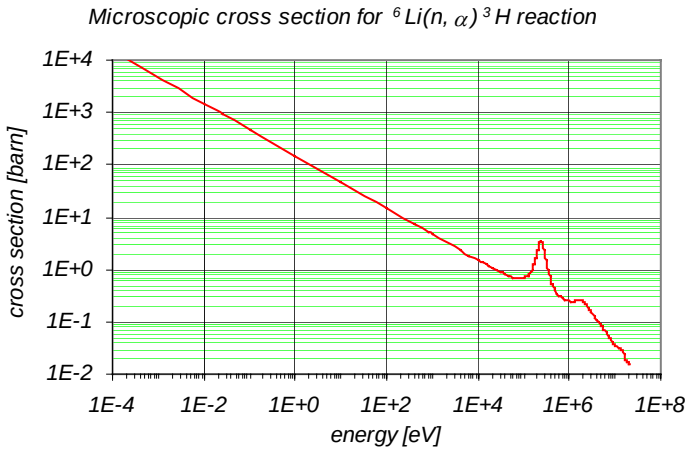

Fig. 2.81: Microscopic cross section for the $^{6}Li(n,\alpha)^{3}H$ reaction that is used for neutron detection in the scintillator.

detection efficiency and high resolution power. Disadvantageous is that online data read out is difficult. This is bothering especially for tomography. High resolution could also be obtained by combination of Gd-layers and X-ray films [16]. This method has also the disadvantage that data read out cannot be performed online. For special purposes (e.g. very thin specimen), α-radiographies can be used: α-particles are produced by neutron capture in a layer with boron content and are detected by a conventional photographic film.

2.9.1.1 CCD Camera

The CCD camera in the ANTARES standard detector system has a CCD-chip with 2048 x 2048 pixels. The dynamic range of each pixel is 2^{16} gray values. The CCD chip can be cooled down to –70°C for reduction of thermal noise. This is done by a built-in Peltier element. All measured data shown in this work is recorded by help of this camera. The behavior of dark currents for the CCD-chip is shown in the next chapter.

Optionally another CCD camera can be mounted in the detector system that is equipped with an image intensifier. The image intensifier enables for detection of a very low photon flux from the scintillator. The disadvantage of this camera is that its CCD chip has only 1024 x 1024 pixels.

2.9.1.1.1 Influence of exposure time and temperature on detector noise

In the CCD chip material free charges are not only produced by visible light but also by thermal energy. Those electrons are then trapped in the CCD potential well [99]. They cause a reading, which is undistinguishable from photoelectrons. The effect of thermal electrons is dependent on the temperature, but does not depend on the photon flux. The resulting current is therefore called *dark current*. Dark currents are bothering when taking radiographies with low intensity (e.g. radiography of high attenuating objects or in phase contrast radiography). In this case dark currents may even exceed the signal from the specimen.

The signal degradation depends on the exposure time, as the deposited charge is the time integral over the dark current.

By cooling the CCD chip it is possible to reduce significantly the number of thermal electrons. The dark current increases with rising temperature. Figs. 2.82 to 2.85 show the mean value, the median value, the maximum value, and the minimum value of dark currents in all pixels represented by the gray levels. The measured signal in the absence of visible light contains an additional component: A pedestal value of the ADC. The mean gray values in Fig. 2.82 show that the dark currents are nearly independent from integration times up to 300 sec for -70°C. Even at -30°C the dark currents are constant (average gray value=340) for up to 30 sec integration time. Here the dominant component is the pedestal value of the ADC. The median value of dark current gray values of all pixels is shown in Fig. 2.83. The *median* value is the gray level for which 1/2 of all pixels show values less than or equal to the *median* and 1/2 of all pixels show gray values equal to or greater than the *median*.

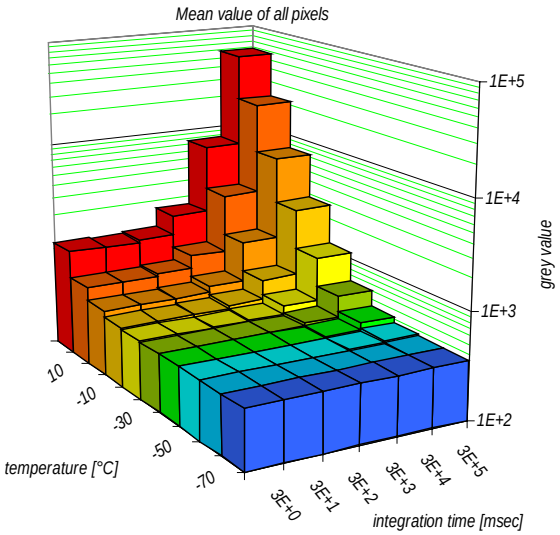

Fig. 2.82: Mean gray value of all pixels in the CCD chip without illumination in dependency of temperature and integration time

From Figs 2.82 and 2.83 one might conclude that subtraction of a constant background (the mean value of dark currents of all pixels) would be a good idea to reduce the influence of the dark current on the image. Due to the different values of the dark currents in each pixel (see standard deviation in Fig. 2.86), reducing the dark currents by a constant does not reduce the noise caused by dark currents. Therefore cooling down the CCD chip and choosing small exposure times are the best means to minimize the impact of dark currents.

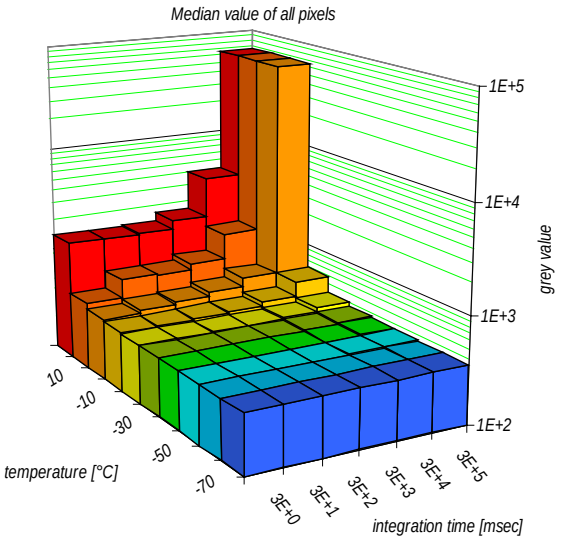

Fig. 2.83: Median gray value of all pixels in the CCD chip without illumination in dependency of temperature and integration time

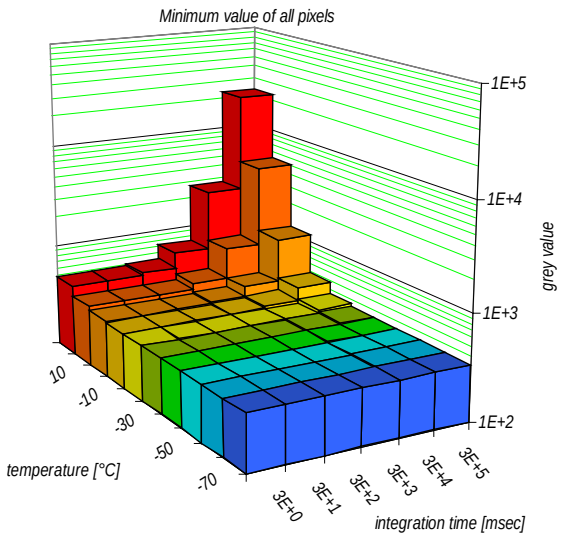

Fig. 2.84: Minimum gray value of all pixels in the CCD chip without illumination in dependency of temperature and integration time

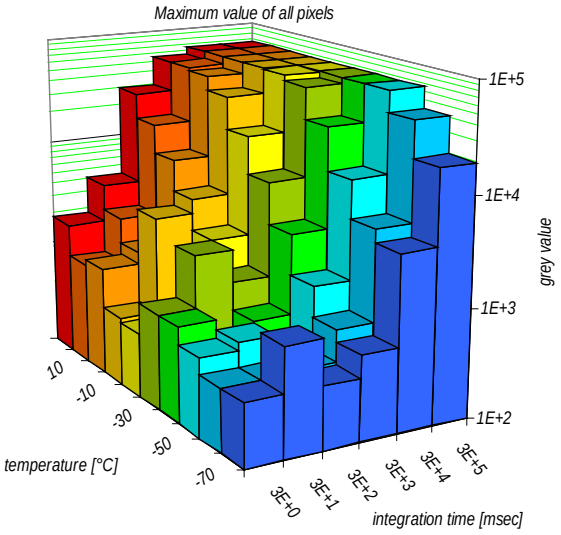

Fig. 2.85: Maximum gray value of all pixels in the CCD chip without illumination in dependency of temperature and integration time

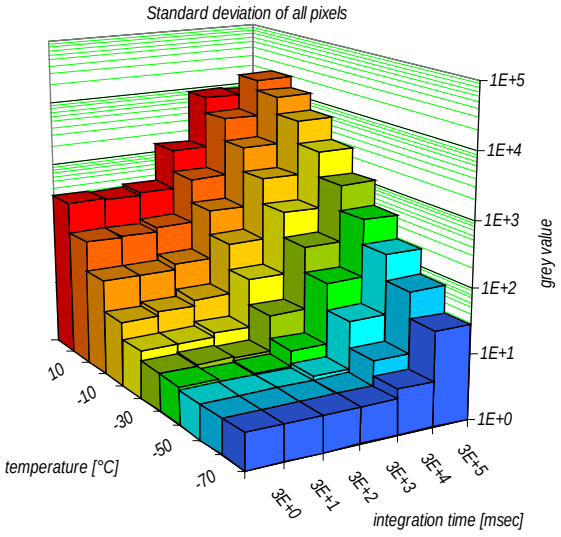

Fig. 2.86: Standard deviation of gray values of all pixels in the CCD chip without illumination in dependency of temperature and integration time

2.10 Radiation shieldings

Main purpose of the radiation shieldings is to guarantee a save access for experimenters to each point outside the shielding during experiments. In addition the background radiation level for other experiments should be as low as possible. The background of neutrons in the thermal and cold energy region is the most disturbing component, as some neighboring experiments in the reactor hall are based on neutron detection yielding only few counts per minute (e.g. the thermal triple axis spectrometer at beam tube SR5 [41]).

2.10.1 Neutron interactions in material

Elastic scattering X(n,n)X

For elastic scattering of a neutron (n) at a nucleus (X) the total kinetic energy of the system is conserved. There are two different processes of elastic scattering: Resonance scattering and potential scattering [39]. In the case of elastic resonance scattering an excited compound nucleus n+X is formed. The compound nucleus decays under emission of a neutron. In the case of potential scattering the incident neutron is not assimilated in the target nucleus. The neutron is scattered by the potential of the nucleus. For low-energy neutrons, elastic scattering is nearly isotropic in the center of mass system. This is a good approximation for hydrogen up to energies of 40 MeV [39]. For target nuclei heavier than hydrogen it is a good approximation (within a factor of about 2) when the incident neutron energy is below $5A^{-2/3}$ MeV where A is the number of nucleons [26]. Anisotropy increases with increasing energy of the incident neutron. For high neutron energies the angular distribution of scattering gets a forward peak due to diffraction around the nucleus (“shadow scattering”).

Inelastic scattering X(n,n’)X*

In the case of inelastic scattering, the incident neutron (n) raises the energy of the target nucleus (X) to the first excited state or above (in most cases by assimilation and reemission of the neutron, sometimes by direct excitation). The excited nucleus decays to the ground state by emission of gamma radiation. The energy of the scattered neutron is in most cases far below the energy of the incident neutron. This is useful for neutron shielding, as neutron energy degradation is done on the average by less interactions compared to elastic scattering. Depending on the energy difference between ground state and excited states of the target nucleus, the energy threshold of the incident neutron for inelastic scattering is generally high [39].

Particle reactions X(n,p)Y, X(n,α)Y, etc.

In particle reactions the neutron is captured in the target nucleus and a particle (e.g. proton or alpha particle) is emitted. The energy threshold for particle reactions is rather high (MeV region) for most target nuclei. For some light nuclei particle reactions also occur in the thermal energy region. One example is the ^{10}B(n,α)^{7}Li reaction. This reaction is useful for the absorption of thermal neutrons without production of high energetic gamma radiation. The resulting Li-Nucleus from the reaction is excited and returns to the ground level by emission of gamma radiation with an energy of only 0.4774 MeV [40]. Attenuation of gamma radiation in this energy region is higher than for bigger energies. Particle reactions in which the incident neutron is captured without subsequent neutron emission can also be classified as ‘neutron absorption’. This holds for most particle reactions (exceptions are reactions where e.g. two neutrons or an α-particle and a neutron are emitted; e.g. ^{12}C(n , n’,α)^{8}Be [39]).

Absorption X(n,γ)Y

In the case of absorption (=neutron capture) the incident neutron is assimilated in the target nucleus. The compound nucleus is excited. The decay is accompanied by the emission of gamma radiation. In most cases absorption cross sections increase with decreasing incident neutron energy, with the exception of resonance absorption in the intermediate energy region [39].

2.10.2 Interaction of gamma radiation in material

The predominant energy range for gamma radiation from the reactor core (gamma radiation from fission and fission products) and from neutron capture in material (structure material and radiation shieldings) is from 0.1 MeV to 10 MeV. In this energy range, three processes of interaction of gamma radiation with material are most important:

Photoelectric effect

The photon is absorbed in an atom and the photon energy is transferred to an electron (mostly an electron in an inner shell). The photoelectric effect is the dominant interaction process for low incident gamma ray energies, in combination with high-Z target atoms (Z = atomic number). The cross section is roughly proportional to Z^5 for incident gamma energies above 0.1 MeV [39]. It decreases rapidly with increasing energy [39].

Compton scattering

A photon is scattered inelastically at an electron of an atom. The electron recoils out of the atom. This process is dominant in the energy range between 1 MeV and 3 MeV in high Z-material (e.g. lead; see cross sections in Fig. 2.88). In materials with low Z, Compton scattering dominates even at higher energies (e.g. iron; see Fig. 2.87) [39]. The cross section of Compton scattering is proportional to Z of the target nuclei [42].

Pair production

A photon disappears and its energy is used to create an electron positron pair in the neighborhood of an atom. Hence, the energy threshold for this reaction is twice the mass of an electron (1.022 MeV). For higher energies, the cross section increases monotonically up to about 50 MeV for high-Z material, for low-Z materials even to higher energies. The cross section is approximately proportional to Z^2 of the target material [39].

Coherent scattering

At low incident photon energies elastic (coherent) scattering occurs, in which the photon is scattered elastically at an atom or a molecule as a whole (Rayleigh scattering [42]). For energies above 1 MeV, the coherent cross section is roughly between one and two orders of magnitude below the Compton scattering cross section. In the interesting energy region this is a minor effect. However, it is considered in all calculations presented in this work.

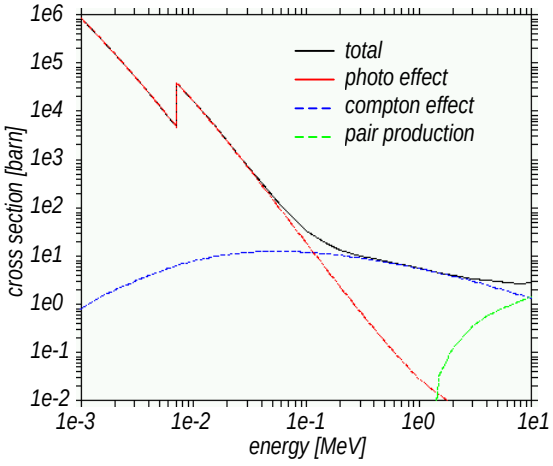

Fig. 2.87: Photon cross sections for iron

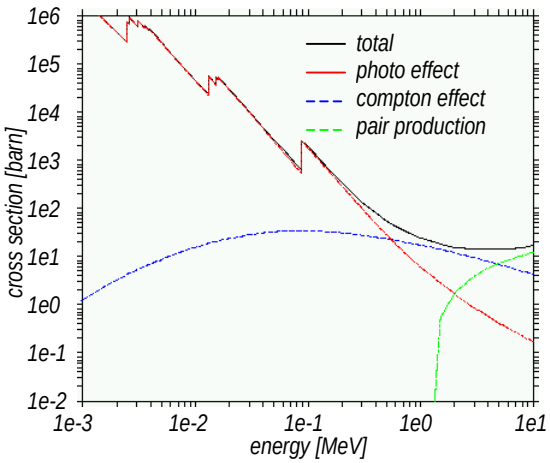

Fig. 2.88: Photon cross sections for lead

2.10.3 Shielding materials

The effectiveness of neutron radiation shieldings depends on the composition of the shielding material and the neutron spectrum itself. For testing different shielding materials for the ANTARES facility the following calculation model was used:

2.10.3.1 Calculation model for testing shielding materials

The calculation model for testing shielding materials for the ANTARES facility is shown in Fig. 2.89. The neutron source is a point source. The neutron energy distribution is that of the ANTARES facility and the angular distribution of emission is isotropic. The source is located in the center of a ball with radius R=80 cm. The ball is filled with the shielding material. For comparison of different shielding materials, the neutron dose and the dose of generated gamma radiation per source neutron on the surface of the ball is considered. As example for the calculation model, the model with an iron and a polyethylene layer (see next chapter) is displayed in Fig. 2.89.

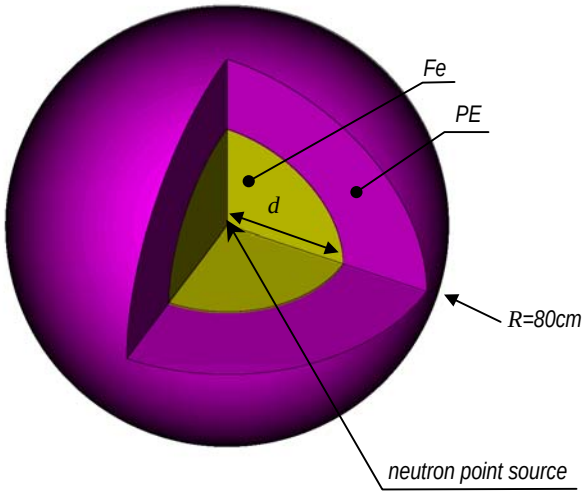

Fig. 2.89: Calculation model for an iron and a polyethylene layer as shielding material.

2.10.3.2 Iron and polyethylene

Heavy materials like iron are used to reduce the neutron energy by inelastic scattering to a level where the cross sections for elastic scattering in light elements are high [26]. Iron has a high density of resonances in the energy region between 0.1 MeV and 0.7 MeV. The inelastic scattered neutrons have energies in the keV region. Similar resonance densities are only found in titan, which is too expensive for shielding purposes. For effective slowing down of fast neutrons, iron (mass density ρ(Fe)=7.86 g/cm^3) is therefore the material of choice. In addition, materials with high atomic number are an effective shielding against gamma radiation. For further deceleration of neutrons, elastic scattering in hydrogen is most effective. Polyethylene (CH_2) has a very high density of hydrogen (the mass density of polyethylene (PE) varies between 0.92 g/cm^3 and 1.0 g/cm^3; for the calculations a density of ρ(PE)=0.95 g/cm^3 was assumed).

2.10.3.2.1 Inhomogeneous arrangement

The shielding effectiveness of a steel/polyethylene combination was tested with the calculation model described above (Fig. 2.89). The inner part of the ball is filled by an iron layer of thickness d. The outer part consists of a polyethylene layer of thickness R-d.

In order to find the optimal shares of iron and hydrogen, the thickness of layers was varied in steps of 5 cm. The neutron dose outside the shielding arrangement (on the surface of the ball) is shown in Fig. 2.90. The total neutron dose decreases for increasing thickness d of the iron layer up to d=45 cm where the lowest dose is reached. Here, the dose is 18 % of the dose outside the ball of pure polyethylene (d=0). The optimal mass fraction of iron and hydrogen along a radial path through the shielding is m_{Fe}/m_H=74:1. For thicker iron layers, the dose increases steeply. The contribution of thermal neutrons is dominant for an iron layer thickness between 55 cm and 75 cm. A pure iron layer (d=80 cm) attenuates the neutron radiation four orders of magnitude less than the pure polyethylene layer (d=0). The contribution of thermal neutrons to the dose is low due to missing moderation in hydrogen. The optimal amount of iron and hydrogen depends on the neutron spectrum and may differ for other spectra [44].

The generated gamma dose on the surface of the ball is displayed in Fig. 2.91. Neutron capture in iron produces gamma radiation with energies up to 7.7 MeV and neutron capture in hydrogen produces gamma radiation with an energy of 2.2 MeV [43]. The step from the pure polyethylene layer (d=0) to the combination of a 5 cm iron layer and a 75 cm polyethylene layer (d=5 cm) causes an increase of total generated gamma dose of more than a factor two. The contribution of high energetic gamma radiation (Fig. 2.91, yellow curve 'E>3 MeV') is increased by two orders of magnitude due to neutron capture in iron. Further increase of the iron layer up to 45 cm reduces the dose of generated gamma radiation due to attenuation in iron. For bigger iron layers the dose slightly increases: Neutrons are thermalized in the polyethylene layer closer to the outer border of the shielding, hence gamma production by thermal neutron capture in hydrogen occurs also closer to the border. For the pure iron ball (d=80 cm) the dose is minimal. Due to the missing moderation in hydrogen, less neutrons are thermalized and captured.

For a combination of a 45 cm iron layer and a 35 cm polyethylene layer, for which optimal neutron attenuation is achieved, the generated gamma dose exceeds the neutron dose by a factor of more than 2000. The iron content of the shielding does not attenuate gamma radiation generated in the outer polyethylene layer. Therefore this shielding is not an optimal solution.

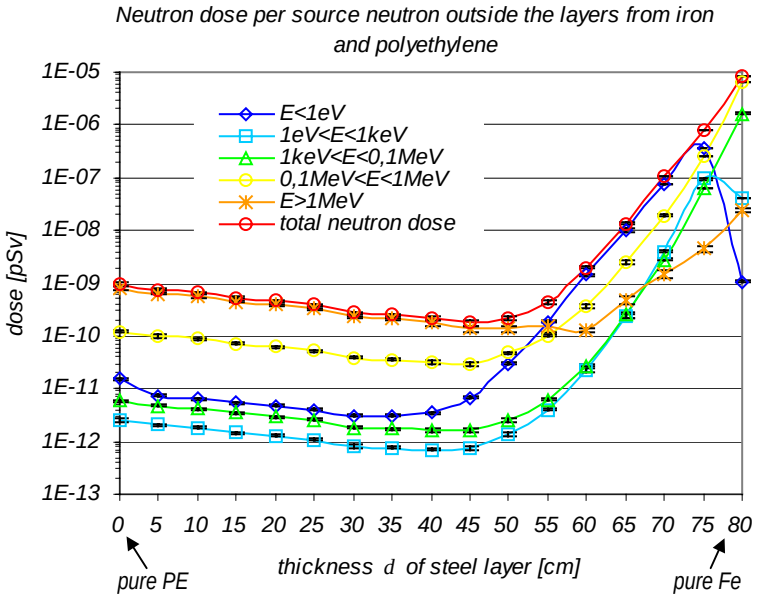

Fig. 2.90: Dose of neutron radiation per source neutron on the surface of the ball consisting of an iron and a polyethylene layer. Minimal neutron dose rate is achieved for 45 cm of iron and 35 cm of polyethylene.

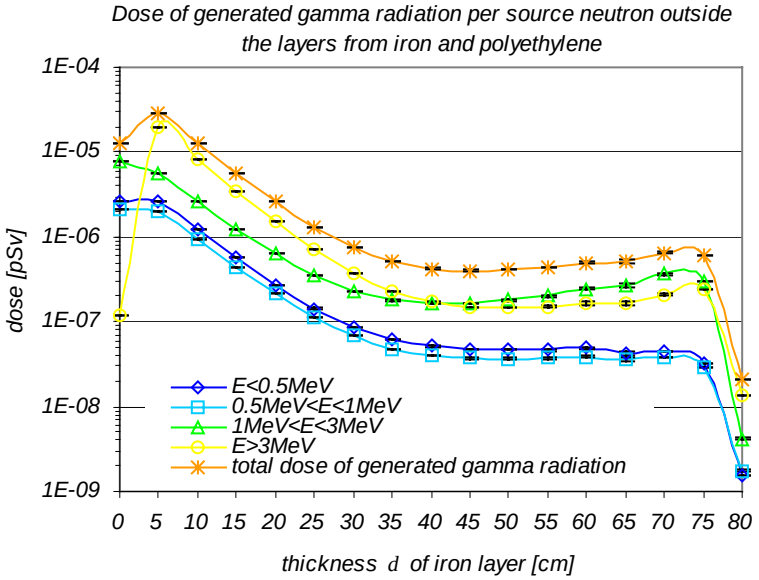

Fig. 2.91: Dose of generated gamma radiation per source neutron on the surface of the ball consisting of an iron and a polyethylene layer. The minimal dose rate of generated gamma radiation is achieved for 45 cm of iron and 35 cm of polyethylene.

2.10.3.2.2 Homogeneous arrangement

For reduction of generated gamma dose, an homogeneous iron and polyethylene mixture might be useful. In practice, such a solution can be approximated by a laminated arrangement of alternating iron and polyethylene layers. For calculation, the limit of tapering was assumed: An homogeneous mixture. In order to find the optimal share, the partial mass densities of iron and polyethylene were varied. This was done in a volume conserving way: A certain volume of the one material replaces the same volume of the other material. For a certain partial mass density of iron $\rho_p(Fe) = m(Fe)/V_{ges}$, the partial mass density of polyethylene $\rho_p(PE) = m(PE)/V_{ges}$ is found by:

$$\rho_p(PE) = \left(1 - \frac{\rho_p(Fe)}{\rho(Fe)}\right) \cdot \rho(PE) \quad (2.12)$$

The minimum of neutron dose is achieved for 4 g/cm^3 partial mass density of iron (the overall density of the mixture is 4.47 g/cm^3). The neutron dose is 69 % higher than for the best case with the pure iron and polyethylene layers described in the previous chapter. The optimal mass ratio of iron to hydrogen is m_{Fe}/m_H=60:1 which is less than for the combination of two layers. For neutron attenuation the homogeneous mixture is less effective than the combination of two layers: Fast neutrons can be moderated by elastic scattering in hydrogen to energies below the iron resonances, hence in this case the shielding quality does not benefit from fast deceleration due to inelastic scattering in iron.

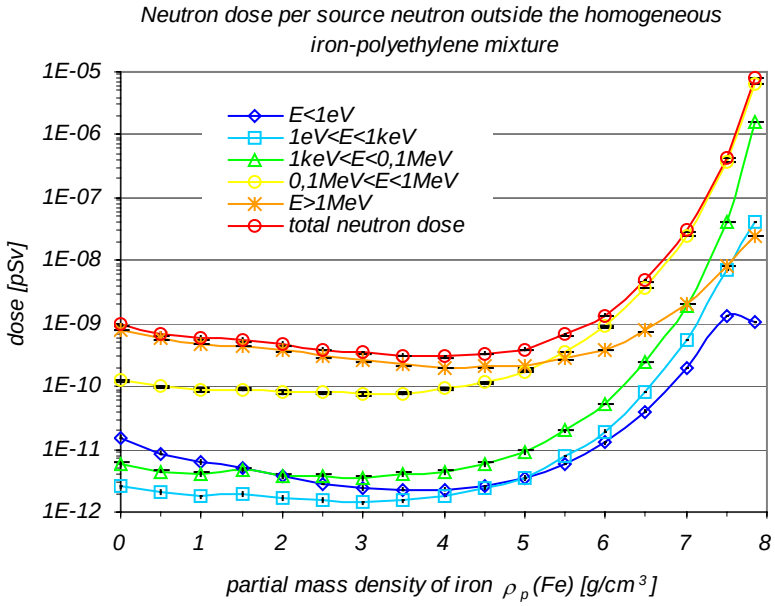

Fig. 2.92: Neutron dose per source neutron on the surface of the ball consisting of an homogeneous iron and polyethylene mixture. The minimal dose rate is achieved for partial mass densities of 4.0 g/cm^3 for iron and 0.47 g/cm^3 for polyethylene.

The dose of generated gamma radiation is for the optimal mass shares for neutron attenuation 10 times less compared to the arrangement of two layers. Further reduction of generated gamma dose could be obtained by avoiding production of high energetic gamma radiation due to thermal neutron capture in iron and polyethylene. For this purpose, materials with high absorption cross sections in the thermal energy range that emit no or only low energetic gamma radiation with neutron capture have to be included in the mixture (e.g. boron). However, besides the relative high attenuation of neutron radiation, polyethylene has also some disadvantages as shielding material. Its mechanical strength is limited, it is flammable, and it is decomposed by radiation. The molecule chains undergo scission, with the consequence of weakened stability. The tensile strength of polyethylene is reduced to 80 % by a dose of about 10^7 Gy [27].

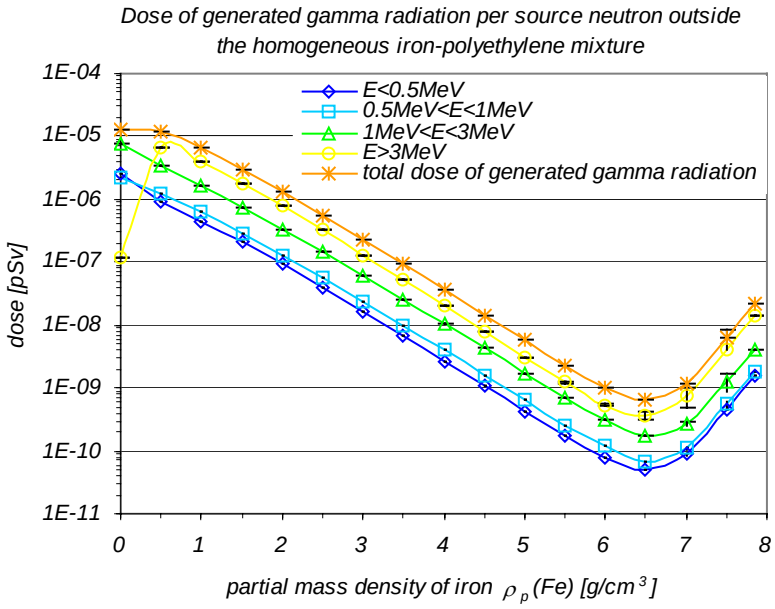

Fig. 2.93: Generated gamma dose per source neutron on the surface of the ball consisting of an homogeneous iron and polyethylene mixture. The minimal dose rate is achieved for partial mass densities of 6.5 g/cm^3 for iron and 0.16 g/cm^3 for polyethylene.

2.10.3.2.3 Conclusion for iron/polyethylene setups.

Given a shielding thickness of 80 cm best shielding for neutrons is achieved with a layer of iron with a thickness of some 45 cm and an adjacent layer of 35 cm polyethylene. This arrangement yields a comparatively high level of generated gamma radiation, the dose of which exceeds by far the remaining neutron dose. Considering total dose (n+γ), a tapered arrangement is superior.

2.10.3.3 Concrete as shielding material

Concrete has many advantageous properties as a radiation shielding material:

- comparatively high hydrogen content (water content is about 100 kg/m^3)
- high mechanical strength
- ease of placement
- low cost

However, the attenuation of neutron radiation by ordinary concrete is less than with the homogeneous iron-polyethylene mixture as described in the previous chapter. Assuming the same source and shielding geometry (ball with radius 80 cm), the neutron dose as well as the dose of generated gamma radiation outside the shielding is more than two orders of magnitude higher (see Figs. 2.107, 2.108).

The shielding power of concrete can be improved considerably by even small amounts of additives. Especially mineral additives, ground to fine powders, are applicable. The purpose of the additives is to increase the macroscopic cross section of the mixture for:

- inelastic neutron scattering
- elastic neutron scattering
- neutron absorption without production of high energetic gamma radiation
- attenuation of gamma radiation by elements with high atomic number

Some promising mineral additives are described below.

Hematite [27, 45, 46]

Chemical composition: Fe_2O_3
Density: 5.2 to 5.3 g/cm^3
Hematite improves both neutron attenuation and gamma attenuation due to its iron content. Ground to a fine powder, it ensures a nearly homogeneous iron distribution in the concrete. The iron ore is mined for steel production and is commercial available at low cost.

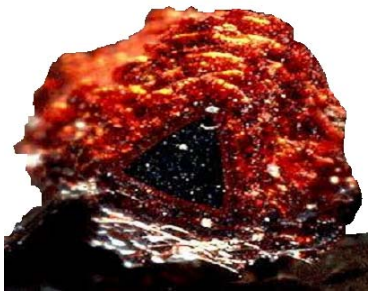

Fig. 2.94: Hematite [46]

Fig. 2.95: Limonite [46]

Limonite [27, 45, 46]

Chemical composition: FeOOH
Density: 3.6 to 3.7 g/cm^3
The advantage of this mineral in comparison to hematite is its hydrogen content. As additive to concrete it rises simultaneously the elastic and inelastic neutron scattering cross sections. Limonite is not a pure mineral but a mixture of hematite and goethite (pure FeOOH; density: 4.3 g/cm^3). It is therefore also called impure goethite. Disadvantage of limonite is the lower iron content compared to hematite. It is no longer mined for steel production and therefore not as easy commercial available as hematite.

Serpentine [27, 46]

Chemical composition: $3MgO{\cdot}2SiO_2{\cdot}2H_2O$
Density: 2.5 to 2.6 g/cm^3
Two properties of this mineral are advantageous for shielding purposes: The high fixed water content and the resistance against high temperatures. The water of crystallization is retained up to about 510°C [27].

Fig. 2.96: Serpentine [46]

Fig. 2.97: Colemanite [46]

Colemanite [27, 46]

Chemical composition: $Ca_2B_6O_{11}{\cdot}5H_2O$
Density: 2.4 g/cm^3
Even small amounts of colemanite (some 10 kg/m^3) as additive in concrete decrease the dose of generated gamma radiation. This is due to its boron content. Production of high energetic gamma radiation by thermal neutron capture in other elements (especially hydrogen and iron) is avoided due to the high thermal neutron absorption cross section of ^{10}B ($\sigma_{(n,\alpha)}$ =3840 barn). Attenuation of the resulting low energetic gamma radiation (0.477 MeV) is much higher than neutron capture gamma radiation from iron or hydrogen. Besides, colemanite has a considerable amount of water of crystallization. In contrast to the other minerals presented here, colemanite deteriorates considerably the mechanical properties of the heavy concrete when applied in concentrations higher than 400 kg/m^3.

Barite [27, 46]

Chemical composition: $BaSO_4$
Density: 4.5 g/cm^3
Barite is used for improving the attenuation of gamma radiation, due to the high atomic number of barium (Z=56).

Fig. 2.98: Barite [46]

Several other mineral additives like borax ($Na_2B_4O_5(OH)_4 \cdot 8H_2O$) and ulexite ($NaCa[B_5O_6(OH)_6] \cdot 5H_2O$) [46] were tested by calculation. As the improvements in shielding quality does not exceed that of the concrete types using the additives described above and no information about the practical feasibility and mechanical stability was available for these theoretical concrete compositions, those other minerals were no longer considered for the ANTARES facility.

In addition, some non mineral additives are proposed in the literature for improving shielding quality of concrete. The most important ones are steel resin, lead resin, and polymer resin. The disadvantage of these materials is that the distribution is usually not as homogeneous as for ground mineral additives. In some cases they weaken the mechanical strength and they may sink to the ground or ascend during the casting of the concrete.

The influence of hematite and colemanite as additives in concrete was tested by the calculation model described in 2.10.3.1 'Calculation model for testing shielding materials' (ball of radius 80 cm with isotropic neutron source in its center). The shielding material is a mixture of ordinary concrete, hematite and colemanite. The partial mass density of hematite was varied from 0 to 3000 kg/m^3 in steps of 100 kg/m^3 and the amount of colemanite was varied from 0 to 200 kg/m^3 in steps of 20 kg/m^3. The mixture for each step was obtained by replacing volume of ordinary concrete by the same volume of additives in a volume conserving way (analogous to the homogeneous iron-polyethylene mixture). The resulting dose outside the shielding is displayed in Fig. 2.99 (mass indications refer to 1 m^3 of shielding material). Even a small fraction of 20 kg/m^3 of colemanite in ordinary concrete reduces the neutron dose rate by a factor of 6. By this, the contribution of thermal neutrons is decreased from "most dominant" to "lowest contribution". The dose of generated gamma radiation is reduced by more than a factor 20 by an amount of 20 kg/m^3 colemanite as additive. Further increase of the colemanite share improves neutron attenuation only slightly. The decrease of generated gamma dose is more distinct.

Hematite as additive in ordinary concrete improves neutron attenuation, but higher amounts are needed than with colemanite. The dose of generated gamma radiation is also decreased, but not as effective than with colemanite. Even with 3000 kg/m^3 hematite, the effect of 20 kg/m^3 colemanite cannot be achieved. This shows that avoiding production of high energetic gamma radiation is more effective than shielding the high energetic generated gamma radiation. Using both additives - colemanite and hematite - small amounts of hematite (up to 500 kg/m^3) even rise the generated gamma dose outside the shielding: Neutrons are captured in iron but the iron density is too small for effective shielding of generated gamma radiation. Higher concentrations of hematite are beneficial for reduction of both dose components.

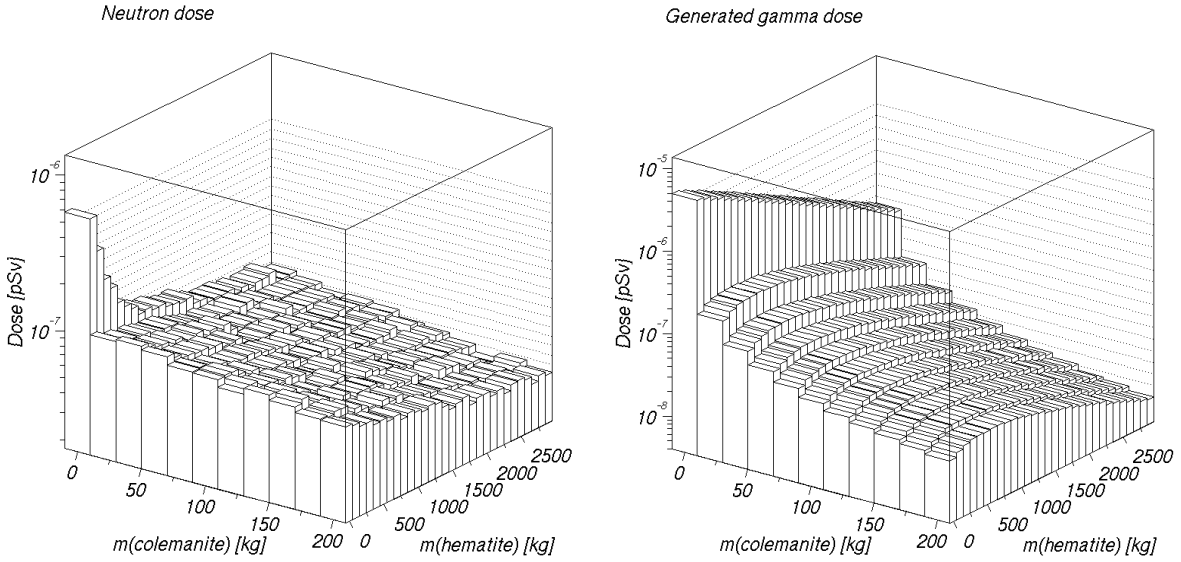

Fig. 2.99: Neutron dose (left hand side) and generated gamma dose (right hand side) per source neutron in ordinary concrete with colemanite and hematite as additives in dependency of the shares of additives. The displayed dose values are achieved at a distance of 80 cm to the point source. All mass indications refer to 1 m^3 shielding material.

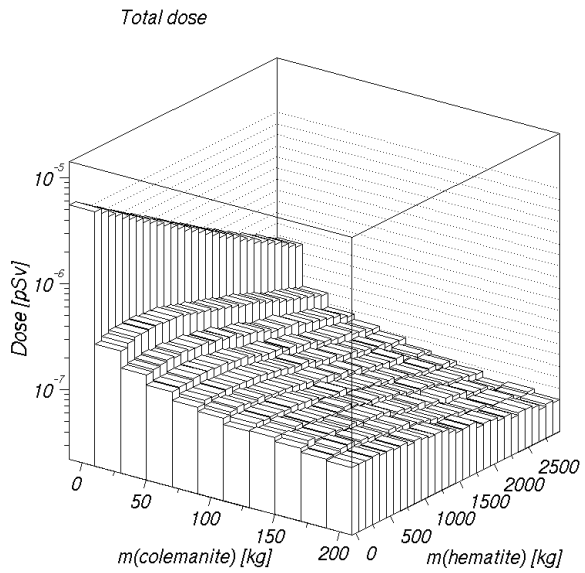

Fig. 2.100: Total dose (sum of neutron dose and generated gamma dose) per source neutron in ordinary concrete with colemanite and hematite as additives in dependency of the mass fractions of additives. The displayed dose values are achieved at a distance of 80 cm to the point source. All mass indications refer to 1 m³ shielding material.

Heavy concrete compositions with more than two additives are described in the following. The water content in heavy concretes (up to 180 kg/m^3) is usually higher than in ordinary concrete (some 100 kg/m^3).

In the following the properties of the infinte number of possible mixtures of concrete types and additives are characterized by a set of six representative types of shielding concrete (type A, B, C, D, E, F).

All concrete types were tested for the ANTARES facility by help of the calculation model described in the chapter 2.10.3.1 'Calculation model for testing shielding materials'. The results are displayed in Figs. 2.107, 2.108, 2.109. The dose indications for neutron radiation and generated gamma radiation are normalized to one source neutron. Dose indications for primary gamma radiation refer to one source photon.

Heavy concrete type A (hematite concrete, ρ=3.6 g/cm^3)

Heavy concrete of type A consists of hematite, steel resin, colemanite, sand and cement. Its water content is (180 kg/m^3 [47]). Therefore neutron attenuation is nearly as effective as in high density heavy concretes. The total mass density is comparatively low (ρ=3.6 g/cm^3 [47]), due to the small amount of steel resin. The mass ratio of iron to hydrogen is m_{Fe}/m_H=80 which is close to the optimal ratio for neutron attenuation that was found for the homogeneous iron/polyethylene mixture described in the previous chapter. The disadvantage of the low iron content is a weak attenuation of gamma radiation (see Figs. 2.108, 2.109). The dose of generated gamma radiation behind 80 cm of concrete type A is 2.1 times higher than the neutron dose rate.

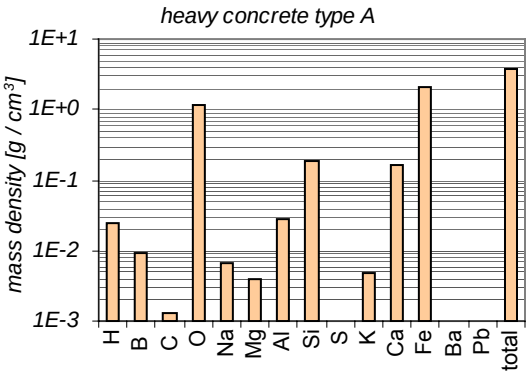

Fig. 2.101: Composition of heavy concrete type A

Heavy concrete type B (hematite concrete, ρ=4.7 g/cm^3)

Compared to heavy concrete type A, type B contains a higher amount of steel resin and hematite, but no sand. The water content is 170 kg/m^3 [47]. Although the total mass density is higher in comparison to heavy concrete type A (ρ=4.7 g/cm^3 [47]), neutron attenuation is only improved by a factor of 1.6 (Fig. 2.107). The mass ratio of iron to hydrogen is m_{Fe}/m_H=172. Considering the generated gamma dose, type B achieves a significantly higher attenuation: Due to the increased iron content, the dose of generated gamma radiation is 10 times less, in comparison with heavy concrete of type A. The same is true for the dose rate of primary gamma radiation.

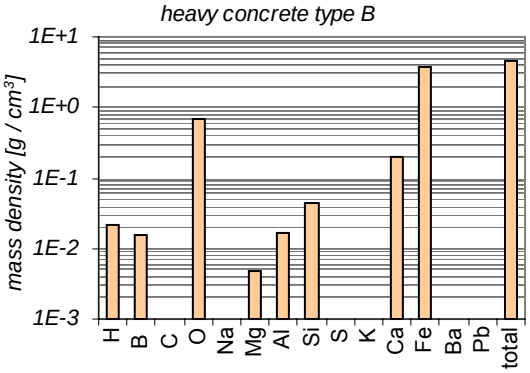

Fig. 2.102: Composition of heavy concrete type B

Heavy concrete type C (hematite+barite concrete, ρ=6.05 g/cm³)

Heavy concrete type C is a high density heavy concrete (ρ=6.05 g/cm³). Steel resin, hematite, barite and colemanite are used as additives. The high density is achieved by a very high share of iron, resulting in a low dose of generated gamma radiation: The gamma dose is reduced by a factor of 7.4 compared to heavy concrete type B. However, the neutron attenuation of this concrete type is disappointing: Due to its low hydrogen content the dose rate is even higher (1.3 times) compared to concrete type B. The mass ratio of iron to hydrogen of m_{Fe}/m_H=330 is far above the optimal value (m_{Fe}/m_H=60). High mass density, high cost, and low shielding power makes this concrete less promising for the ANTARES facility.

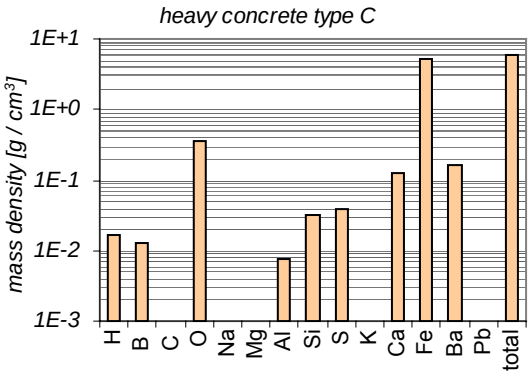

Fig. 2.103: Composition of heavy concrete type C

Heavy concrete type D (serpentine concrete ρ=3.06 g/cm³)

Type D is a serpentine concrete. Steel resin, serpentine and colemanite are used as additives. In contrast to the concrete types described above, it contains no hematite. The serpentine mineral retains the water of crystallization up to temperatures of 510°C. Serpentine concrete is therefore resistant against high temperatures (the recommended temperature limit for serpentine concrete is 427°C [27]). The mass density of concrete type D is 3.06 g/cm³. The density of hydrogen is the biggest one of all examined concrete compositions due to the high amount of serpentine as additive (1 m³ concrete contains 1.28 t serpentine). This concrete is used as filling material for the primary shutter inside the biological shielding, where heat production by radiation is relevant. For the ANTARES facility, outside the biological shielding, heat resistance is less important, due to the much lower radiation levels. Anyway, application of this concrete type for the radiography facility was tested. Despite the high hydrogen content the neutron attenuation is only slightly better than in the case of concrete type B (Fig. 2.107). The mass ratio of iron to hydrogen of m_{Fe}/m_H=27 is below the optimal value. The fraction of thermal neutrons is the lowest one compared to all other considered concrete types, due to the high amount of colemanite (240 kg/m³). The high boron density keeps the dose of generated gamma radiation at a moderate level (Fig. 2.108). However, the dose of generated gamma radiation is 5.4 times higher than in the case of concrete type B.

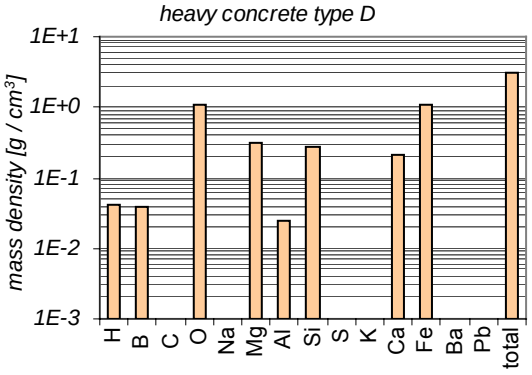

Fig. 2.104: Composition of heavy concrete type D

Heavy concrete type E (lead concrete ρ=6.3 g/cm³)

Lead as additive is used in this concrete type for improvement of gamma attenuation. Due to the lead content (1.8 g/cm³ [48]) a very high total mass density is achieved (ρ=6.3 g/cm³). Besides lead and steel resin no additional additives (like colemanite) are used. Despite the extreme density this type of concrete has rather poor shielding properties (Fig. 2.107). Due to the high lead and steel amount, only a low hydrogen concentration can be obtained. Therefore neutron attenuation is even worse than in the case of concrete type A, that attenuates 4 times better and has a density of only 57 %. The mass ratio of iron to hydrogen is m_{Fe}/m_H=321. Despite the high density of heavy elements (lead and iron) the generated gamma dose is only reduced by a factor of 1.76 compared to heavy concrete type B (Fig. 2.108). In contrast to the concrete types described above, type E contains no boron. More neutrons are therefore captured in hydrogen and iron, causing high energetic gamma radiation (E_γ=2.2 MeV, 7.7 MeV [43]) that is difficult to shield even with heavy elements like lead. This example shows again that it is much more efficient to avoid production of high energetic gamma radiation than improving gamma attenuation. For primary gamma radiation this concrete type would be advantageous compared to the other investigated types (Fig. 2.109). However, this property is not

appealing for the ANTARES facility: The contribution of primary gamma radiation outside the shieldings is negligible, except for the location where the direct beam is shielded (in the experimental chamber). But even here, an additional beam catcher from pure lead outside the shielding would be more effective than using this type of concrete.

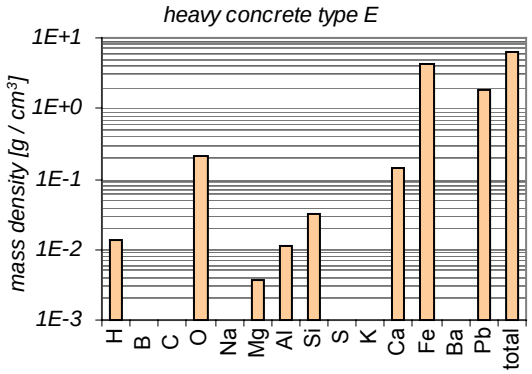

Fig. 2.105: Composition of heavy concrete type E

Heavy concrete type F (barite concrete, ρ=3.2 g/cm^3)

This type is a barite concrete. Originally it was designed as gamma ray shielding and is widely used at medical facilities [49]. Its advantage compared to the other concrete types is that it is commercially available in the form of standard bricks (trade mark 'Röbalith', Seitz + Kerler GmbH & Co. KG). Several types of Röbalith with different densities (due to different fractions of additives) are available. In this context the type 'Rö4' is considered. It has a density of 3.2 g/cm^3. For attenuation of gamma radiation it contains barite. As Röbalith is not optimized for neutron shielding purposes, its water content is similar to that of ordinary concrete and it contains no absorbers for thermal neutrons that avoid production of high energetic gamma radiation. There is no specific material for inelastic scattering like iron. The neutron attenuation is similar to that of ordinary concrete (Fig. 2.107). The biggest contribution is from thermal neutrons. The dose of generated gamma radiation is the biggest of all examined heavy concrete types. For attenuation of primary gamma radiation this material would be effective (Fig. 2.109).

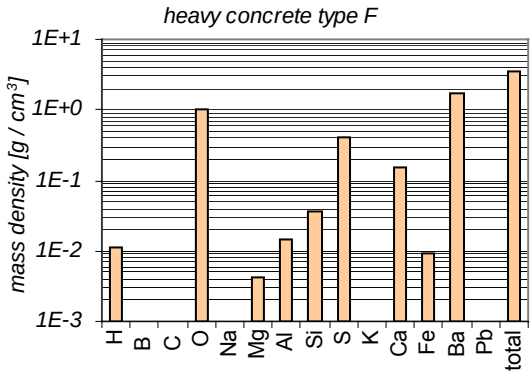

Fig. 2.106: Composition of heavy concrete type F

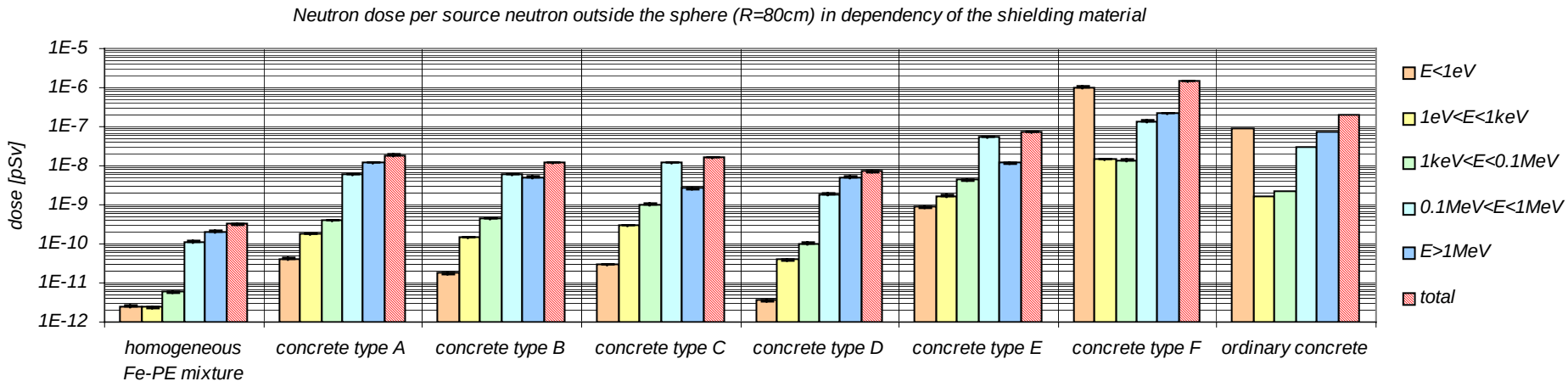

Fig. 2.107: Neutron dose per source neutron outside the shielding ball (R=80 cm) in dependency of the shielding material.

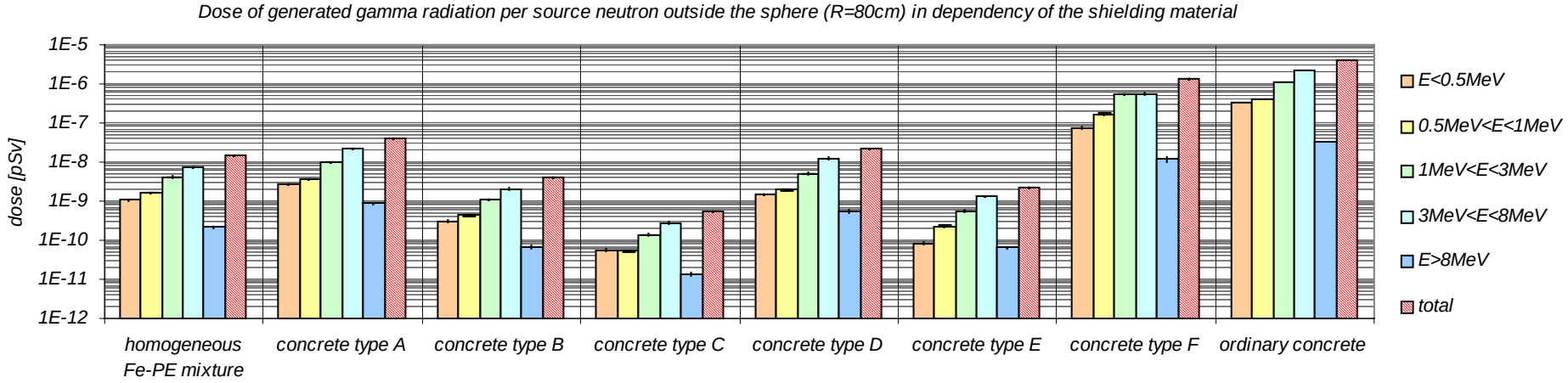

Fig. 2.108: Dose of generated gamma radiation per source neutron outside the shielding ball (R=80 cm) in dependency of the shielding material.

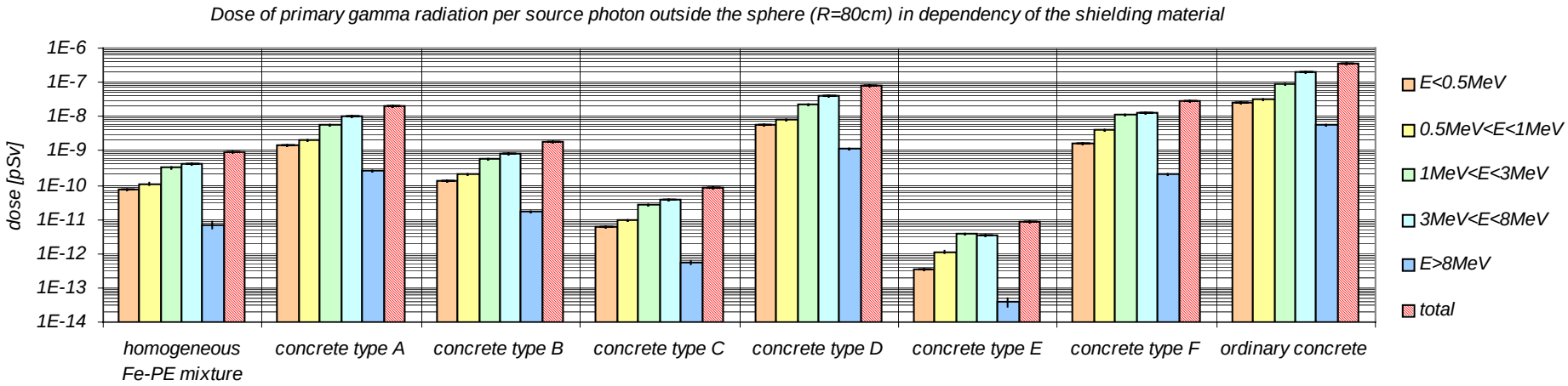

Fig. 2.109: Dose of primary gamma radiation per source photon outside the shielding ball (R=80 cm) in dependency of the shielding material.

Considering all criteria, as there are radiation attenuation, weight, and cost, concrete types A and B (having hematite, steel resin, and colemanite as additives) are the best choice for the ANTARES facility. With both types similar neutron attenuation is achieved. Type B provides higher gamma attenuation due to its bigger iron content. Type A can be applied at locations with low external gamma radiation level, for locations with higher gamma radiation levels type B should be applied.

Before commissioning the concrete, the question arose whether the compositions can be improved by slight modifications. Due to the sensitivity of neutron attenuation and gamma production on the colemanite and iron share, shielding quality can be varied by modification of mass fractions. For both concrete compositions, the dose of neutron radiation and generated gamma radiation was considered for various colemanite and iron amounts. Steel resin was replaced by colemanite stepwise in a volume conserving way. Besides, it was tested whether serpentine as an additional additive improves the shielding quality. The results for heavy concrete type B are shown in Fig. 2.110.

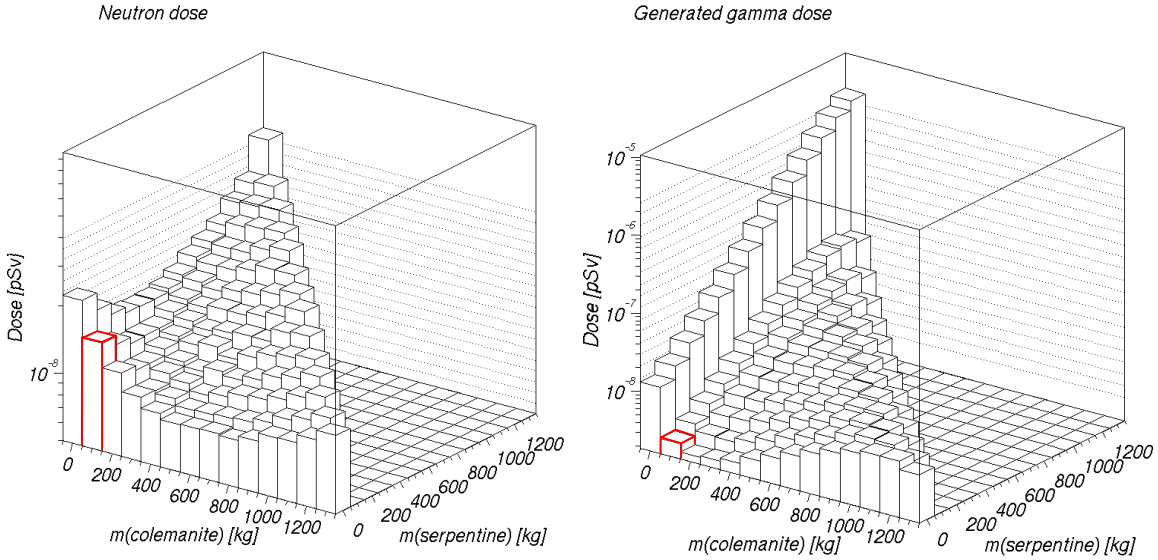

Fig. 2.110: Neutron dose (left hand side) and generated gamma dose (right hand side) per source neutron obtained by concrete type B for variations of the shares of colemanite and serpentine as additional additives. Both additives replace steel resin. Mass indications refer to 1 m^3 of bulk shielding material. The original composition of concrete type B contains 100 kg/m^3 colemanite and no serpentine (red marked position).

Neutron attenuation of concrete Type B can be improved:

The minimal neutron dose is reached for a colemanite density of 600 kg/m^3 (instead of 100 kg/m^3 in the original composition). The gain in neutron attenuation due to the modification would be in the region of some 40 %. However, such high colemanite shares are not practicable because they prevent the concrete from setting. Densities of up to 400 kg/m^3 are feasible.

Considering the dose of generated gamma radiation, a higher colemanite amount would also be desirable. The minimum dose is reached for 200 kg/m^3. But the gain compared to the original composition with 100 kg/m^3 is only in the region of some 30 %.

Replacing a certain amount of steel resin in the original composition of concrete type B by serpentine would also improve neutron attenuation but less effective than with colemanite. For the reduction of generated gamma dose, serpentine is not beneficial.

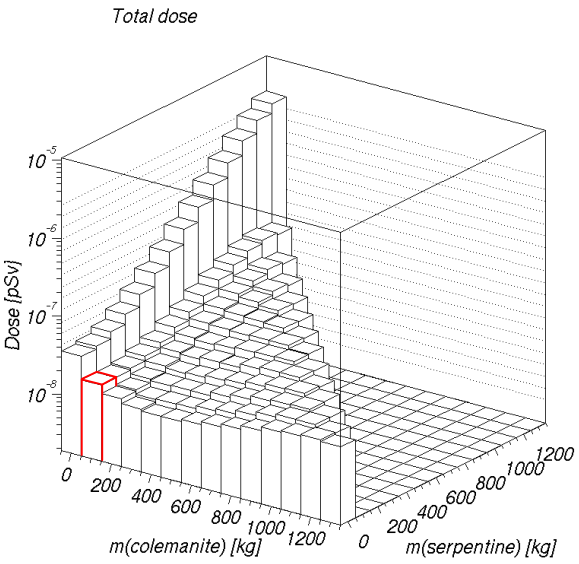

Fig. 2.111: Total dose (sum of neutron and generated gamma dose) obtained by concrete type B for variations of the steel resin and colemanite fractions and for serpentine as additional additive. Mass indications refer to 1 m^3 of bulk shielding material. The original composition of concrete type B contains 100 kg/m^3 colemanite and no serpentine (red marked position).

Considering the expenditure for the necessary tests of mechanical strength of the modified concrete composition, the improvement of shielding power is not worth realizing the new composition. For heavy concrete type A (ρ=3.6 g/cm^3) the modifications yield even smaller improvements in attenuation.

Spectral flux densities in heavy concrete type B in dependency of the distance from the source are shown in Fig. 2.112. Contribution of the cold energy range around 1 meV is decreased by more than 14 orders of magnitude by 80 cm of concrete. In the thermal energy range (around 20 meV), flux density is decreased by 10 orders of magnitude.
Attenuation for a pure thermal neutron spectrum would be even higher, but in the case of the ANTARES spectrum, this energy region is populated by down scattered neutrons from higher energy groups. Attenuation in the fast energy region above 0.1 MeV is about 8 orders of magnitude. After 80 cm of concrete fast neutrons deliver the highest contribution to total flux (see appendix A.10).

The spectral flux density of generated gamma radiation is shown in Fig. 2.113. Energy resolution was 200 keV for this calculation. Close to the source, where most thermal and cold neutrons are captured, distinct peaks occur in the spectrum. Most of the peaks are caused by neutron capture in the

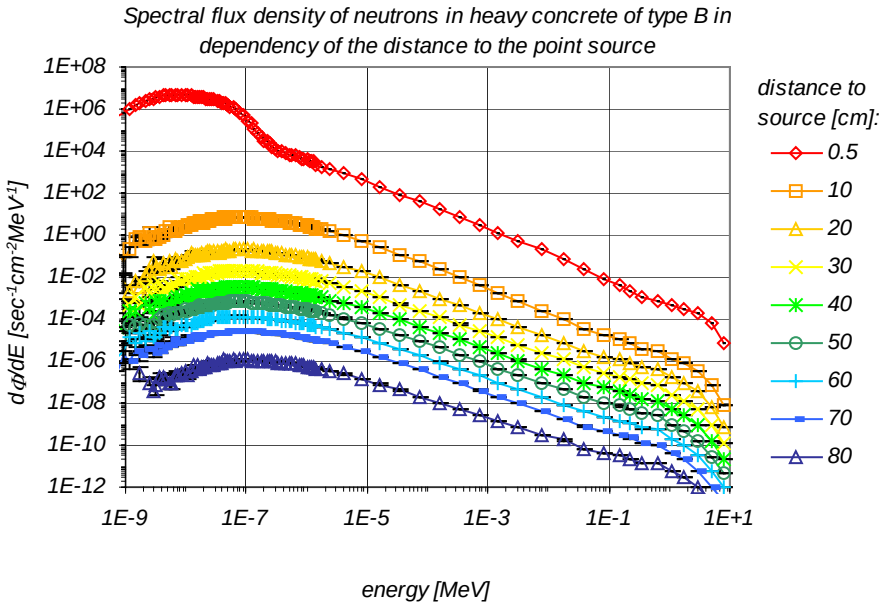

Fig. 2.112: Spectral flux density per source neutron in heavy concrete type B (ρ=4.7 g/cm^3) in dependency from the distance to source. The source spectrum is the ANTARES spectrum, dominated by cold and thermal neutrons.

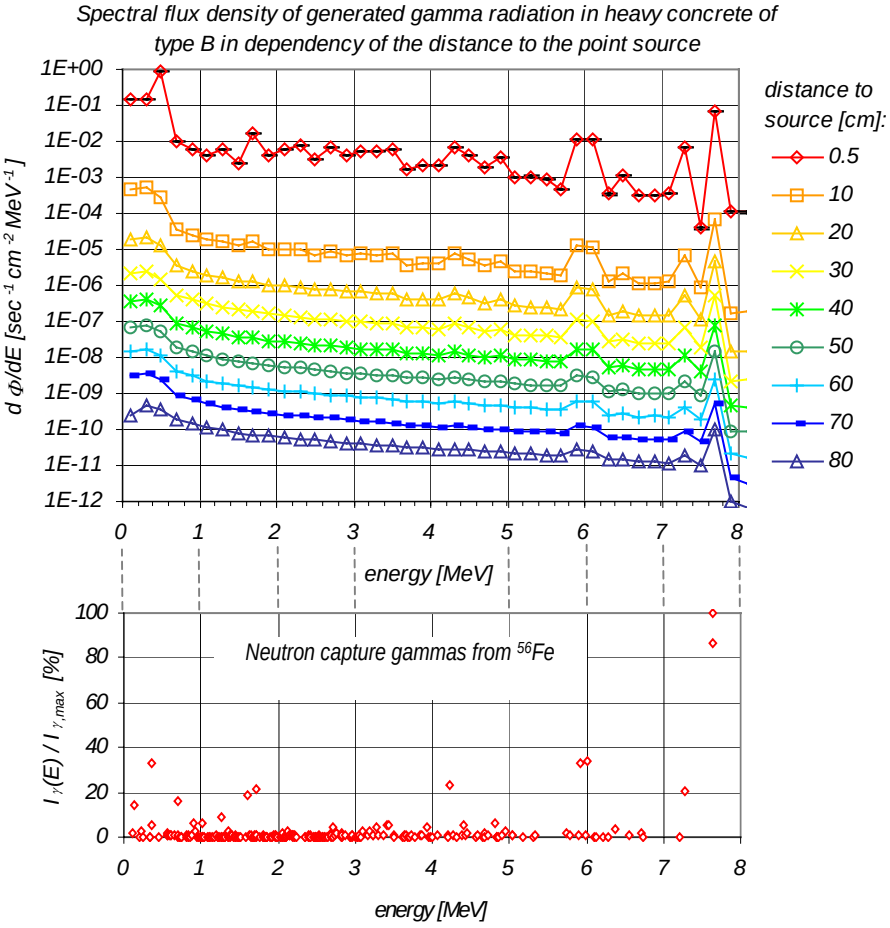

Fig. 2.113: Top: Spectral flux density of generated gamma radiation per source neutron in heavy concrete type B (ρ=4.7 g/cm^3)
Bottom: Neutron capture gamma radiation from ^{56}Fe [43] (91.72 % in natural isotope composition)

iron isotope ^{56}Fe (the energy distribution of neutron capture gamma radiation from this isotope is shown at the bottom of Fig. 2.113; data from [43]). Highest flux density is reached in the energy range from 0.4 MeV to 0.6 MeV: Within this energy group, the neutron capture gamma radiation from boron isotope ^{10}B (478 keV [40]) and electron-positron annihilation radiation (511 keV) is located. For bigger distances from the source, peaks become washed out due to Compton scattering.

2.10.3.4 Inhomogeneities in heavy concrete

Some of the additives are admixed not as fine powders but as bigger pieces. Therefore effects from heterogeneity have to be taken into consideration. Different paths through the material traverse different amounts of additives. As in principle paths that traverse no additives are possible, a lower overall attenuation can be expected for these inhomogeneous concrete compositions. The influence of inhomogeneities was tested for steel resin in serpentine concrete (concrete type D as described in the preceding chapter). This type of heavy concrete was chosen because steel resin is the only additive that contains iron. For other concrete types containing hematite as additive, inhomogeneities caused by steel resin have less influence due to the additional iron content in the nearly homogeneous hematite distribution. Usually, steel resin is added to heavy concrete as spherical pieces up to diameters of 5 mm. An example for the steel resin distribution in heavy concrete is shown in Fig. 2.114: Cut through a block of heavy concrete. For estimation of the influence of inhomogeneities, steel spheres with radii of 4.5 mm and 1 cm were modeled. The steel pieces were distributed randomly in heavy concrete. A vertical cut through the calculation model considering spherical steel pieces with a radius of 4.5 mm is shown in Fig. 2.115. The same for a radius of 1 cm is shown in Fig. 2.116. In each model all pieces have same diameters. The different sizes of the circles in the cuts stem from non central cuts through the spheres.

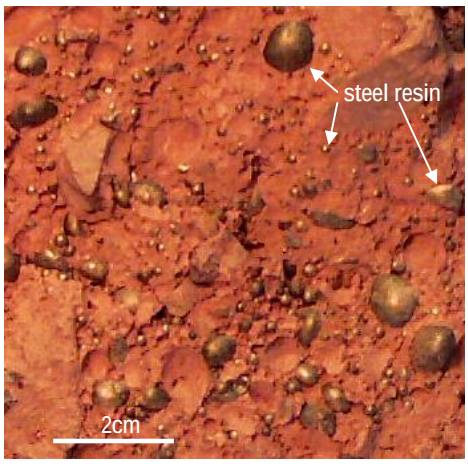

Fig. 2.114: Distribution of steel resin in heavy concrete

The neutron dose distribution in homogeneous and inhomogeneous serpentine concrete is shown in Fig. 2.117 left hand side. The loss of shielding power due to inhomogeneous distribution of iron is rather low. After 20 cm of shielding material both inhomogeneous mixtures yield some 33 % more dose compared to the homogeneous mixture. The influence on the dose of generated and primary gamma radiation is even lower.

For the concrete types A and B, as used for the ANTARES facility, much smaller steel grains are used. Hematite adds further iron to the mixture. Therefore the influence of inhomogeneous concrete composition is negligible for the ANTARES facility.

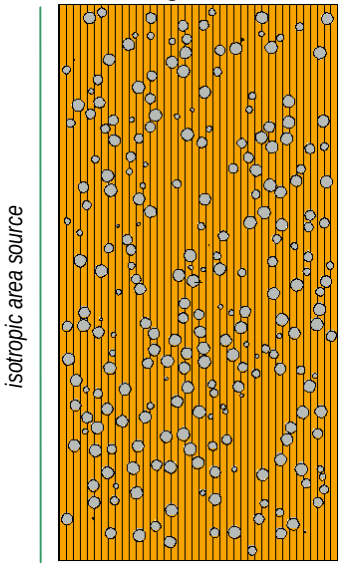

Fig. 2.115: Vertical cut through the calculation model for testing inhomogeneities in heavy concrete. The radius of spherical steel pieces is 4.5 mm.

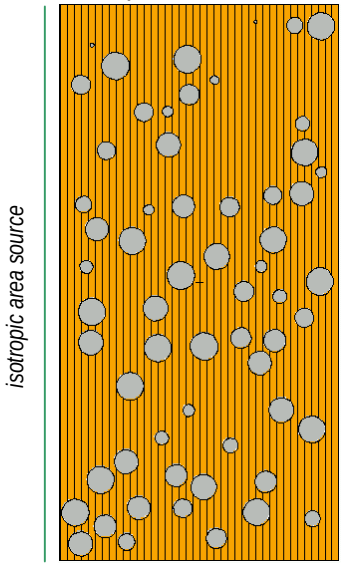

Fig. 2.116: Vertical cut through the calculation model for testing inhomogeneities in heavy concrete. The radius of spherical steel pieces is 1 cm.

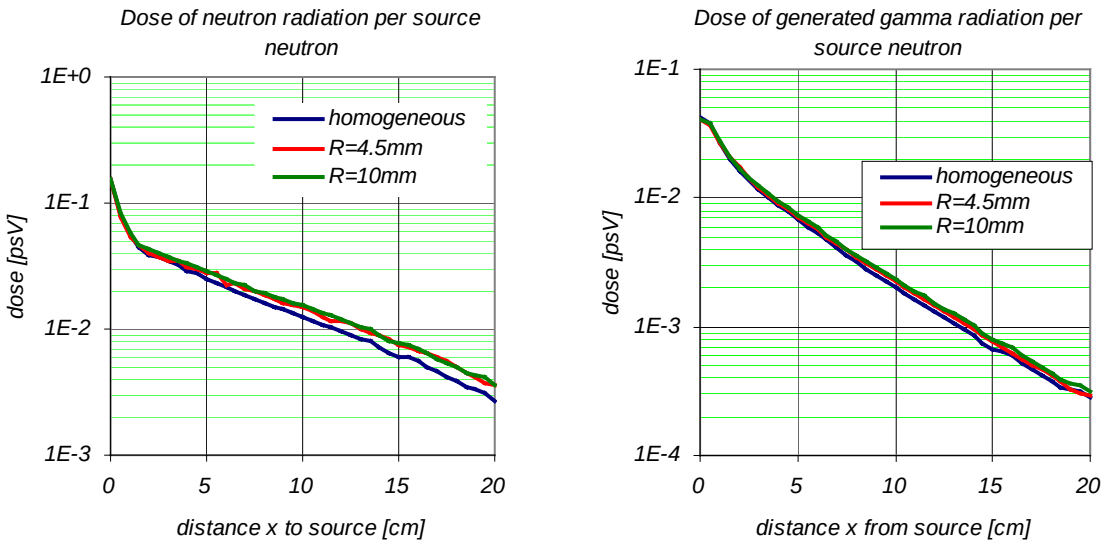

Fig. 2.117: Dose distributions in serpentine concrete (concrete type D) with homogeneous steel additive in comparison to inhomogeneous steel additive. The steel balls have radii of 4.5 mm or 10 mm. All dose values refer to one source neutron.
Left hand side: Dose of neutron radiation.
Right hand side: Dose of generated gamma radiation.

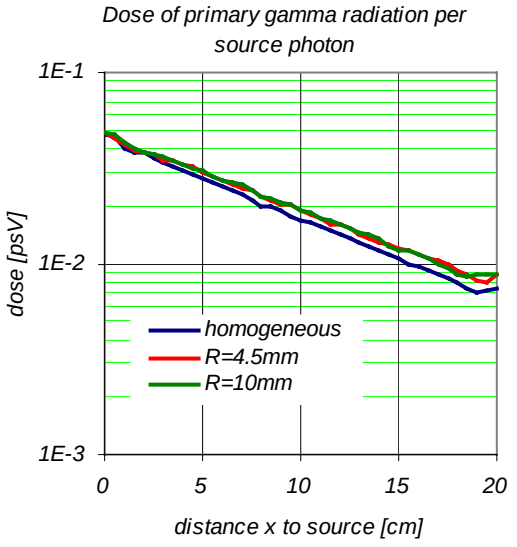

Fig. 2.118: Dose distribution of primary gamma radiation in serpentine concrete (concrete type D) with homogeneous steel additive in comparison to inhomogeneous steel additive. The steel balls have radii of 4.5 mm and 10 mm. All dose values refer to one source photon.

2.10.4 Gaps in radiation shieldings

It is neither possible nor desirable to construct the shielding arrangement as a monolith. The ANTARES facility has this in common with most neutron experiments. Problems would arise with the assembly, the accessibility, and the flexibility. In addition, the lift capacity of the reactor hall crane is limited to 10 t. At special locations, cuts are even welcome due to the requirement that parts of the shielding roof can be moved on top of the lateral walls. Therefore a modular construction has to be preferred. The single modules cannot be shaped to a precision so that there will be no gaps between the elements. Gaps in the range from a few millimeters up to one centimeter may occur in the final shielding construction. The question is how much the dose is increased outside the shielding due to the gaps and what is the best shape of interfaces with regard to the ANTARES neutron spectrum taking into account the shielding material and the steel liners for the shielding elements.

2.10.4.1 Calculation model

The calculation model for testing the influence of gaps in the shielding of the ANTARES facility is shown in Fig. 2.119. The neutrons are emitted (isotropic or monodirectional) from an area source on one side of the shielding. The incident neutron flux is 1 $cm^{-2}sec^{-1}$. The dose on the opposite side of the shielding is calculated with a spatial resolution of 2 mm. The shielding has a thickness of 60 cm (typical value in the surrounding of the flight tube). Length and height are assumed close to infinity. The gaps have a repetition period of 50 cm. The shielding material is heavy concrete type A (density: 3.6 g/cm^3, the composition is shown in the chapter 2.10.3.3 ‘Concrete as shielding material’). The shielding elements are coated by steel liners of 1 cm thickness along the gap (in the final version of the shielding elements, steel liners have a thickness of 6 mm).

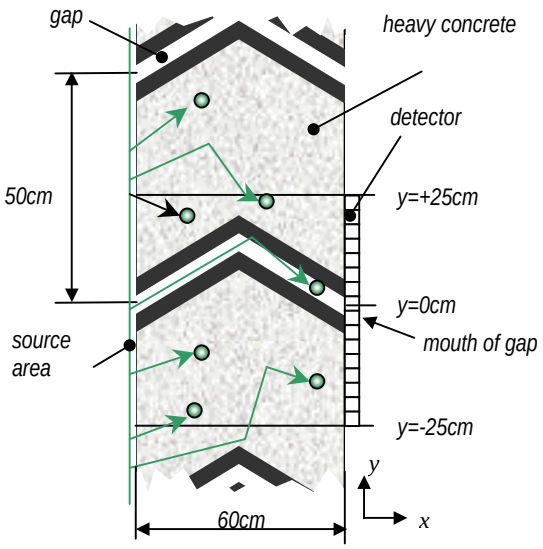

Fig. 2.119: Calculation model for testing the influence of gaps in the radiation shieldings for the ANTARES facility

2.10.4.2 Shape of gaps

Radiation transport through three different shaped gap configurations was examined (Fig. 2.120) [83]:

- Labyrinth: Two 90° bends, 20 cm offset (configuration *C* in Fig. 2.120).
- Angular: One bend with an angle of 120° (configuration *D* in Fig. 2.120).
- Curved: The surfaces of shielding elements at the border between shielding elements are cylinder barrels (configuration *E* in Fig. 2.120).

In a first step, a gap width of 1 cm was assumed in all cases.

Two additional ´ideal´ configurations were calculated for comparison with the gap configurations:

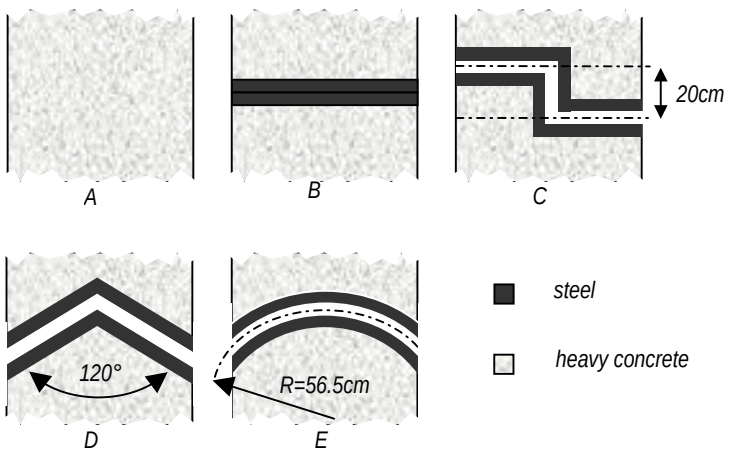

Fig. 2.120: Examined gap configurations in the radiation shielding: A: monolithic, B: simple brick, C: labyrinth (two 90° bends), D: angular (one 120° bend), E: curved gap

- Monolithic: Homogeneous shielding without any gaps (configuration *A* in Fig. 2.120).
- Simple brick: Planar steel liners of shielding elements in direct contact without any gap between (configuration *B* in Fig. 2.120).

Dose outside the shielding is calculated with a spatial resolution of 2 mm. The mouth of the gap is located at y=0 for all gap configurations as illustrated in Fig. 2.119.

2.10.4.3 Isotropic neutron source

In this chapter the case of an isotropic neutron area source is considered. The spatial neutron dose distribution outside the different shielding configurations is shown in Fig. 2.121. The curved structure (configuration E) yields the lowest dose peak at the gap mouth but the widest dose distribution in the surrounding. In the case of the labyrinth structure (configuration C) it is vice versa: The dose peak at the gap mouth is the biggest one of all gap configurations but dose distribution in the surrounding is the narrowest one. The dose integral in the entire detector area is in all cases about 120 % of the integral dose obtained by a shielding without gap (monolithic configuration A). Hence, considering an extended area outside the shielding, the attenuation of neutron radiation does not so much depend on the configuration of gaps. Only the local neutron dose distribution varies with different gap

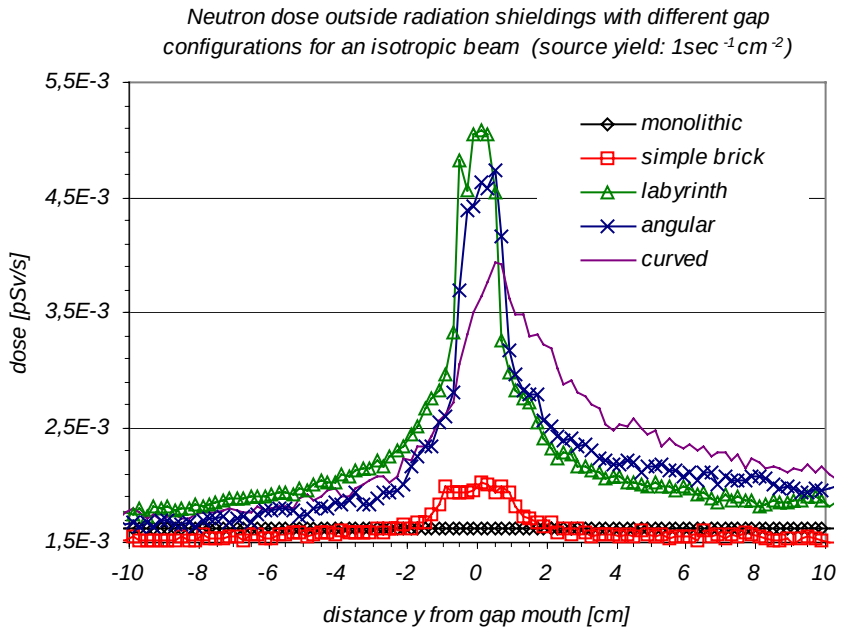

Fig. 2.121: Spatial neutron dose distribution outside shieldings with different gap configurations for an isotropic neutron beam (gap width=1 cm)

configurations. The increase of neutron dose due to the different gap systems compared to the monolithic shielding is shown in Fig. 2.122: The 'peak' value is the dose increase at the gap mouth and the average value is the dose increase in the entire detector area.

The spatial dose distribution of generated gamma radiation for the labyrinth gap system (configuration C) is shown in Fig. 2.123. Similar to the neutron dose distribution, the biggest dose value occurs at the mouth of the gap. Contrary to the neutron dose distribution, a second distinct dose maximum occurs at y=20 cm, caused by the inner leg of the gap system (see illustration below).

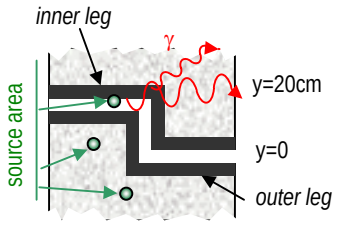

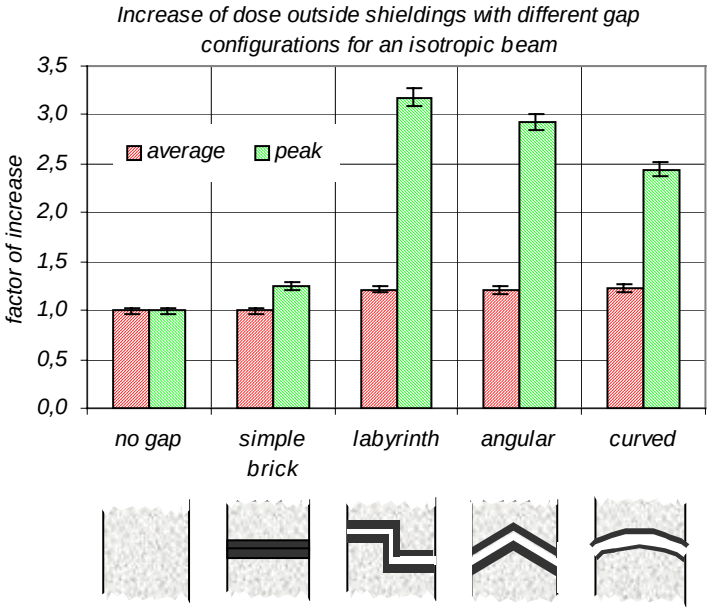

Fig. 2.122: Factors of neutron dose increase outside shieldings with different gap configurations compared to the monolithic shielding in the case of an isotropic beam. The 'average' values show the average dose increase on the shielding surface, and the 'peak' values the increase at the gap mouth.

The source of the gamma radiation is capture of cold and thermal neutrons in the steel liners along the inner leg. As the inner leg is fully illuminated by the direct beam, the flux of thermal and cold neutrons is higher as in the outer leg. However the dose of generated gamma radiation keeps below the neutron dose at each location outside the shielding.

The conclusion is that the labyrinth layout has no advantage above angular and curved layouts considering radiation transport.

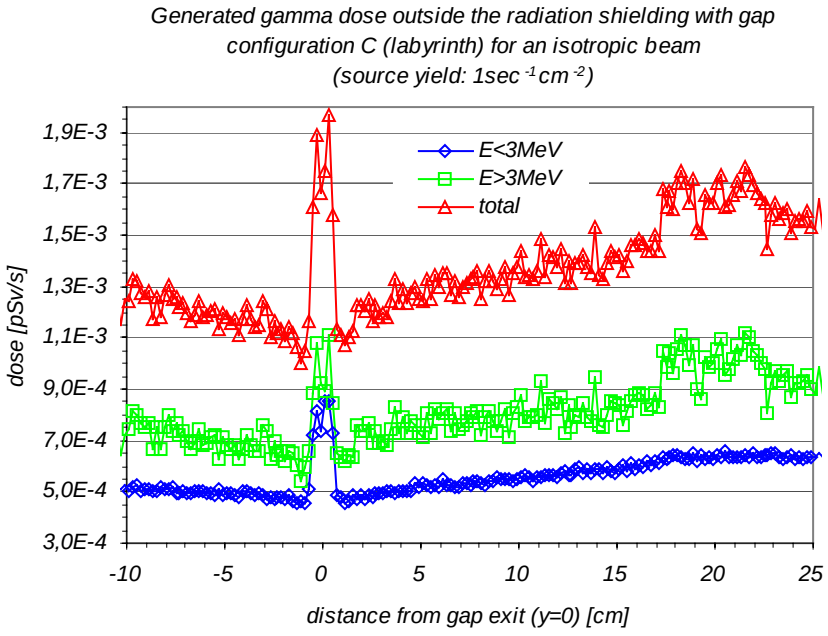

Fig. 2.123: Spatial distribution of generated gamma dose outside the radiation shielding with gap configuration C (labyrinth) for an isotropic neutron beam (gap width=1 cm)

2.10.4.4 Parallel neutron beam

In this chapter a parallel incident neutron beam is considered. The neutrons impinge perpendicular on the shielding surface.

The dependency of the shielding power on the gap layout is more significant than with the isotropic area source. The lowest neutron dose (Fig. 2.124) at the mouth of the gap system (y=0) is obtained with the curved gap system (configuration E). The highest dose peak at the gap mouth occurs with the labyrinth gap system (configuration C). It exceeds the values obtained by the other gap configurations by about a factor of two. A second distinct dose peak that is nearly as high as the peak at the gap mouth occurs at y=20 cm caused by the inner leg. Inner and outer leg of the gap system are parallel to the incident beam, hence unscattered neutrons can propagate undisturbed along the legs (see illustration below).

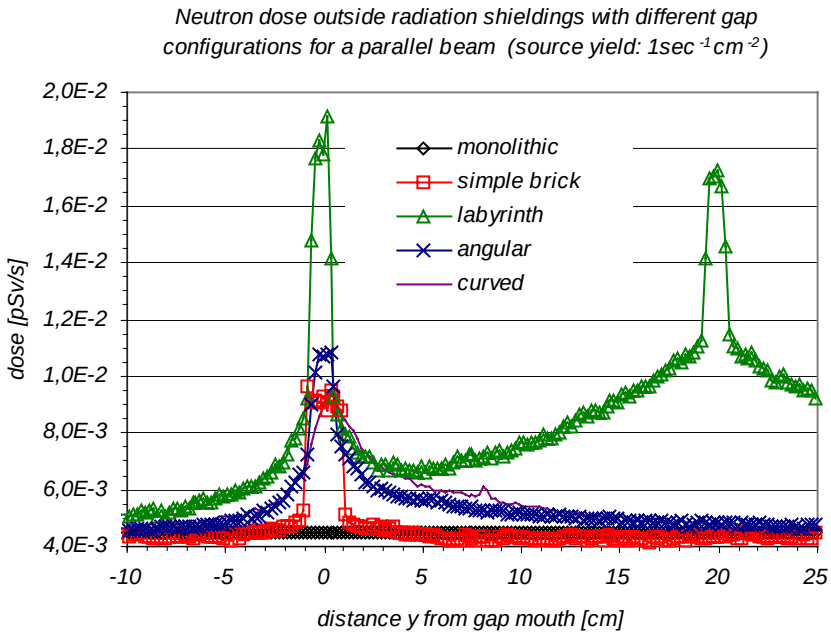

Fig. 2.124: Spatial neutron dose distribution outside shieldings with different gap configurations for a parallel neutron beam (gap width=1cm)

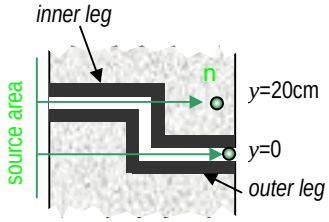

The peak of unscattered neutrons at y=20 cm is surrounded by a widely increased dose distribution caused by scattered neutrons from the shielding material behind (in beam direction) the inner leg. The increase of neutron dose peak values at the mouth of gap systems (y=0) and the integral dose increase in the entire detector area compared to the monolithic shielding is displayed in Fig. 2.125. For the angular gap system (configuration D) and the curved gap system (configuration E) the factor of dose increase in the entire detector area is even smaller (about 115 %) than with an isotropic neutron source, as there are no neutrons in the incident beam traversing in gap direction. The dose increase by the labyrinth gap system (configuration C) in the entire detector area is 178 % compared to the monolithic shielding. In the case of a parallel beam, the disadvantage of a labyrinth gap system is even more distinct than with an isotropic source.

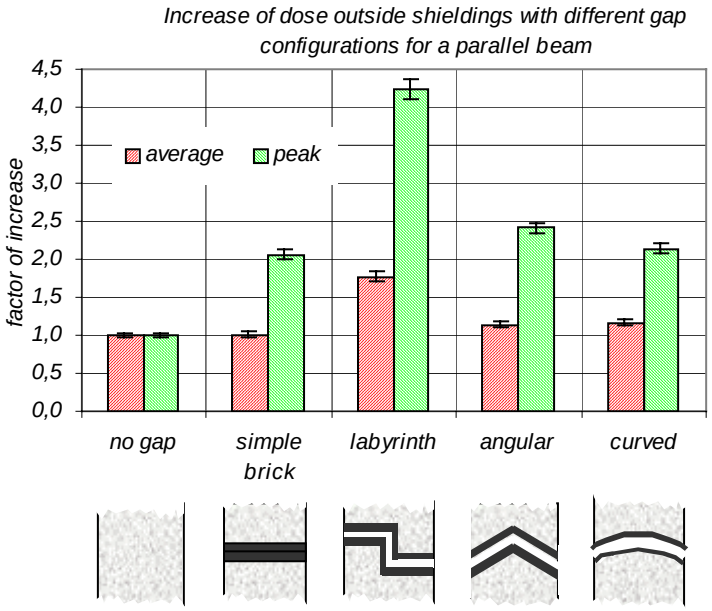

Fig. 2.125: Factors of neutron dose increase outside shieldings with different gap configurations compared to the monolithic shielding in the case of a parallel beam. The 'average' values show the average dose increase on the shielding surface, and the 'peak' values the increase at the gap mouth.

The spatial dose distribution of generated gamma radiation for the labyrinth gap system (configuration C) is shown in Fig. 2.126. The biggest dose value does not occur at the mouth of the gap system, but at the location y=20 cm; this is behind the inner leg of the labyrinth. This wide spread dose increase is caused by the inner leg of the gap system. Neutrons from the incident beam traverse the complete length of the inner leg and are captured at the steel liner at the end of the inner leg and the adjacent shielding material (see illustration below).

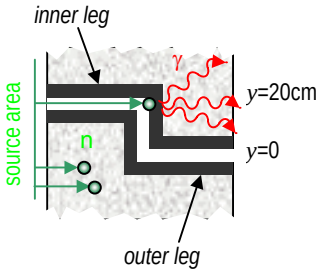

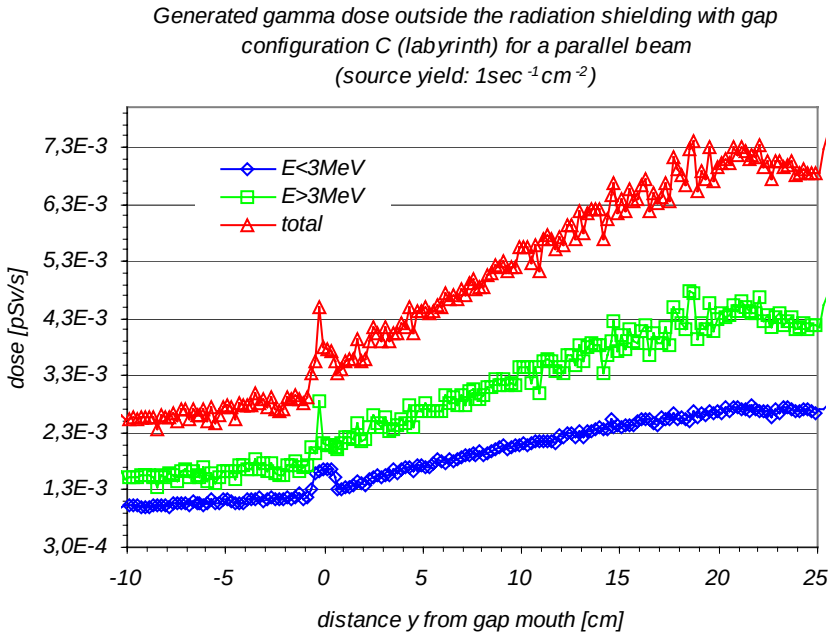

Fig. 2.126: Spatial distribution of generated gamma dose rate outside the radiation shielding with gap configuration C (labyrinth) for a parallel neutron beam (gap width=1 cm)

Hence an intense local source of secondary gamma radiation is generated in the middle of the shielding element. However, the dose of generated gamma radiation does not exceed the neutron dose at any location.

2.10.4.5 Practical aspects

Although radiation transport through the labyrinth gap system (configuration C) provides increased dose values outside the shielding compared with all other examined gap configurations, it has some advantages: As all angles along the gap system are 90° angles and all surfaces are planar, construction is easier as e.g. for the curved gap system, where the exact machining of cylinder barrels is complicated. An easy construction can be realized with higher precision and gap width can be kept small therefore. Considering horizontal gap systems, the labyrinth configuration provides more mechanical stability than the other systems. At the ANTARES facility, labyrinth gaps are used therefore at all locations where the incident beam is not a parallel beam. There is only one location where an approximately parallel beam hits the radiation shielding: The rear wall of the experimental chamber. As the beam cross section at this location is only about 40 cm x 40 cm, a monolithic shielding can be applied at this location.

2.10.4.6 Gap width

The previous dose distributions result for a gap width of 1 cm. This is a conservative assumption, which covers the worst case. In practice smaller gaps are feasible, especially when using steel liners.

The influence of the gap width on the radiation transmission through the shielding was investigated by variation of the gap width in the labyrinth system (configuration C) assuming an isotropic incident beam. Fig. 2.127 shows the factors of neutron dose increase compared to the monolithic case for the gap mouth and for the entire detector area as function of the gap width. A nearly linear relation was found between the dose peak at the gap mouth and the gap width.

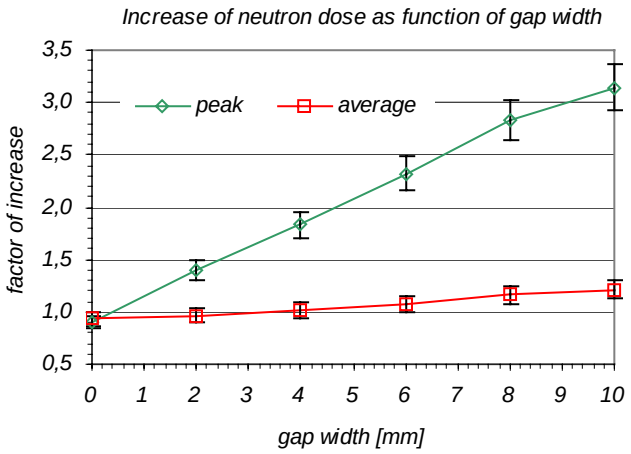

Fig. 2.127: Factors of dose increase for gap configuration C (labyrinth) as function of gap width

The gradient is about 0.24 mm^{-1}. The average transmission shows a smaller increase: all factors of increase are below 0.2 mm^{-1} for gap widths between 0 mm and 10 mm.

2.10.4.7 Offset in labyrinth gaps

In the previous chapters, an offset *y* between inner and outer leg of 20 cm was assumed for the labyrinth gap system (configuration C, see illustration below).

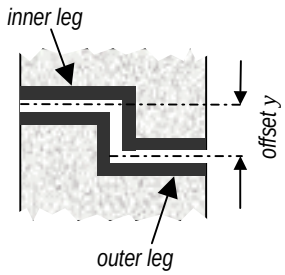

Neutron dose outside of the radiation shielding with gap configuration C (labyrinth) for an isotropic beam in dependency of gap offset (source yield: 1sec $^{-1}$cm $^{-2}$)

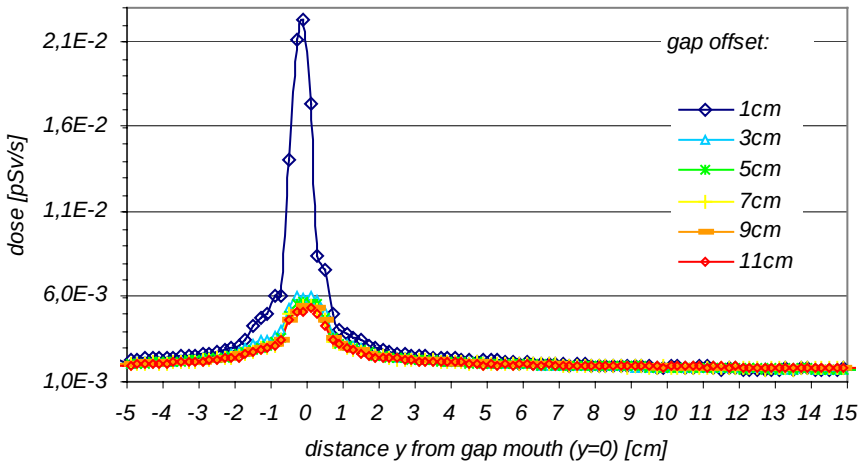

Fig. 2.128: Spatial neutron dose distribution outside the shielding with gap configuration C for an isotropic neutron beam in dependency of the offset between inner and outer part of the gap (gap width=1 cm).

In this chapter the influence of the offset is investigated by modification of the offset size. Fig. 2.128 shows the spatial neutron dose distributions for offsets between 1 cm and 11 cm for an isotropic incident neutron beam (gap width is 1 cm in all cases). The factor of dose increase at the mouth of the gap system compared to the dose obtained by the monolithic shielding is shown in Fig. 2.130. Most advantageous is the step of increasing the gap offset from 1 cm to 2 cm: The dose at the gap mouth is decreased by a factor of three. Further expansion of the offset results only in a slight dose decrease, i.e. the size of the offset between the legs of the gap system should be at least two times the gap width.

Neutron dose outside of the radiation shielding with gap configuration C (labyrinth) for a parallel beam in dependency of gap offset (source yield: 1sec $^{-1}$cm $^{-2}$)

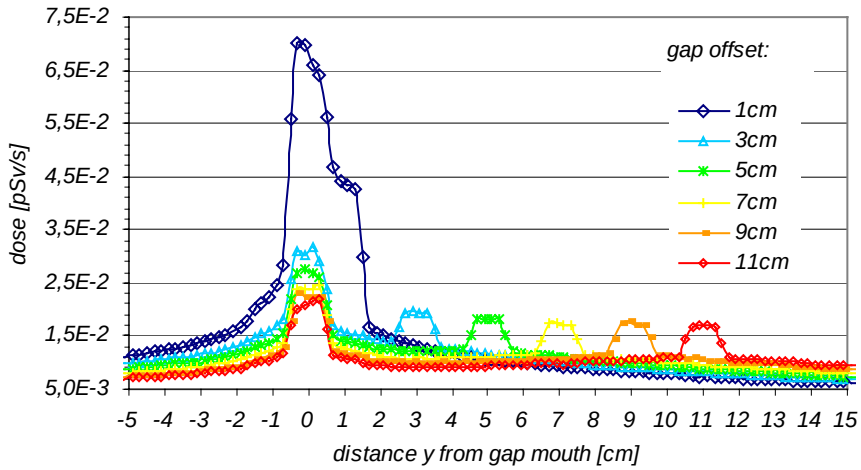

Fig. 2.129: Spatial neutron dose distribution outside the shielding with gap configuration C for a parallel neutron beam in dependency of the offset between inner and outer part of the gap (gap width=1cm).

The spatial neutron dose distribution outside the radiation shielding with labyrinth gap system for a parallel incident beam is shown in Fig. 2.129 in dependency of the offset. The factors of dose increase at the mouth of the gap system are shown in Fig. 2.130. For the labyrinth gap system, increasing the offset from 1 cm to 2 cm results only in a neutron dose decrease of a factor two. Further expansion of the offset is more beneficial than in the case of an isotropic incident neutron beam. The end of the inner leg is an intense local source of scattered neutrons (similar to the case of generated gamma radiation as described above). Increasing the offset means to increase the distance between this source of scattered neutrons and the outer leg

of the gap system. Hence a big offset between inner and outer leg is more effective in the case of a parallel incident neutron beam.

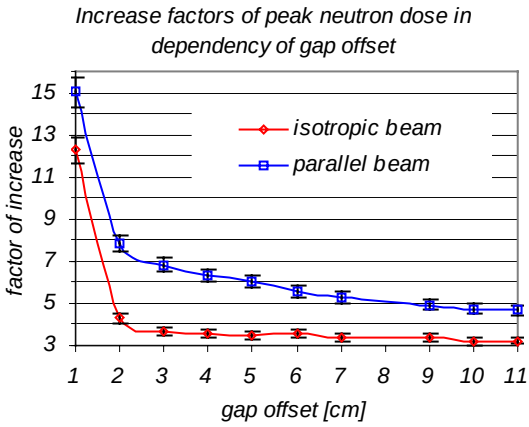

Fig. 2.130: Increase factors of neutron dose at the mouth of the labyrinth gap system (configuration C) compared to the monolithic shielding in dependency of the offset between inner and outer leg of the gap system.

2.10.4.8 Contributions of different energy groups

If neutron transmission through gap systems is above the desired level, the mouth of the gap can be covered by absorbers like e.g. boron rubber mats. This holds when transmission is dominated by neutrons in the thermal energy range. The gap can be filled with thin polyethylene layers when fast or epithermal neutrons are dominant. The choice of an additional shielding therefore depends on the energy distribution of transmitted neutrons.

The increased neutron transmission through the gap systems is due to two different mechanisms:

- Radiation follows the whole gap system by multiple scattering.
- Transport through only one leg and transmission through adjacent shielding material or vice versa. Here, the effective shielding thickness is only half of the monolithic shielding.

In the first case, scattering events must occur close to the channel. Otherwise the radiation could not follow the legs of the gap system. As the mean free path of thermal neutrons in material is much smaller than that of fast neutrons, especially thermal neutrons are transmitted by this mechanism.

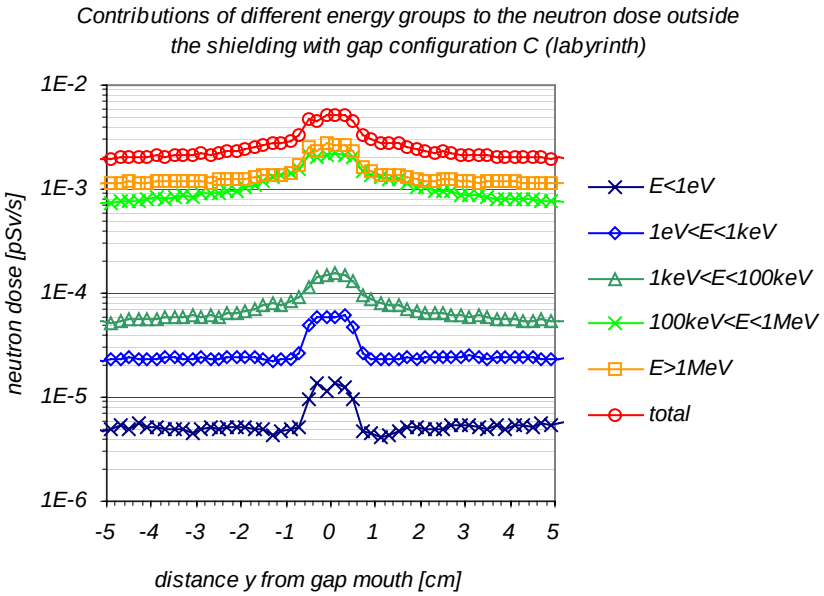

Fig. 2.131: Contributions of different energy groups to the neutron dose outside the shielding with gap configuration C (labyrinth) for an isotropic neutron beam. The offset between inner and outer part of the gap is 20 cm and the gap width is 1 cm. The source yield is 1 $sec^{-1}cm^{-2}$.

In the second case, radiation still has to cross a considerable amount of shielding material (here at least 30 cm). Due to the boron content of the heavy concrete, the contribution of neutrons in the thermal energy range is much smaller compared to fast and epithermal neutrons. Therefore especially fast and epithermal neutrons are transmitted in this way.

Contributions of different energy groups to the spatial neutron dose distribution around the mouth of the gap are shown in Fig. 2.131 (configuration C, offset between inner leg and outer leg is 20 cm, gap width is 1 cm, an isotropic neutron source is applied). The highest contribution to neutron dose at the mouth is from neutrons in the fast energy range above 0.1 MeV. For reduction of neutron transmission through the gap system, filling the gaps with polyethylene layers is therefore effective.

In the final assembly of the ANTARES facility nearly all gaps could be kept below a few millimeters. Hence the desired radiation level outside the shieldings is not exceeded by transmission through gap systems.

2.10.5 Radiation shieldings for the ANTARES facility

2.10.5.1 Practical aspects

From the point of view of radiation protection at FRM-II, the dose rate must not exceed 5 µSv/h at any accessible point in the reactor hall. This dose level comprises neutron as well as gamma radiation. As radiation from neighbor experiments also contribute to the dose rate level, all parts of the shielding that are close to the shielding of neighbor experiments have to be designed for a maximum dose rate of about 2.5 µSv/h for the stand alone case. Additional requirements are:

- Shieldings should be of low weight: The mechanical load of the floor is limited to 10 t/m^2 and the lifting-capacity of the hall crane is restricted to 10 t. High density shielding material creates therefore the necessity of subdivision into small shielding elements, resulting in more gaps.
- Due to limited space in the reactor hall, the shieldings should be as small as possible.
- The cost of shieldings should be kept at a minimum.

2.10.5.2 Radiation shielding for the secondary shutter

2.10.5.2.1 Dose rate sideways the secondary shutter

Space sideways the secondary shutter is very limited due to other experiments. Even if heavy concrete type B (mass density ρ=4.7 g/cm^3; the composition is shown in chapter 2.10.3.3 'Concrete as shielding material') is used as shielding material for the secondary shutter, the radiation level beside the shielding exceeds the constraint (as well neutron radiation as generated gamma radiation). The dose rate distributions for neutron radiation and generated gamma radiation in a vertical plane on the right hand side (in beam direction) of the secondary shutter is shown in Figs. 2.133 and 2.134 (x is the distance from the cold source and z is the height above beam axis). The plane is shown in the horizontal cut through the secondary shutter in Fig. 2.132 (red line). Adjacent to the biological shielding (x=420 cm) at the height of the beam axis (z=0; 120 cm above the floor of reactor hall) a dose rate of about 30 µSv/h occurs (neutron radiation 10 µSv/h; generated gamma radiation 20 µSv/h; primary gamma radiation is negligible at this location). The high dose rate of generated gamma radiation is caused by neutron capture in the steel structure (steel liners and collimators) inside the secondary shutter.

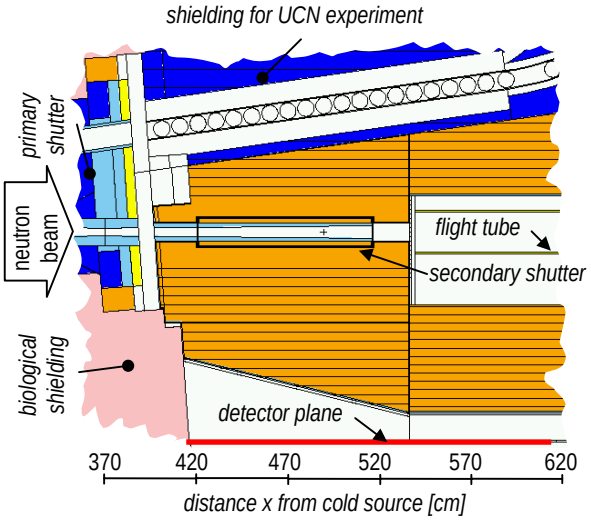

Fig. 2.132: Horizontal cut through the Monte Carlo model of the secondary shutter on beam level

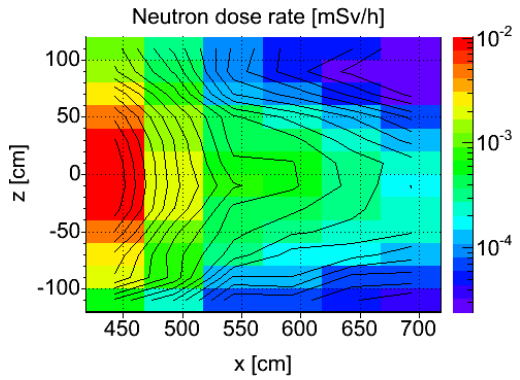

Fig. 2.133: Neutron dose rate [mSv/h] in a vertical plane on the right hand side (in beam direction) of the secondary shutter (the position of the plane is shown in Fig. 2.132). x is the distance from the cold source and z is the height above beam axis.

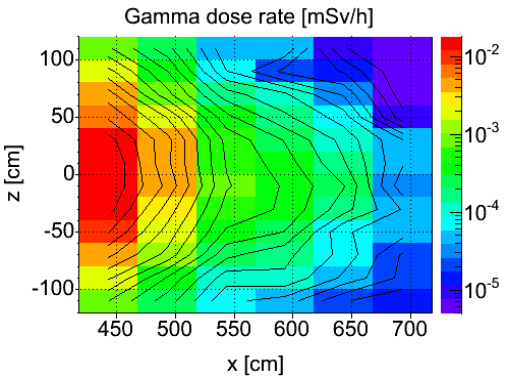

Fig. 2.134: Dose rate of generated gamma radiation [mSv/h] in a vertical plane on the right hand side (in beam direction) of the secondary shutter (the position of the area is shown in Fig. 2.132). x is the distance from the cold source and z is the height above beam axis.

The location where the dose peak occurs is not accessible: The outer surface of the secondary shutter touches the shielding of the neighbor experiment at beam tube SR5 (the detector plane as shown in Fig. 2.132 would be located within the shielding of the neighbor experiment). Exceeding the desired dose level at this position is not relevant for radiation protection. For bigger distances from the cold source, where the ANTARES shielding and the shielding of the neighboring experiment separate (at x=530 cm), the desired dose level is not exceeded.

2.10.5.2.2 Dose rate above the secondary shutter

The beam of the positron experiment (SR11) leaves the biological shielding above the beam line for the ANTARES facility. On top of the secondary shutter, a platform for the positron experiment is located. A safe stay of experimenters on this platform must be guaranteed even during operation of the ANTARES facility.

Secondary shutter version A: Basic

A vertical cut along the beam axis through the Monte Carlo model of the secondary shutter is shown in Fig. 2.135 (version A). The unavoidable gaps, which surround the moveable part of the shutter have a width of 2 mm and are bordered by steel liners of 5 mm thickness. No labyrinth structure is applied for the gap system. In the closed position of the shutter, the L/D=800 collimator is shifted 35 cm from the beam axis and the L/D=400 collimator is shifted 45 cm. Between the aluminum cover plate of the beam tube at the outer margin of the biological shielding and the secondary shutter, there is a void volume. This space must not be filled with shielding material in order to prevent any force propagation from the ANTARES shielding to structures inside the biological shielding e.g. in case of an earthquake or crash of an airplane on the reactor hall.

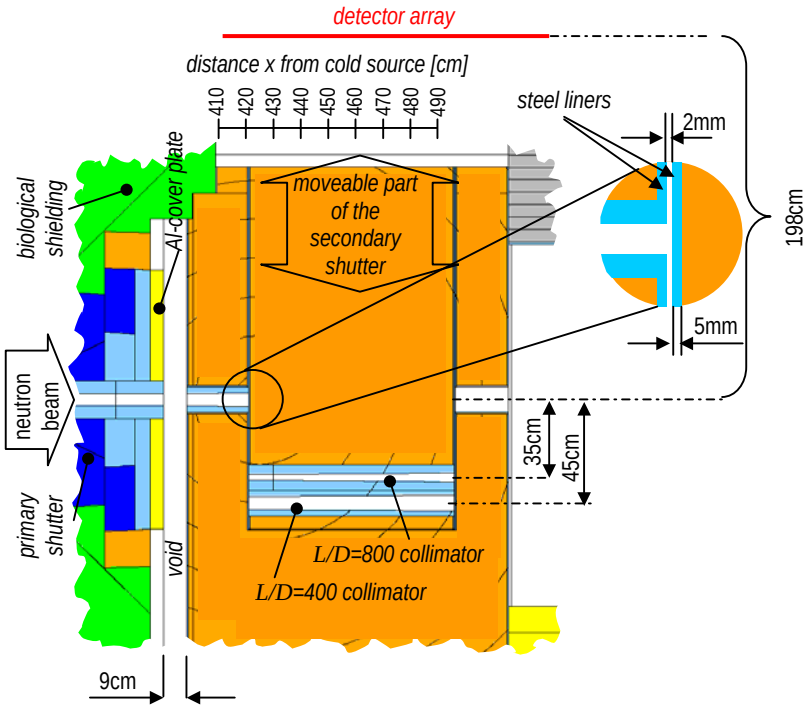

Fig. 2.135: Vertical cut through the Monte Carlo model of the secondary shutter version A.

The dose rate was calculated at a level of 198 cm above the beam axis of the ANTARES beam line (this level corresponds to the bottom of the platform of the positron experiment). The neutron dose rate is shown in Fig. 2.136. A distinct dose rate peak of 43 µSv/h occurs above the gap system at 420 cm distance to the cold source. The front surface of the moving part of the secondary shutter, where the incident beam is stopped by the steel liner and the adjacent heavy concrete, becomes an intense source of scattered neutrons that can traverse along the gap to outside

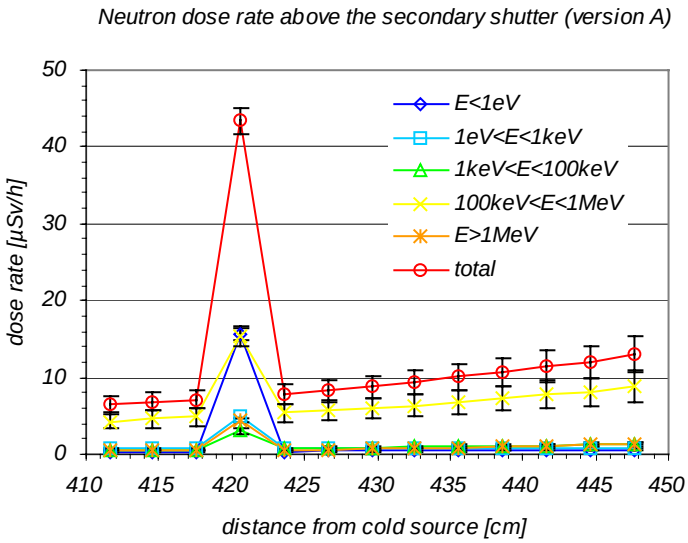

Fig. 2.136: Spatial neutron dose distribution on top of the secondary shutter (version A) 198 cm above the ANTARES beam axis.

the shielding.

The performance of the secondary shutter version A is not satisfying with regard to the radiation protection requirements. Therefore version B was developed. It is aimed to diminish the influence of scattered neutrons.

Secondary shutter version B: Cup

In version B of the secondary shutter a cup on the surface of the moveable part is included (Fig. 2.137). By help of this cup the intense source of scattered neutrons (where the incident beam impinges the shielding material) is shifted away from the gap. Hence the probability of neutron paths traversing the gap is reduced. The depth of the cup is 3.5 cm. In the final version of the secondary shutter, all surfaces of the cup are covered by boral plates in order to reduce production of high energetic gamma radiation by thermal and cold neutron capture. The neutron dose rate distribution above the secondary shutter is shown in Fig. 2.138. The peak value is reduced by a factor of 1.5 to 28 µSv/h. Hence the cup is effective but not sufficient for dose reduction above the secondary shutter down to the necessary level.

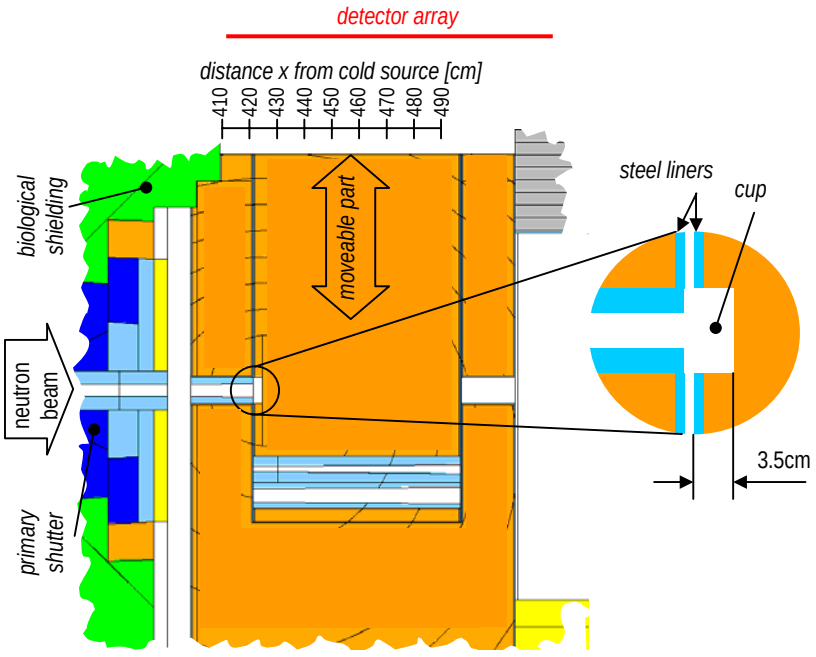

Fig. 2.137: Vertical cut through the Monte Carlo model of the secondary shutter version B.

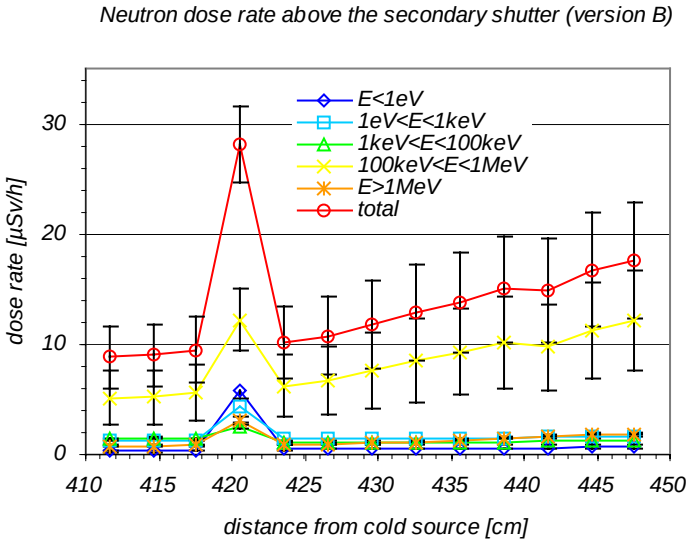

Fig. 2.138: Spatial neutron dose distribution on top of the secondary shutter (version B) 198 cm above the ANTARES beam axis.

Secondary shutter version C: Labyrinth

For further reduction of radiation transport through the gap system around the moveable part of the secondary shutter, a labyrinth structure was included. The offset between inner and outer leg of the gap system is 2 cm. As shown in the chapter 2.10.4 'Gaps in radiation shieldings', even small offsets yield a considerable dose rate reduction (when the offset is bigger than the gap width). A bigger offset is not feasible here, because a gap with the width of the offset occurs in the opened shutter (Fig. 2.146). Nevertheless, the labyrinth system reduces the peak of dose rate above the gap by a factor of 2.8 down to 9.8 µSv/h (the spatial neutron dose rate distribution on top of the secondary shutter is shown in Fig. 2.141). Radiation transport through the gap system is no longer the leading issue for the radiation level above the secondary shutter. The dose rate for distances of more than 440 cm from the cold source exceeds the dose peak above the gap. This radiation level is caused by the void between the secondary shutter and the biological shielding (Fig. 2.140). In this void a cloud of scattered neutrons is formed. From the upper margin of the void, the radiation has to cross only 30 cm of shielding material on its way to the top of the secondary shutter (see Fig. 2.140). For small distances from the biological shielding, the dose rate contribution from the void to the dose rate on the platform is smaller than for bigger distances because radiation has to traverse a longer path through heavy concrete in the biological shielding (Fig. 2.140).

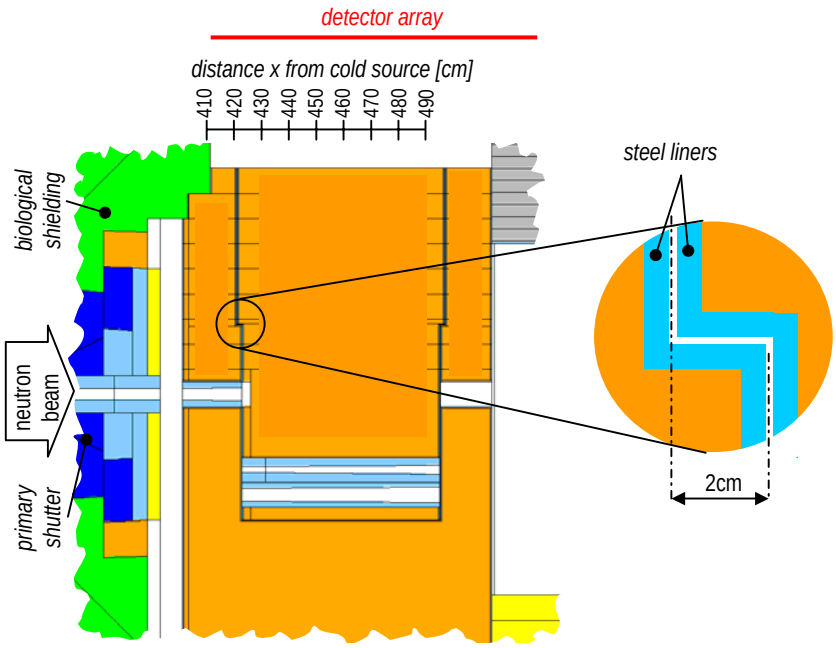

Fig. 2.139: Vertical cut through the Monte Carlo model of the secondary shutter version C.

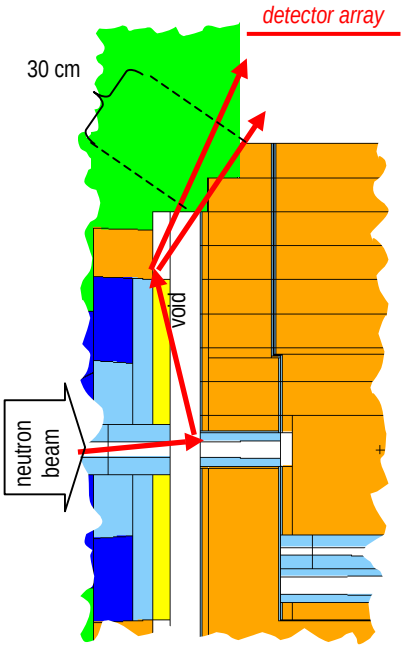

Fig. 2.140: Vertical cut through the void between secondary shutter and biological shielding. From the upper margin of the void, radiation has to cross only 30 cm of shielding material in order to reach the top of the secondary shutter

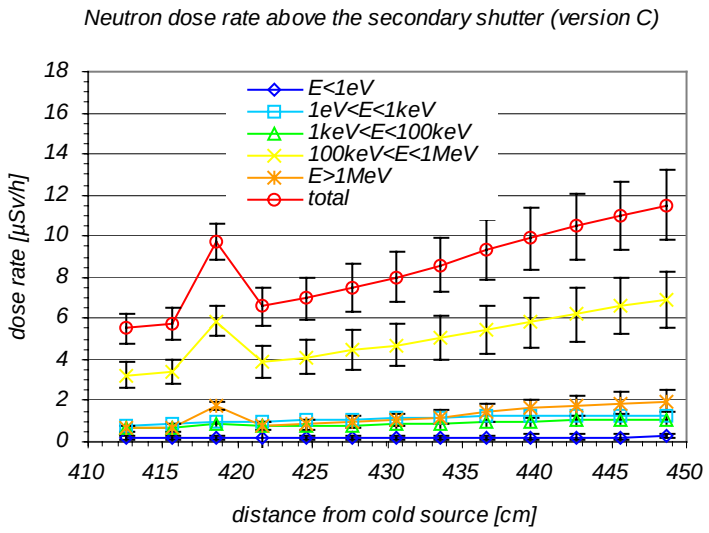

Fig. 2.141: Spatial neutron dose distribution on top of the secondary shutter (version C) 198 cm above the ANTARES beam axis.

In spite of the most promising effect of a labyrinth layout, the shielding power still has to be increased for radiation protection purposes.

Secondary shutter version D: Groove at the entrance to the shutter

In version D of the secondary shutter, the collimator in the entrance window of the shutter has a groove (see Fig. 2.142) similar to the cup described in version B. By this, neutron scattering in the void between secondary shutter and biological shielding is reduced. In the final version, the groove is lined by boral plates in order to reduce production of high energetic gamma radiation. This slight modification of geometry decreases neutron dose on top of the secondary shutter by about a factor of two (except for the dose rate peak directly above the gap, which is not affected by the modification).

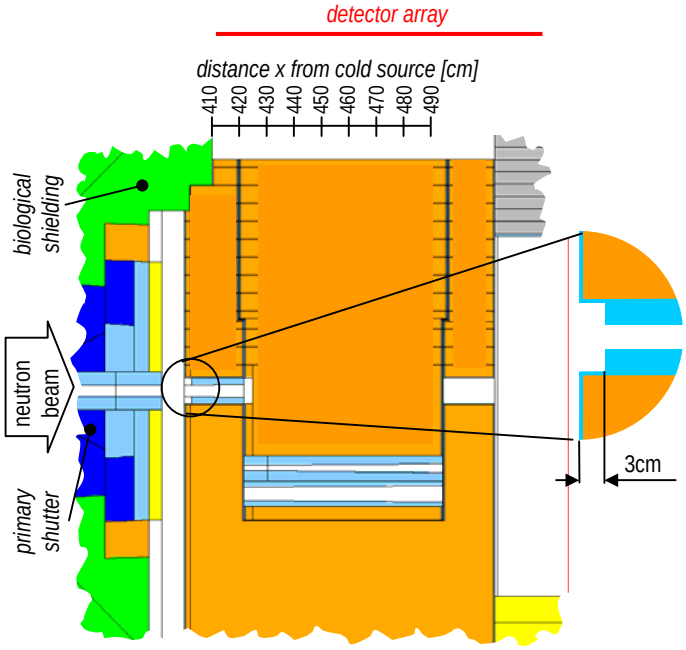

Fig. 2.142: Vertical cut through the Monte Carlo model of the secondary shutter version D.

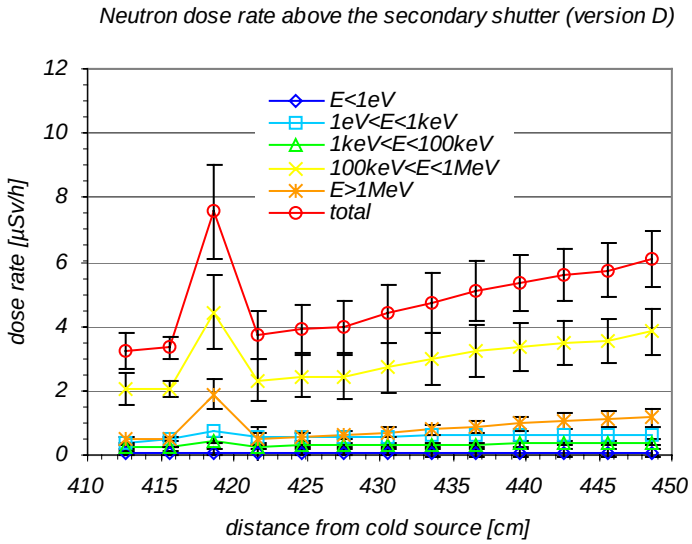

Fig. 2.143: Spatial neutron dose distribution on top of the secondary shutter (version D) 198 cm above the ANTARES beam axis. The peak is not significantly reduced in comparison with version C. In the surrounding area the dose reduction is relevant.

Secondary shutter version E: Reduced void between shutter and biological shielding

During the calculations for the radiation transport in the secondary shutter it turned out that the width of the void between secondary shutter and biological shielding may be smaller than 9 cm without loss of security. Voids with a width of down to 1 cm are feasible without danger of force transfer between shielding and structures inside the biological shielding in emergency situations. A decrease of the width from 9 cm to 3 cm decreases the dose rate on top of the secondary shutter considerably. A vertical cut through the Monte Carlo model of the secondary shutter with decreased width of the void is shown in Fig. 2.144. The dose rate on top of the shutter is shown in Fig. 2.145. The dose rate is about three times smaller than with version D with exception of the peak above the gap system between fixed and moveable part of the secondary shutter. The dose rate above the secondary shutter consists of two components: The leakage through the gap between the biological shielding and the secondary shutter and the leakage through the gaps between the fixed and the moveable parts of the shutter setup. The first component yields a broad spatial distribution, the second component causes a comparatively narrow peak. By decreasing the gap between the biological shielding and the secondary shutter the peak component remains nearly unaltered but it adds to a substantially reduced background. Thus the sum is reduced to a level small enough to meet the radiation protection needs for all locations above the secondary shutter.

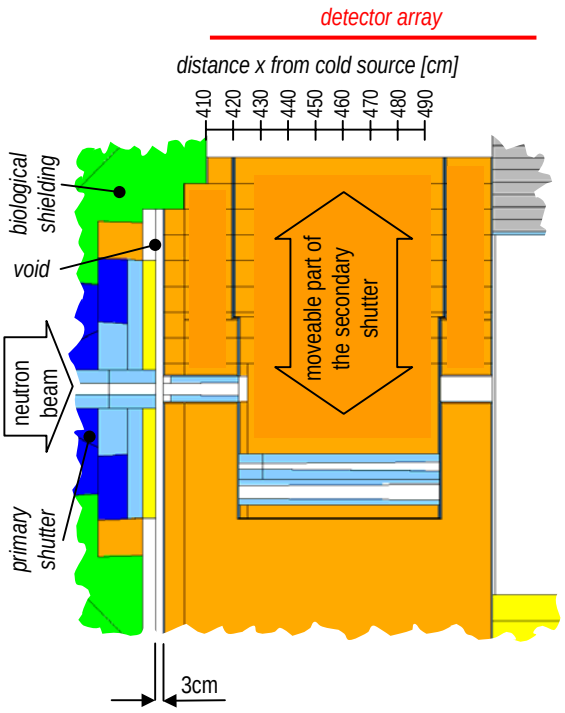

Fig. 2.144: Spatial neutron dose distribution on top of the secondary shutter (version E) 198 cm above the ANTARES beam axis.

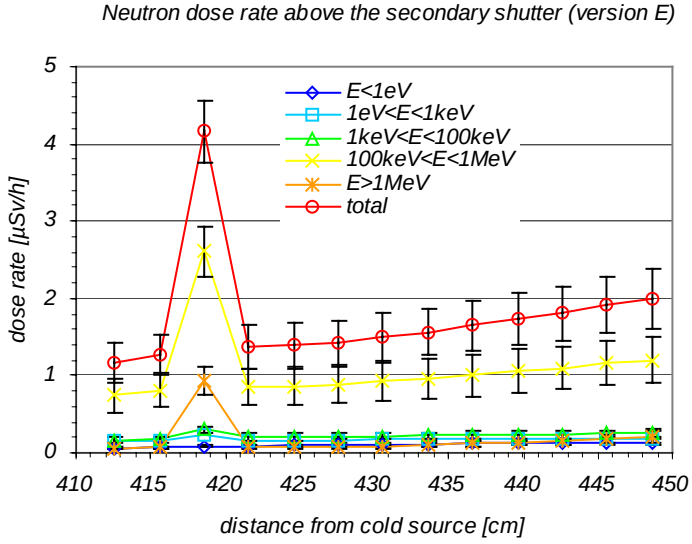

Fig. 2.145: Spatial neutron dose distribution on top of the secondary shutter (version E) 198 cm above the ANTARES beam axis.

Shift length between collimators and beam axis for the closed shutter

The previous chapters describe the minimization of the dose rate for the closed secondary shutter. The labyrinth is a superior design for the gaps, which surround the moveable part of the shutter. On the other hand this design causes a void with 2 cm width when the shutter is opened (Fig. 2.146). The maximal extension of the void equals the maximal drive length of the moveable part of the secondary shutter. It is given by the distance which the moveable part of the shutter has to be lifted for positioning the *L/D*=400 collimator on the beam axis. If this distance is kept small, the void surrounding the moveable part of the opened secondary shutter can also be kept small. On the other hand, radiation transport through the closed shutter in direction to the experimental chamber is diminished by a big drive length. The shifted collimators in the closed shutter represent voids parallel to the beam direction (Fig. 2.147). A compromise has to be found between minimal radiation transport to the top of the opened secondary shutter and minimal radiation transport through the closed shutter in beam direction. Vertical cuts of different variants of the secondary shutter with different maximal drive lengths are shown in Figs. 2.147 to 2.151. The maximal drive lengths were varied between 20 cm and 40 cm. The dose rate of neutron radiation, generated gamma radiation, and primary gamma radiation for the closed secondary shutter in the experimental chamber of the ANTARES facility (at detector position) in dependency of the maximal drive length is shown in Fig. 2.152.

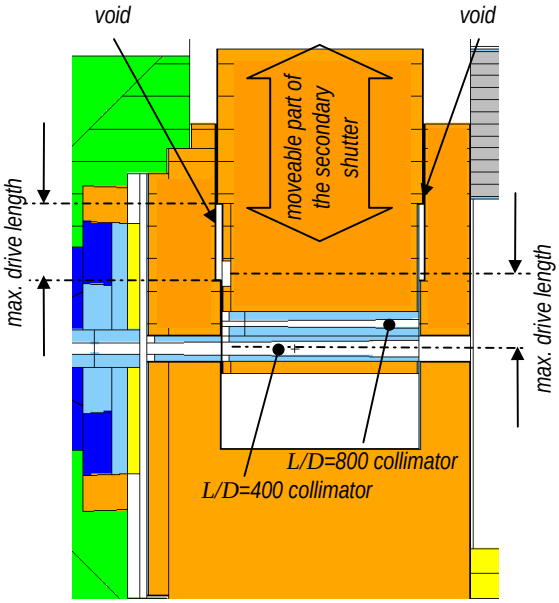

Fig. 2.146: Vertical cut through the Monte Carlo model of the opened secondary shutter

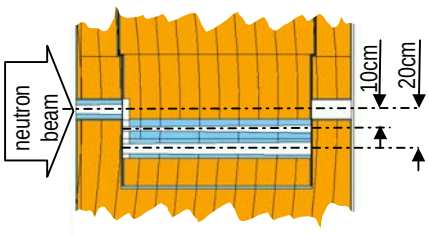

Fig. 2.147: Vertical cut through the closed secondary shutter with a maximal drive length of 20 cm

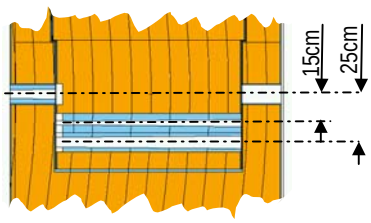

Fig. 2.148: Vertical cut through the closed secondary shutter with a maximal drive length of 25 cm

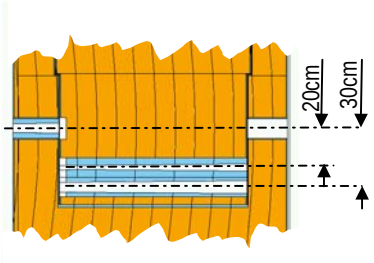

Fig. 2.149: Vertical cut through the closed secondary shutter with a maximal drive length of 30 cm

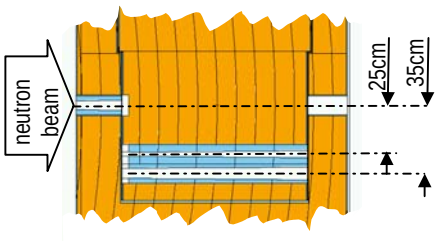

Fig. 2.150: Vertical cut through the closed secondary shutter with a maximal drive length of 35 cm

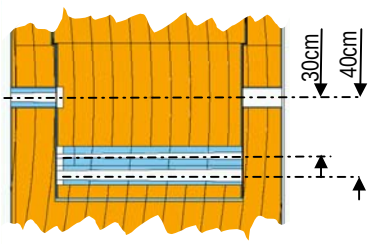

Fig. 2.151: Vertical cut through the closed secondary shutter with a maximal drive length of 40 cm

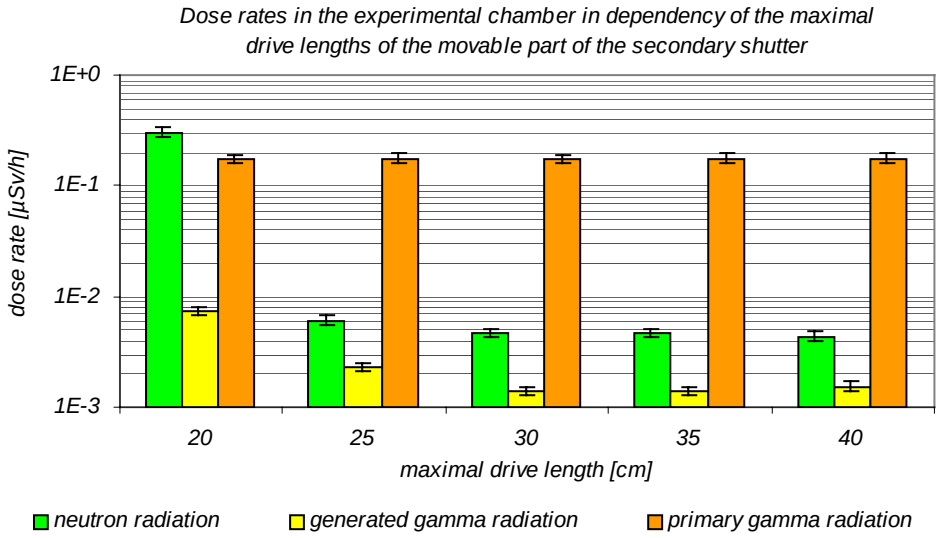

Fig. 2.152: Dose rate in the experimental chamber of the ANTARES facility at the position of the specimen when the secondary shutter is closed for different maximal shift length between beam axis and shifted collimators.

The neutron dose rate in the case of the closed shutter is nearly constant for maximal drive lengths bigger than 25 cm. Neutron radiation is dominated by transmission through the shielding material and not by radiation transport through the shifted collimators. For a maximal drive length of 25 cm a slight increase of neutron dose rate is observable. For smaller maximal drive lengths neutron transport through the shifted collimators becomes more dominant. For a maximal drive length of 20 cm, the neutron dose rate is increased by a factor of 65 compared to the value obtained for maximal drive lengths with more than 25 cm. The dose rate of generated gamma radiation behaves similar to that of neutron radiation, but all values are at least a factor of three below the neutron dose rate. The dose rate of primary gamma radiation is for all examined maximal drive lengths nearly the same, as transport through voids by multiple scattering is less important than for neutron radiation. The primary gamma dose rate delivers the biggest contribution to the total dose rate in the experimental chamber. This is due to the big distance between secondary shutter and experimental chamber (16 m). Scattered neutrons emerge nearly isotropic from the closed secondary shutter. High energetic gamma radiation has a strong forward direction after Compton scattering. Hence, for big distances from the shielding, the ratio of primary gamma dose to neutron dose is increased.

For a closed secondary shutter the dose rate in the experimental chamber does not decrease if the maximal drive length is increased to more than 30 cm.

Opened shutter

A vertical cut through the Monte Carlo model of the opened secondary shutter with 30 cm drive length is shown in Fig. 2.153. For further reduction of the radiation on top of the secondary shutter from the gap between biological shielding and secondary shutter, a socket of heavy concrete was included on top of the secondary shutter adjacent to the biological shielding. The dose rates of neutron radiation and generated gamma radiation above the opened secondary shutter is shown in Fig. 2.154 (L/D =400 collimator is driven on beam axis). Despite the void (width 2 cm, extension 30 cm) around the moveable part of the secondary shutter, the dose rate is not increased compared to the closed secondary shutter. In contrary to the closed shutter, there is no intense source of scattered neutrons close to the gap system around the moveable part of the shutter.

The dose of generated gamma radiation above the gap system is 6.3 µSv/h and exceeds the neutron dose rate by a factor of 2.6. Similar values are obtained by application of the L/D =800 collimator (for the L/D =800 collimator the source of scattered neutrons is more intense due to the smaller cross section of the collimator compared to the L/D =400 collimator, but the extension of the void is only 20 cm). The high contribution from generated gamma radiation is caused by capture of cold and thermal neutrons in the steel structure of the collimators. In the final version of the secondary shutter the frontal areas of all collimator parts are therefore covered with boral masks. In addition, a shielding plate (heavy concrete type B; ρ=4.7 g/cm^3) of 5 cm thickness is mounted on top of the moveable part of the secondary shutter. The plate protrudes from the moveable part of the secondary shutter by 5 cm

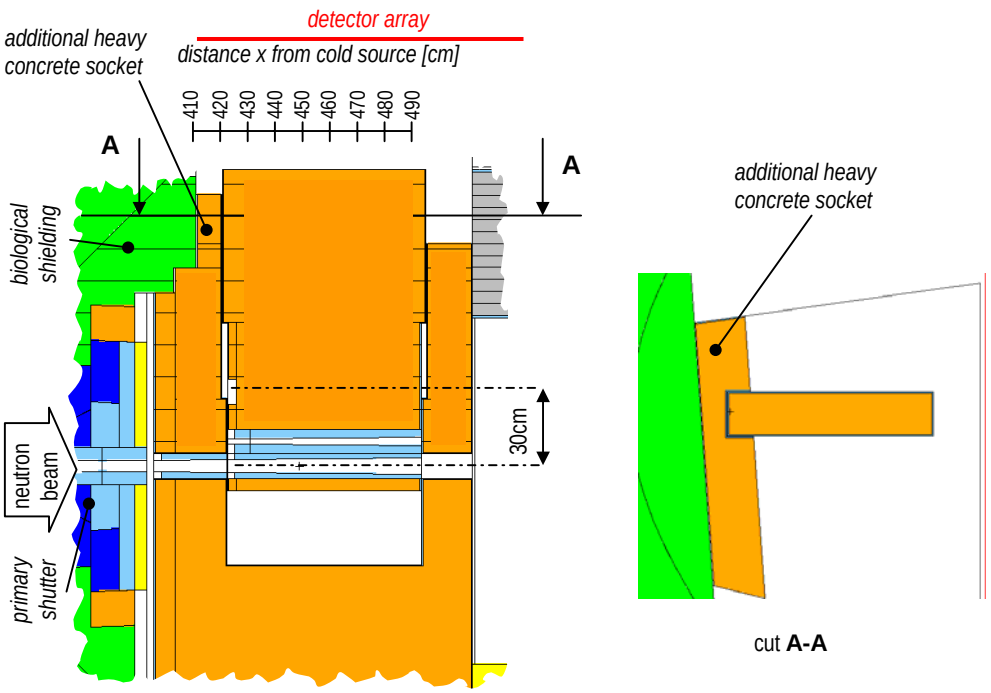

Fig. 2.153: Left hand side: Vertical cut through the Monte Carlo model of the secondary shutter with a maximal drive length of 30 cm and an additional heavy concrete socket adjacent to the biological shielding on top of the secondary shutter. Right hand side: Horizontal cut through the additional heavy concrete socket on top of the secondary shutter adjacent to the biological shielding.

and covers therefore the complete gap system around the secondary shutter. The maximal drive length in the final version is 30 cm.

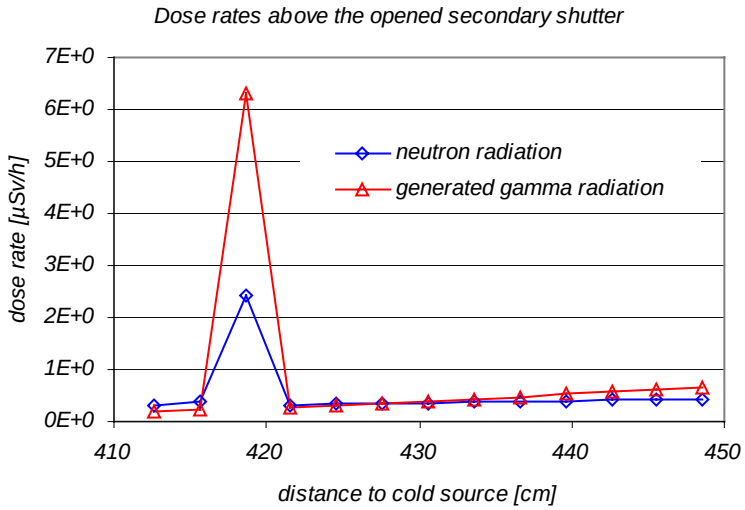

Fig. 2.154: Dose rates of neutron radiation and generated gamma radiation on top of the opened secondary shutter (application of L/D =400 collimator) with a maximal drive length of 30 cm and an heavy concrete socket on top of the shutter adjacent to the biological shielding).

2.10.5.3 Radiation shielding for the flight tube

2.10.5.3.1 Optimization of the shielding

Version A: Basic

The flight tube walls are made from aluminum because this material combines a rather low neutron cross section with high mechanical strength. With regard to weight and cost, the flight tube should be as narrow as possible [83]. A flight tube that confines the fully illuminated region of the neutron beam as close as possible and that has a simple shape is desirable. The shape of a flight tube that confines

exactly the fully illuminated area would be similar to the collimator surface described in chapter 2.3.5 'Collimators'. Machining of a flight tube with this complex geometry would be very expensive. Therefore this shape is approximated with a series of cylinders. Anyway, a flight tube that confines the fully illuminated region closely touches the penumbra region of the neutron beam. In version A of the arrangement flight tube – radiation shielding, a cylindrical flight tube is used that cuts into the penumbra region at certain locations, but does not hamper any neutrons in the fully illuminated area. For mechanical support of the flight tube, a steel structure is mounted below the flight tube (outside the penumbra region, Figs. 2.155, 2.156). As shielding material heavy concrete type A (ρ=3.6 g/cm^3) is used. This concrete type is cheaper and of lower weight than the other examined concrete types. The shielding wall has a thickness of 80 cm. A vertical cut perpendicular to the beam axis through the arrangement at a distance of 12 m from the cold source is shown in Fig. 2.155. A vertical and a horizontal cut along the beam axis are shown in Fig. 2.156 and Fig. 2.157.

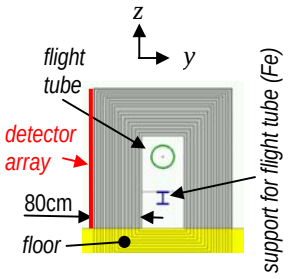

Fig. 2.155: Vertical cut perpendicular to beam axis through the Monte Carlo model of the radiation shielding version A for the flight tube.

Spatial flux and dose distributions were calculated on all outer surfaces of the radiation shielding with a spatial resolution of 0.5 m in beam direction and 0.2 m perpendicular to beam direction. Since the distributions on the right hand side (in beam direction), the left hand side, and on top of the shielding are very similar (due to same shielding thicknesses), only the values on the right hand side are shown here. The location of the detector plane on the right side (in beam direction) of the shielding on which the spatial radiation distribution was calculated is shown as red line in Fig. 2.155 and Fig. 2.157. The neutron dose rate in this plane is shown in Fig. 2.158 and the dose rate of generated gamma radiation is shown in Fig. 2.159. The dose rate of primary gamma radiation is negligible at this location (values are some orders of magnitude below the contributions of the other radiation components). Considering the neutron dose rate outside the radiation shielding, two distinct dose peaks occur on beam level (120 cm above the floor of the reactor hall) at a distance of 940 cm and 1150 cm from the cold source. These are the locations where the flight tube mantle cuts into the penumbra region of the neutron beam. The peak values of neutron dose rate are 0.2 µSv/h. At the same locations, dose rate peaks of generated gamma radiation occur (due to neutron capture in aluminum: ^{27}Al(n,γ)^{28}Al. The peak values (2.5 µSv/h) exceed the neutron dose rate by more than a factor of 10. The shielding material itself is not the major source of generated gamma radiation: As shown in chapter 2.10.3.3 'Concrete as shielding material', the generated gamma dose rate in heavy concrete type A exceeds the neutron dose rate only by a factor of two. The main contribution to generated gamma radiation outside the radiation shielding is

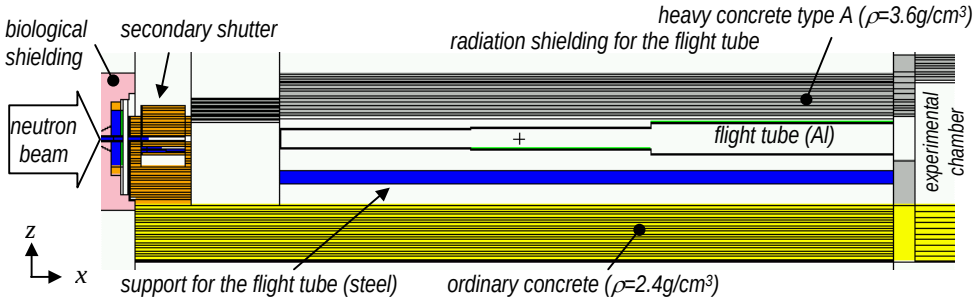

Fig. 2.156: Vertical cut along the beam axis through the Monte Carlo model of the radiation shielding version A for the flight tube. As shielding material heavy concrete type A (ρ=3.6 g/cm^3, displayed in grey) is used. Shielding thickness is 80 cm.

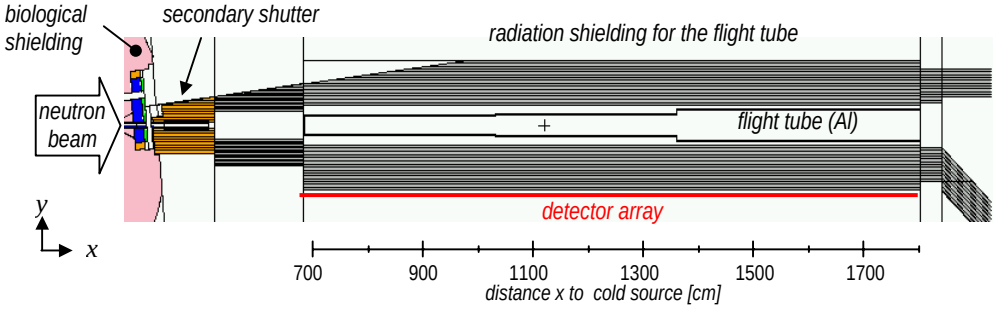

Fig. 2.157: Horizontal cut along the beam axis through the Monte Carlo model of the radiation shielding version A for the flight tube. As shielding material heavy concrete type A (ρ=3.6 g/cm^3, displayed in grey) is used. Shielding thickness is 80 cm.

caused by structure elements in the interior of the shielding. The contribution from the flight tube mantle is dominant.

Though the cross section of aluminum for thermal neutrons is rather low (σ_{abs}=0.23 barn [32]), there is considerable encounter with aluminum in the penumbra region, because in this region the paths of the neutrons are nearly parallel to the tube wall. This is an unwanted side effect of having a good collimation. A neutron crossing the inner tube boundary has a long path (about 30 cm) through aluminum. Hence, the intersections of the beam penumbra with the walls of the flight tube are intense sources of scattered neutrons and generated gamma radiation (illustration in Fig. 2.160). Thermal neutron capture in ^{27}Al produces gamma rays; the most frequent energy of this gamma radiation is 7.7 MeV [43].

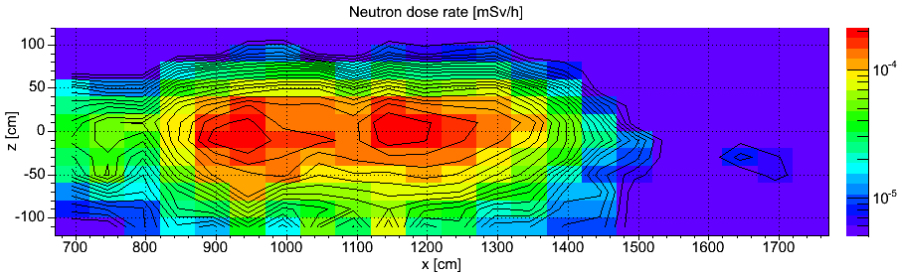

Fig. 2.158: Spatial distribution of neutron dose rate [mSv/h] on the right hand side of the shielding version A. x is the distance from the cold source and z is the height related to the beam axis level. As shielding material heavy concrete type A (ρ=3.6 g/cm^3) is used. Shielding thickness is 80 cm.

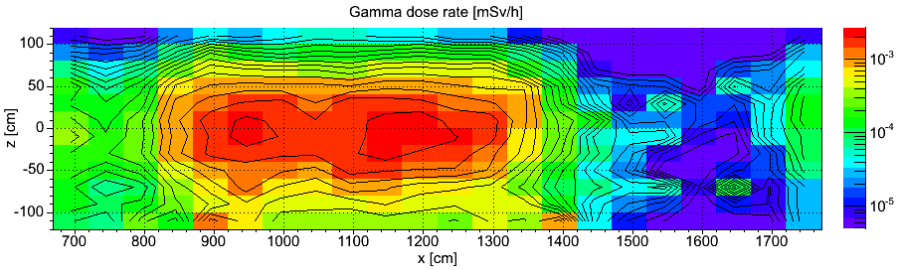

Fig. 2.159: Spatial distribution of generated gamma dose rate [mSv/h] on the right hand side of the shielding version A. x is the distance from the cold source and z is the height related to the beam axis level. As shielding material heavy concrete type A (ρ=3.6 g/cm^3) is used. Shielding thickness is 80 cm.

For overcoming this radiation protection problem, obviously there are three ways:

- additional shielding against gamma rays (voluminous, heavy, and expensive especially for high energetic gamma radiation)
- enlargement of the flight tube that even penumbra neutrons will not hit the flight tube (higher weight and cost for the flight tube)
- limitation of the penumbra region by additional collimators or absorber masks

However, the desired dose rates are not exceeded by version A of the flight tube – radiation shielding arrangement. Investigations were carried out, whether a further reduction of radiation outside the shielding can be achieved without enlargement of shielding size and whether shielding size can be even reduced.

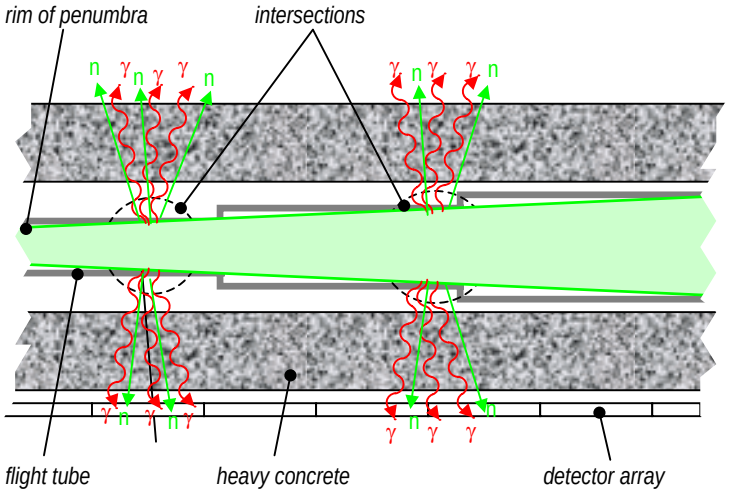

Fig. 2.160: Schematic overview of neutron scattering and gamma production at the walls of the flight tube.

Version B: High density concrete at hot spots

For reduction of the high dose rate of generated gamma radiation, in version B of the radiation shielding, heavy concrete type A is replaced by heavy concrete type B (ρ=4.7 g/cm^3) within a slab of 40 cm height (Fig. 2.162). The layer is arranged at beam axis level, where the dose peaks of generated gamma radiation occur in version A. Due to the higher iron content in heavy concrete type B, attenuation of gamma radiation from the structure elements inside the shielding is higher than with heavy concrete type A. The spatial distribution of neutron dose rate is shown in Fig. 2.164. It is very similar to that achieved by version A. Neutron attenuation by heavy concrete of type A (ρ=3.6 g/cm^3) and of type B (ρ=4.7 g/cm^3) is similar (see chapter 'Concrete as shielding material'). The dose of generated gamma radiation (Fig. 2.165) is reduced considerably: At beam axis level the maximal dose rate is 0.3 mSv/h. The disadvantage of this shielding arrangement

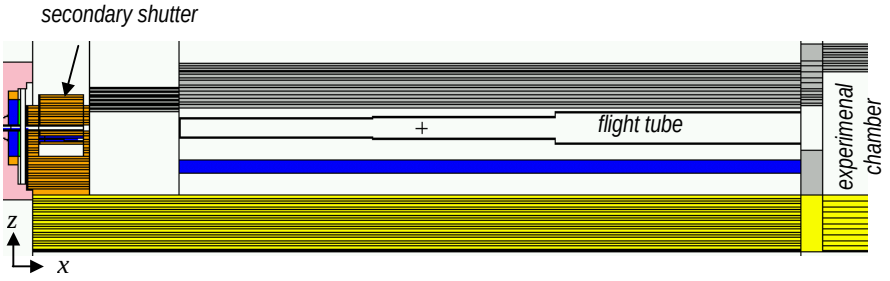

Fig. 2.161: Vertical cut along the beam axis through the Monte Carlo model of the radiation shielding version B for the flight tube. Shielding materials are heavy concrete type A (ρ=3.6 g/cm^3) and heavy concrete type B (ρ=4.7 g/cm^3). Shielding thickness is 80 cm.

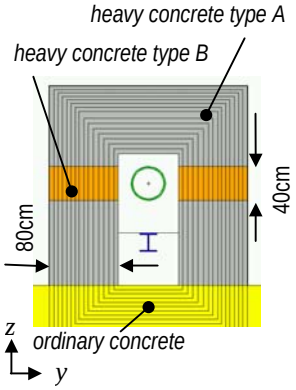

Fig. 2.162: Vertical cut perpendicular to the beam axis through the Monte Carlo model of the arrangement flight tube – radiation shielding version B. Shielding thickness is 80 cm.

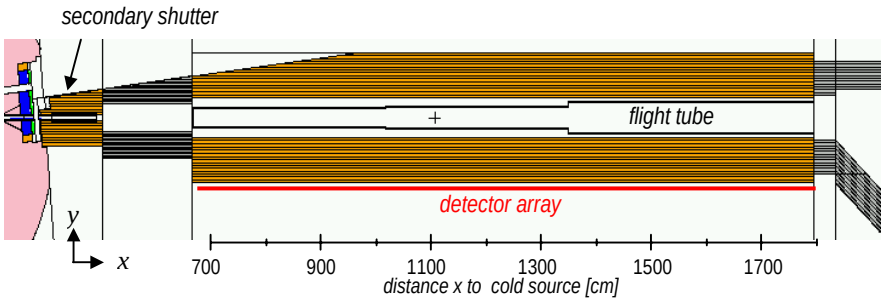

Fig. 2.163: Horizontal cut along the beam axis through the Monte Carlo model of the radiation shielding version B for the flight tube. Shielding materials are heavy concrete type A (ρ=3.6 g/cm^3) and heavy concrete type B (ρ=4.7 g/cm^3). Shielding thickness is 80 cm.

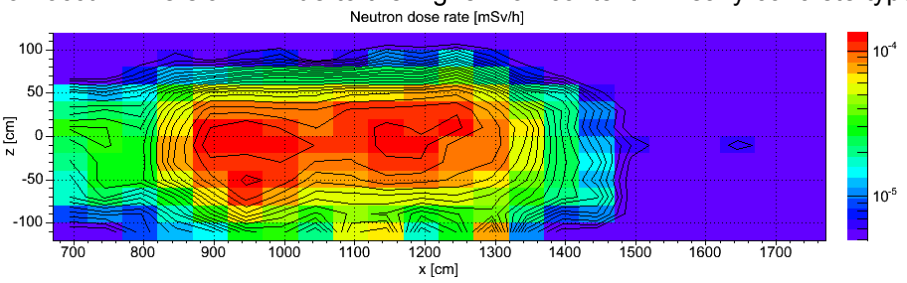

Fig. 2.164: Spatial distribution of neutron dose rate on the right hand side of the shielding version B. x is the distance from the cold source and z is the height related to beam axis level. Shielding materials are heavy concrete type A (ρ=3.6 g/cm^3) and heavy concrete type B (ρ=4.7 g/cm^3). Shielding thickness is 80 cm.

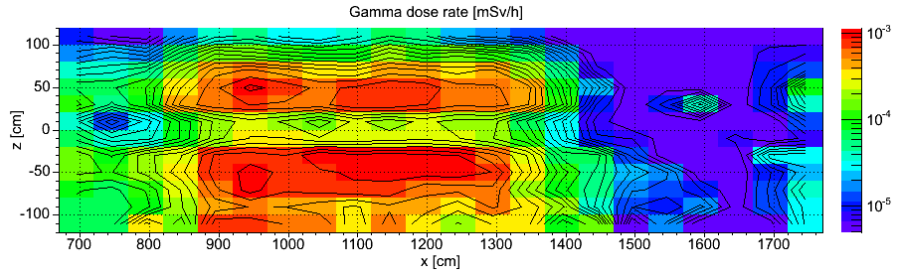

Fig. 2.165: Spatial distribution of generated gamma dose rate on the right hand side of the shielding version B. x is the distance from the cold source and z is the height related to beam axis level. As shielding material heavy concrete type A (ρ=3.6 g/cm^3) and heavy concrete type B (ρ=4.7 g/cm^3) is used. Shielding thickness is 80 cm.

is that below and above the layer with heavy concrete of type B still high dose rates occur. Hence the layer has to be enlarged with the consequence of a considerable increase of weight and cost. Thus a further option for dose reduction was tested.

Version C: Auxiliary collimator

In version C of the flight tube shielding, the penumbra of the neutron beam is cut by an additional collimator at the beginning of the flight tube. The collimator consists of steel and has a length of 40 cm (Figs. 2.166, 2.167). By reduction of the penumbra, neutron scattering and gamma production in the flight tube walls are reduced. The collimator is surrounded by a shielding wall of 40 cm thickness consisting of heavy concrete type B. However, for the flight tube geometry, as used here, it is not possible to completely avoid intersections of the flight tube wall and the beam penumbra. For this purpose, multiple collimators would be necessary.

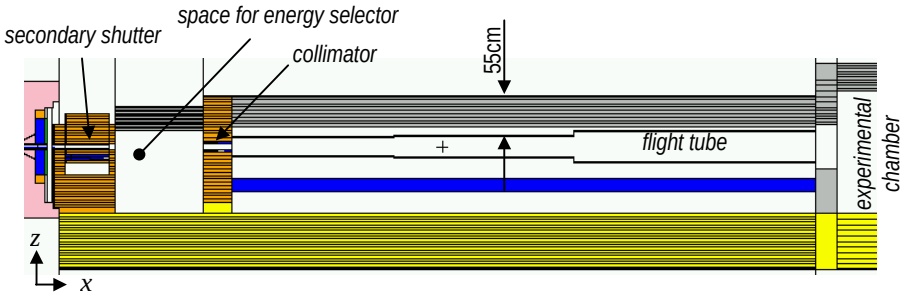

Fig. 2.166: Vertical cut along beam axis through the Monte Carlo model of version C of the radiation shielding for the flight tube. As shielding material heavy concrete type A (ρ=3.6 g/cm^3) is used. Shielding thickness is 55 cm. The shielding wall surround the additional collimator consists of heavy concrete type B (ρ=4.7 g/cm^3).

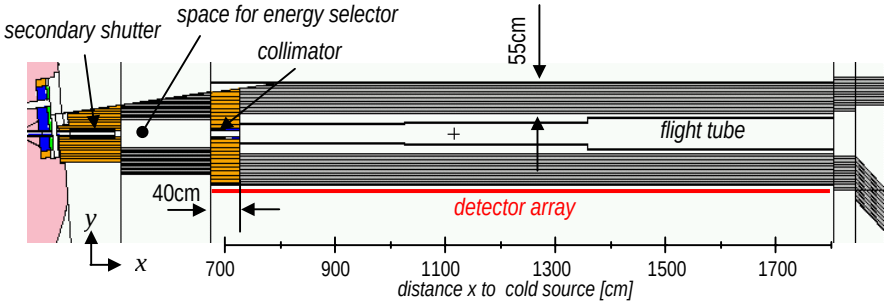

Fig. 2.167: Horizontal cut along beam axis through the Monte Carlo model of version C of the radiation shielding for the flight tube. As shielding material heavy concrete type A (ρ=3.6 g/cm^3) is used. Shielding thickness is 55 cm. The shielding wall surround the additional collimator consists of heavy concrete type B (ρ=4.7 g/cm^3).

Nevertheless, the thickness of the shielding around the flight tube was reduced to 55 cm because of the expected lower amount of neutron scattering and gamma production in the flight tube walls.

The space before (in beam direction) the additional collimator is reserved for an optional energy selector.

The spatial distribution of neutron dose rate and generated gamma dose rate is shown in Fig. 2.169 and Fig. 2.170. The neutron dose rate does not exceed the desired threshold at any point. A maximum of neutron dose rate appears at a distance of 750 cm from the cold source (close to the collimator) due to neutron scattering in the collimator material. A second peak occurs where the penumbra still intersects with the flight tube walls. At the same locations, peaks of generated gamma radiation occur. The dose rate peaks of generated gamma radiation (10 µSv/h) exceed the desired value by far. Hence the collimator and the surrounding shielding do not reduce the penumbra region sufficiently.

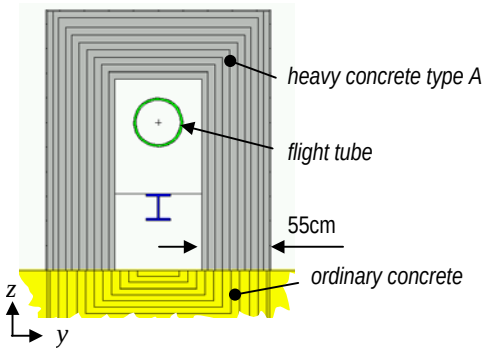

Fig. 2.168: Vertical cut at a distance x from the cold source of 11 m through the Monte Carlo model of version C of the shielding for the flight tube. As shielding material heavy concrete type A (ρ=3.6 g/cm^3) is used. Shielding thickness is 55 cm.

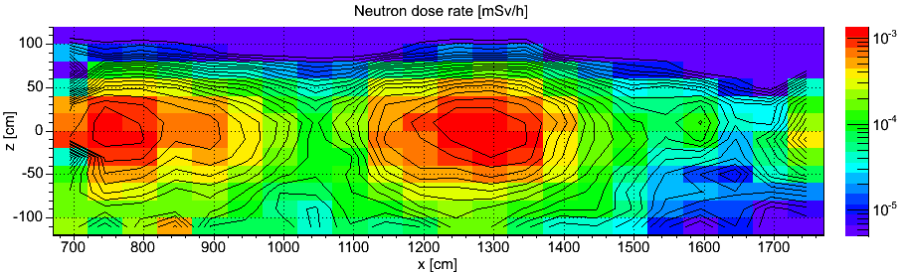

Fig. 2.169: Spatial distribution of neutron dose rate on the right hand side of the shielding version C. x is the distance from the cold source and z is the height related to beam axis level. As shielding material heavy concrete type A (ρ=3.6 g/cm³) is used. Shielding thickness is 55 cm. The shielding wall around the additional collimator consists of heavy concrete type B (ρ=4.7 g/cm³).

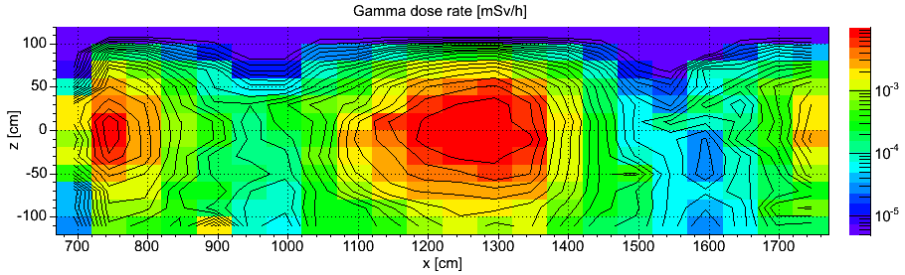

Fig. 2.170: Spatial distribution of generated gamma dose rate on the right hand side of the shielding version C. x is the distance from the cold source and z is the height related to beam axis level. As shielding material heavy concrete type A (ρ=3.6 g/cm³) is used. Shielding thickness is 55 cm. The shielding wall around the additional collimator consists of heavy concrete type B (ρ=4.7 g/cm³).

Version D: Absorber masks and enlarged flight tube diameters

In version D the shielding walls around the flight tube consist of heavy concrete type A (thickness 55 cm). The influence of an absorber mask for cold and thermal neutrons and the geometry of the flight tube on the dose rate outside the radiation shielding was tested with this version. For this purpose the dose rates outside the radiation shielding were calculated for different arrangements inside the shielding:

- The whole flight tube is omitted
- The flight tube is mounted inside the shielding
- An absorber mask is mounted at the beginning (in beam direction) of the flight tube
- The diameters of the flight tube segments are increased

The neutron dose rates and the dose rates of generated gamma radiation outside the shielding obtained by the different arrangements at level of the beam axis (where the dose rate maxima occur) are shown in Figs. 2.173 and 2.174.

Version D without flight tube

Without flight tube, the neutron dose rate would be rather low (<1 µSv/h) up to a distance of 14 m from the cold source as no neutron scattering at structures inside the radiation

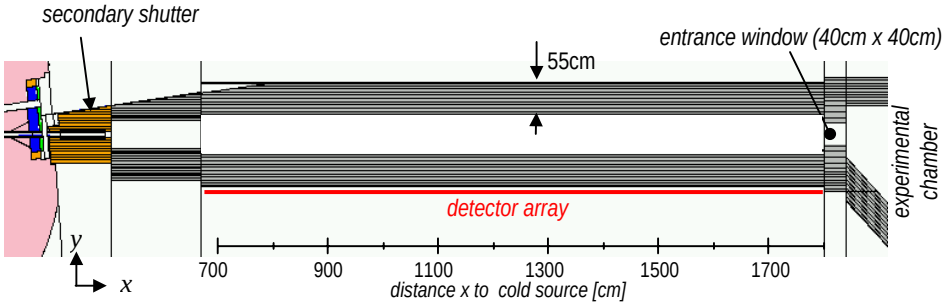

Fig. 2.171: Horizontal cut along beam axis through the Monte Carlo model of the radiation shielding version D without flight tube. As shielding material heavy concrete type A (ρ=3.6 g/cm³) is used. Shielding thickness is 55 cm.

shielding takes place (red curve in Fig. 2.173). For distances bigger than 14 m from the cold source, dose rate rises (up to 5 µSv/h) due to back scattering from the shielding around the entrance window of the experimental chamber. Omitting this shielding is not possible, as background radiation inside the experimental chamber would rise.

The dose rate of generated gamma radiation shows a similar behavior (red curve in Fig. 2.174): As there are no structures inside the shielding that capture neutrons, the dose rate is low up to a distance of 14 m from the cold source. For bigger distances from the cold source, neutron capture in the heavy concrete around the entrance window of the experimental chamber causes an increase of dose rate of generated gamma radiation (up to 25 µSv/h).

Version D with small flight tube

When a flight tube with the same geometry as in the preceding chapters is mounted inside the shielding, two dose rate peaks occur where the penumbra intersects with the flight tube walls (as with this flight tube geometry the cross section of the flight tube is minimized, it is called 'small flight tube' in the following). This is true for both neutron radiation and generated gamma radiation. The dose rates of neutron radiation and generated gamma radiation outside the shielding on beam axis level are shown in Figs. 2.173 and 2.174 (orange curves in both diagrams). The effect causing the dose peaks is the same as described with version A (neutron scattering and gamma production in the flight tube walls), but dose rate values are much higher in version D due to the smaller shielding thickness (maximal neutron dose rate: 5 µSv/h; maximal dose rate of generated gamma radiation: 30 µSv/h). For distances of more than 14 m from the cold source, the dose rate is even smaller than with the arrangement without flight tube. This is because a smaller amount of radiation reaches the shielding around the entrance window of the experimental chamber (due to absorption and scattering in the flight tube walls).

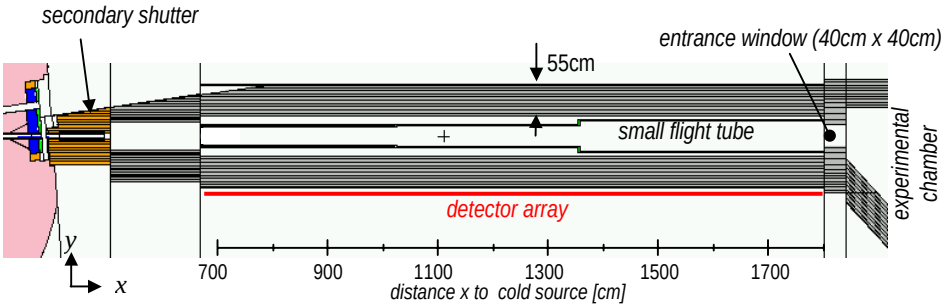

Fig. 2.172: Horizontal cut along beam axis through the Monte Carlo model of version D of the radiation shielding with small flight tube. As shielding material heavy concrete type A (ρ=3.6 g/cm^3) is used. Shielding thickness is 55 cm.

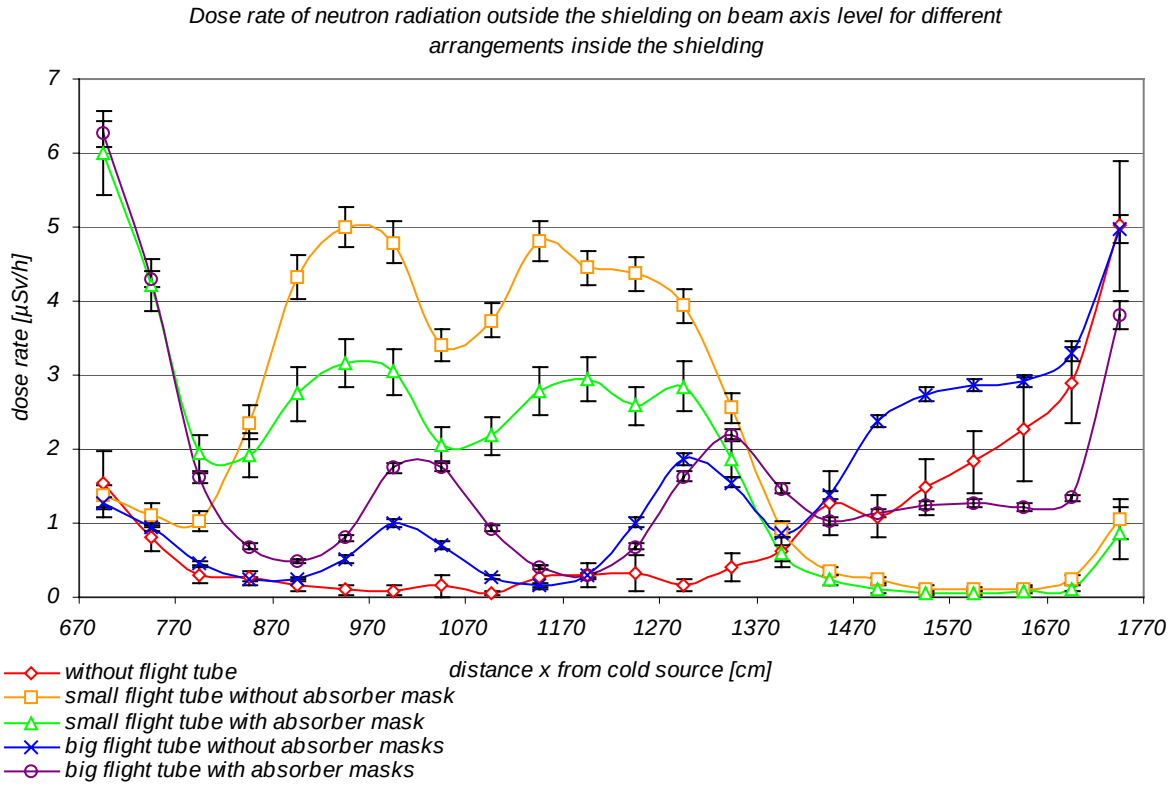

Fig. 2.173: Dose rates of neutron radiation on the right hand side (in beam direction) of the radiation shielding on beam axis level for different setups of the flight tube and absorber masks inside the shielding.

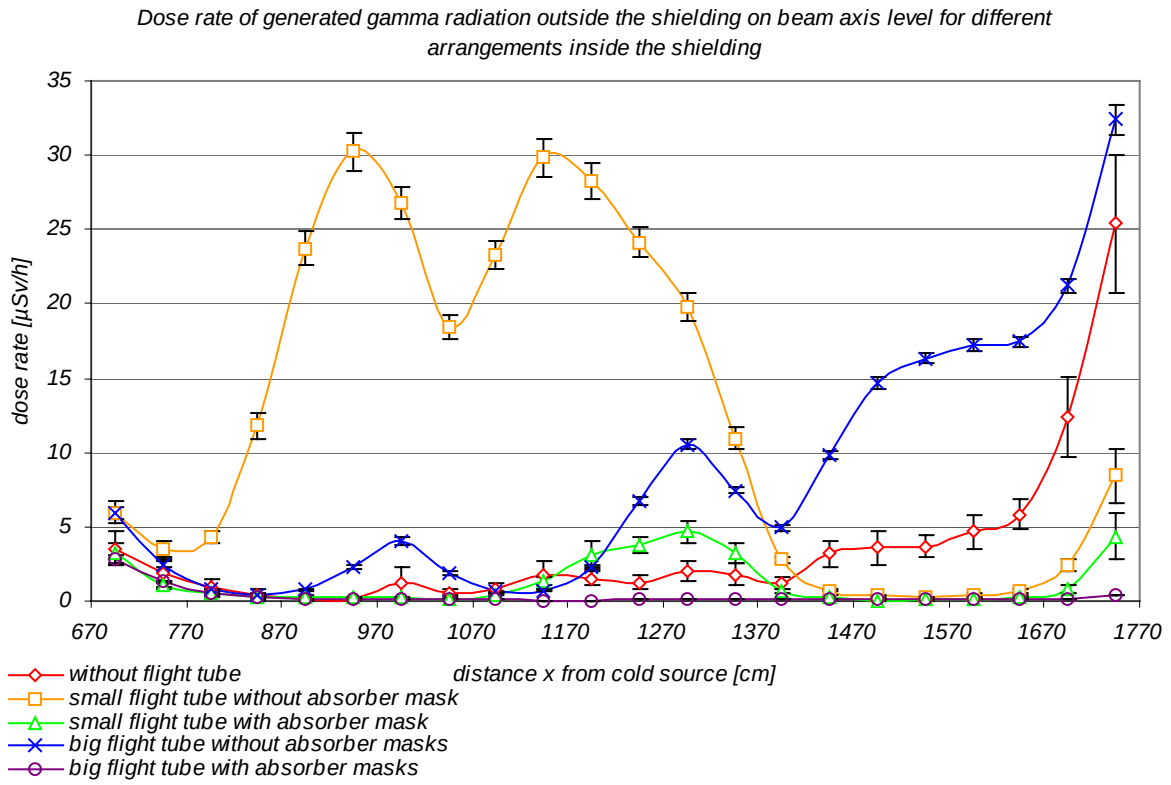

Fig. 2.174: Dose rates of generated gamma radiation on the right hand side (in beam direction) of the radiation shielding on beam axis level for different setups of the flight tube and absorber masks inside the shielding.

Version D with small flight tube and absorber mask

For reduction of the size of regions where the penumbra intersects with the flight tube walls, an absorber mask is located at the beginning of the flight tube (the geometry of the flight tube is the same as in the preceding chapters). The mask consists of boron carbide (thickness 3 cm; enclosed in an aluminum case) and cuts the penumbra region as far as possible, similar to the steel collimator that was tested with version C. In contrary to the collimator, only cold and thermal neutrons are attenuated significantly by the mask but the mask is much easier to mount and cheaper to fabricate than the collimator. The dose rates of neutron radiation and generated gamma radiation outside the shielding on beam axis level are shown in Figs. 2.173 and 2.174 (green curves in both diagrams). Of course, due to the low attenuation in the fast energy region, reduction of neutron dose rate outside the radiation shielding is low. Close to the mask (at a distance of 7 m from the cold source) even an increase of neutron dose rate by a factor of four is observable (from 1.5 µSv/h without mask to 6 µSv/h with mask) due to scattering of epithermal and fast neutrons at the carbon of the mask material. Boron carbide is therefore not optimal for bordering the penumbra region. For large distances from the cold source, the neutron dose rate is decreased to about 60% of the dose rate obtained without mask. The mask is not very efficient for limitation of the neutron dose rate. For reduction of the generated gamma radiation it is useful: Production of high energetic gamma radiation in the flight tube walls by capture of cold and thermal neutrons is avoided by the mask. The peak of the dose rate of generated gamma radiation is reduced by a factor of six by the mask (from 30 µSv/h without mask to 5 µSv/h with mask). For reduction of generated gamma radiation, the boron carbide mask is even more useful than the steel collimator used in version C.

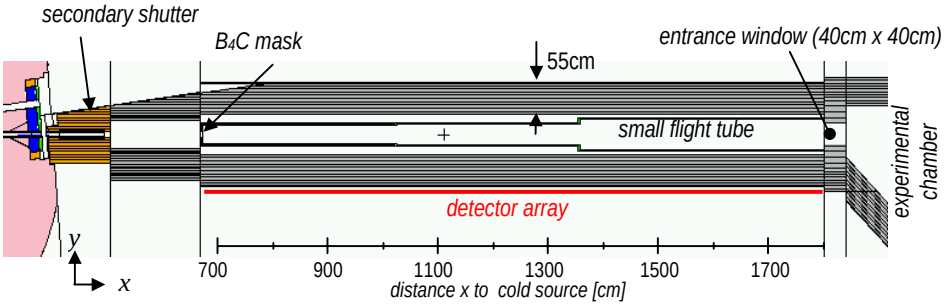

Fig. 2.175: Horizontal cut along beam axis through the Monte Carlo model of version D of he radiation shielding with small flight tube and absorber mask. As shielding material heavy concrete type A (ρ=3.6 g/cm^3) is used. Shielding thickness is 55 cm.

Version D with big flight tube

In the chapters above, the cross sections of flight tube segments were minimized in order to keep cost and weight of the flight tube small. As it was shown, the interaction of the flight tube walls with the neutron beam increases the dose rate considerably (especially the contribution from generated gamma radiation). A shielding thickness of 55 cm is not sufficient to obtain the desired dose rate values outside the shielding. Increasing the shielding thickness would increase cost, weight, and required space even more than increasing the cross sections of flight tube segments. With a bigger cross section of the segments, the interaction rate of neutrons with material of the flight tube walls is decreased due to the neutron flux decrease in the outer regions of the penumbra. Hence the influence of increased cross sections of the flight tube segments on the dose rate outside the shielding was tested (this version of the flight tube is called ‘big flight tube’ in the following). No absorber masks are included in this version. The diameters of the first two segments (in beam direction) of the flight tube are chosen in a way that the outer rim of the penumbra region touches the flight tube walls only in small regions. The

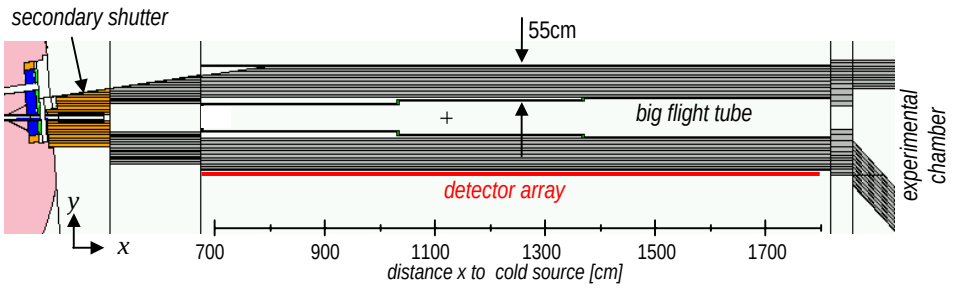

Fig. 2.176: Horizontal cut along beam axis through the Monte Carlo model of the radiation shielding version D with big flight tube. As shielding material heavy concrete type A (ρ=3.6 g/cm^3) is used. Shielding thickness is 55 cm.

diameter of the last flight tube segment could not be chosen this way due to the limited space inside the shielding. Intersection regions of the flight tube walls with the penumbra are therefore bigger than for the first two segments. The dose rates of neutron radiation and generated gamma radiation on beam axis level outside the shielding are shown in Figs. 2.173 and 2.174 (blue curves in both diagrams). Up to a distance of 14 m from the cold source the neutron dose rate and the dose rate of generated gamma radiation is decreased considerably compared to the small flight tube without absorber masks. In this region the maximal neutron dose rate is 1.9 µSv/h (40 % of the value obtained by the small flight tube) and the maximal dose rate of generated gamma radiation is 10 µSv/h (33 % of the value obtained by the small flight tube). For bigger distances to the cold source (x>14 m; location of the last flight tube segment) the dose values obtained by the big flight tube exceed the values obtained by the small flight tube because neutron radiation in the penumbra is not attenuated as much by the flight tube walls of the first two segments.

Version D with big flight tube and absorber masks

For further reduction of the dose rate of generated gamma radiation, absorber masks are included into the setup of the flight tube. The first mask (in beam direction) is identical with the mask tested with the small flight tube. It consists of boron carbide (thickness 3 cm) and is located at the beginning of the flight tube (at a distance of x=6.7 m from the cold source). Two other masks consisting of boral (thickness 3 mm) are arranged at the beginning of the second and the third segment of the flight tube (at distances x from the cold source of 10.2 m and 13.5 m; see Figs. 2.177 and 2.178). In addition several structure elements and shielding modifications were tested with this version:

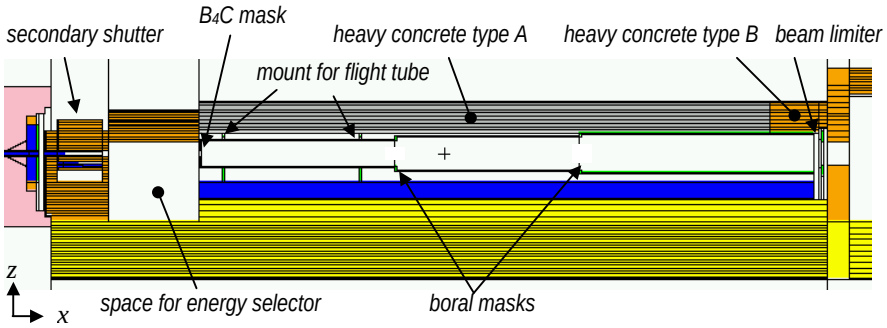

Fig. 2.177: Vertical cut along beam axis through the Monte Carlo model of the radiation shielding version D with big flight tube and absorber masks. As shielding materials heavy concrete type A (ρ=3.6 g/cm³) and heavy concrete type B (ρ=4.7 g/cm³) are used. Shielding thickness is 55 cm.

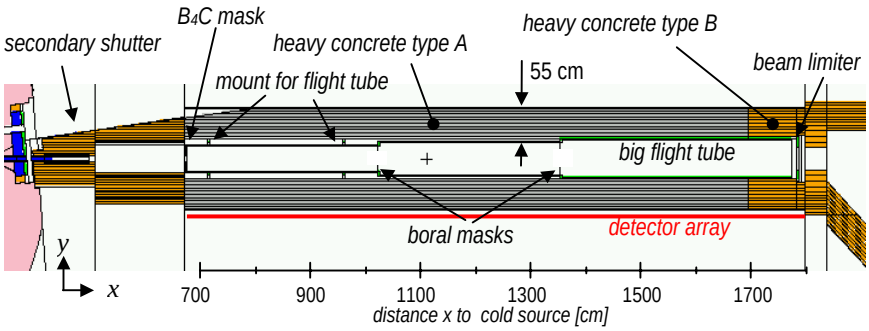

Fig. 2.178: Horizontal cut along beam axis through the Monte Carlo model of the radiation shielding version D with big flight tube and absorber masks. As shielding materials heavy concrete type A (ρ=3.6 g/cm³) and heavy concrete type B (ρ=4.7 g/cm³) are used. Shielding thickness is 55 cm.

- Mounts for the flight tube are included into the Monte Carlo model (aluminum plates of 3 cm thickness; this is a conservative assumption; the real mounts are much smaller).
- The beam limiter (see chapter 2.6) is included at the entrance window of the experimental chamber. Around the beam limiter the shielding thickness is reduced to 50 cm. This is necessary because of the size of the device.

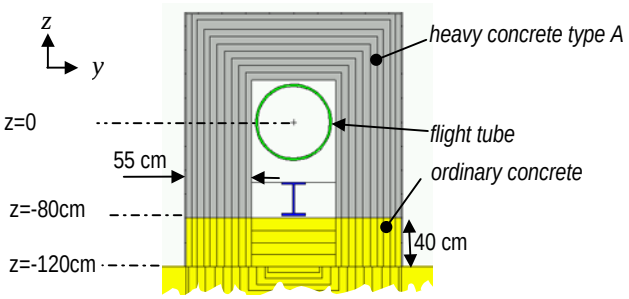

Fig. 2.179: Vertical cut at a distance x of 11 m from the cold source through the Monte Carlo model of the radiation shielding version D with big flight tube and absorber masks. As shielding materials heavy concrete type A (ρ=3.6 g/cm³) and heavy concrete type B (ρ=4.7 g/cm³) are used. Shielding thickness is 55 cm.

- In the region of the entrance window of the experimental chamber heavy concrete type B is used because of its higher gamma attenuation.
- In the lower part of the shielding walls on the left and on the right side of the flight tube, heavy concrete type A is replaced by ordinary concrete (up to a height of 40 cm above the floor level; 80 cm below beam axis; see Fig. 2.179). By this it was tested whether cost and weight of the shielding can be reduced by using heavy concrete only in regions close to the neutron beam.

The dose rates of neutron radiation and generated gamma radiation at the level of the beam axis outside the shielding are shown in Figs. 2.173 and 2.174 (violet curves in both diagrams). Dose rates of both radiation components are below the threshold value, with exception of a region close to the entrance window of the experimental chamber: The highest neutron dose rate occurs at the entrance to the experimental chamber (at a distance x=18 m from the cold source) where the shielding thickness was reduced to 50 cm for installation of the beam limiter. The dose rate of generated gamma radiation at this location shows only a slight increase (in contrast to all other versions of the arrangement inside the shielding) due to the higher attenuation power of heavy concrete type B for gamma radiation.

At locations of the boral masks (at distances x from the cold source in the interval between 10.2 m and 13.5 m) neutron dose rate peaks occur due to neutron scattering in the masks (each some 2 µSv/h). Here the neutron dose rate is even slightly increased compared to the big flight tube without masks. But the dose increase due to the boral masks is much smaller in comparison with the boron carbide mask at the beginning of the first segment of the flight tube (at a distance x of 6.7 m from the cold source). For reduction of the production of high energetic gamma radiation the boral masks are even more effective than the boron carbide mask: The dose rate of generated gamma radiation falls below 1 µSv/h with exception of the location around the boron carbide mask where scattered neutrons cause gamma production in heavy concrete. Boral masks are therefore superior to boron carbide masks.

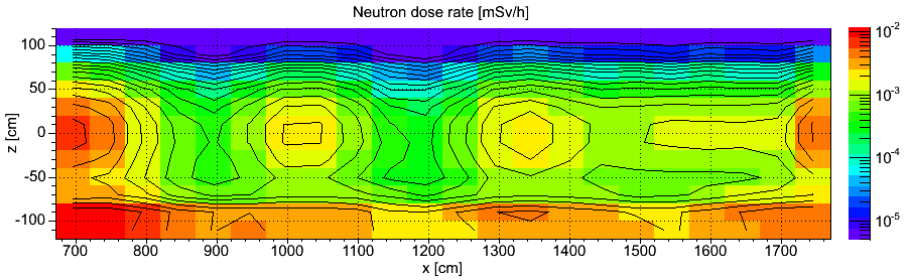

Fig. 2.180: Spatial distribution of neutron dose rate on the right side (in beam direction) of version D of the shielding for the flight tube. x is the distance from the cold source and z is the height related to beam axis level. As shielding materials heavy concrete type A (ρ=3.6 g/cm^3), heavy concrete type B (ρ=4.7 g/cm^3), and ordinary concrete (ρ=2.4 g/cm^3) are used. Shielding thickness is 55 cm. The increased dose rate below z=-80 cm is caused by transmission through ordinary concrete.

The aluminum mounts of the flight tube don't cause a significant increase in dose rates because they are outside the penumbra.

The replacement of heavy concrete type A by ordinary concrete in the side walls of the shielding above the floor causes a considerable dose increase above the floor up to a height of 40 cm (80 cm below the beam axis) as well for neutron radiation as for generated gamma radiation. The spatial neutron dose rate distribution on the right side of the shielding is shown in Fig. 2.180 and the dose rate distribution of generated gamma radiation in Fig. 2.181. Dose rates above the floor (-120 cm < z < -80 cm with z: height relative to beam axis level) even exceed the

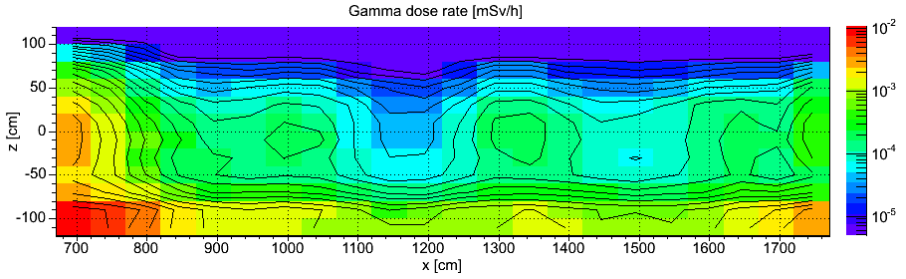

Fig. 2.181: Spatial distribution of dose rate of generated gamma radiation on the right side (in beam direction) of version D of the shielding for the flight tube. x is the distance from the cold source and z is the height related to beam axis level. As shielding materials heavy concrete type A (ρ=3.6 g/cm^3), heavy concrete type B (ρ=4.7 g/cm^3), and ordinary concrete (ρ=2.4 g/cm^3) are used. Shielding thickness is 55 cm. The increased dose rate below z=-80 cm is caused by transmission through ordinary concrete.

values at beam axis level (z=0). Above the floor, the dose rate threshold cannot be reached with ordinary concrete as shielding material. Heavy concrete has to be used everywhere as shielding material in the shielding elements around the flight tube.

Version E: Final layout

With version A to D it was shown that the intersections of the flight tube walls with the penumbra of the neutron beam cause a considerable increase of dose rate outside the shielding. Therefore a flight tube was tested that has no intersections with the penumbra. At big distances to the aperture, the neutron beam has a quadratic cross section (fully illuminated area and penumbra). Enclosing such a beam with cylindrical flight tube segments without intersections would require large diameters of the segments. In this case it would be necessary to increase the inner profile of the radiation shielding considerably. More shielding material (even if the shielding wall thickness is kept constant) and more space would be needed. In order to avoid these disadvantages, a flight tube with quadratic cross section was tested in version E. This version is the final layout of the ANTARES facility.

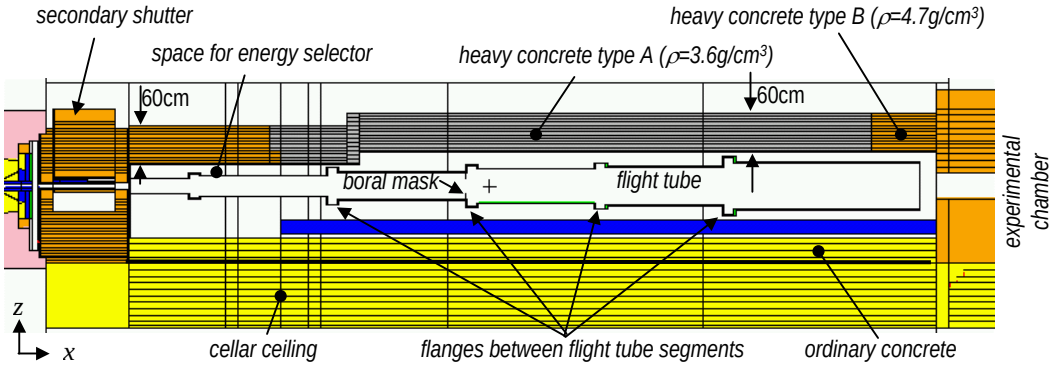

Fig. 2.182: Vertical cut along beam axis through the Monte Carlo model of version E of the shielding for the flight tube. Shielding materials are heavy concrete type A (ρ=3.6 g/cm³; displayed in grey color) and heavy concrete type B (ρ=4.7 g/cm³; displayed in orange color).

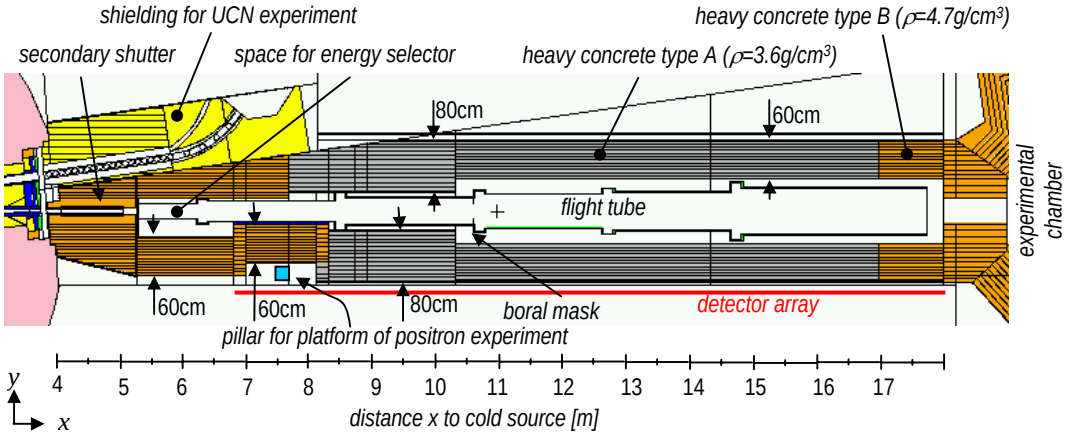

Fig. 2.183: Horizontal cut along beam axis through the Monte Carlo model of version E of the shielding for the flight tube. Shielding materials are heavy concrete type A (ρ=3.6 g/cm³; displayed in grey color) and heavy concrete type B (ρ=4.7 g/cm³; displayed in orange color).

The shielding thickness is 60 cm except for the side walls at a distance x from the cold source between 8.2 m to 10.3 m (Fig. 2.183). Here the side walls have a thickness of 80 cm. This is not for radiation protection purposes but for mechanical reasons as described in the appendix A.5 ‘Mounting the roof elements of the radiation shielding of the flight tube’. The neutron dose rate distribution on the right side (in beam direction) of shielding version E is shown in Fig. 2.185 and the dose rate of generated gamma radiation in Fig. 2.186. Neither the neutron dose rate

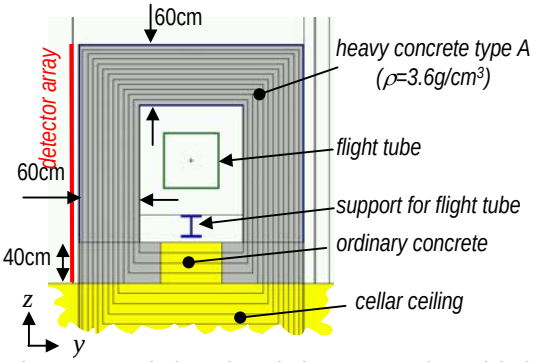

Fig. 2.184: Vertical cut through the Monte Carlo model of version E of the shielding for the flight tube at a distance x of 11 m from the cold source.

nor the dose rate of generated gamma radiation exceeds 2 µSv/h.

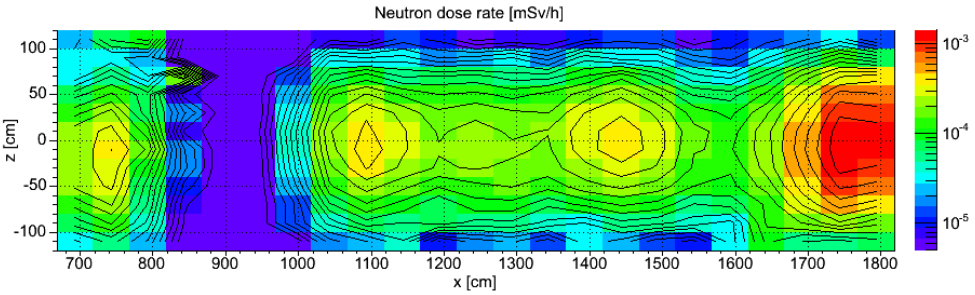

Fig. 2.185: Spatial distribution of neutron dose rate [mSv/h] on the right side (in beam direction) of the final version E of the shielding for the flight tube.

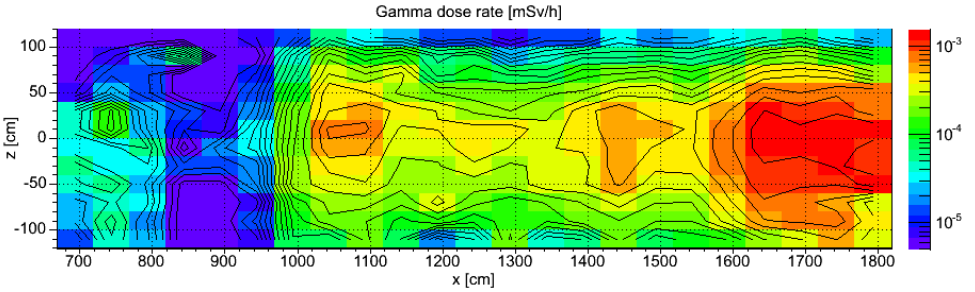

Fig. 2.186: Spatial distribution of dose rate of generated gamma radiation [mSv/h] on the right side (in beam direction) of the final version E of the shielding for the flight tube.

Dose rate contributions from all radiation components on the right side of the shielding on the level of the beam axis (where the dose rate maxima occur) are shown in Fig. 2.187. The radiation components are: neutron radiation, generated gamma radiation and primary gamma radiation. The contribution of primary gamma radiation is at least two orders of magnitude less than the total dose rate at all locations. There is a distinct minimum of dose rate between a distance of 8.2 m and 9.5 m from the cold source due to the bigger shielding thickness at this location. Small local maxima of the dose rates appear at positions of the flanges which connect the single flight tube segments. Although the flanges are outside the direct beam (no intersections with the penumbra), the dose rate is increased due to scattered neutrons that interact with the flange material (Al). The spatial flux distribution of scattered neutrons inside the shielding around the flight tube is shown in Fig. 2.48 in the chapter 2.5 ‘Flight tube’. The neutron flux around the flight tube outside the penumbra is some 10^4 $sec^{-1}cm^{-2}$.

Dose rates at beam axis level on the left side of the shielding with regard to different radiation components are shown in Fig. 2.188. The values are similar to the values on the right side, due to same shielding thickness and material. The contribution of primary gamma radiation is ommitted in this diagram: Values are as low as on the right side of the shielding.

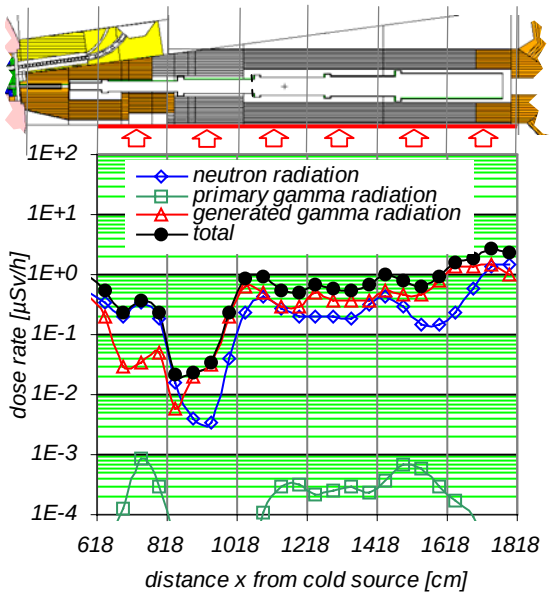

Fig. 2.187: Dose rates on the right side (in beam direction) of the shielding of the flight tube at beam axis level. Dose rates for smaller distances x from the cold source are displayed in chapter 2.10.5.2.1 'Dose rate beside the secondary shutter'.

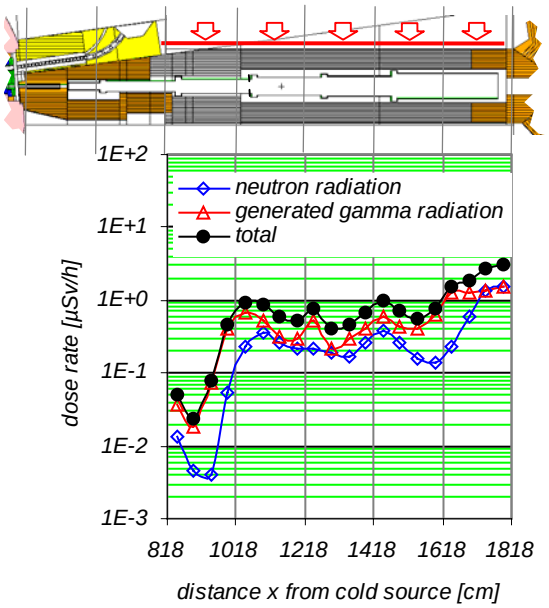

Fig. 2.188: Dose rates on the left side (in beam direction) of the shielding for the flight tube at beam axis level.

The dose rates on top of the shielding are shown in Fig. 2.189. The detector array above the shielding is not arranged directly on the outer surface of the shielding (as in the case of the detector arrays for the side walls), but at the level of the positron platform (1.98 cm above ANTARES beam axis). Due to the bigger distance between detector array and shielding, dose rates are less than at the lateral sides of the shielding, in spite of same shielding thickness and material. Dose rates were calculated for this level, because it was intended to connect two platforms of the positron experiment by a bridge (platform 1 and 2 as shown in the appendix A.5 'Mounting the roof elements of the radiation shielding of the flight tube), that would be located on this level. Therefore the dose rate at this level is of more practical interest than the dose rates in the near neighborhood of the upper shielding.

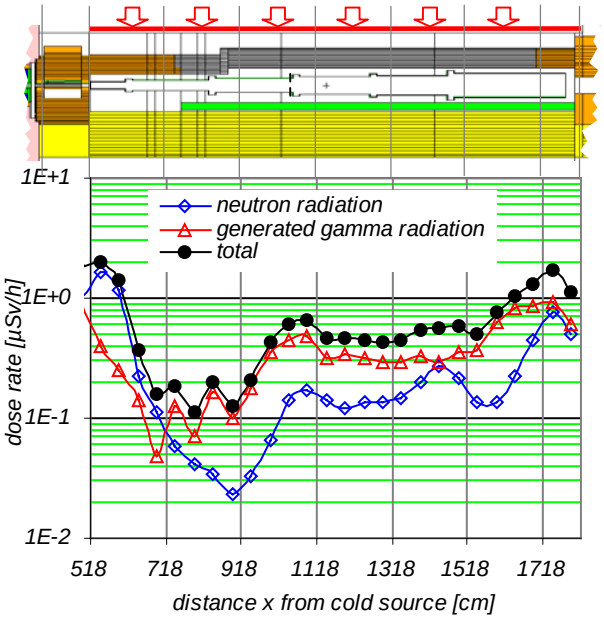

Fig. 2.189: Dose rates on top of the shielding of the flight tube above beam axis.

The influence of an absorber mask at flange position

Although the flight tube has no intersections with the penumbra, a boral mask is mounted at the flange between the third and the fourth segment (in beam direction) of the flight tube. The thickness of the boral plate is 4 mm. It covers the complete flange (Fig. 2.190). For the fully illuminated region of the neutron beam, there is a quadratic passage with a cross section of 24 cm x 24 cm. (Fig. 2.191). The mask is aimed to avoid interactions of cold and thermal neutrons emerging outside of the direct beam with the flight tube material. The source of this neutron radiation is e.g. neutron scattering in the collimator structure and in the material of the secondary shutter. As only cold and thermal neutrons are absorbed significantly, the mask is not beneficial for reduction of neutron dose rate outside the shielding. The latter is dominated by fast neutrons. The mask is useful for avoiding production of high energetic gamma radiation by capture of cold and thermal neutrons in the flight tube wall. For illustration of the effectiveness of the mask, calculations were carried out for an arrangement with mask and without mask. The results for the

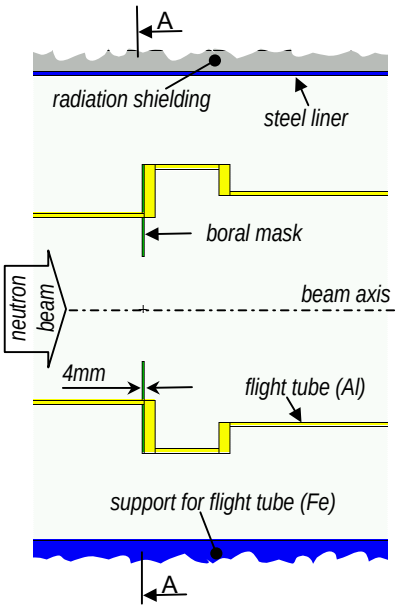

Fig. 2.190: Vertical cut through the flight tube along beam axis at a distance of 1062 cm from the cold source

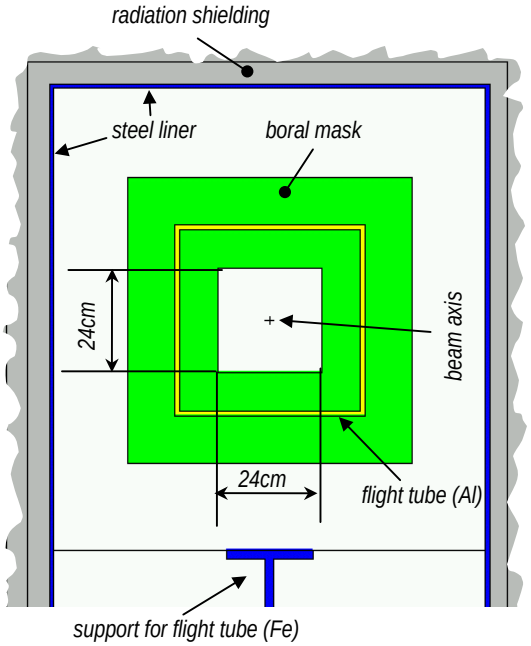

Fig. 2.191: Vertical cut through the flight tube perpendicular to beam axis at a distance of 1062 cm from the cold source (cut A-A in Fig. 2.190)

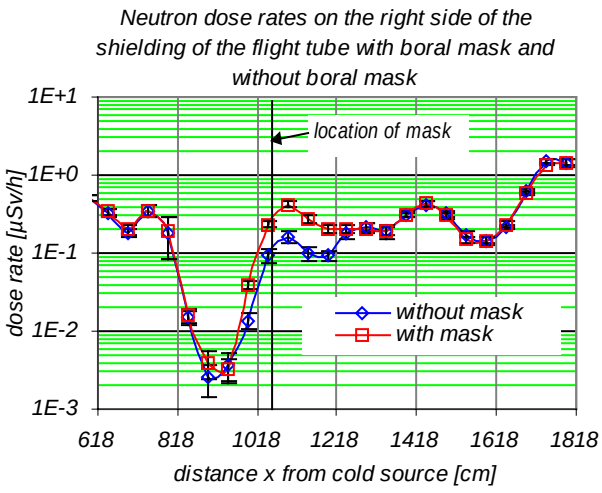

Fig. 2.192: Comparison of neutron dose rates on the right side of the shielding for the arrangements with and without boral mask

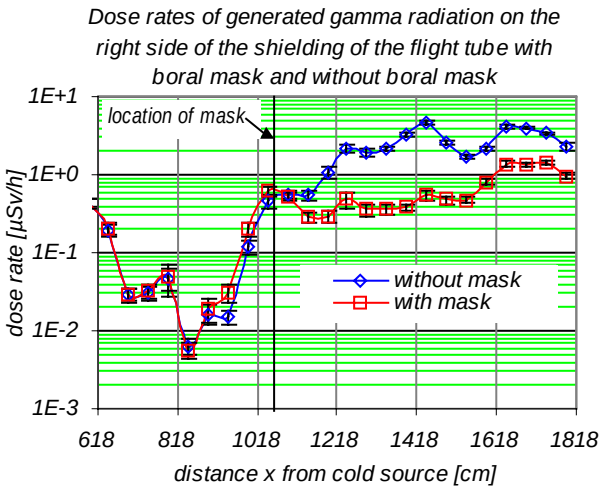

Fig. 2.193: Comparison of dose rates of generated gamma radiation on the right side of the shielding for the arrangements with and without boral mask

neutron radiation on the right side of the shielding are shown in Fig. 2.192. The neutron dose rate is slightly increased by the mask due to scattering of fast and epithermal neutrons in the mask material. The maximal dose increase of a factor of 2.5 occurs at the location of the mask (x=1062 cm). Nevertheless, the neutron dose rate (0.42 µSv/h) at this position is below the threshold. The dose increase due to the mask is limited to a distance of 1.5 m before and 1.5 m after the position of the

mask. In all other regions no influence of the mask on the neutron dose rate outside the shielding is observable.

A comparison of dose rates of generated gamma radiation outside the shielding (right side in beam direction) for the arrangements with and without the boral mask is shown in Fig. 2.193. In the whole region after the boral mask (in beam direction; x>1062 cm), the dose rate of generated gamma radiation is decreased considerably by the mask. Dose rates obtained by the arrangement with mask are reduced by factors between three and eight (depending on location) compared to the arrangement without mask. The dose rate maximum without mask (4.5 µSv/h) occurs at the flange between the fifth and sixth segment of the flight tube (at x=1443 cm), where even the desired value (2.5 µSv/h) is exceeded. Here, the boral mask decreases the dose rate of generated gamma radiation by a factor of eight to 0.55 µSv/h. For the arrangement without boral mask the generated gamma radiation delivers the dominant contribution to the total dose rate. Hence the boral mask is a very effective means for reduction of radiation level outside the shielding (see total dose rate in Fig. 2.194). In contrary to an increased shielding thickness (additional heavy concrete), the boral mask is a space saving, low cost, low weight, and 'easy to mount' solution.

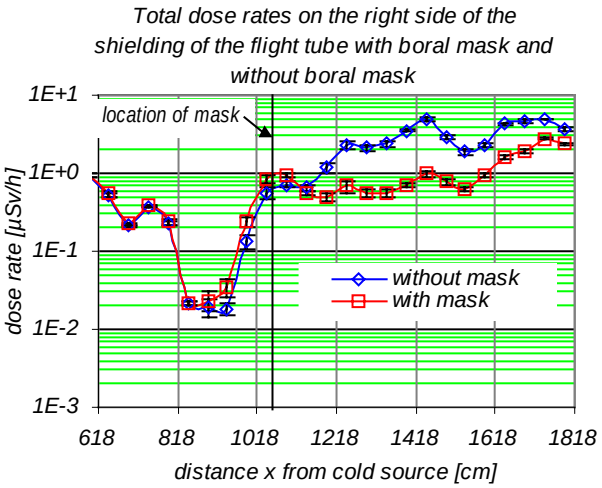

Fig. 2.194: Total dose rates on the right side of the shielding for the arrangements with and without boral mask

Contributions from different energy groups to the dose rate outside the shielding

Contributions from different energy groups to the dose rate of neutron radiation on the right side (in beam direction) of the shielding of the flight tube are shown in Fig. 2.195. The dose rate is dominated by fast neutrons with energies higher than 0.1 MeV. The contributions from neutrons in the epithermal and thermal energy regions are at least one order of magnitude below the contribution from fast neutrons.

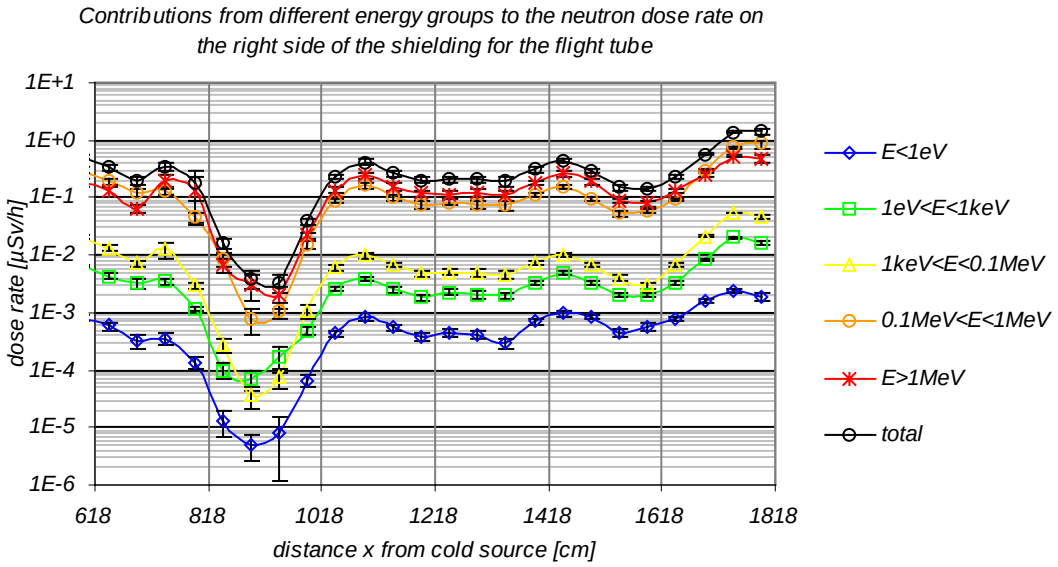

Fig. 2.195: Contributions from different energy groups to the neutron dose rate on the right side (in beam direction) of the shielding for the flight tube (final version E).

Contributions from different energy groups to the dose rate of generated gamma radiation on the right side (in beam direction) of the shielding of the flight tube are shown in Fig. 2.196. The contributions are not spread as wide as for the neutron radiation. Even gamma radiation with low energy ($E\gamma$<0.5MeV) contributes considerably to the dose rate. This energy group is populated e.g. by gamma radiation from the reaction ^{10}B(n,α)^{7}Li ($E\gamma$=0.4774MeV [43]) and by Compton scattered photons from higher energy groups.

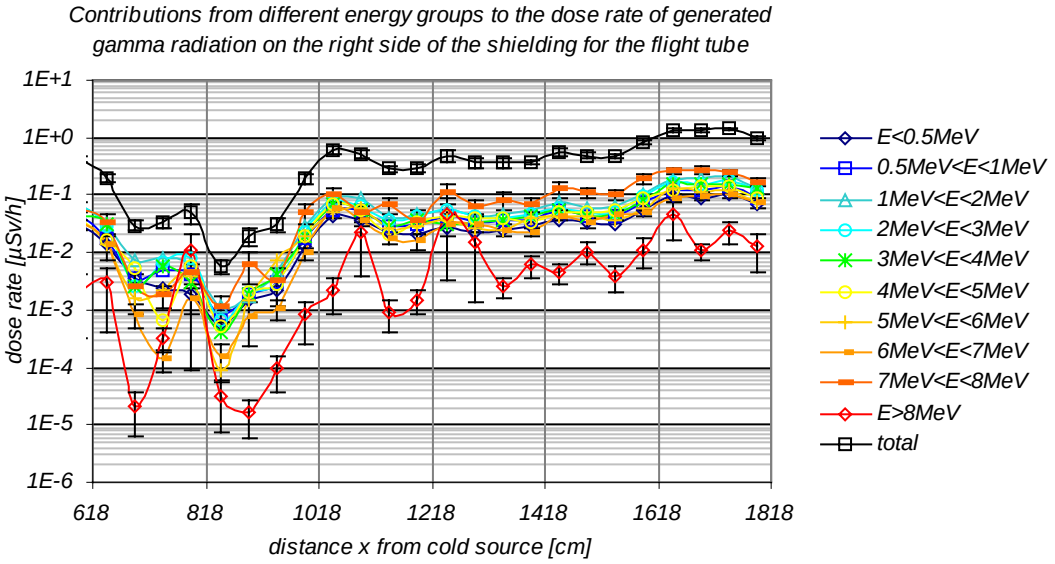

Fig. 2.196: Contributions from different energy groups to the dose rate of generated gamma radiation on the right side (in beam direction) of the shielding of the flight tube (final version E).

2.10.5.3.2 Comparison of the shielding versions

An overview of the shielding power, weight and volume of the different shielding versions of the flight tube as described in the preceding chapters is given in Fig. 2.197 to Fig. 2.200. In Fig. 2.197 the dose rate maxima of neutron radiation and generated gamma radiation are shown (the contribution of primary gamma radiation is not considered here because it is negligible compared to the other radiation components). Here only the range of heights z between –60 cm< z <60 cm is considered in order to exclude the effect of replacing heavy concrete by ordinary concrete in the side walls above the floor (-120 cm< z <80 cm) as tested with version D. The average dose rates on the outer surface of the different shielding versions are shown in Fig. 2.198. For the same reason the vertical size of the area for averaging was also limited to –60 cm< z <60 cm. The total volume and total mass of the different versions of the shielding (roof and side walls) is shown in Figs. 2.199, 2.200.

The lowest dose rate peak as well for neutron radiation as for generated gamma radiation is achieved with version B. The smallest total average dose rate (sum of neutron radiation and generated gamma radiation; 0.32 µSv/h) is also obtained by version B. But this version has the highest requirement of shielding mass (183.7 t) due to a shielding thickness of 80 cm and the application of heavy concrete type B (ρ=4.7 g/cm^3). The total shielding volume is 48.8 m^3. With version E (shielding thickness 60 cm), the average dose rate is only slightly increased (0.59 µSv/h) but it requires only a volume of 33.2 m^3 and a shielding mass of 123.4 t. This version shows even a lower total average dose rate than version A (shielding thickness 80 cm), which has a volume of 48.8 m^3 and a mass of 175.7 t. Hence by optimization of the flight tube shape and application of an absorber mask, the required volume of the shielding is decreased by 15.6 m^3 and the required mass is decreased by 52.3 t.

The radiation levels outside the shielding versions C and D are higher due to lower shielding thicknesses (55 cm) and a less optimized shape of flight tube and arrangement of absorber masks.

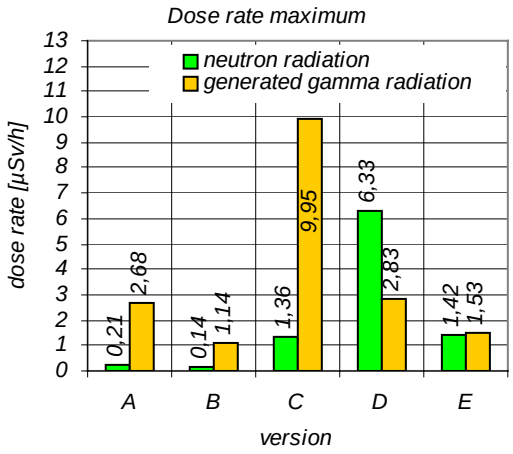

Fig. 2.197: Maxima of dose rates outside the different shielding versions for the flight tube

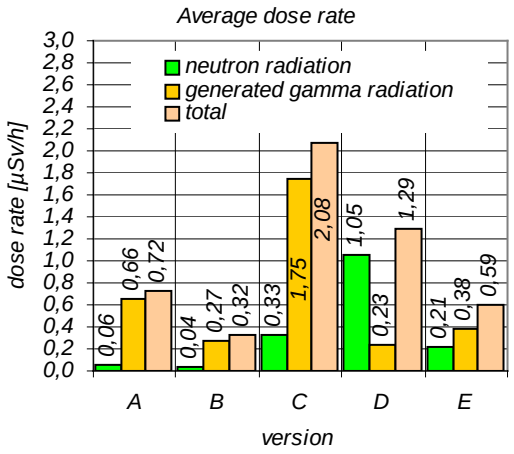

Fig. 2.198: Average dose rates outside the different versions of the shielding for the flight tube (averaged over the area 6.7m<x<18m and –0.6m<z<0.6m).

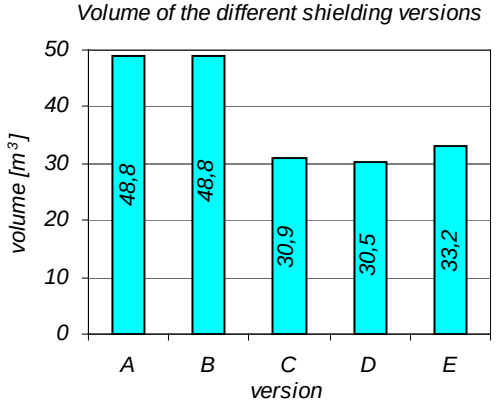

Fig. 2.199: Volumes of the different shielding versions for the flight tube

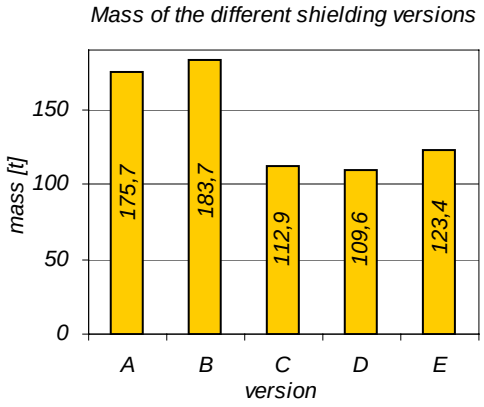

Fig. 2.200: Weights of the different shielding versions for the flight tube

2.10.5.3.3 Verification by measurements

The calculated dose rates outside the radiation shieldings were verified by measurements at the realized version of the radiation shielding (version E). Anyway, there was one difference between real arrangement and version E: Instead of the boral mask for the flight tube, a mask of pure polyethylene (thickness 2 cm) was used (during the assembly of the facility temporarily no boral was commercially available). This mask was replaced by a boral mask after the first reactor cycle. The production of high energetic gamma radiation by neutron capture in hydrogen (E_γ=2.2 MeV [43]) is increased considerably by the mask. Measured and calculated dose rates of gamma radiation on the right side of the shielding of the flight tube are shown in Fig. 2.201. The reactor power was 20 MW and the L/D=400 collimator was inserted for both calculation and measurement. As gamma detector the dosimeter automess 6150 AD6 [50] was used. The green curve in Fig. 2.201 shows the Monte Carlo data and the red marks represent the measured data. A distinct peak occurs around the location of the mask at a distance x of 1060 cm from the cold source. Good agreement between measured and calculated data is found, especially in regions of high dose rate. In regions of low dose rates (below 1 µSv/h), high fluctuations occurred during the measurement. This is due to the low count rate (see confidence intervals in Fig. 2.201).

Comparison of Monte Carlo data with measured data for the dose rate of gamma radiation on the right side (in beam direction) of the radiation shielding for the flight tube

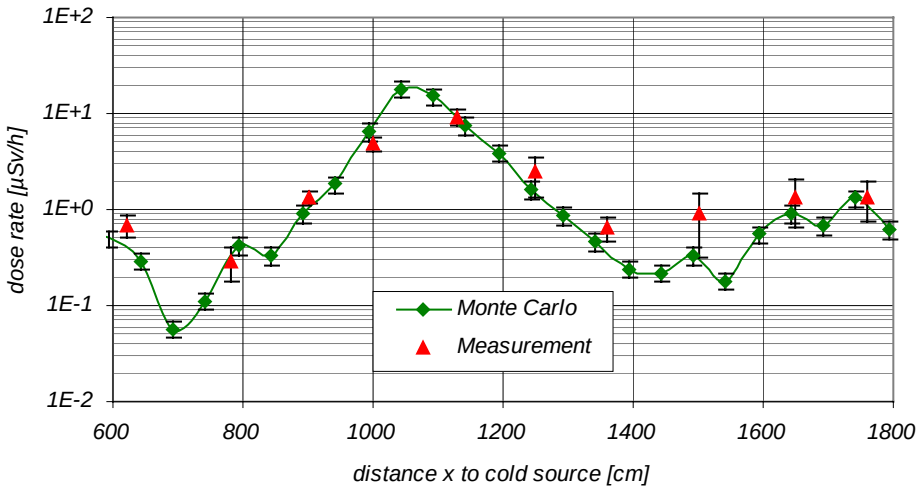

Fig. 2.201: Comparison of Monte Carlo data with measured data for the dose rate of gamma radiation on the right side (in beam direction) of the radiation shielding for the flight tube

A comparison of measured and calculated neutron dose rate is shown in Fig. 2.203. The green curve shows the calculated data, the red marks the measured data. The measurement was carried out by help of the FHT751 Biorem dosimeter [51]. This dosimeter consists of a BF_3 counter tube that is surrounded by a polyethylene cylinder for moderation of fast and epithermal neutrons. The cylinder has a diameter of 20 cm (the dosimeter is described in more detail in the appendix A.7 'Response function of a neutron detector'). In contrast to the data of the Monte Carlo calculation, where the dose rate is calculated directly on the outer surface of the shielding, the measured dose rate data represents the average value of the whole dosimeter volume. Hence, the measured data are related to a bigger distance from the shielding and comprise information from a more extended region due to scattered neutrons impinging the dosimeter on the sides as illustrated in Fig. 2.202, i.e. the measured data is blurred in the spatial domain. Especially dose rates in regions with big radiation gradients and sharp local minima and maxima are not resolved correctly by the measurement. The measured data can therefore not be compared directly to the Monte Carlo data. For better comparability, the Monte Carlo data were blurred in the spatial domain, too. The neutron

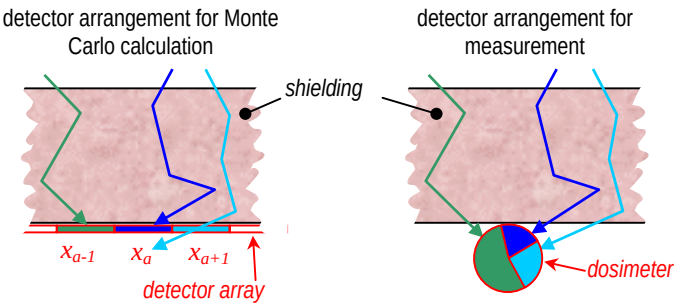

Fig. 2.202: Comparison of the detector arrangements for Monte Carlo calculations and measurements

dose rate $D(x_a)$ in a detector cell that has its center at a distance x_a to the cold source was merged with the data from the neighboring detector cells in the following way:

$$D(x_a) = 0.125 \cdot D(x_{a-2}) + 0.21875 \cdot D(x_{a-1}) + 0.3125 \cdot D(x_a) + 0.21875 \cdot D(x_{a+1}) + 0.125 \cdot D(x_{a+2}) \quad (2.12)$$

The result is shown as blue curve (*Monte Carlo blurred*) in Fig. 2.203. This smoothed data fits the measured data better than the unprocessed Monte Carlo data, especially at the local minimum at a distance of x=900 cm from the cold source. A difficulty during the measurement was the high fluctuation rate of values due to the low count rate. Fluctuations were at about a factor of two. Hence, the confidence intervals of the measurements are rather extensive (Fig. 2.203).

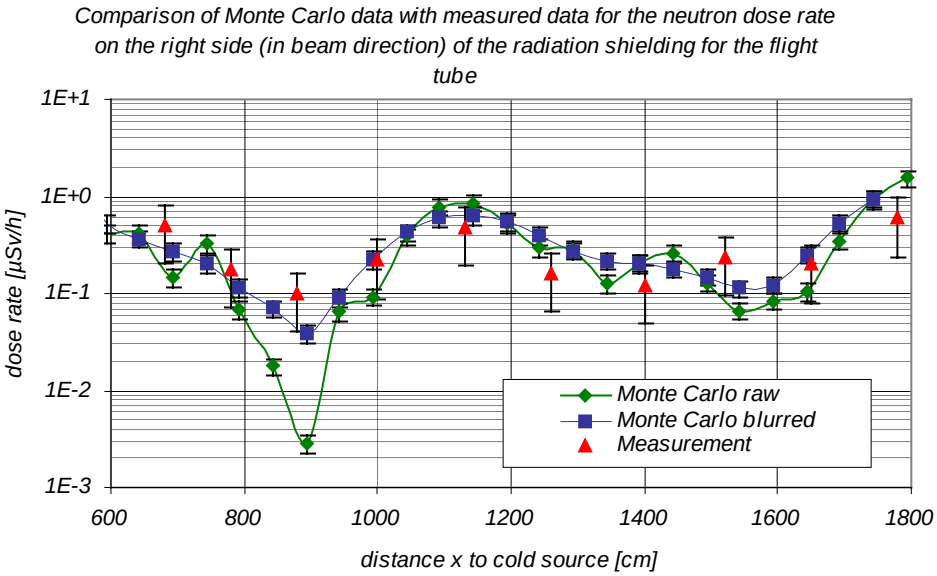

Fig. 2.203: Comparison of Monte Carlo data with measured data for the dose rate of neutron radiation on the right side (in beam direction) of the radiation shielding for the flight tube

2.10.5.4 Radiation shielding for the experimental chamber

2.10.5.4.1 Radiation levels outside the shielding without specimen

Interactions of neutrons in the penumbra of the beam with material of small structure elements have a noticeable issue on the dose rate outside the shielding (as shown in the preceding chapters). This is due to neutron scattering and even more to high energetic gamma radiation produced by neutron capture. The setup of the flight tube and its surrounding is fixed and will not be changed in the near future. This does not hold for the arrangement inside the experimental chamber, where specimens are exposed to the direct neutron beam (fully illuminated area). Materials and sizes of the specimens are not known in advance, hence gamma production and neutron scattering inside the experimental chamber are variable. Therefore the shielding must be designed in a conservative way. It has to be expected that an irradiated specimen increases the dose outside the experimental chamber due to scattering and gamma production. Therefore the dose rate without a specimen has to be considerably below the given dose rate threshold. As shielding material heavy concrete type B (ρ=4.7 g/cm^3) is used because of its higher gamma attenuation due to the higher steel content compared to heavy concrete type A (ρ=3.6 g/cm^3).

The advantage of a LiF-beam catcher with regard to the beam quality at detector position is shown in chapter 2.7 ‘Experimental chamber’: Less scattered cold and thermal neutrons and smaller flux of generated gamma radiation. This beam catcher is not only beneficial for background reduction at detector position but also for the reduction of dose rate of generated gamma radiation outside the experimental chamber. Cold and thermal neutrons are captured in lithium without production of gamma radiation. As 91 % of all neutrons are in the energy range below 1 eV, the dose rate of generated gamma radiation is decreased considerably by the beam catcher. This is illustrated by the

spatial distributions of dose rates of generated gamma radiation in a horizontal plane at beam axis level through two different versions of the experimental chamber:

- The shielding walls are covered by steel liners, no beam catcher is used (see chapter 2.7 ‘Experimental chamber’; version B).
- The steel liners of the shielding walls are covered by boron carbide rubber mats and a LiF beam catcher is applied (see chapter 2.7 ‘Experimental chamber’; version E).

The dose rate distribution for the experimental chamber without beam catcher (version B) is shown in Fig. 2.204 and the distribution for the experimental chamber with LiF beam catcher is shown in Fig. 2.205. Without the beam catcher (version B), the maximal dose rate of generated gamma radiation outside the shielding is 0.7 µSv/h. The LiF beam catcher reduces the dose rate of generated gamma radiation at the same position by more than a factor of ten down to 0.06 µSv/h. The total dose rate is not decreased as much, since the influence of the beam catcher on fast neutron radiation and primary gamma radiation is rather low.

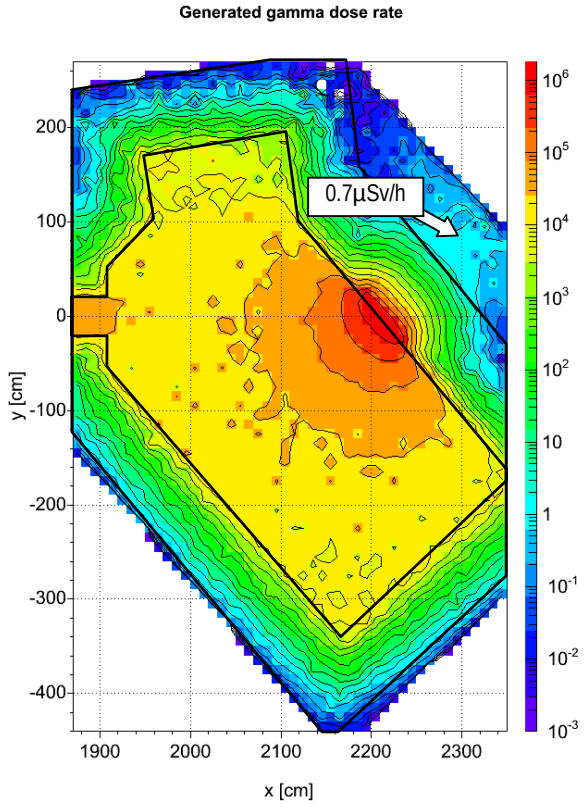

Fig. 2.204: Spatial dose rate distribution of generated gamma radiation in a horizontal plane at beam level through the experimental chamber with steel liners but without beam catcher (chapter 2.7 ‘Experimental chamber‘, version B).

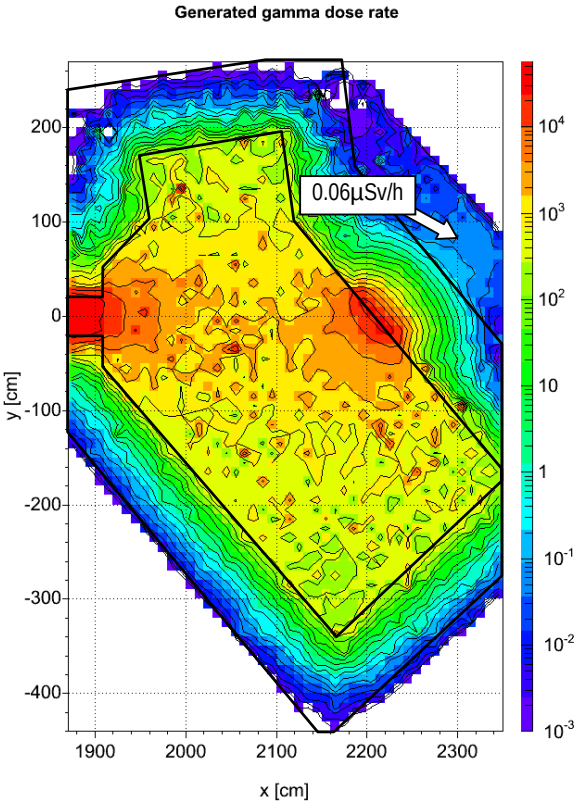

Fig. 2.205: Spatial dose rate distribution of generated gamma radiation in a horizontal plane at beam level through the experimental chamber with boron carbide rubber mats, steel liners, and LiF beam catcher (chapter 2.7 ‘Experimental chamber’, version E).

Several different shielding arrangements of the experimental chamber were tested by calculation. A horizontal cut through one of the Monte Carlo models of the experimental chamber is shown in Fig. 2.206. A vertical cut is shown in Fig. 2.207. The thicknesses of shielding walls correspond to the final version: The side walls have a thickness of 80 cm except for the wall that faces the direct beam (wall A in Fig. 2.206). Wall A has a thickness of 90 cm. The roof of the experimental chamber has a thickness of 60 cm. Contrary to the final inner arrangement of the experimental chamber, the beam catcher, steel liners and boron carbide rubber mats are not included in this model in order to get a conservative estimate for the radiation outside the shielding (this version corresponds to model version A in chapter 2.7 'Experimental chamber').

The spatial dose rate distributions outside the shielding walls are shown in the following.

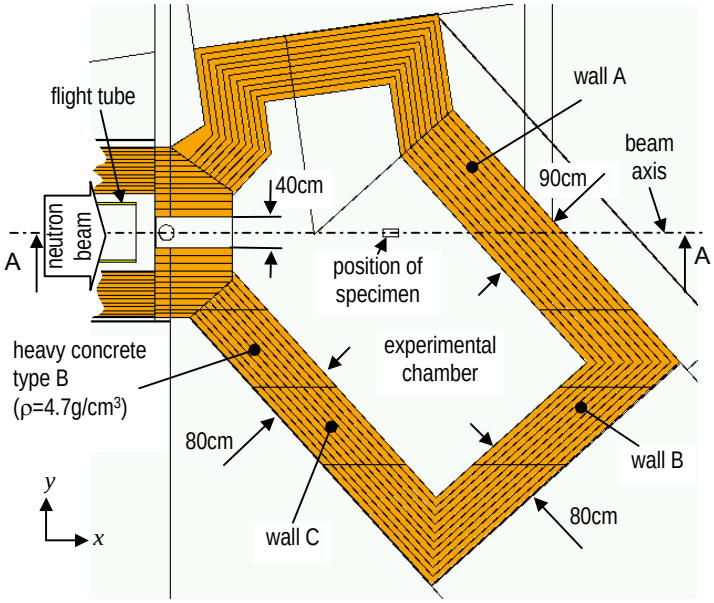

Fig. 2.206: Horizontal cut at beam axis level through the Monte Carlo model of the experimental chamber

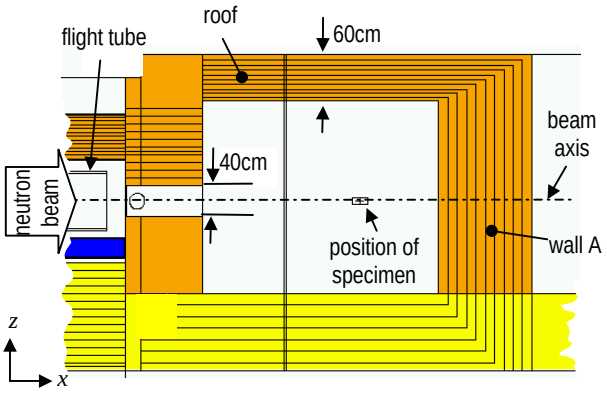

Fig. 2.207: Vertical cut along beam axis (cut A-A in Fig. 2.206) through the Monte Carlo model of the experimental chamber

Dose rates outside wall A

The spatial dose rate distribution outside shielding wall A was calculated in a plane parallel to the outer surface of wall A (red line in the horizontal cut in Fig. 2.208) with a spatial resolution of 20 cm x 20 cm. The distance between outer surface and detector plane is 89 cm. This distance was chosen because there is an accessible passage between the wall of the reactor hall and the ANTARES shielding.

The neutron dose rates in the plane are shown in Fig. 2.209. The maximal neutron dose rate is 0.9 µSv/h. The peak is not located on the beam axis but it is shifted to the left (in beam direction). This shift is because the neutron beam impinges the shielding wall A not perpendicular but with an angle of 48° (Fig. 2.208).

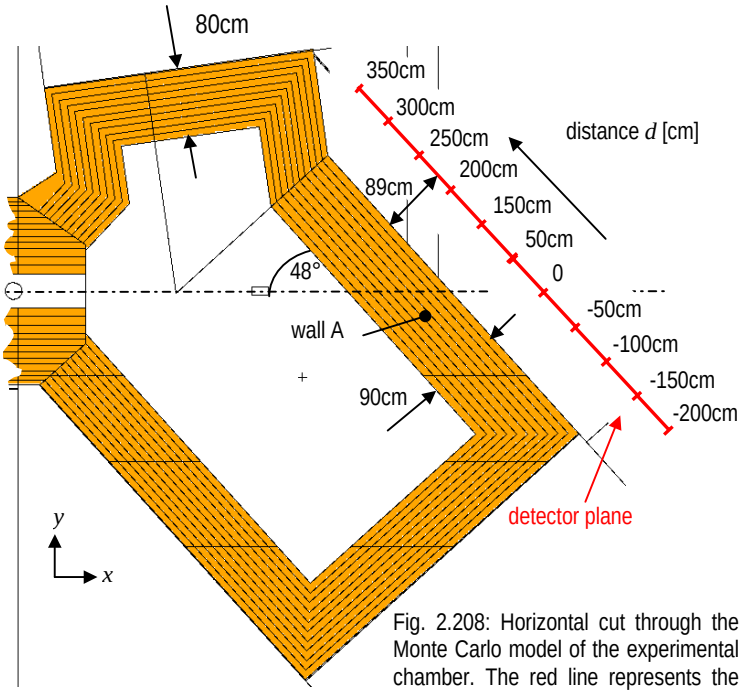

Fig. 2.208: Horizontal cut through the Monte Carlo model of the experimental chamber. The red line represents the detector plane

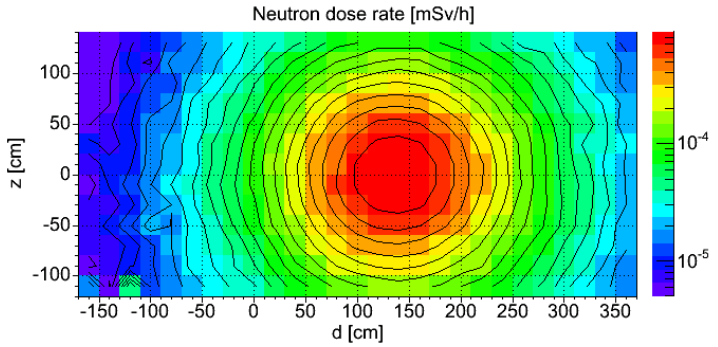

Fig. 2.209: Spatial distribution of the neutron dose rate [mSv/h] outside of the shielding wall A. z is the height relative to the beam axis level and d is the distance as shown in Fig. 2.208.

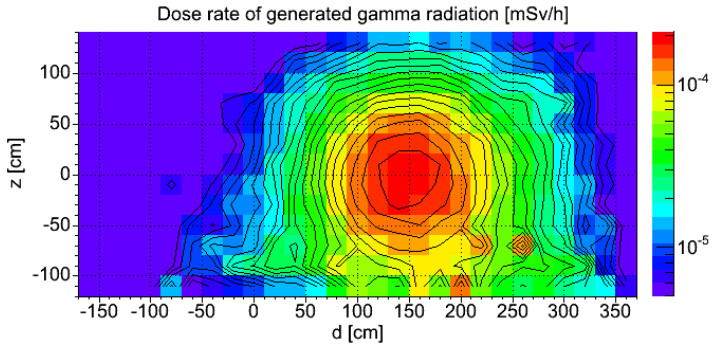

Fig. 2.210: Spatial distribution of the dose rate [mSv/h] of generated gamma radiation outside of the shielding wall A. z is the height relative to the beam axis level and d is the distance as shown in Fig. 2.208.

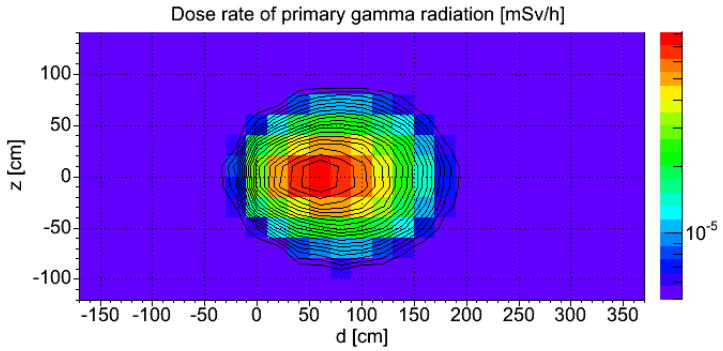

Fig. 2.211: Spatial distribution of the dose rate [mSv/h] of primary gamma radiation outside of the shielding wall A. z is the height relative to the beam axis level and d is the distance as shown in Fig. 2.208.

The smallest path length through shielding material is not obtained for a path that is parallel to the beam axis but for a path that is rotated 42° to the left (in beam direction).

The distribution of the dose rate of generated gamma radiation is shown in Fig. 2.210. The peak value occurs at the same location as the neutron peak. The maximal value is 0.2 µSv/h (This value is smaller than that one in Fig. 2.204 because no steel liners are used). By application of a beam catcher even smaller dose rates of generated gamma radiation can be obtained.

The dose rate of the primary gamma radiation is shown in Fig. 2.211. The maximal value is 0.08 µSv/h. The peak is not located at the same position as the peaks of neutron dose rate and of generated gamma dose rate. It is not shifted as much from the beam axis and the width of the peak is much smaller compared to the other radiation components. This is caused by the directional distribution of Compton scattering: Small scatter angles (relating to incident direction) are more probable for high energetic gamma radiation (E_γ >1 MeV). For lower energies (E_γ <1 MeV), scattering in forward direction is less pronounced. The contribution of gamma radiation in low energy groups to the dose is low because of higher attenuation.

Dose rates outside wall B

Wall B (Fig. 2.212) of the experimental chamber has a thickness of 80 cm. The dose rate outside of wall B was calculated for a plane adjacent to the outer surface of the shielding wall (red line in Fig. 2.212). The spatial resolution in the plane is 40 cm x 40 cm for the calculation. The distribution of neutron dose rate in the plane is shown in Fig. 2.213. The coordinates in this plot are the height z relative to the beam axis and d the distance from the outer corner between wall B and wall C. In contrast to wall A, where a small area of 40 cm x 40 cm is exposed to the direct beam with nearly parallel directional distribution, wall B is exposed more homogeneously to scattered neutrons with a higher divergence of flight paths. Hence, the radiation distribution outside wall B is more homogeneous. The highest neutron dose rate occurs near the floor (-120 cm< z <80 cm) and not at the level of the beam axis. This is caused by transmission of neutron radiation through the ceiling of the basement. The ceiling is made from ordinary concrete. However, the maximal dose rate (0.13 µSv/h) does not exceed the dose rate threshold.

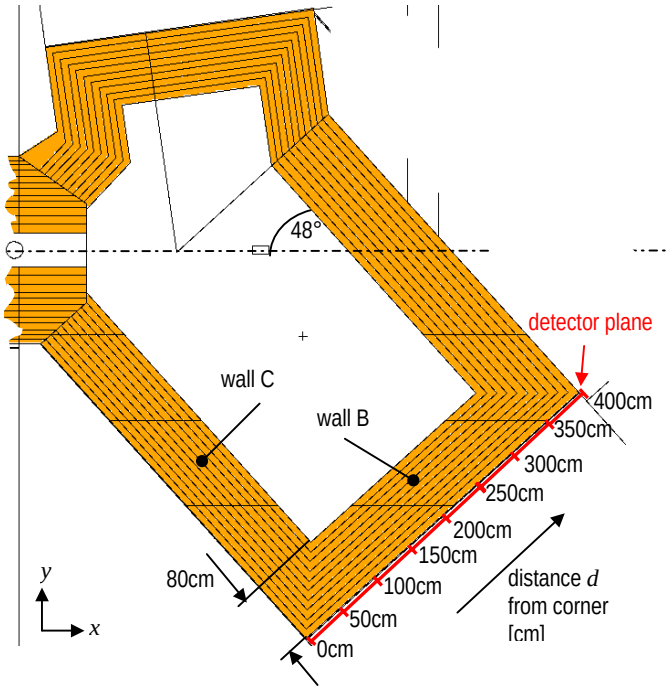

Fig. 2.212: Horizontal cut through the Monte Carlo model of the experimental chamber. The red line is the detector plane

The spatial distribution of generated gamma radiation outside wall B is shown in Fig. 2.215. The distribution is similar to that of neutron radiation. Again, the maximal dose rate occurs near the floor (-120 cm< z <80 cm). This is caused by neutron capture in the ordinary concrete of the ceiling of the basement. Although the maximal dose rate of generated gamma radiation is even higher than the maximum dose rate of neutron radiation, the dose rate threshold is not exceeded.

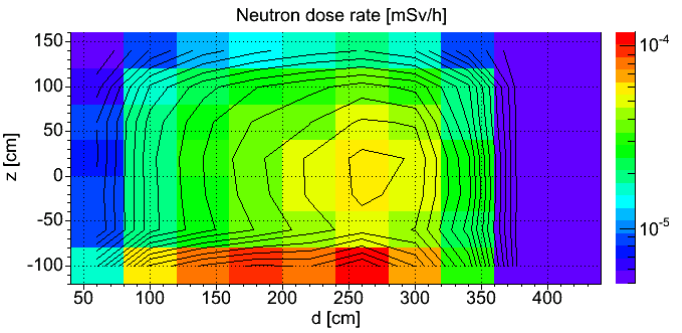

Fig. 2.213: Spatial neutron dose rate distribution [mSv/h] outside of wall B. d is the distance to the corner between wall B and wall C and z is the height related to the beam axis.

An additional step was added at the bottom of the shielding elements of the side walls (see illustration Fig. 2.214). Beside the reduction of

radiation transmission through the ceiling of the basement, this additional step has two other desired issues:

- The weight of the shielding is distributed to a bigger area of the floor.
- The mechanical stability of the shielding structure is increased.

The dose rate of primary gamma radiation outside wall B of the shielding is negligible compared to the other radiation components.

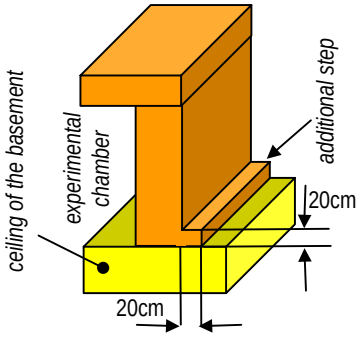

Fig. 2.214: Additional step at the bottom of the shielding elements of the lateral walls of the experimental chamber.

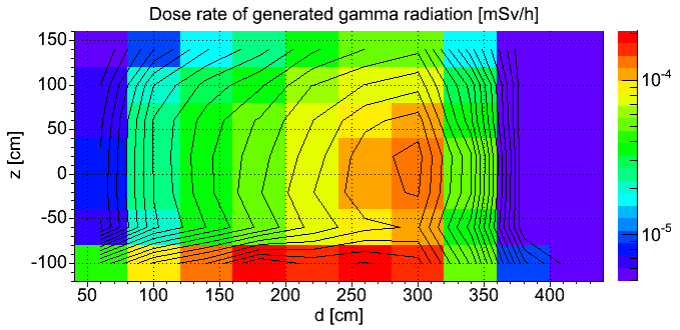

Fig. 2.215: Spatial dose rate distribution of generated gamma radiation [mSv/h] outside wall B. d is the distance to the corner between wall B and wall C and z is the height relative to the beam axis.

Dose rates outside wall C

Wall C (Fig. 2.216) of the experimental chamber has also a thickness of 80 cm. The spatial dose rate distribution outside wall C was calculated in a plane adjacent to the outer surface of the shielding wall (red line in Fig. 2.216) with a resolution of 40 cm x 40 cm. The neutron dose rate is shown in Fig. 2.217. The coordinates in the plot are the height z relative to the beam axis and the distance d to the outer corner between wall B and wall C (at the bottom of Fig. 2.216). The maximum dose rate occurs close to the entrance window (d=400 cm) of the neutron beam. This is due to scattered neutrons from the direct beam. A dose increase close to the floor is observable due to the transmission through the ordinary concrete of the ceiling of the basement. An additional step as described in the previous chapter (see Fig. 2.214) is therefore also applied to wall C (the step is not included in the Monte Carlo model).

The spatial distribution of generated gamma radiation is shown in Fig. 2.218. Similar to the neutron dose rate, the dose rate of generated gamma radiation increases with increasing distance d from the corner between wall B and wall C, due to decreasing distance to the entrance window for the neutron beam. The maximal dose occurs above the ceiling of the basement because of neutron capture in ordinary concrete.

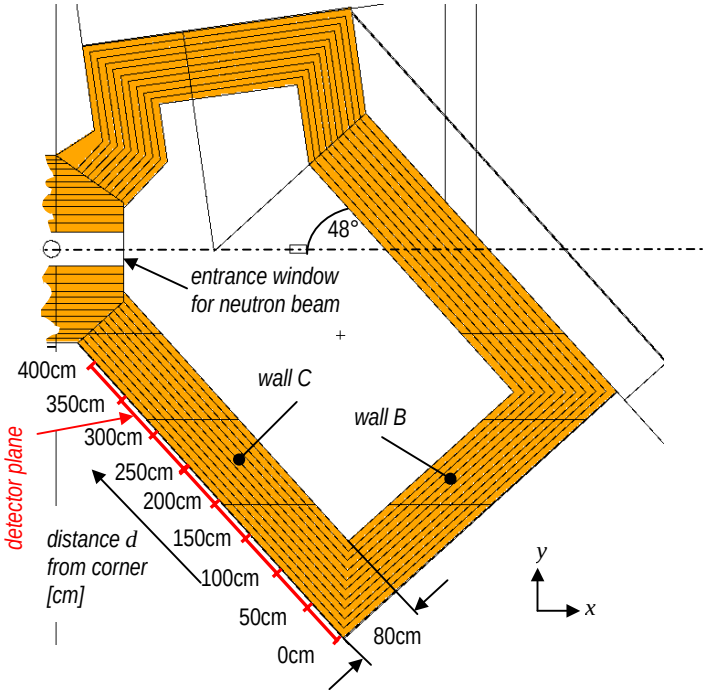

Fig. 2.216: Horizontal cut through the Monte Carlo model of the experimental chamber. The red line is the detector plane

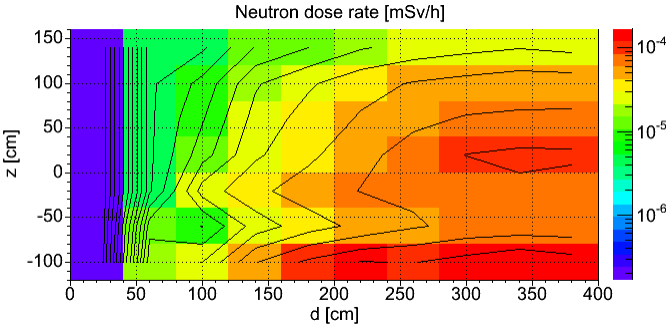

Fig. 2.217: Spatial distribution of neutron dose rate [mSv/h] outside wall C

Dose rates on top of the experimental chamber

The roof of the experimental chamber has less thickness than the lateral walls (thickness of the roof: 60 cm). The resulting higher radiation level on the roof is not disturbing as no other experiments are located on top of the experimental chamber and access to the roof is not intended. If necessary, the attenuation of the radiation shielding can be simply increased by placing layers of borated polyethylene and lead on the roof. However, from the point of view of radiation protection, the dose rate threshold on top of the roof is not exceeded.

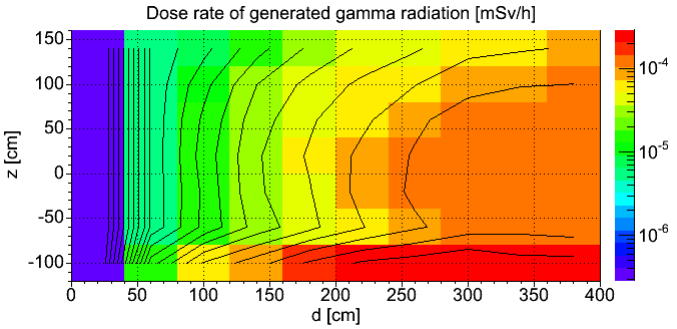

Fig. 2.218: Spatial distribution of dose rate of generated gamma radiation [mSv/h] outside wall C

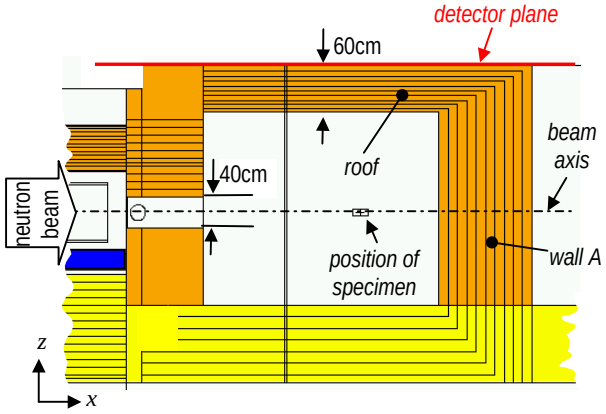

Fig. 2.219: Vertical cut along beam axis (cut A-A in Fig. 2.206) through the Monte Carlo model of the experimental chamber

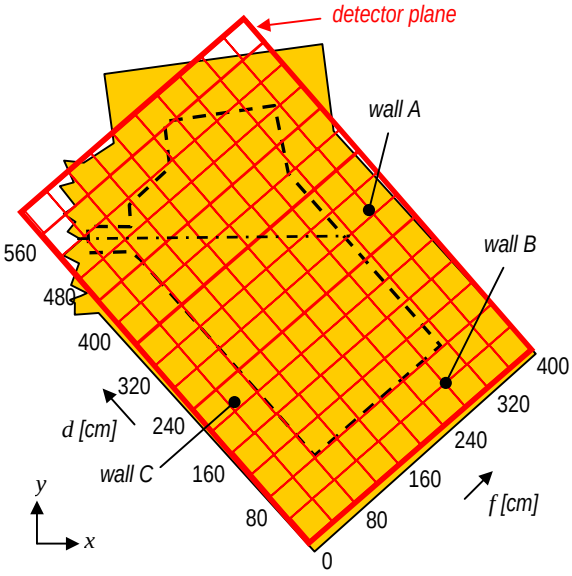

Fig. 2.220: Detector plane on top of the experimental chamber

The spatial distribution of the dose rate on top of the experimental chamber was calculated in a plane adjacent to the upper surface of the roof (see Figs. 2.219 and 2.220). The spatial resolution for the calculation was 40 cm x 40 cm. Positions in the plane are defined by the coordinates d and f as shown in Fig. 2.220. The origin of the coordinate system is the outer corner between wall B and wall C.

The spatial neutron dose rate distribution is shown in Fig. 2.221. The maximal dose rate occurs directly above the position where the direct beam impinges on wall A. The peak value is 1.3 µSv/h. If neutron dose rates below 1 µSv/h should be necessary for special purposes, it is sufficient to cover an area of about 1.5 m x 1.5 m by an additional polyethylene layer.

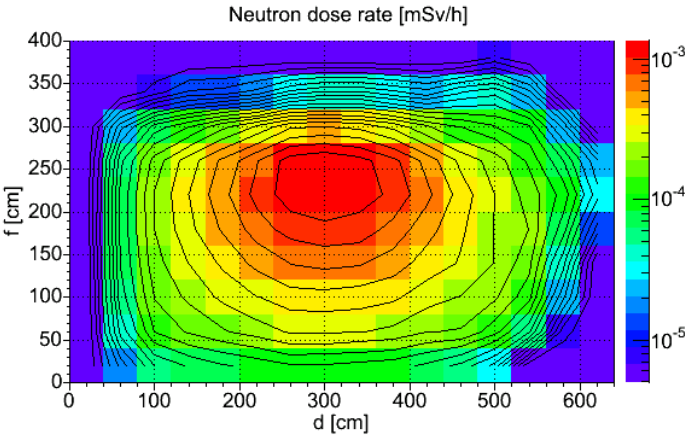

Fig. 2.221: Spatial distribution of neutron dose rate [mSv/h] on top of the experimental chamber

The spatial distribution of dose rate of generated gamma radiation on top of the experimental chamber is shown in Fig. 2.222. The distribution is similar to the neutron dose rate distribution. The peak value (3 µSv/h) is about two times higher than that of the neutron dose rate. This relatively high value is caused by the superposition of generated gamma radiation from the roof and from wall A. Application of a beam catcher reduces the contribution from wall A considerably. Hence, the displayed values are a conservative estimate of dose rates. Even without beam catcher the dose rate threshold from the point of view of radiation protection is not exceeded.

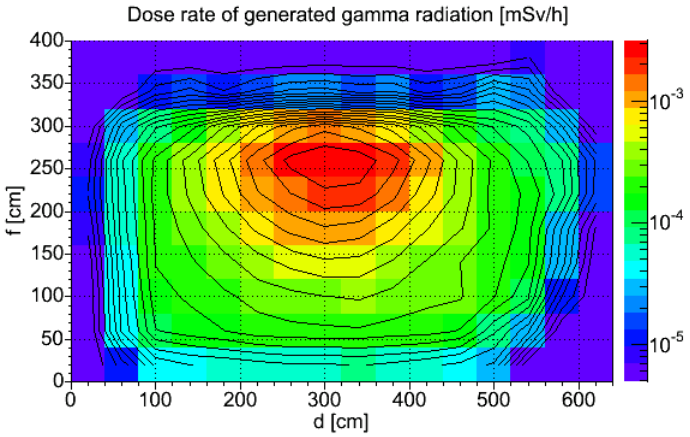

Fig. 2.222: Spatial distribution of dose rate of generated gamma radiation [mSv/h] on top of the experimental chamber

2.10.5.4.2 Influence of the specimen on the radiation levels

The specimen inside the experimental chamber becomes a source of scattered neutrons and generated gamma radiation when irradiated with the neutron beam. The influence of a specimen on the radiation levels was tested with a cubic object. The cube has a size of 20 cm x 20 cm x 20 cm and its center is located on the beam axis. The distance from the cold source is 21 m. Its position inside the experimental chamber is shown in Fig. 2.223. The flux and the dose rate of scattered neutrons and generated gamma radiation from the specimen strongly depend on the composition of the investigated object. As an example for a specimen with a high elastic neutron cross section polyethylene was chosen as cube material because of its big hydrogen content. Hydrogen becomes a source of 2.2 MeV gamma radiation when irradiated with neutrons [43] due to the H(n,γ)D reaction. As an example for objects with high inelastic neutron cross section, a cube consisting of iron was also considered. Gamma radiation from neutron capture in iron has energies up to 7.7 MeV [43]. The spatial distributions of neutron and generated gamma radiation were calculated in a horizontal cut through the experimental chamber. The section of the plane for which the dose rate distributions are displayed in the following diagrams is shown in Fig. 2.223. Calculations were carried out for both specimen, the iron cube and the polyethylene cube. In all cases the data refer to the L/D=400 collimator/aperture setup and a reactor power of 20 MW. The setup of the experimental chamber corresponds to version D as shown in the chapter 2.7 ‘Experimental chamber’ (realized version). The walls of the chamber consist of heavy concrete type B (ρ=4.7 g/cm^3). All shielding elements are covered by steel liners. The steel liners inside the chamber are covered by boron carbide rubber mats and a LiF beam catcher is located in front of wall A (Fig. 2.52a).

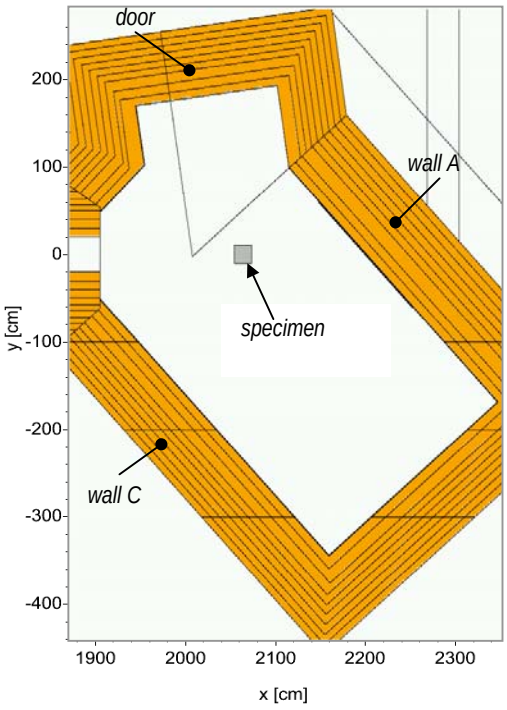

Fig. 2.223: Horizontal cut at the level of the beam axis through the Monte Carlo model of the experimental chamber with specimen. The specimen is a cube with a volume of 20 cm x 20 cm x 20 cm. The dose rate distributions in this plane are shown below.

Neutron dose rate

The spatial distribution of neutron dose rate in the horizontal plane (Fig. 2.223) through the experimental chamber without specimen is shown in Fig. 2.224. The neutron dose rate distribution with the specimen from polyethylene is shown in Fig. 2.225. The dose rates at location of the specimen and its surrounding are increased due to scattering in the specimen. However, the transmission through the shielding walls is only slightly increased at position I (outside wall C) and position II (outside door). Same is true when the iron cube is used as specimen. The neutron dose rate distribution when the iron cube is located in the experimental chamber as specimen is shown in Fig. 2.226. Transmission through the shielding walls is dominated by fast neutrons. Due to scattering in the specimen, a lower amount of neutrons is scattered in wall A of the experimental chamber (absorption in the beam catcher is only effective for neutrons in the cold and thermal energy region). Hence including a specimen causes a spatial shift of the source of fast scattered neutrons, but does not increase the average neutron dose rate outside the shielding significantly. The slight increase at positions I and II is due to this shift: The specimen (source of scattered neutrons) is closer to position I and position II than the center of neutron scattering in wall A. Despite the dose increase at certain positions, the desired dose rate level is not exceeded at any position.

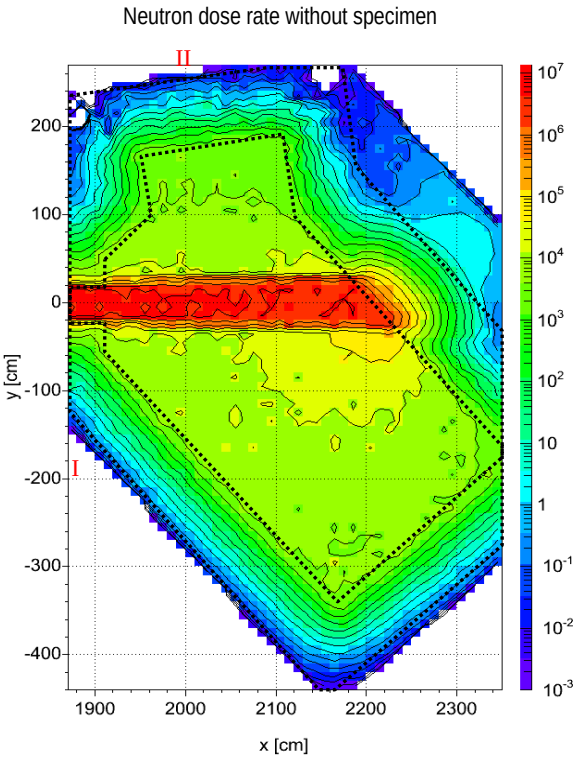

Fig. 2.224: Spatial distribution of neutron dose rate [µSv/h] in a horizontal plane at level of the beam axis through the experimental chamber without specimen.

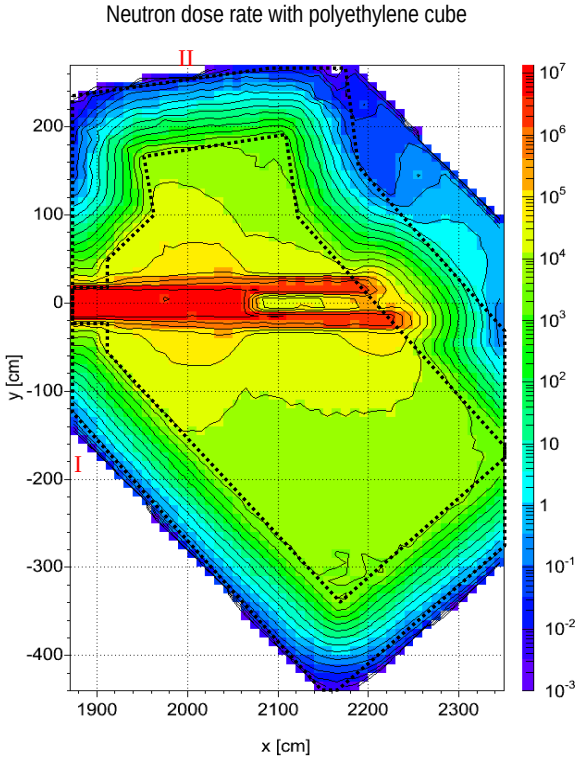

Fig. 2.225: Spatial distribution of neutron dose rate [µSv/h] in a horizontal plane at level of the beam axis through the experimental chamber with a cube of polyethylene as specimen.

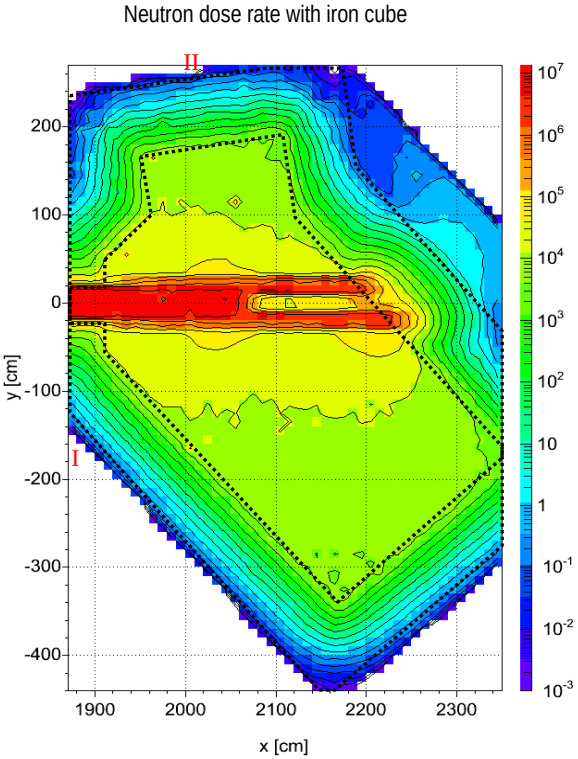

Fig. 2.226: Spatial distribution of neutron dose rate [µSv/h] in a horizontal plane at level of the beam axis through the experimental chamber with a cube of iron as specimen.

Generated gamma dose rate

The spatial distribution of generated gamma radiation in the horizontal cut through the experimental chamber without specimen is shown in Fig. 2.227. Due to the LiF beam catcher moderate dose rate values are achieved. The Li component of the beam catcher absorbs cold and thermal neutrons without production of gamma radiation. 91 % of all neutrons are within this energy region. The spatial distribution of generated gamma dose for the experimental chamber with the polyethylene cube as specimen is shown in Fig. 2.228. A considerable fraction of cold and thermal neutrons is captured in hydrogen. The specimen becomes an intense source of gamma radiation with an energy of 2.2 MeV. This gamma radiation from the specimen causes a slight increase especially at positions I (outside wall C) and II (outside the door). When the iron cube is inserted in the experimental chamber as specimen, the dose increase at both positions is more distinct due to the higher energy of generated gamma radiation from iron. The spatial distribution of generated gamma radiation for the iron cube as specimen is shown in Fig. 2.229. The iron cube becomes a source of gamma radiation with an energy up to 7.7 MeV. The factor of dose increase at positions I and II is about one order of magnitude. However, the level of 2 µSv/h is not exceeded at any position on the outer surfaces of the shielding.

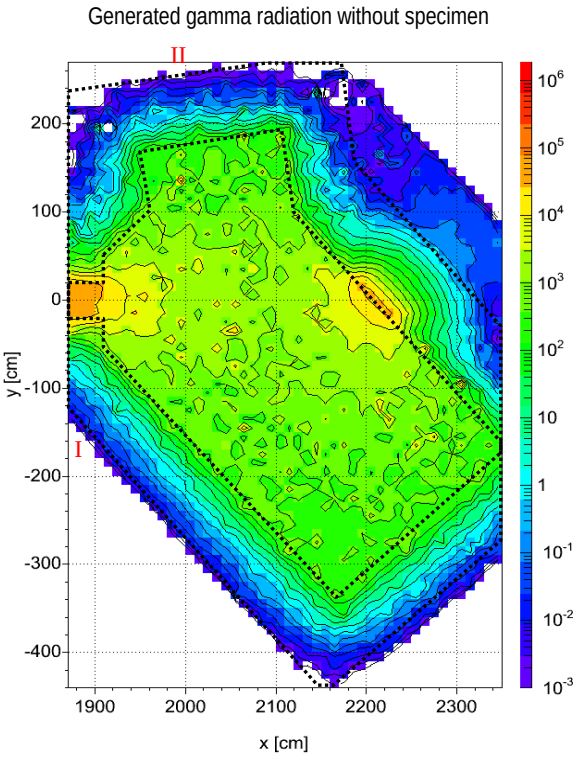

Fig. 2.227: Spatial distribution of generated gamma dose rate [µSv/h] in a horizontal plane at level of the beam axis through the experimental chamber without specimen.

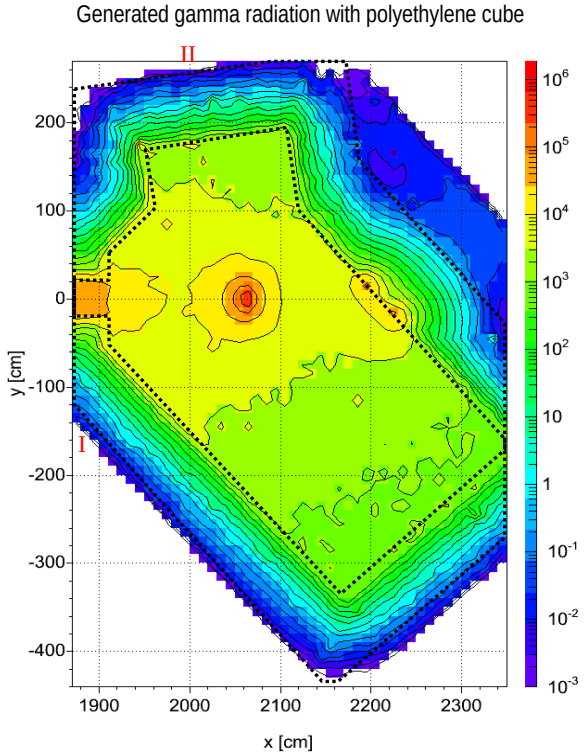

Fig. 2.228: Spatial distribution of generated gamma dose rate [µSv/h] in a horizontal plane at level of the beam axis through the experimental chamber with a cube of polyethylene as specimen.

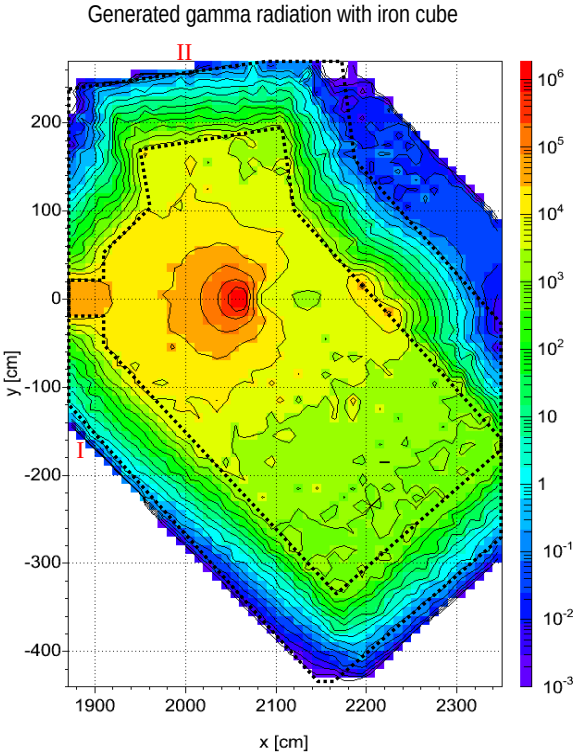

Fig. 2.229: Spatial distribution of generated gamma dose rate [µSv/h] in a horizontal plane at level of the beam axis through the experimental chamber with a cube of iron as specimen.

2.11 Conclusion

- Neutron source
  - At FRM-II a variety of neutron spectra (fast, hot, thermal and cold) is available. For most applications of radiography a cold neutron spectrum proves to be superior with regard to contrast in projections, exploitation of the phase contrast effect, and energy selective radiography. Source of the cold neutrons is the 'cold source' in which neutrons are moderated down to the energy region around 3 meV. The cold source is an asymmetric and inhomogeneous structure inside the moderator vessel. Anyway, it could be shown that due to compensating effects the flux distribution at the position of the specimen is rather flat.
  - For spatial resolution the L/D ratio is of eminent importance. A high L/D ratio is always accompanied by a comparatively small flux. In the case of the ANTARES facility L/D=400 results in a flux of 10^8 $sec^{-1}cm^{-2}$ in the detector plane. Given this L/D ratio the flux density is higher than in all other known neutron radiography facilities.
- Collimation
  - A simple aperture is not sufficient for beam shaping. As there are no black materials for neutrons, an extended structure is necessary for beam shaping. The constraint of a rectangular source area (entrance window of the beam tube) and the goals of a pill-box shaped point spread function PSF and a quadratic fully illuminated area in the detector plane afford a complex shape of the collimator.
  - As collimator material iron is used. Multilayer constructions from iron, cadmium, and polyethylene yield an insignificant lower neutron leakage through the collimator material but provide a rise in gamma background of some 6 %.
- Flight tube
  - An evacuated flight tube for the neutron beam between the collimator and the specimen is useful. Without the flight tube the total neutron flux would be reduced by 52 % due to scattering and absorption in air. Due to beam hardening, the spectrum would be shifted to higher energies. Attenuation of neutrons with an energy of 1 meV in air would be even 80 %. Besides, the flight tube reduces considerably the activation of the air (activation of air is mainly caused by the reaction $^{40}Ar(n, \gamma)^{41}Ar$).
  - Despite the low neutron cross section of aluminum the flight tube becomes an intense source of high energetic gamma radiation and scattered neutrons due to the small incident angle between neutron flight paths and tube walls. Using a flight tube that is kept as narrow as possible makes necessary a shielding thickness of 80 cm (shielding material: heavy concrete) in order to meet radiation protection purposes. An adjustment of the shape of the flight tube to the outer rim of the penumbra region of the neutron beam and the installation of an absorber mask reduces the necessary shielding thickness to 60 cm. By the optimization of the flight tube arrangement and the surrounding shielding 52.3 t of shielding material and a volume of 15.6 m^3 were saved.
- Shielding
  - Radiation shieldings are necessary for radiation protection purposes and for reduction of radiation background level for vicinal experiments. Best neutron attenuation could be achieved by a combination of an iron and a polyethylene layer but both materials become an intense source of high energetic gamma radiation. Polyethylene becomes brittle when irradiated with high neutron fluence; it is flammable and its mechanical load is comparatively small. Due to these practical reasons, heavy concrete has to be preferred as shielding material. The shielding quality of heavy concrete strongly depends on its composition. Taking into account the attenuation power for neutron and gamma radiation, the gamma production, weight and cost the optimal choice is an heavy concrete with steel resin, hematite, and colemanite as additives (mass density ρ between 3.6 g/cm^3 and 4.7 g/cm^3). With expensive high density concrete types (mass densities up to ρ=6.3 g/cm^3) even higher radiation levels outside the shielding would be obtained.

- Additives cause inhomogeneities in the heavy concrete due to the granularity. It was shown that granules with up to some 2 cm do not change significantly the neutron and gamma attenuation in comparison to a fully homogeneous structure.
- Steel liners around the shielding elements cause an increase of the flux of scattered thermal neutrons. At position of the detector of the ANTARES facility the increase amounts to some 50 %. However, steel liners are useful for practical reasons: They increase the mechanical stability of the shielding and enable for an easy decontamination. Covering the steel liners with boron carbide rubber mats decreases the background of scattered neutron radiation by a factor of 1.5 but the background of generated gamma radiation is increased by 13 %.
- The shielding was constructed with discrete shielding elements. Even when using steel liners, it is not possible to fully avoid gaps between the elements. The radiation transport through gaps in a shielding depends on the shape and on the width of gaps. Lowest radiation transport is obtained for a gap with cylindrical surfaces, highest transmission occurs with a labyrinth configuration with two 90 ° bends. Nevertheless, the labyrinth configuration was realized for the ANTARES facility for practical reasons. The neutron dose outside the shielding is increased by about a factor of three by the gaps (for an isotropic incident beam) when the gap width is 1 cm. Gap widths in the realized shielding are much lower (<5 mm).
- Radiation transport through the gap systems in the secondary shutter was reduced by help of cups and labyrinths by more than a factor of 10.

- Beam catcher
  - The background level of scattered cold and thermal neutrons at position of the detector is reduced by more than a factor 16 by help of a lithium fluoride beam catcher.
  - The dose rate outside the shielding of the experimental chamber (in which the specimen and the detector is placed) depends on the structure elements and the specimen. The lithium fluoride beam catcher is primarily aimed for reduction of the neutron background radiation within the experimental chamber. A wanted side effect is that this device reduces the dose of generated gamma radiation outside the shielding by more than a factor of 10.

- Reliability of calculations
  - The results of Monte Carlo calculations for the facility were compared with measurements. The surrounding of the shielding was scanned with dosimeters with respect to neutron dose rate and gamma dose rate. The total neutron flux and the fraction of fast and epithermal neutrons at position of the specimen were measured by help of the gold activation method. The spectral neutron flux density of the beam was measured by means of the time of flight method. In all cases there was a good accordance between measurement and calculation.

3 Deconvolution algorithms and coded masks

3.1 Introduction

Nearly all neutron radiography facilities use a setup similar to a pinhole camera with a single hole. With such facilities a compromise between intensity in the detector plane and spatial resolution has to be made: High resolution can be obtained with a small aperture diameter D and a large distance L between aperture and object. As flux is proportional to $(D/L)^2$, high resolution requires a long exposure time and yields a bad signal to noise ratio. Small L/D ratios provide a low noise level but the resulting image is blurred. Investigations were carried out whether this situation can be improved by reconstruction of blurred images that were recorded with high fluence. Several image deconvolution algorithms were tested for this purpose. It is shown that the application of those algorithms in neutron radiography is useful only in some special cases: For a given radiography setup the resolution can be increased considerably. Without restrictions for L and D there is in most cases a combination of L and D that provides a better resolution and higher signal to noise ratio SNR without algorithmic reconstruction. An exception are projections in which the signal of the specimen does not exceed the noise level of the detector system (e.g. thermal noise of the CCD chip). In this case choosing a lower L/D ratio and algorithmic reconstruction of the blurred data is useful.

The quality of reconstructed images strongly depends on the point spread function of the optical system. The point spread function is an issue of the aperture layout. Therefore the performances of different aperture shapes were tested by the Monte Carlo Method. It is shown that optimized apertures (like multiple hole masks) improve the quality of reconstructed images compared to a single hole system of same transmission area.

Image reconstruction is widely used in X-ray astronomy. High energetic X-rays and thermal neutrons have in common that the construction of lens systems is very difficult because the refraction index of all materials is very close to one.

3.2 Virtual radiography station

The investigations were carried out by modeling a ‘virtual radiography station’. The dimensions of the virtual radiography station are not similar to the ANTARES experiment. The distance between aperture and object is chosen much smaller. This is necessary to obtain a distinct blur effect. For the ANTARES facility the geometric blur effect is less dominant. Fig. 3.1 shows a schematic overview of this virtual facility.

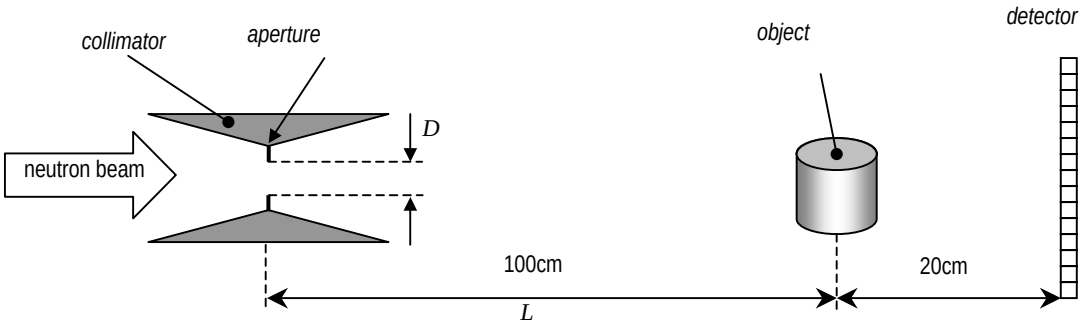

Fig. 3.1: The virtual radiography station (schematic overview)

For the neutron source, the energy spectrum of the ANTARES facility was used. The diameter of the collimator is 4 cm at the narrowest part. This is the mounting position for different apertures. The specimen is positioned 100 cm from the aperture for all simulated projections with one exception: For testing time multiplexing a distance of 141 cm was applied. The detector is located 20 cm behind the object; it has an extension of 7 cm x 7 cm. Neutrons are detected in a 300 x 300 pixel pattern by use of the ^{6}Li(n,α)^{3}H-reaction like in the case of the ANTARES standard detector. In the following, the gray values in all simulated projections are proportional to the number of (n,α)-events in this ‘virtual scintillator’. Of course, all simulations include bothering effects that appear in real radiographies, like e.g. transmission through aperture material and scattering in the specimen.

Each Monte Carlo run comprised $2 \cdot 10^9$ particle histories. The test specimen is shown in Fig. 3.2. It is an aluminum cylinder containing a conglomeration of elements which might occur in mechanical engineering: An iron screw, iron balls (ball bearings), transformer like structures consisting of iron and

plastics, and a wedge shaped gap of a depth of 1 cm filled with cadmium. These elements were chosen because they give an impression of the resolution power to be expected in practical applications.

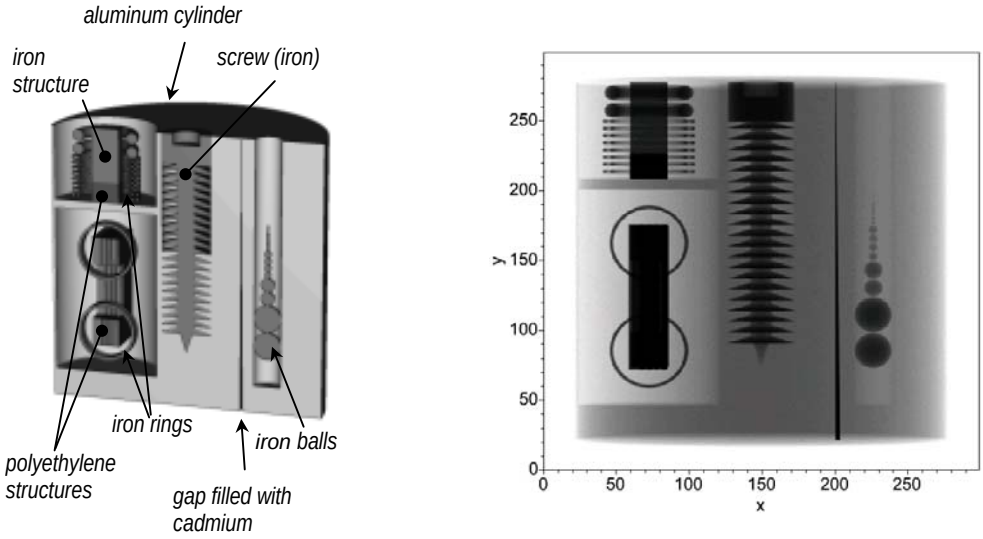

Fig. 3.2: Vertical cut through the test specimen for the radiographies: aluminum cylinder with structures from iron and plastics (left hand side) and an 'ideal' projection of the test specimen that is produced by a neutron point source of infinite source yield (right hand side).

An "ideal" projection of the test specimen is displayed in Fig. 3.2 right hand side. "Ideal" in this context means that it was recorded using a neutron point source of infinite source yield. Such neutron sources do not exist in reality.

3.3 Image degradation in neutron radiography

Neutron radiographies are degraded for several reasons:

- Geometry effects due to the extended "source" (aperture) cause a blur. This blurring is the most important contribution to image degradation in neutron radiography especially at low L/D ratios.
- Neutron scattering in the object causes an additional blur. With increasing distance between object and detector this effect becomes less important. In the case described here, the distance of 20 cm is sufficient to make this effect negligible (the effect is included in the simulations, however). The distribution of scattered neutrons from the test specimen in a horizontal plane through the middle object is shown in Fig. 3.5. Compared to the total neutron distribution (Fig. 3.4) it decreases much faster with increasing distance from the specimen due to the nearly isotropic direction distribution after the impact. At the location of the detector (x=20 cm) the maximal contribution of scattered neutrons to total neutron fluence is some percent.
- There is no material, which is totally black for neutrons; thus the aperture material, especially the rim, is semipermeable for neutrons. With a pure thermal neutron spectrum (without contributions from higher energy groups) this is no severe problem because there are materials, which are nearly black for neutrons in this energy range (e.g. cadmium, gadolinium). Anyway, semi transparency has to be taken into account whenever the diameter of the aperture hole is very small. In order to get high L/D ratios very small diameters (1/10 mm) could be taken into consideration. In this case the thickness of the aperture structure has to be very small, too (otherwise the aperture would act like a collimator). Even cadmium layers are no longer black for thermal neutrons when they are very thin. However, at reactor based neutron radiography facilities a pure thermal neutron beam can rarely be found. For the ANTARES spectrum, the fraction of epithermal neutrons is not negligible (like for most spectrums at other facilities) and even transmission through 2 mm cadmium plates affects image precision.
- Neutron detection is often done with scintillators. A captured neutron gives rise to a flash of visible light. The flash is extended over some 10 µm. In most applications of neutron radiography 10 µm are dwarfed by all other effects of image degradation. On the other side there are some applications where the scintillator screen is regarded on a microscopic scale.

The influence of scattered neutrons from the specimen was estimated using the setup shown in Fig. 3.3. In a horizontal plane through the middle of the test specimen the total neutron fluence and the fluence of scattered neutrons were calculated. The result for the total fluence is shown in Fig. 3.4 and the result for scattered neutrons is shown in Fig. 3.5. At x=20 cm where the detector of the radiography station is located the fraction of scattered neutrons is rather low. It amounts at maximum to a few percent of the total fluence.

In most applications of neutron radiography the dominant contribution to image degradation is caused by geometry effects.

As the aperture (that is the effective "source" for radiography setups) has a non-zero diameter, the information of a single point in the specimen is mapped to a circular area in the detector plane. If two points in the specimen are close together,

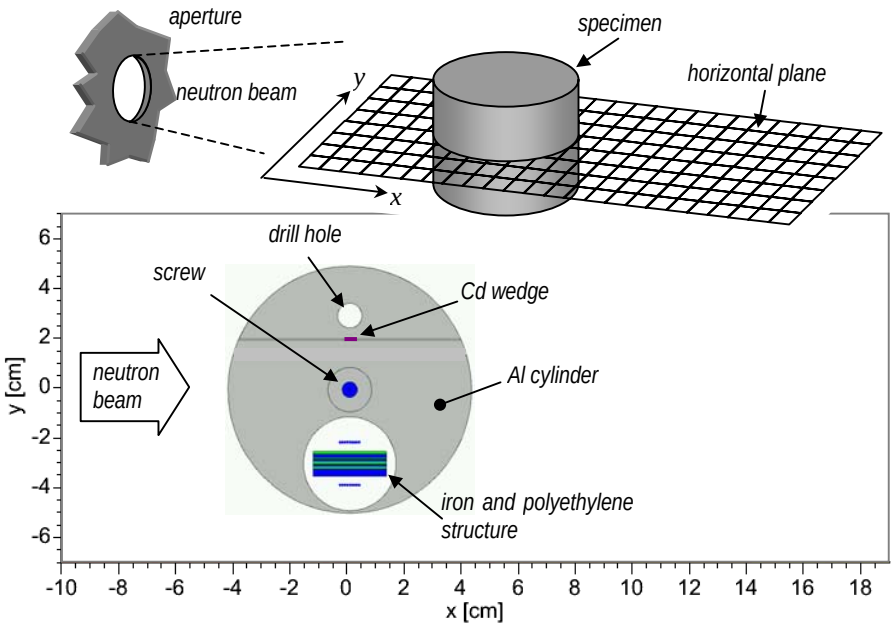

Fig. 3.3: Top: Overview of the setup for estimation of the influence of scattered neutrons from the specimen. The total neutron fluence and the fluence of scattered neutrons is calculated in a horizontal plane.
Bottom: Horizontal cut through the test specimen at the level of the plane in which the neutron fluences are calculated

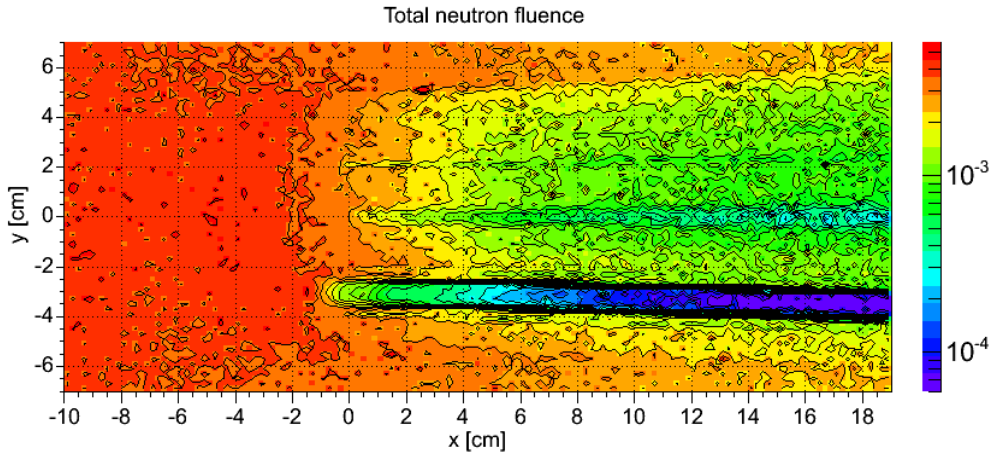

Fig. 3.4: Total neutron fluence [cm^{-2}] per source neutron in the horizontal plane through the middle of the object as shown in Fig. 3.3.

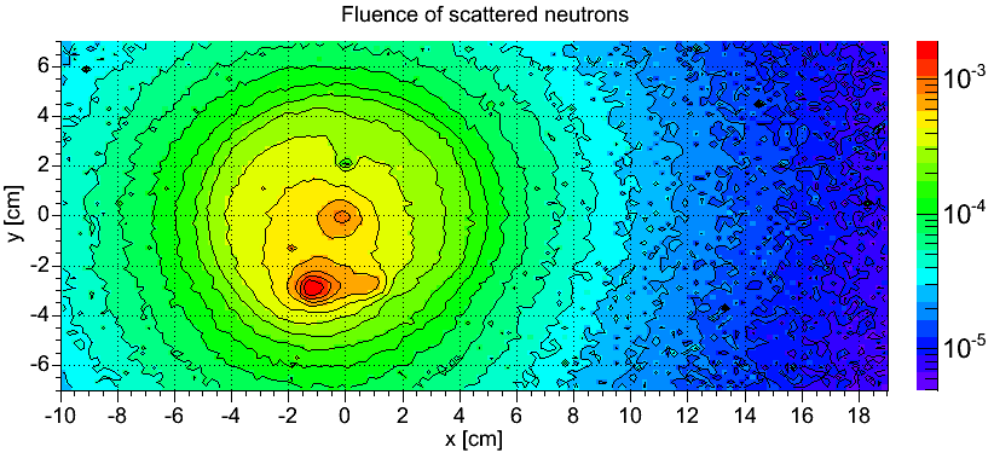

Fig. 3.5: Fluence of scattered neutrons [cm^{-2}] per source neutron in the horizontal plane through the middle of the object as shown in Fig. 3.3.

their images overlap and it is impossible to decide which of the two original points in the object was traversed by the incoming neutron. One point in the detector plane contains therefore the information of several points in the object (Fig. 3.6).

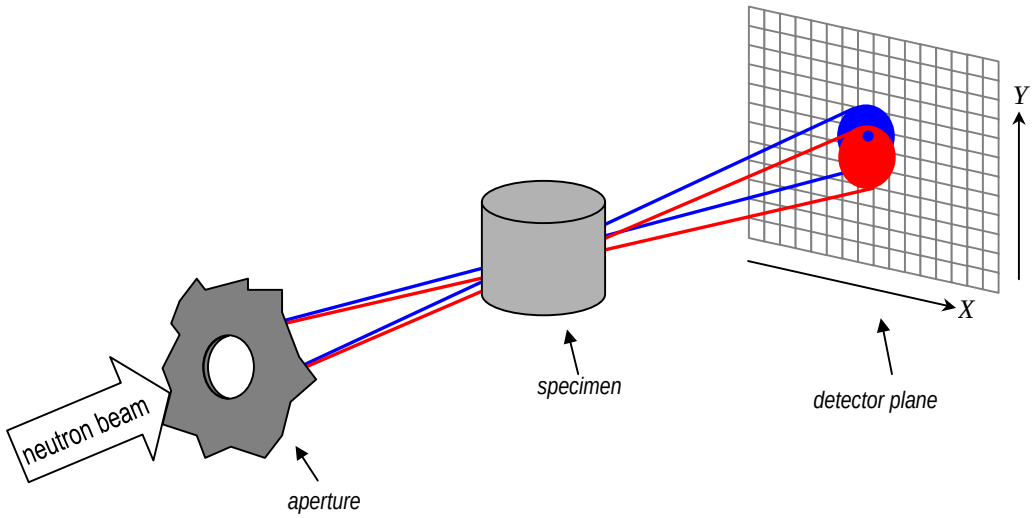

Fig. 3.6: Image degradation by geometry effects. The extended aperture causes an overlap of information from several object points in the detector plane.

The *point spread function* (*PSF*) describes how one point in the specimen is mapped to the detector plane [21]. In the case of a circular aperture, the *PSF* is a pill-box function (Fig. 3.9 left hand side). Considering all points of the specimen, their projection $I_{blurred}$ in the detector plane is the correlation of the 'ideal' image I_{ideal} (obtained by a point source) with the *PSF* [21][52]:

$$I_{blurred}(X,Y) = \int_{-\infty}^{\infty}\int_{-\infty}^{\infty} I_{ideal}(x,y)\cdot PSF(X+x,Y+y)dxdy = I_{ideal} \otimes PSF \qquad (3.1)$$

Eq. 3.1 implies shift invariance of the *PSF* and a flat object. These preconditions are not exactly fulfilled with most real setups, but it is a good approximation within the fully illuminated area of a neutron radiography facility.

A degraded projection of the test specimen as it would be recorded at a real radiography station with a *L/D* ratio of 50 is shown in Fig. 3.7 on the right hand side. An aperture (Cd plate, 2 mm thick) with a hole diameter of 2 cm (Fig. 3.7 left hand side) was mounted at the narrowest part of the collimator for this projection.

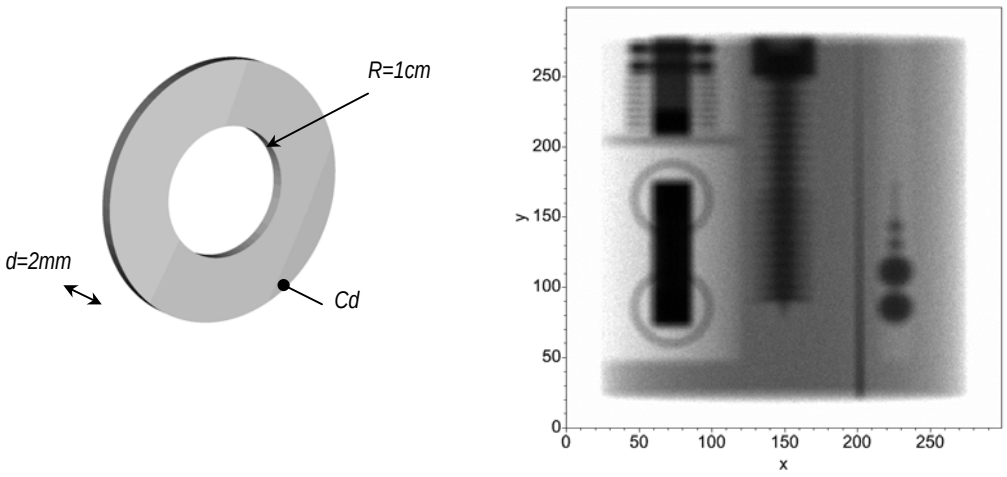

Fig.3.7: Aperture for the *L/D* =50 projection (left hand side) and *L/D* =50 projection of the test specimen (right hand side).

3.4 Image deconvolution

3.4.1 Inverse filter

The correlation in Eq. 3.1 is equivalent to a convolution. This is because the PSF is point symmetric. A convolution in the spatial domain corresponds to a multiplication in the Fourier domain [54].

$$FT\{I_{blurred}\} = FT\{I_{ideal}\} \cdot FT\{PSF\} \qquad (3.2)$$

where FT denotes the Fourier transform:

$$FT\{I\}(u,v) = \int_{-\infty}^{\infty}\int_{-\infty}^{\infty} I(x,y)e^{-i\cdot 2\pi(ux+vy)}dx\ dy \qquad (3.3)$$

Therefore it is convenient to carry out image deconvolution by help of the Fourier transform (even if the point spread function is not point symmetric, the Fourier transform can be used when the PSF is mirrored subsequently at two perpendicular axes) In principle the 'ideal' image can be reconstructed by dividing the blurred image by the PSF in the Fourier domain and transforming the result back into the spatial domain. This procedure is referred to as an inverse filter [55].

$$I_{ideal} = FT^{-1}\left\{\frac{FT\{I_{blurred}\}}{FT\{PSF\}}\right\} \qquad (3.4)$$

where FT^{-1} denotes the Fourier back transform:

$$I(x,y) = \int_{-\infty}^{\infty}\int_{-\infty}^{\infty} FT\{I\}(u,v)e^{i\cdot 2\pi(ux+vy)}du\ dv \qquad (3.5)$$

For most real projections, the application of an inverse filter is very disappointing: The result of reconstruction of the L/D =50 projection from Fig. 3.7 is shown in Fig. 3.8. The structure of the object is no longer to be recognized, the deblurred image consists only of noise. This is due to the immense noise sensitivity of inverse filtering.

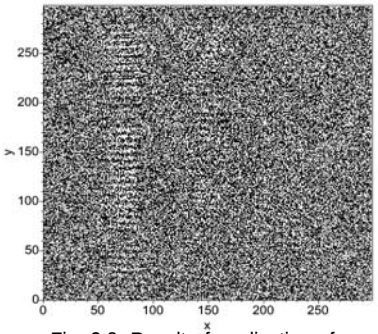

Fig. 3.8: Result of application of an inverse filter to the L/D =50 projection

The data in the projection I_{proj} is not only blurred but contains also noise (N).

$$I_{proj} = I_{blurred} + N \qquad (3.6)$$

The application of an inverse filter to the noisy data I_{proj} results therefore in:

$$I_{inverse} = FT^{-1}\left\{\frac{FT\{I_{proj}\}}{FT\{PSF\}}\right\} = FT^{-1}\left\{\frac{FT\{I_{blurred}\} + FT\{N\}}{FT\{PSF\}}\right\} \qquad (3.7)$$

The values in the Fourier domain are complex numbers. Making the denominator in Eq. 3.7 real, the Fourier transform of $I_{inverse}$ becomes:

$$\begin{aligned} FT\{I_{inverse}\} &= \frac{FT\{I_{proj}\}}{FT\{PSF\}} = \frac{FT\{I_{proj}\}}{\mathrm{Re}(FT\{PSF\}) + i\,\mathrm{Im}(FT\{PSF\})} = \\ &= \frac{FT\{I_{proj}\}\cdot\left(\mathrm{Re}(FT\{PSF\}) - i\,\mathrm{Im}(FT\{PSF\})\right)}{\mathrm{Re}(FT\{PSF\})^2 + \mathrm{Im}(FT\{PSF\})^2} \end{aligned} \qquad (3.8)$$

The denominator in the last expression of Eq. 3.8 is the square of the absolute values of the PSF in the Fourier domain. The absolute value of the PSF in the Fourier domain is the *modulation transfer function (MTF)* [21]:

$$\left|FT\{PSF\}(u,v)\right| = MTF(u,v) \qquad (3.9)$$

Under consideration of Eq. 3.9, Eq. 3.8 becomes:

$$FT\{I_{inverse}\} = \frac{FT\{I_{proj}\} \cdot FT\{PSF\}^*}{MTF^2} = \frac{(FT\{I_{blurred}\} + FT\{N\}) \cdot FT\{PSF\}^*}{MTF^2} \quad (3.10)$$

where * denotes the conjugated complex value.

From Eq. 3.10 follows: Whenever the MTF has small values, a numerical problem arises. Without noise, the denominator would be small at the same frequencies as the enumerator and thus the problem be restricted to a few pixels. In the presence of noise this holds no longer and the division scheme yields erratic results. The reconstruction $I_{inverse}$ strongly deviates from the ideal image I_{ideal}.

The PSF for the L/D =50 projection in Fig. 3.7 is shown in Fig. 3.9 (left hand side). In continuous space it is a pill-box function, taking only the values 0 and 1. However, the gradients at the edges of the function displayed in Fig. 3.9 appear to be finite due to the discretization caused by the pixel structure: For pixels that are crossed by the rim of the pill-box, values according to their area fraction within the pill-box have to be allocated. Fig. 3.9 (right hand side) shows the MTF for the L/D =50 projection: It has the shape of the absolute value of a sine cardinal (Bessel function).

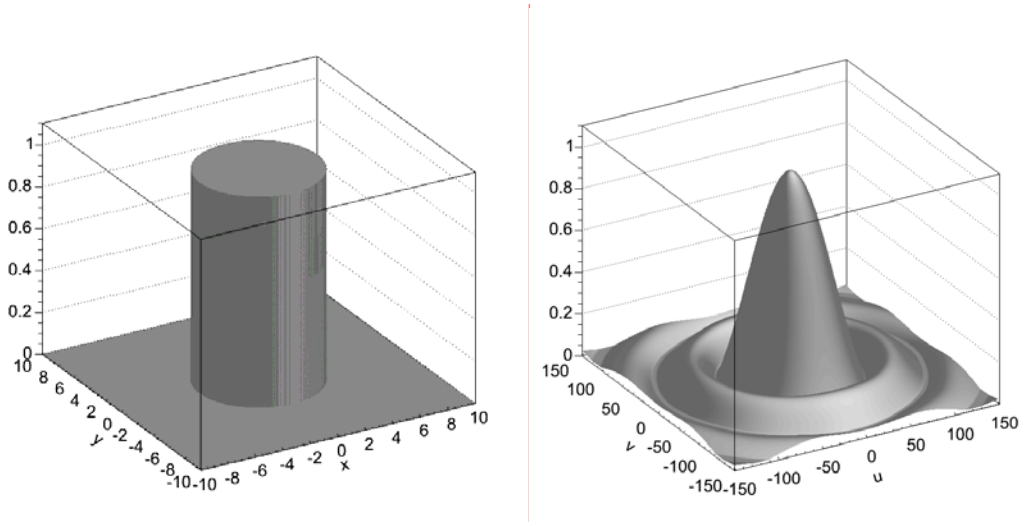

Fig. 3.9: The point spread function $PSF(x,y)$ (left hand side) for the L/D =50 projection of Fig. 3.7 and the modulation transfer function $MTF(u,v)$ (right hand side)

In real projections noise is unavoidable. It occurs for several reasons:

- Quantum noise in the neutron beam
- Counter noise in the detector
- Noise due to the neutron detection scheme
- Noise produced in the camera setup, e.g. thermal noise [97], on chip electronic noise, and quantization effects in the discrete pixel structure (this type of noise is not included in the Monte Carlo data)

3.4.2 Wiener filter

One approach to overcome the problem of near zero denominators in the Fourier domain is the Wiener filter [92][55]. A real constant c_{wiener} is added in the denominator (Eq. 3.11). At frequencies where the MTF becomes small, the denominator is now dominated by the constant c_{wiener}. The constant itself is a measure for the average noise in the picture. As this method is just a modification of the inverse filter, it is also sometimes called ‘inverse filter’.

The Wiener filter executes an optimal tradeoff between inverse filtering and noise smoothing. It compensates the additive noise to some degree and inverts the blurring simultaneously.

$$I_{wiener} = FT^{-1}\left\{\frac{FT\{I_{proj}\}}{FT\{PSF\}} \cdot \frac{|FT\{PSF\}|^2}{|FT\{PSF\}|^2 + c_{wiener}}\right\} = FT^{-1}\left\{\frac{FT\{I_{proj}\}}{FT\{PSF\}} \cdot \frac{MTF^2}{MTF^2 + c_{wiener}}\right\} \quad (3.11)$$

The Wiener filter is optimal in terms of the mean square error. In other words, it minimizes the overall mean square error in the process of inverse filtering and noise smoothing.

The result of a Wiener filter applied to the L/D =50 projection of Fig. 3.7 is shown in Fig. 3.17. The reconstruction is considerably sharper than the raw data. In contrast to the raw data, even details like the screw thread are now clearly recognizable. However, compared to the raw data, noise is amplified considerably by the reconstruction algorithm. In principle one is free to choose the value of the constant c_{wiener}. The choice of its value strongly depends on the purpose of the reconstruction. Big values result in a faint gain of sharpness but low noise amplification. Small values are much more effective for deblurring but also cause high noise amplification. In some applications, e.g. for measurement of distances within the inner structure of the specimen, even high noise amplification is acceptable when details are revealed that are not recognizable otherwise. This is demonstrated in the image sequence of Fig. 3.10: The screw in the L/D =50 projection is reconstructed with different values of c_{wiener} .The values are given as fraction of the maximum value of the square of the MTF, i.e. as fraction of the maximum value of the denominator in the last expression of Eq. (3.11). Assuming the purpose of the radiography is to count the number of windings of the screw, the unprocessed raw data (left hand side) and all reconstructions with $c_{wiener} > 1\% \cdot \max(MTF^2)$ are barely useful. Despite the high noise levels in the reconstructions with smaller values of c_{wiener} , the aim can be achieved: The windings are clearly distinguishable.

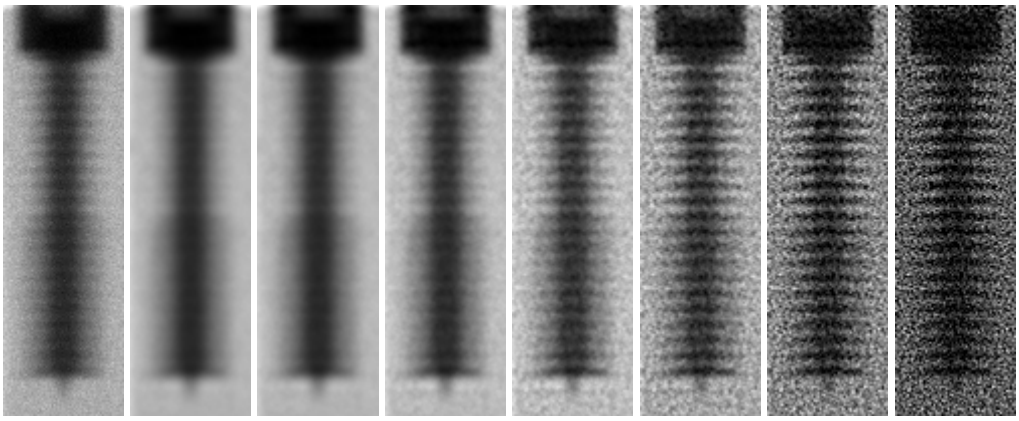

Fig. 3.10: From left to right: unprocessed data from the L/D =50 projection of the screw; reconstruction with c_{wiener}=50 % of the maximum of MTF^2, c_{wiener} =30 %, c_{wiener} =10 %, c_{wiener} =3 %, c_{wiener} =1 %, c_{wiener} =0.3 %, c_{wiener} =0.1 %. The smaller c_{wiener} is chosen the sharper becomes the reconstruction but the signal to noise ratio SNR decreases as well.

3.4.3 Iterative algorithms

Another approach to overcome the problem of noise amplification by small numbers in the denominator of the Fourier domain are iterative algorithms. The idea is to guess the 'ideal' image, to convolute it with the point spread function and to compare the result with the measured projection. After an appropriate adjustment of the guessed image, the procedure is started again. Usually the blurred image is taken as guessed image for the first iteration.

3.4.3.1 Van Cittert algorithm

One variant of this class of procedures is the Van Cittert algorithm [56] described by Eq. 3.12:

$$I_{guess}^{new}(x,y) = I_{guess}^{old}(x,y) + \left(I_{blurred}(x,y) - I_{guess}^{old}(x,y) \otimes PSF(x,y)\right) \qquad (3.12)$$

The guessed image is convoluted with the PSF. The difference between the blurred image and the convolution result is then added to the guessed image. Convergence is not granted and there is no unique criterion for the end of iterations.

The result of reconstruction of the L/D =50 projection by 30 iterations of Van Cittert algorithm is shown in Fig. 3.18. The image becomes sharper but not as sharp as with the Wiener filter. Details like the screw thread are still not to be recognized. Further iterations make appear speckles in the reconstruction. The speckles do not represent any real structure in the object, but occur due to fitting the noise in the object too closely. Assuming the purpose of the radiography is to count the number of windings of the screw, the Van Cittert algorithm is not beneficial, as shown in the image sequence

below (Fig. 3.11): The screw is reconstructed with different numbers of iterations. In none of the reconstructions the windings are distinguishable. Speckles appear after 15 iterations. For more than 30 iterations speckles become dominant, and for more than 35 iterations even the total structure of the screw is barely cognizable. However, there are regions where the Van Cittert algorithm enhances resolution. Single edges in the object can be deblurred quite well by the algorithm. This is demonstrated with the transformer like structures in the sequence of Fig. 3.11: Edges become considerably sharper even before speckles dominate the reconstruction. With simultaneous regard to sharpness and noise level the quality of the Wiener filter is not reached. Therefore the Van Cittert algorithm clearly succumbs to the Wiener filter.

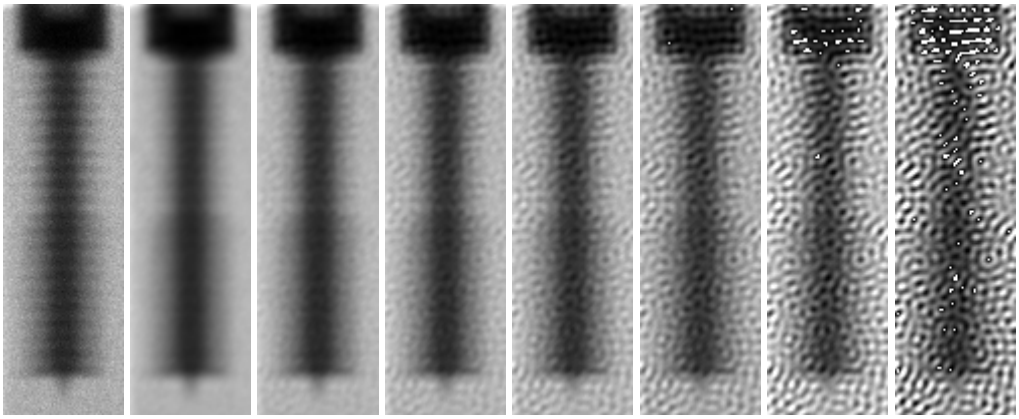

Fig. 3.11: Reconstruction of the screw with Van Cittert algorithm in dependency of the number of iterations. From left to right: 0, 5, 10, 15, 20, 25, 30, 35 iterations. For this region of the projection the reconstruction does not become sharper with increasing number of iterations

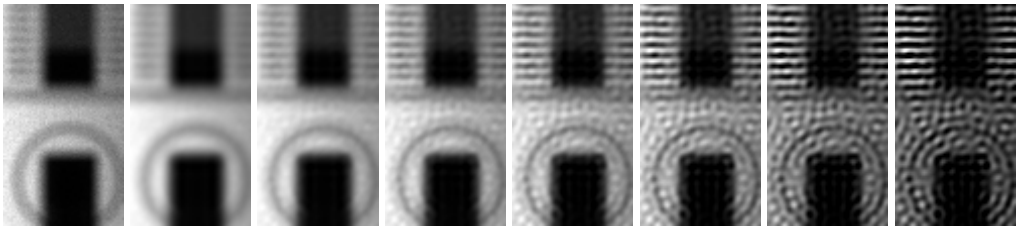

Fig. 3.12: Reconstruction of the transformer like structure with Van Cittert algorithm in dependency of the number of iterations. From left to right: 0, 5, 10, 15, 20, 25, 30, 35 iterations.

3.4.3.2 Richardson-Lucy maximum likelihood algorithm

An other iterative algorithm is the Richardson-Lucy maximum likelihood algorithm [57][58]. It uses a statistical model for image formation and is based on the formula of Bayes. The iteration converges to the maximum likelihood solution for Poisson statistics in the raw data. A modified algorithm assumes Gauss statistics [59]. These statistics are a good modeling for both quantum noise of the neutron beam and counter noise in the detector and camera itself. The maximum likelihood algorithm makes use of the a priori information that intensity may never become negative and total intensity in the reconstruction must be conserved. This additional information is not used by the algorithms described above: Reconstructions obtained by a Wiener filter as well as by Van Cittert algorithm may include negative values.

The maximum likelihood algorithm for Gauss statistics is shown in Eq. 3.13.

$$I_{guess}^{new}(x,y) = I_{guess}^{old}(x,y)\frac{I_{blurred}(x,y)\otimes PSF(-x,-y)}{\left[PSF(x,y)\otimes I_{guess}^{old}(x,y)\right]\otimes PSF(-x,-y)} \qquad (3.13)$$

The result of 60 iterations with this procedure is displayed in Fig. 3.19. The reconstruction is less noisy compared to the reconstructions obtained by the algorithms described above and deblurring is more completed. Therefore the Richardson-Lucy algorithm is superior to all reconstruction procedures taken into consideration.

Assuming the purpose of the radiography is to count the number of windings of the screw, about 30 iterations of the Richardson-Lucy algorithm are sufficient. In contrast to the Van Cittert algorithm, the noise level keeps within an acceptable limit even for more than 100 iterations. The dependency of noise amplification on the number of iterations is demonstrated in the sequence of Fig. 3.13.

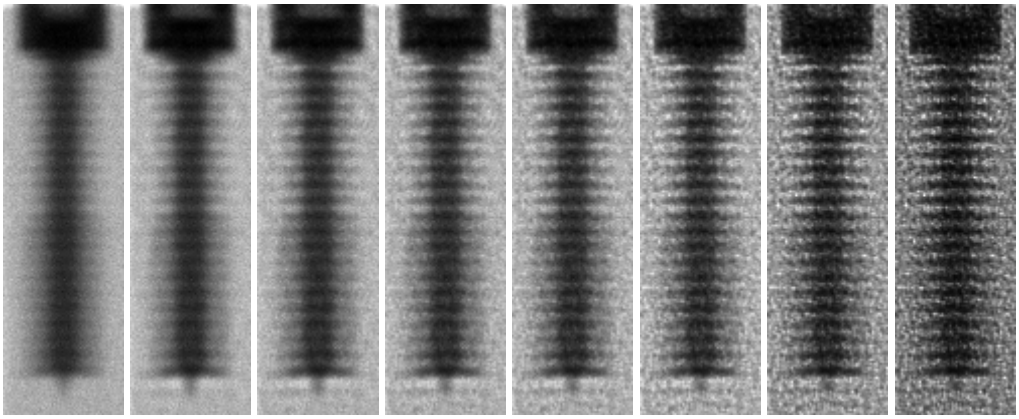

Fig. 3.13: Reconstruction of the screw with Richardson-Lucy maximum likelihood algorithm in dependency of the number of iterations. From left to right: 0, 10, 20, 30, 40, 60, 100, 150 iterations.

3.4.4 Comparison

The reconstructions of the entire L/D =50 projection with the different algorithms described above is shown in Fig. 3.17 to Fig. 3.19. For comparison the 'ideal' projection (obtained by a neutron point source of infinite source yield), unprocessed raw data of a L/D =122 projection and the unprocessed raw data of the L/D =50 projection, that is the input data set for reconstructions, are displayed in Fig. 3.14 to Fig. 3.16.

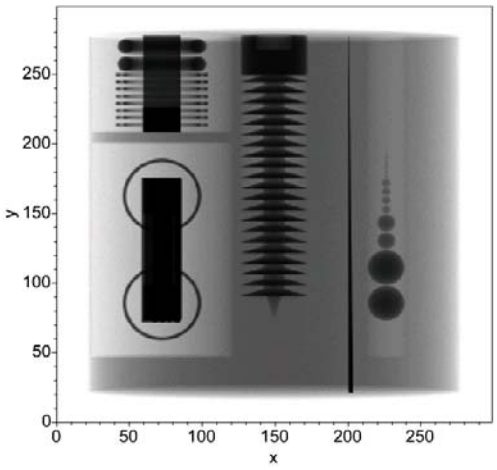

Fig. 3.14: ‚Ideal' projection of the test specimen (obtained by a neutron point source of infinite source yield)

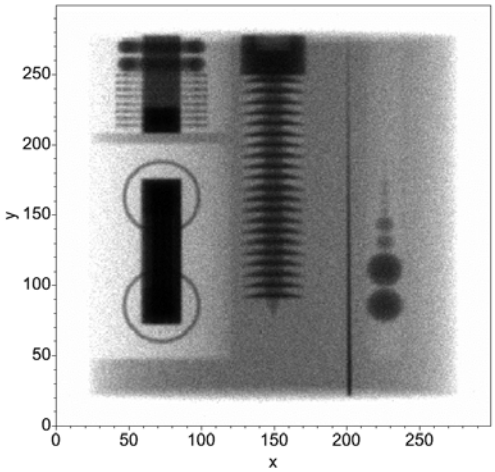

Fig. 3.15: Unprocessed raw data of a L/D=122 projection of the test specimen.

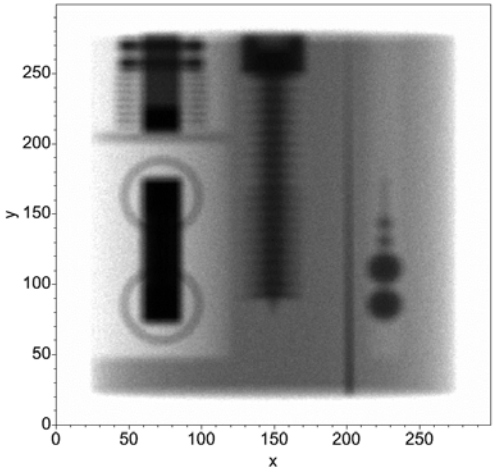

Fig. 3.16: Unprocessed raw data of a L/D=50 projection of the test specimen

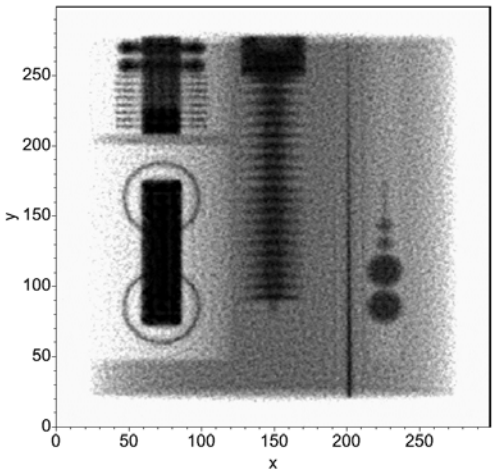

Fig. 3.17: Reconstruction of the L/D=50 projection in Fig. 3.16 with a Wiener filter

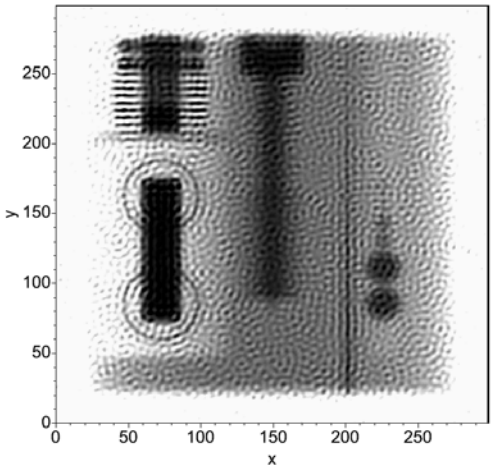

Fig. 3.18: Reconstruction of the L/D=50 projection of Fig. 3.16 with 30 iterations of Van Cittert algorithm

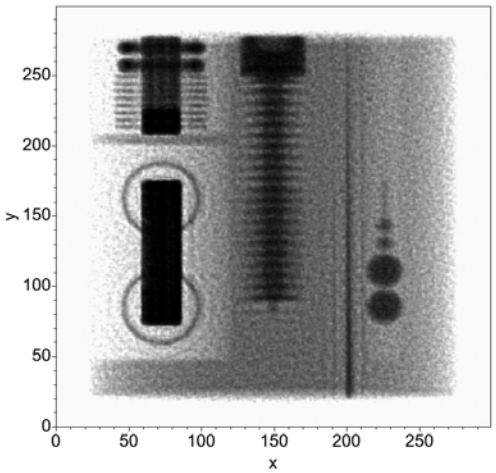

Fig. 3.19: Reconstruction of the L/D=50 projection of Fig. 3.16 with 60 iterations of Richardson-Lucy maximum likelihood algorithm

The “quality” of an image depends on the purpose for which the image is intended. It is delicate to find an universal definition of image quality [52]. Therefore comparison of the reconstructions and the raw data is somehow difficult. Common criteria are sharpness and signal to noise ratio SNR. For assessment of sharpness, the line profiles for the edge of the transformer structure (edge along x=87) are displayed in Fig. 3.20 for the different reconstructions. In order to suppress noise in the profiles, the values along columns (i.e. x=const.) were averaged between the two coils of the transformer (from y=115 to y=135). All restoration methods improve the sharpness considerably compared to the unprocessed raw data (black line in Fig. 3.20). The reconstruction obtained by 60 iterations of Richardson-Lucy algorithm shows the sharpest signal. For all other deblurred data sets, the gradient at the edge is nearly the same. A similar sharpness can be obtained by increasing the L/D ratio. The orange line shows unprocessed data from a L/D =122 projection of the test specimen. Due to the smaller transmission area of the aperture, fluence is only 16 % of the L/D =50 setup. Nevertheless the signal to noise ratio (SNR) in the unprocessed L/D =122 data is even higher than in the best reconstruction. It is about 40% of the SNR of the unprocessed L/D =50 projection, as it can be expected for counter noise. The best reconstruction result is obtained by the maximum likelihood method that provides a SNR of 10.1. Lowest SNR is obtained by the Van Cittert algorithm. The signal to noise ratios of the different reconstructions are displayed in Fig. 3.21. They are estimated along a line along x=185 from y=50 to y=250. The specimen is homogeneous in this region and therefore any variance in the signal along the line must be caused by noise.

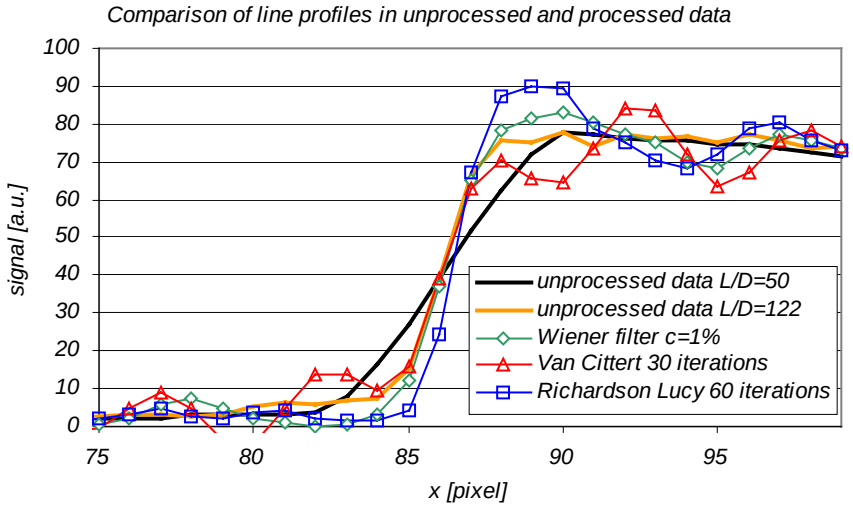

Fig. 3.20: Line profiles across the edge of the transformer-like structure (at column x=15) in raw data and reconstructed data

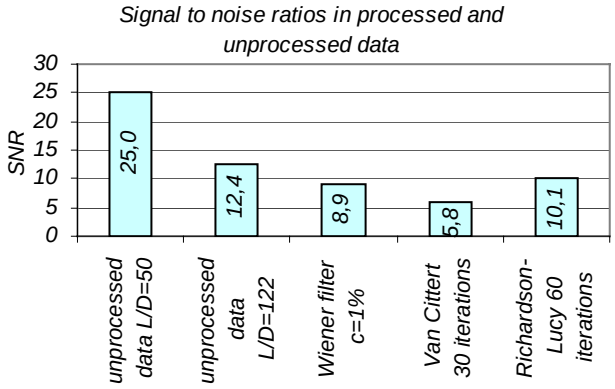

Fig. 3.21: Signal to noise ratios (SNR) in unprocessed projections and reconstructions from the L/D =50 data

3.4.5 Conclusion

The quality of reconstructions from low L/D projections never reaches the quality of unprocessed data from higher L/D setups whenever noise is dominated by quantum and counter noise. The signal to noise ratio is decreased more by reconstruction algorithms than by increasing the L/D ratio [82]. In special cases, the application of image deconvolution algorithms is of interest in neutron radiography nevertheless:

- Resolution can be improved in old raw data from specimen that cannot be examined again.
- Unsharpness from neutron detection that cannot be removed by increasing the L/D ratio can be revised. This application is demonstrated for the ANTARES standard detector below.
- Depending on the neutron energy, the thickness of aperture material has a lower limit, given by transmission through aperture material (this is especially the case for epithermal and fast

neutrons). For small aperture diameters, the thickness of aperture material has also to be small, in order to avoid collimation effects. Therefore there is a lower limit for the aperture diameter. If the desired resolution cannot be achieved due to this limitation, reconstruction algorithms can be useful.

- Noise in low intensity radiographs is dominated by detector noise, e.g. thermal noise in the CCD chip (see chapter 2.9.1 'ANTARES detector system'). When the signal from the specimen does not clearly exceed the detector noise, it is useful to increase intensity by increasing the aperture diameter and to remove the resulting blur by image deconvolution (see chapter 3.6.1.3 'Image deconvolution in low fluence radiographs').

3.5 Coded masks

The idea of coded mask imaging [78] is to use a PSF for which a special 'decoding pattern' DP exists. The cross correlation of the PSF with the DP must be a good approximation of a delta function [64].

$$PSF \otimes DP \approx \delta \qquad (3.14)$$

By definition the recorded projection I_{proj} is the correlation of the ideal image with the PSF (in context with coded masks the PSF is sometimes called 'coding pattern'):

$$I_{proj} = I_{ideal} \otimes PSF \qquad (3.15)$$

Adding a correlation with DP to Eq. 3.15 will give:

$$I_{proj} \otimes DP = I_{ideal} \otimes PSF \otimes DP \qquad (3.16)$$

If DP satisfies condition 3.14, Eq. 3.16 becomes:

$$I_{proj} \otimes DP \approx I_{ideal} \qquad (3.17)$$

The problem of deconvolution has been reduced to a convolution in Eq. 3.17. In contrary to deconvolution the convolution algorithm has no necessity for divisions. Therefore the sensitivity to quantum or counter noise is less than with deconvolution techniques. Of course, noise will cause image degradations also with this method, but the algorithm does not create artifacts like the bubble pattern in Fig. 3.18. However, in this method a new type of noise occurs when the correlation of the PSF with the DP is not exactly a delta function. Image degradation caused by this deviation is called *inherent noise* [60].

The PSF is a property of the aperture. Thus the problem is to find an aperture arrangement, the PSF of which meets the requirement of Eq. 3.14 and which can be machined with a reasonable effort.

In the literature, image restoration of projections obtained by coded masks is always described in combination with correlation techniques as described above. For some types of coded masks the MTF has less near zero zones than a single pin hole of same transmission area (e.g. non redundant arrays). In these cases it should be promising to use deconvolution techniques.

3.5.1 Ring apertures

One of the first applications of coded mask imaging was in X-ray astronomy. A mask with several concentric rings with certain radii (Fresnel zone plate) is used as aperture [61]. Each source point casts a shadow of the ring system in the X-ray projection. Correlation is not performed by computation but with an analogous setup. For reconstruction, a reduced size transparency of the X-ray projection is illuminated by visible monochromatic light. Each ring system in the X-ray projection acts like a lens for the visible light and focuses it to a point due to diffraction. The disadvantage of this method is the high amount of undiffracted light passing the transparency, causing a high background level.

For neutron radiography this method was tested by computational correlation technique.

3.5.1.1 Correlation method

Ring structures as aperture are interesting because the autocorrelation function of the resulting PSF is similar to a delta function. The autocorrelation of the PSF is the correlation $PSF \otimes PSF$. For ring structures there holds the approximation $PSF \otimes PSF \approx \delta$. That means, that the PSF can be used as decoding pattern DP as described in Eq. 3.14. To a certain degree this is also true for a single ring (Fig. 3.23): The autocorrelation has a big central peak, a flat plateau around the peak and an elevated rim. A projection taken with a ring aperture can therefore be restored to a certain degree by correlating the projection with the PSF (in this case the PSF itself is the decoding pattern). The resolution in the projection is defined by the width of the transmitting area of the ring. As this width is far below the diameter of a single hole aperture of same transmitting area, the resolution for a ring aperture is higher. A single ring aperture (Fig. 3.22) was tested for the virtual neutron radiography station. It consists of a 2 mm cadmium plate; the inner diameter of the ring is 1.5 cm, the outer diameter of the ring is 1.8 cm. The transmission area is as big as for the single hole aperture of Fig. 3.7 left hand side, which was used for the L/D=50 projection. The autocorrelation of the PSF for the ring aperture is shown in Fig. 3.23. It corresponds to the reconstructed signal of a single point source. As the central peak is 10 times higher than the side lobes, a point source (e.g. a star) would be restored satisfactorily. However, the reconstruction of the neutron radiography of the test specimen is disappointing (Fig. 3.23 right hand side): A weak very sharp projection is recognizable on top of an intense blurred projection caused by the side lobes in the autocorrelation function: even low value side lobes can cause a huge damage to the reconstruction when they spread over big regions, because the number of pixels that contribute to one point in the correlation function is increased considerably. For the expanded, structured object, the influence of the small side lobes in the autocorrelation function is not negligible anymore. This degradation of the reconstruction appears independently from noise in the projection. It is called 'inherent noise' [60] (degradation due to deviations of the autocorrelation function of the PSF from a delta-function). In a certain sense the correlation technique deblurs and blurs the image at the same time. The additional blur causes the SNR in the reconstruction to be even much higher than in the unprocessed raw data: The original projection has a SNR of 25 (like the L/D =50 single hole projection); the reconstruction has a SNR of 138.

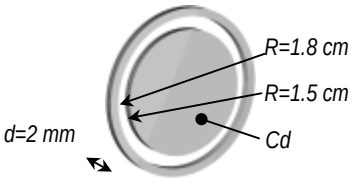

Fig. 3.22: Ring aperture

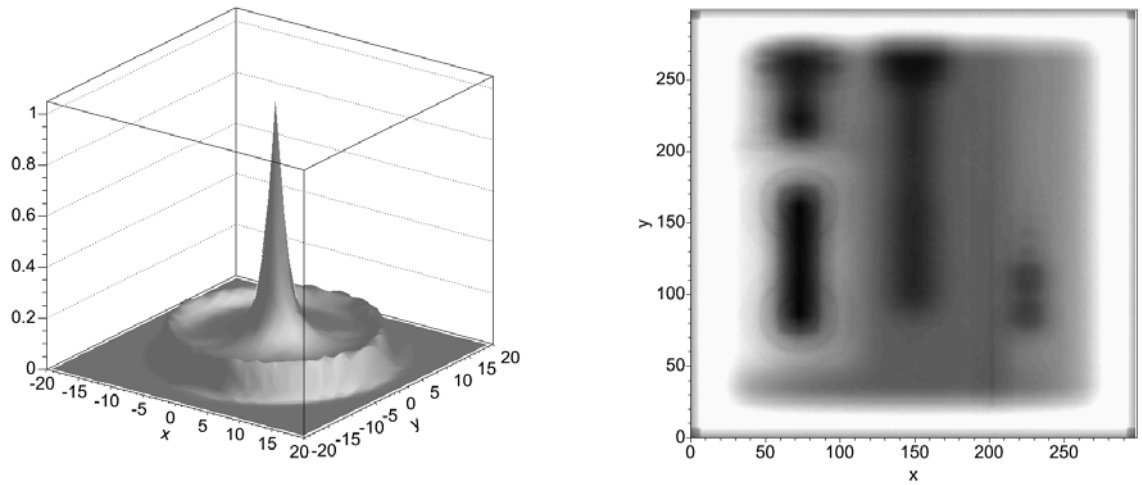

Fig. 3.23: Autocorrelation function of the PSF for the ring shaped aperture (left hand side) and the reconstruction of the projection using correlation technique (right hand side).

For standard applications in neutron radiography the ring aperture in combination with the correlation method is not interesting. Nevertheless some special applications are imaginable:

- For nearly homogeneous objects with vesicular voids the method may be applicable
- For laminography it can be useful

Laminography is a technique to detect the 3d structure of a specimen. For small distances between aperture and object, a high divergence of the neutron beam (as e.g. at the end of a neutron guide) and an extended object in beam direction, the approximation that the PSF is constant for the whole object

is no longer valid: The *PSF* depends on the distance of a point in the object to the detector. For layers in the object with big distance to the detector, the *PSF* spreads over a wider area than for layers close to the detector. Correlation with a ring of certain diameter reconstructs therefore only one layer in the object. Subsequent reconstructions with scaled *PSFs* reveal information about the structure in beam direction.

3.5.1.2 Deconvolution method

The ability for deconvolution strongly depends on the modulation transfer function *MTF*. As shown above, deconvolution is less sensitive to noise in the case of *MTFs* with small near-zero zones (see Eq. 3.10). The *MTF* for the ring aperture of Fig. 3.22 is shown in Fig. 3.24 middle. It exceeds the *MTF* of the single hole aperture with equal transmission area (Fig. 3.24 left hand side) that was used for the *L/D* =50 projection in large regions of the Fourier domain. Therefore the ring aperture was tested for image deconvolution: the projection was reconstructed by help of a Wiener filter. The result is shown in Fig. 3.24 right hand side. Compared to the reconstruction of the *L/D* =50 single hole projection (Fig. 3.17), the screw is resolved much better and the signal to noise ratio *SNR* is improved slightly from 8.9 to 9.3. However, the *SNR* of the unprocessed *L/D* =122 single hole projection (*SNR* =12.4) is also not obtained by this method. A ring aperture combined with deconvolution technique is therefore not advantageous in neutron radiography, with exception of all cases mentioned in 3.4.5.

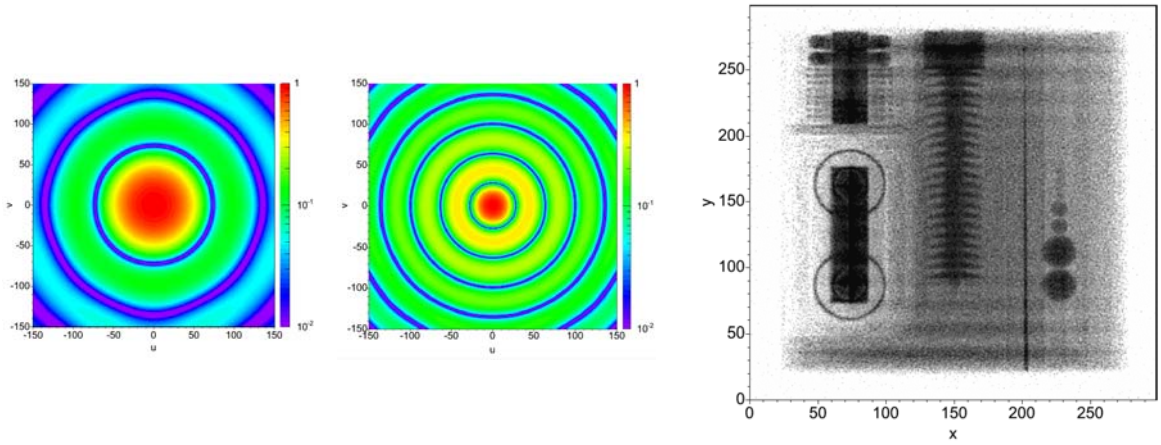

Fig. 3.24: *MTF* for the single hole aperture used for the *L/D* =50 projection (left hand side), *MTF* for the ring aperture with same transmission area (middle) and deconvoluted (by Wiener filter) projection obtained by the ring aperture (right hand side).

3.5.1.2.1 Time multiplexing

The ring aperture improves the image deconvolution properties of the projection compared to the single hole aperture of same transmission area. On the other hand there are still near-zero zones in the *MTF* (blue concentric rings in Fig. 3.24 middle). To avoid even these small zones, time multiplexing of two ring apertures (aperture A and B; Fig. 3.25) with different radii was tested. Time multiplexing in this context means to carry out two different projections of the specimen: The first one using aperture A and the second one using aperture B. The transmission area of each ring aperture is as big as for the single hole aperture that was used for the *L/D*=50 projection. Due to the different radii of the rings in the spatial domain, the minima of the *MTFs* for both ring apertures appear at different locations. For each aperture a projection of the test specimen was recorded. Each projection comprises only $1 \cdot 10^9$ particle histories, hence the sum of exposure times with both rings is the same as for all other simulated projections. For additional improvement of resolution, the distance between aperture and object is 141 cm for these projections. Reconstruction was performed by a Wiener filter using data from both projections: If the absolute value of the *MTF* for ring A is bigger at a certain location (u,v) in the Fourier domain, the data for ring A are reconstructed and vice versa. The reconstructed image in the Fourier domain is therefore:

if $MTF_A(u,v)^2 \geq MTF_B(u,v)^2$

$$FT\{I\}_{reconst}(u,v) = \left\{ \frac{FT\{I_{projA}\}(u,v)}{FT\{PSF_A\}(u,v)} \cdot \frac{MTF_A(u,v)^2}{MTF_A{}^2(u,v) + c_{wiener}} \right\} \qquad (3.18)$$

if $MTF_A(u,v)^2 < MTF_B(u,v)^2$

$$FT\{I\}_{reconst}(u,v) = \left\{ \frac{FT\{I_{projB}\}(u,v)}{FT\{PSF_B\}(u,v)} \cdot \frac{MTF_B(u,v)^2}{MTF_B{}^2(u,v) + c_{wiener}} \right\} \qquad (3.19)$$

The $MTFs$ for the ring apertures and the effective MTF from time multiplexing is shown in Fig. 3.26.

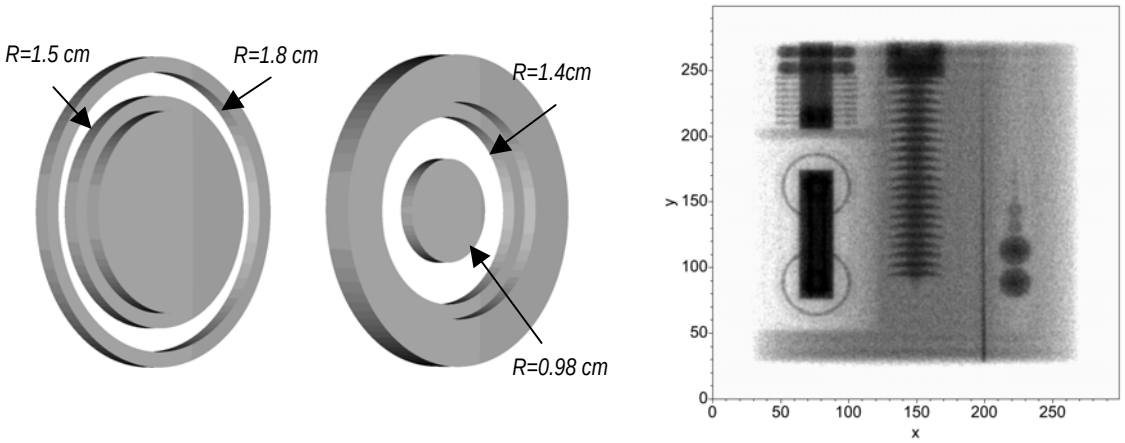

Fig. 3.25: The ring apertures A and B with different radii (left hand side) and the reconstruction from time multiplexing with ring A and B (right hand side)

The reconstruction obtained by time multiplexing with the two rings is shown in Fig. 3.25 right hand side. The constant c_{wiener} was set to 5% of the maximum of the square of the effective MTF. The line profile for the edge of the transformer structure (x=87) is plotted in Fig. 3.27. The gradient at the edge is very similar to that of the unprocessed L/D =122 projection and the reconstruction of the L/D =50 projection. The signal to noise ratio is higher than for the reconstructed L/D =50 projection and for the single ring projection described in the last chapter. However the SNR of the unprocessed L/D =122 projection is not achieved. This method is therefore not interesting for standard neutron radiography applications.

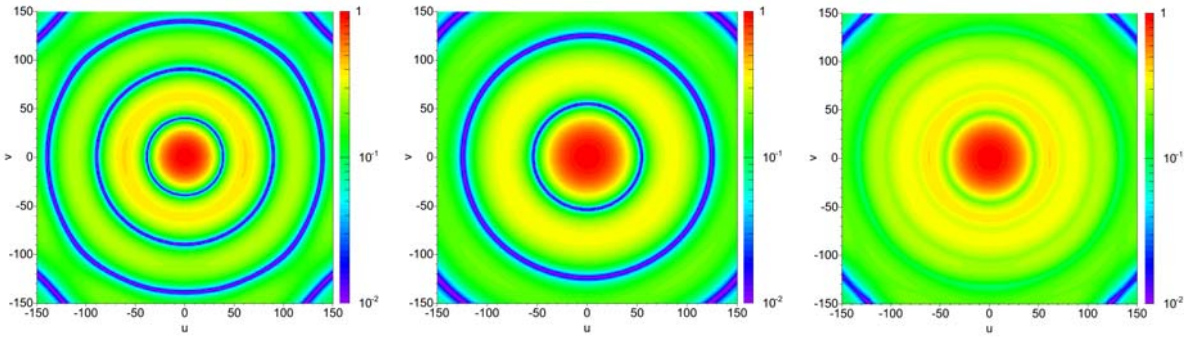

Fig. 3.26: MTF for ring A (left hand side), MTF for ring B (middle) and effective MTF for time multiplexing (right hand side). The combination of the $MTFs$ for both rings reduces near zero areas considerably.

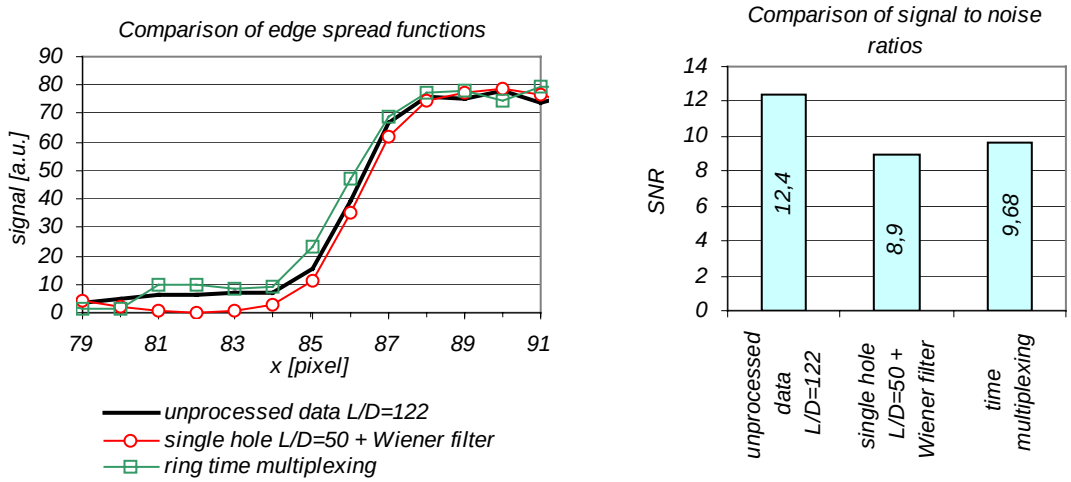

Fig. 3.27: Left hand side: Edge spread functions for unprocessed raw data with L/D =122, for the reconstruction of the single hole L/D =50 projection with Wiener filter, and for the reconstruction of the time multiplexed projection using the two rings (c_{Wiener}=5 % of $\max(MTF^2)$). All methods provide similar resolutions. Right hand side: Comparison of signal to noise ratios. The time multiplexing method achieves a better SNR than the reconstruction of the single hole L/D =50 projection, but the quality of the unprocessed L/D =122 projection is not achieved.

3.5.2 Random array mask

The idea of random array masks also has its origin in X-ray astronomy [60][70]. Equally sized holes are arranged randomly in a regular mesh in an absorber plate. The number of holes is chosen in a way that 50 % of the mesh area is transparent (hence the mesh has the same number of transparent and opaque elements).

The PSF of such masks can be interpreted as coding pattern. From each point in the specimen the total mask pattern is projected to the detector. Illuminated fields in the detector plane are interpreted as ones, dark fields as zeros. The decoding pattern DP looks similar, but all zeros are replaced by minus ones. If the elements of the mesh are numerated with i in the horizontal direction and j in the vertical direction, the decoding pattern DP is

$$DP_{i,j} = \begin{cases} 1 \;\; if \;\; PSF_{i,j} = 1 \\ -1 \;\; if \;\; PSF_{i,j} = 0 \end{cases} \qquad i \in [1,n] \;\; , \;\; j \in [1,n]$$

with n: number of elements in horizontal or vertical direction

For infinite pattern sizes the correlation function of both patterns is a delta function: For a zero shift between coding and decoding pattern, all ones in the coding pattern are multiplied with ones in the decoding pattern, hence the value of the correlation function at this point is the number of transparent fields in the mask. The minus ones of the decoding pattern doesn't come into account because they are multiplied with zeros of the coding pattern. For all other shifts between coding and decoding pattern, the same number of ones in the coding pattern are multiplied with ones and with minus ones in the decoding pattern, due to the random statistical distribution of transparent and opaque fields. I.e. for infinite mask size, the correlation function would be zero for all non-zero shifts between coding and decoding pattern:

$$PSF \otimes DP = \delta \qquad (3.20)$$

Therefore image reconstruction for this mask type can be performed by correlating the raw data with the decoding pattern.

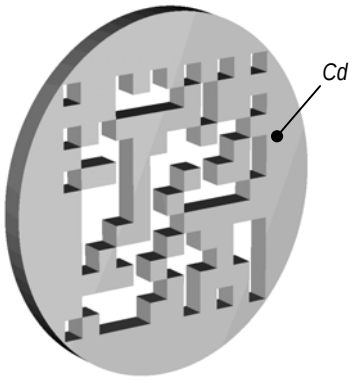

Fig. 3.28: Random array mask

For testing random arrays in neutron radiography the mask shown in Fig. 3.28 was used. It is made of a Cadmium plate with 2 mm thickness. Each hole has a size of 2.3 mm x 2.3 mm. The number of holes in the pattern is rather small. Most neutron radiography facilities have a narrow beam that doesn't allow bigger masks.

The PSF or coding pattern for the mask, the decoding pattern, and their correlation function are displayed in Fig. 3.29. Compared to the transmission function of the

aperture, the PSF is mirrored at a point and scaled. Due to the finite size of the mask, the correlation function is not a delta function: Small side lobes around the central peak occur. Therefore the projection of a single point of the specimen would be reconstructed satisfying (the correlation function displayed in Fig. 3.29 right hand side corresponds to the reconstruction of a single transmitting point in the specimen).

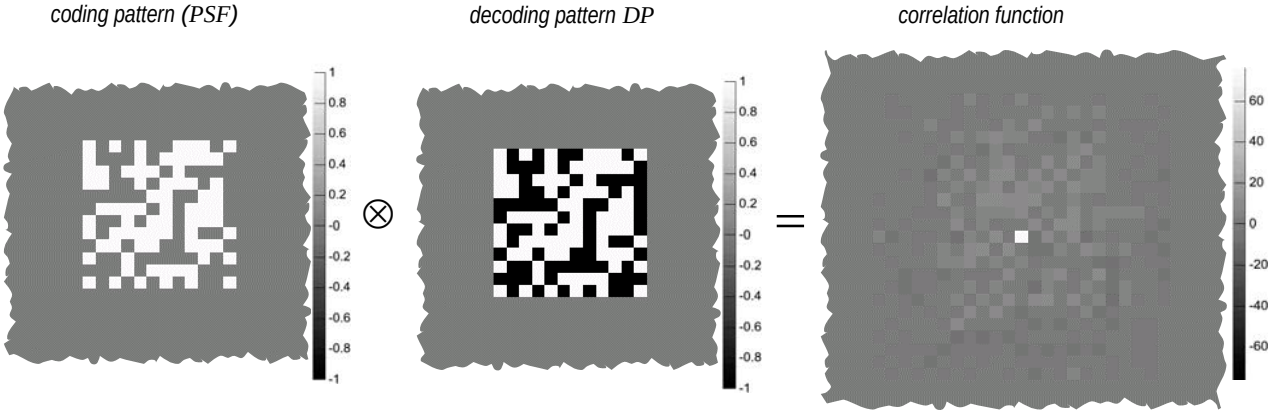

Fig. 3.29: The PSF or coding pattern for the random array mask (left hand side), the decoding pattern DP (middle) and the correlation function (right hand side) of PSF and DP. In the correlation function a bright single spot with small side lobes appear. All values beyond the displayed regions are zero.

The reconstruction of the neutron radiography of the test specimen obtained by the random mask is shown in Fig. 3.30: A faint but sharp image is superposed by many 'ghost images', caused by the small side lobes in the correlation function. Although inherent noise is reduced compared to the ring aperture, the result of reconstruction is also not satisfying. For extended structured objects this method is not advantageous. Inherent noise decreases for an increasing number of holes. Even masks with some 100 holes were tested but didn't achieve significantly better results. However, like in the case of the ring aperture, special applications are imaginable: e.g. detection of vesicular voids in homogeneous materials. Here the random array mask gets ahead the ring aperture due to less inherent noise from the correlation function of the coding and decoding pattern.

It is also proposed to reconstruct images obtained by random array masks by periodic correlation of coding and decoding pattern. This method avoids a problem that occurs for non periodic correlation: for big shifts between coding and decoding pattern the overlap of both patterns is rather small, i.e. values of the correlation function at these locations are determined by the values of only a few fields in both patterns. The basic assumption that the ones in the coding pattern overlap with exactly the same number of ones and minus ones in the decoding pattern (due to the statistical distribution of transparent and opaque mesh elements) is no longer well satisfied [63]. On the other hand periodic correlation has also disadvantages: The reconstruction is only performed for a number of pixels in the detector equal to the number of fields in the mask. Here periodic correlation would reconstruct only a region of 12 x 12 pixels. Non periodic correlation reconstructs the whole data in one step. A general problem that occurs with random array masks is that the shadow of the mask caused by a point in the specimen must fit exactly into the pixel structure of the detector. I.e. for a given pixel size in the detector and a given field size in the mask, one is not free to choose the distance between mask and object and the distance between object and detector.

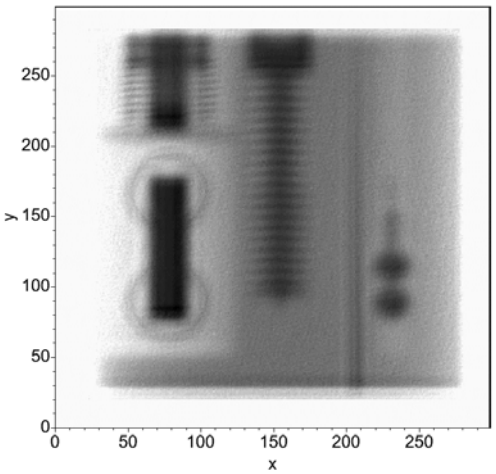

Fig. 3.30: Reconstruction of the projection of the test specimen obtained by the random array mask

3.5.3 Uniformly redundant array mask

Reconstructions from projections obtained by random array masks suffer from inherent noise caused by the finite extension of the array (see previous chapter). However, special mask patterns and

decoding patterns can be found for which inherent noise in reconstructions is exactly zero even for finite mask extensions [60] when the reconstruction is performed by periodic correlation. The periodic correlation of coding and decoding pattern is exactly a δ -function:

$$PSF \otimes DP = \delta \quad (3.21)$$

The arrays are called 'pseudo-noise arrays' [76] or 'uniformly redundant arrays' (URA). Uniform redundance means that the periodic autocorrelation of the pattern consists of a central peak and flat side lobes, i.e. if the mask pattern is periodically overlapped with itself, exactly the same transmission area occurs for all non-zero shifts between the masks. The mask pattern is arranged in a regular mesh. Fig. 3.31 shows an example for a 13 x 11 mesh [60]. The decoding pattern for the array is found by replacing all zeros (opaque fields) in the coding pattern (=mask pattern) by minus ones. Reconstruction of projections obtained by a URA mask is performed similar to that of random array masks (see previous chapter), but in contrast to random array maks correlation between coding pattern and decoding pattern has to be peridioc.

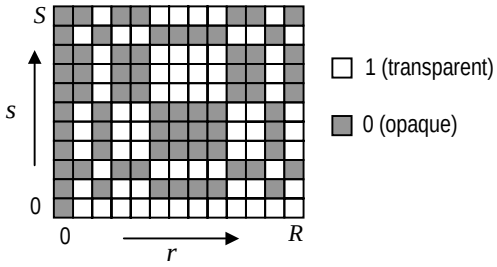

Fig. 3.31: Illustration of the mesh for a 13 x 11 URA basic pattern

The advantages of this mask type are a relative high transmission through the aperture (about 50 %) and the absence of inherent noise. However this mask type has also disadvantages:

- Each point of the specimen projects a shadow of the mask pattern on the detector. The shadow of the mesh must fit exactly to the pixel structure of the detector system. Hence the distance between mask and specimen and the distance between specimen and detector has to be chosen very carefully.
- Each point of the specimen must project a full shadow of the mask pattern to the detector. This is especially a problem for regions at the margin of the detector area where some points of the specimen project only a part of the mask pattern to the detector area (Fig. 3.32 left hand side). In this case the projection cannot be reconstructed correctly. To avoid this problem, an additional mask that limits the illuminated area of the specimen is necessary (Fig. 3.32 right hand side).

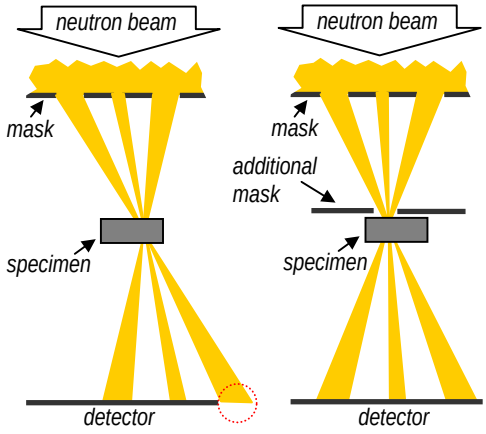

Fig. 3.32: Due to the limited detector area, some points in the object project only a part of the mask pattern to the detector area (left hand side). The projection cannot be reconstructed correctly in this case. In order to avoid this problem an additional mask that limits the illuminated area of the specimen is necessary (right hand side).

- Since a periodic correlation is used for reconstruction, only a region of the projection that has the dimension of the basic mask pattern (in pixels) can be reconstructed.

These three disadvantages make this mask type uninteresting for day-to-day use in neutron radiography. The first two points are less important when the distance between

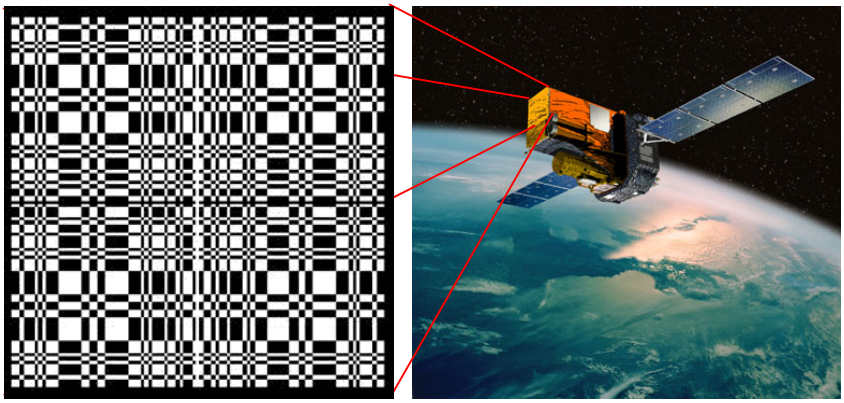

Fig. 3.33: The INTEGRAL (International Gamma-Ray Astrophysics Laboratory) satellite (right hand side) and the URA mask (left hand side) of the IBIS (Imager on Board INTEGRAL Satellite) instrument for observation of gamma radiation in the energy range from 20 keV up to 10 MeV [74].

observed object and detector is fixed, like e.g. in X-ray astronomy where all observed objects are practically at infinity (unlike in neutron radiography). A modified uniformly redundant array (MURA) is used on board the INTEGRAL (International Gamma-Ray Astrophysics Laboratory) satellite for the IBIS experiment (Imager on Board INTEGRAL Satellite) [75]. The mask pattern and the satellite [74] are shown in Fig. 3.33. The energy range for observation is from 20 keV to 10 MeV. The basic mask pattern has 53 x 53 pixels.

3.5.4 Non redundant array mask

The examined combinations of coded mask and reconstruction algorithm do either not achieve the quality of a projection obtained by a single hole aperture using an appropriate L/D ratio or are not applicable in neutron radiography for practical reasons. Although the transmission area of the single hole aperture is much smaller compared to coded masks, reconstruction results of data obtained by coded masks do not achieve the same SNR. Results of convolution techniques suffer from inherent noise caused by the mask pattern and deconvolution techniques suffer from noise amplification by reconstruction algorithms. Therefore it is in general advisable to use a single hole aperture and no reconstruction algorithm. The L/D ratio has to be chosen with regard to the wanted compromise between sharpness and noise in the projection.

However, there are limits: A free choice of the L/D ratio is not always possible. Examples for restrictions are:

- Low intensity due to nearly black regions in the specimen result in zero count regions in the projection and desired resolution is prohibitive for decreasing the L/D ratio.
- In phase contrast radiography (see chapter 3.6.2.2) very high L/D ratios (above some 5000) are necessary to get an observable phase shift effect. If the desired SNR in a projection is not reached, the L/D ratio cannot be decreased.

The case of a high resolution projection of the test specimen taken with a single hole aperture (Fig. 3.35) is shown in Fig. 3.34. The size of the hole is 2.3 mm x 2.3 mm (the L/D ratio in vertical and horizontal direction is 430). For this projection, in many pixels no neutrons were counted due to the low transmission through the mask. The SNR in this projection is 3.2. With phase contrast radiography even much higher L/D ratios are necessary. In these cases the coded mask as described below is applicable.

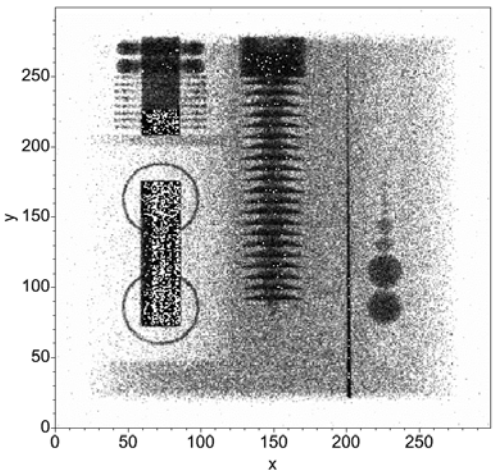

Fig. 3.34: Projection obtained by a single hole aperture (L/D =430)

A non redundant array (NRA) [64] is a pattern of which the autocorrelation function has minimal side lobes. All holes in a non redundant array mask are arranged in a regular mesh. The special property of the non redundant arrangement of holes in a NRA mask is: If the mask is overlapped with itself without any shift, all holes of the masks overlap. If the masks are shifted one or an integer multiple of a mesh unit, only one or no holes overlap (unlike in a redundant array mask, where the number of overlapping holes can be anywhere between zero and the total number of holes). Hence, the ratio between the height of the side lobes and the central peak in the autocorrelation function of a non redundant array is maximal $1/n$, where n is the number of holes in the mask. In the case of a redundant array this ratio can be up to $(n-1)/n$. As shown in the chapters above, side lobes in the autocorrelation function are bothering in a reconstruction using correlation techniques because the side lobes are the origin of inherent noise in the reconstruction. The non redundant array mask is therefore advantageous compared to a redundant array. However, non redundant arrays are not proposed to improve the quality of a projection [65]. Their original purpose is to provide depth information about the specimen: When the distance between aperture and object is chosen small, the PSF is not constant for an extended object (extended in beam direction), but depends on the depth in the specimen. For layers close to the detector, the PSF is scaled small, for layers at big distances to the detector the PSF is scaled big. Scaling the PSF by a certain factor and correlating the image with this

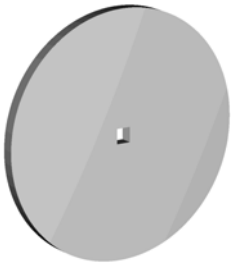
Fig. 3.35: Single pin hole aperture for the L/D =430 projection

PSF reveals therefore more information of one selected layer in the object than of other layers. By the scaling factor, the depth of the reconstructed layer is chosen. For this technique it is essential to have minimal overlap between two different scaled *PSFs*. Otherwise bothering effects from other layers that exist anyway would be pronounced.

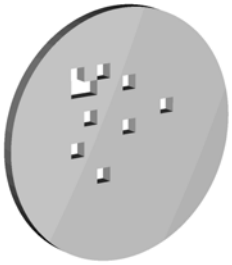

Fig. 3.36: 10 hole non redundant array mask (NRA)

The NRA mask was tested using the aperture shown in Fig. 3.36. It is a 10 hole aperture. Each hole has the same size as the single hole of the aperture shown in Fig. 3.35. Neutron fluence at the object is therefore 10 times higher than with the single hole mask. The unprocessed raw data is the superposition of 10 sharp projections of the test specimen.

3.5.4.1 Correlation technique

For the setup of the virtual radiography station and the test specimen as described above, the *PSF* can be assumed to be constant for the whole object: The object size is always small compared to the distance between aperture and object. The correlation of the projection with the *PSF* reconstructs therefore not only one layer but the whole object. The result of the reconstruction is shown in Fig. 3.38. Like for the correlation methods using other coded masks as described in the preceding chapters, a faint but sharp image is superposed by many ghost images, caused by the small side lobes in the autocorrelation function of the *PSF* (Fig. 3.37). However, the structure of the specimen is much better recognizable compared to the other correlation methods. The level of inherent noise caused by the NRA mask is lower than e.g. with the ring mask.

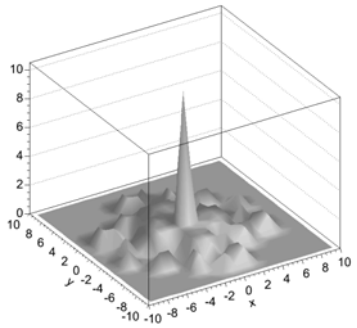

Fig. 3.37: Autocorrelation function of the *PSF* for the 10 hole NRA

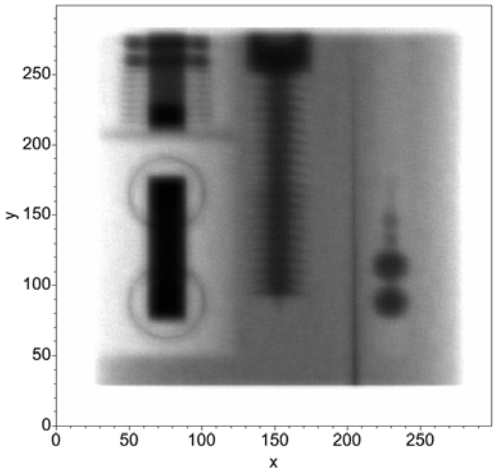

Fig. 3.38: Reconstruction by correlation method of the projection of the test specimen, obtained by a 10 hole NRA mask.

3.5.4.2 Deconvolution technique

The *MTF* for the 10 hole non redundant array (NRA) mask is shown in Fig. 3.53. It has only small near zero zones. This is a good condition for the application of deconvolution algorithms. The result of a reconstruction of a projection obtained by the 10 hole NRA mask by a Wiener filter with c_{wiener}=5 % of the maximum of the square of the *MTF* is shown in Fig. 3.39. The reconstruction is considerably less noisy (*SNR*=5.0) and shows no major loss in resolution compared to the projection obtained by the single hole mask (Fig. 3.34). The line profiles at the edge of the transformer like structure are shown in Fig. 3.40 for the reconstruction of the projection obtained by the NRA mask and the unprocessed data from the single hole projection. For comparison the diagram shows also the line profile for a single hole aperture with same transmission area as the sum of all holes in the NRA mask: Due to the extended aperture opening, the gradient at the edge of the transformer like structure is much lower.

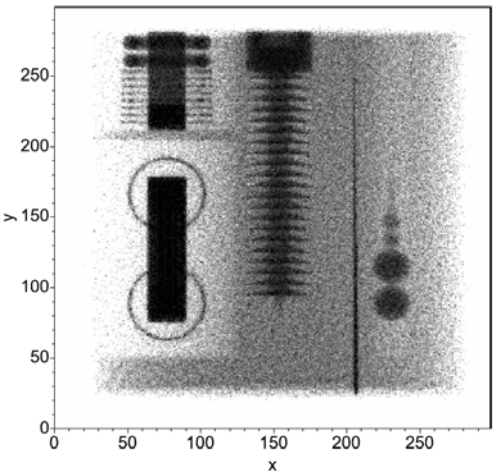

Fig. 3.39: Reconstruction of the test specimen obtained by the 10 hole NRA mask with deconvolution by wiener filter (c_{wiener}=5 % of $max(MTF^2)$).

From the result for the 10 hole NRA, the question arises

how many holes provide optimal deconvolution properties: A small number of holes keeps near zero zones in the *MTF* small (Figs. 3.49 to 3.54), but transmission through the aperture is also limited, resulting in a high noise level in the projection. For a big number of holes, transmission through the aperture is higher and the noise level is reduced. But the *MTF* shows bigger near zero zones. These are two competitive effects that were investigated with the apertures shown in Figs. 3.41 to 3.45. Each aperture consists of a cadmium plate (thickness 2 mm) with a different number of holes, each of the same size (2.3 mm x 2.3 mm). The 10 hole NRA arrangement is the same as described above (Fig. 3.36). For comparison Fig. 3.46 shows a 10 hole redundant array mask with same transmission area as the 10 hole NRA mask.

The *MTFs* for these apertures, when applied to the setup of the virtual radiography station, are shown in Fig. 3.49 to Fig. 3.54. The size of near zero zones increases fast with each additional hole for small hole numbers. For big hole numbers the near zero zones are growing much slower. The advantage of the non redundant arrangement compared to a redundant arrangement is visible by comparison of the *MTFs* for the 10 hole NRA mask and the 10 hole redundant array mask (Figs. 3.53 and 3.54): Despite the same transmission area, the redundant array shows considerably larger near zero zones and succumbs therefore to the NRA.

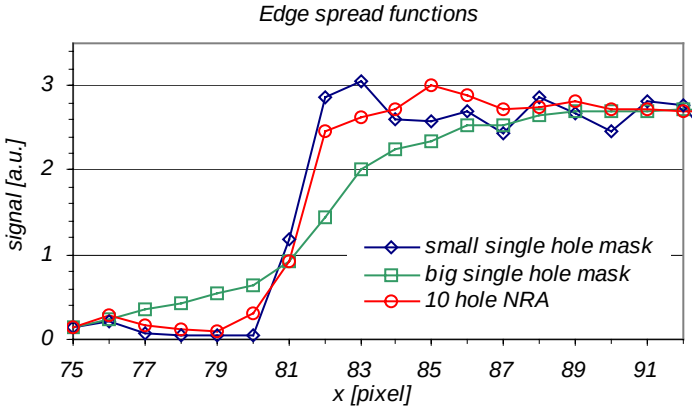

Fig. 3.40: Line profiles at the transformer like structure in the projection obtained by a big single hole mask (transmission area 54 mm^2), a small single hole mask (transmission area 5.4 mm^2), and a 10 hole NRA mask (total transmission area 54 mm^2). The transmission area of the big hole mask is as big as the transmission area of the 10 holes in the NRA mask. The transmission area of the small single hole mask is as big as one hole in the 10 hole NRA mask. The displayed data for the single hole masks are unprocessed raw data and the data for the NRA is a reconstruction obtained by a Wiener filter with c_{wiener}=5 % of max(MTF^2).

The *SNR*s in reconstructions from projections obtained by the apertures is shown in Fig. 3.47. Wiener filters were used for the reconstructions. As the signal to noise ratio in restored data strongly depends on the choice of the constant c_{wiener}, deconvolution was performed with a set of five different constants for each aperture. The results are compared with the unprocessed data of the single hole aperture. Fig. 3.47 shows, if c_{wiener} is chosen bigger than 5 % of the maximum of the squared *MTF*, the *SNR* in the reconstructions from the multiple hole NRAs is higher than in the unprocessed single hole data. The *SNR* increases with increasing number of holes (of course, the lower limit of c_{wiener} as described here can not be generalized for other projections and is only valid for the setup described here; it strongly depends on exposure time, source yield and attenuation in the specimen). If the constant c_{wiener} is chosen smaller, the *SNR* in the reconstructions is even worse than in the unprocessed single hole data. Although the *SNR* rises slightly for more than four holes, even the *SNR* of the 10 hole reconstruction is below the single hole arrangement. I.e. multiple hole NRA apertures are interesting whenever deconvolution has to be performed only to a certain degree. Contrary to deconvolution of data from an extended single hole aperture (e.g. the *L/D* =50 projection described above), where the goal of reconstruction is to improve resolution, here

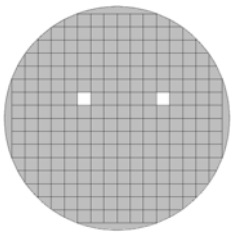

Fig. 3.41: 2 hole NRA mask

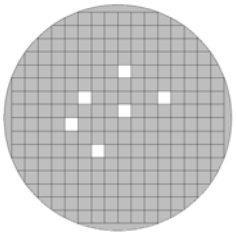

Fig. 3.43: 6 hole NRA mask

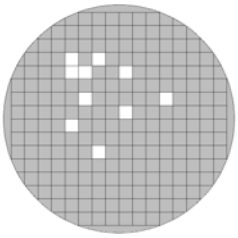

Fig. 3.45: 10 hole NRA mask

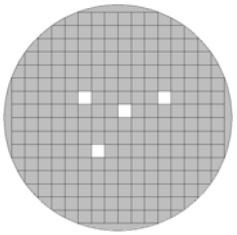

Fig. 3.42: 4 hole NRA mask

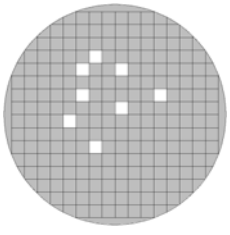

Fig. 3.44: 8 hole NRA mask

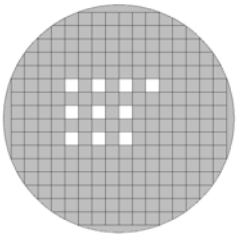

Fig. 3.46: 10 hole redundant array mask

only the superimposed sharp signals have to be merged. Therefore, even high values of c_{wiener} result in satisfying results. This is demonstrated with the projection obtained by the 2 hole NRA mask in the sequence of Fig. 3.48: The unprocessed data (left hand side) shows two superposed shadows of the transformer like structure, each with same intensity. Deconvolution with c_{wiener}=70 % of the maximum of the squared MTF results in an intense single shadow and a weak ghost image. For values of c_{wiener} below 10 %, the ghost image is barely recognizable.

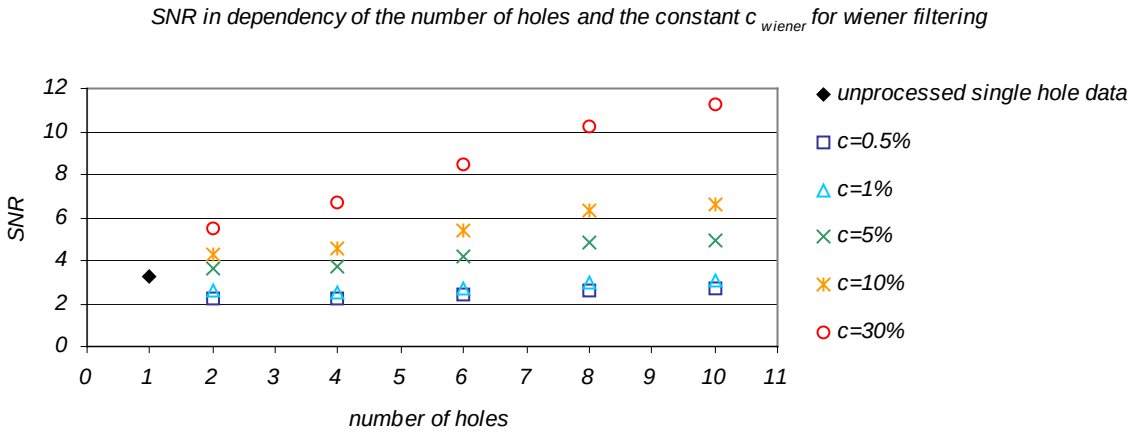

Fig. 3.47: Signal to noise ratios ($SNRs$) in the reconstructions of the projections obtained by NRA masks in dependency of the number of holes and the constant c_{wiener} for wiener filtering

The NRA mask is the only one of all investigated coded masks that is advantageous in a wide field of applications in neutron radiography. Possible applications are in phase contrast radiography, where the necessity of a very high L/D ratio limits intensity, or in dynamic radiography of non-periodic processes, where exposure time is limited by the observed process. The number of holes should be as big as possible. However, due to the special arrangement of holes, the density of possible holes is decreasing very fast with increasing hole number, hence NRA masks with much more than about 20 holes are difficult to use in neutron radiography. A wide neutron beam at the location of the aperture is necessary in this case.

In contrary to the random array mask and the uniformly redundant array (URA) mask, the mesh size of the NRA has not to be adjusted exactly to the pixel mesh of the detector system. Hence there are less restrictions for the distance between mask and object and the distance between object and detector.

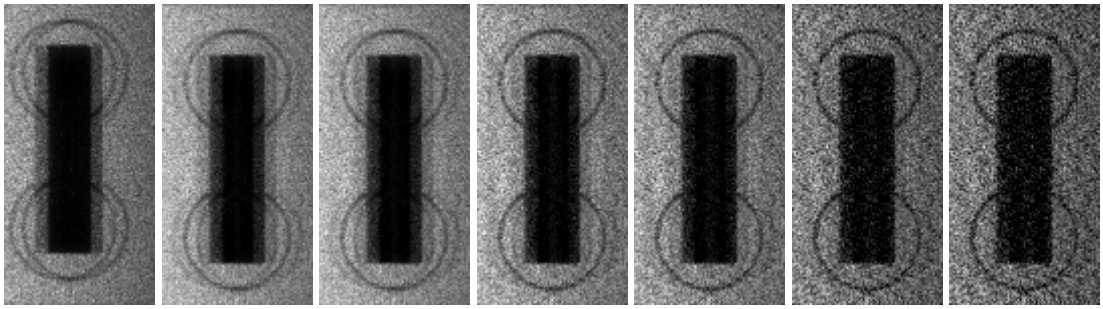

Fig. 3.48: Reconstructions of the data obtained by the 2 hole mask (Fig. 3.41) for different constants c_{wiener} for wiener filtering. From left to right: unprocessed raw data, reconstruction with c=70 % of the maximum of MTF^2, c_{wiener}=50 %, c_{wiener}=10 %, c_{wiener}=5 %, c_{wiener}=1 %, c_{wiener}=0.5 %

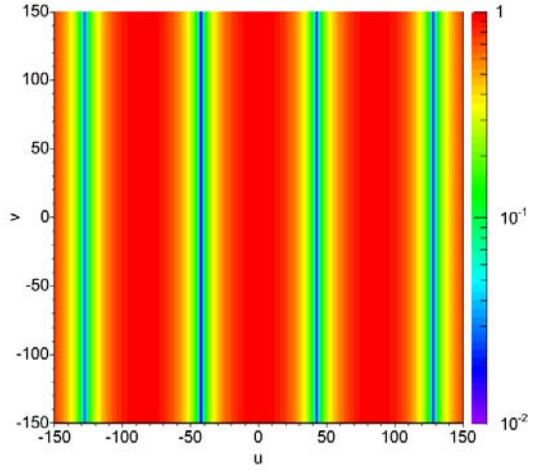

Fig. 3.49: MTF for the 2 hole NRA mask (Fig. 3.41)

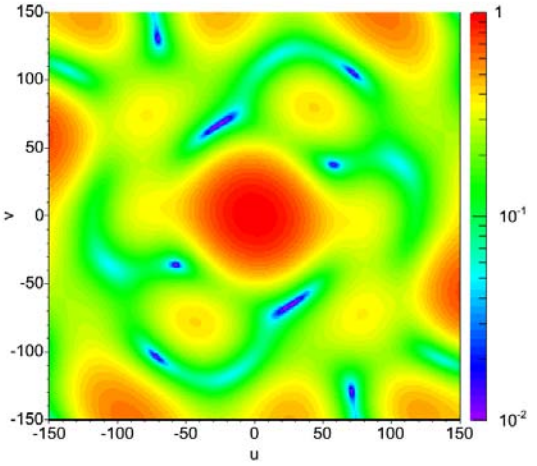

Fig. 3.52: MTF for the 8 hole NRA mask (Fig. 3.44)

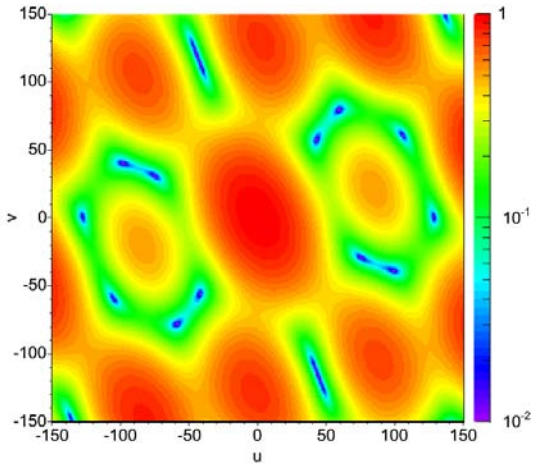

Fig. 3.50: MTF for the 4 hole NRA mask (Fig. 3.42)

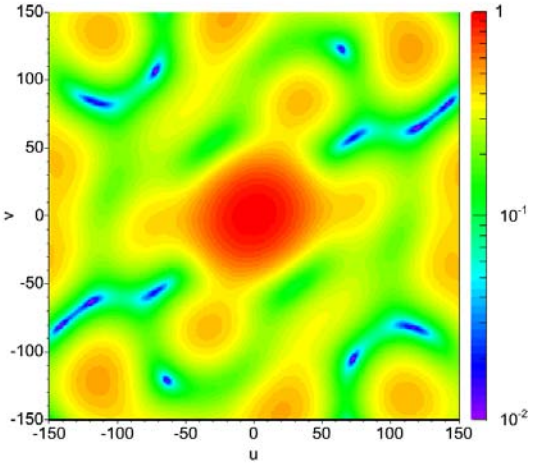

Fig. 3.53: MTF for the 10 hole NRA mask (Fig. 3.45)

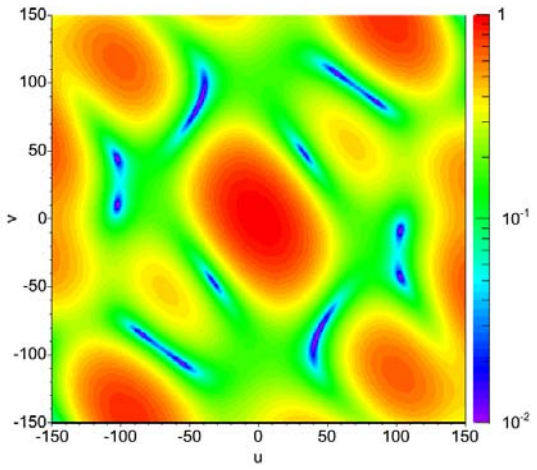

Fig. 3.51: MTF for the 6 hole NRA mask (Fig. 3.43)

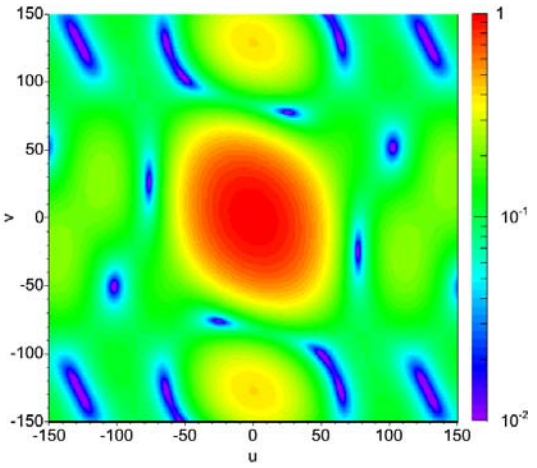

Fig. 3.54: MTF for the 10 hole redundant array mask (Fig. 3.46)

A circular single hole mask with equal transmission area as the 10 hole NRA mask (Fig. 3.45) and the 10 hole redundant array mask (Fig. 3.46) is shown in Fig. 3.55. The resulting MTF for this aperture when applied to the virtual radiography station is shown in Fig. 3.56. On the one hand in some regions of low frequencies the values of the MTF even exceed the values of the MTF of the 10 hole masks. On the other hand the near zero zones (blue and violet regions in Figs. 3.53, 3.54, 3.56) that are most bothering for reconstruction are much larger for the single hole arrangement. They are located at high frequencies and limit therefore the resolution of fine structures in the projection considerably. The information about frequencies in a projection in near zero zones of the MTF is lost. Comparing all masks with equal transmission area, the MTF of the NRA mask shows the lowest size of near zero zones and the single hole arrangement shows the biggest size of near zero areas. Hence, the loss of information in the projection is minimized with the NRA mask without reduction of neutron flux.

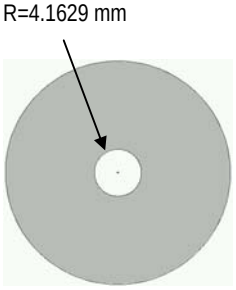

Fig. 3.55: Circular single hole aperture with equal transmission area than the 10 hole NRA mask (Fig. 3.45) and 10 hole redundant array mask (Fig. 3.46)

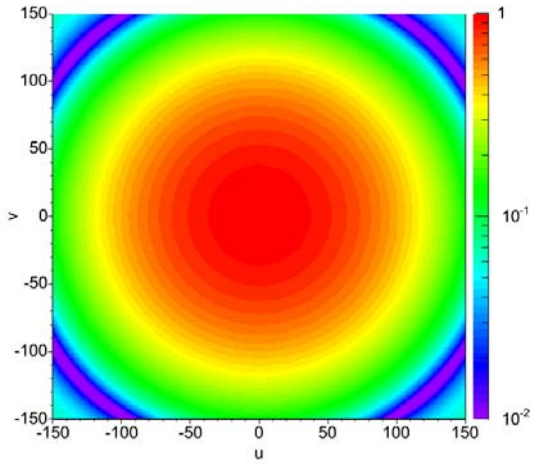

Fig. 3.56: MTF for the circular single hole aperture (Fig. 3.55) with equal transmission area than the 10 hole masks (Figs. 3.45, 3.46)

3.5.5 Apodization

The original idea of apodization [66] is to modify a measured signal in a way that bothering effects from the experimental setup are suppressed. These bothering effects can be e.g. diffraction patterns from pinhole apertures when the wavelength of radiation is close to the diameter of the aperture: The sharp edges of the aperture, where the transmission decreases abruptly from one to zero, cause side maxima in the measured signal. The signal of a point source looks similar to the sine cardinal function shown in Fig. 3.9 right hand side. In order to suppress these side maxima, an aperture with smaller gradients in the transmission function can be applied, i.e. a semi transparent aperture material has to be used. Another example for application of apodization is in Fourier transform infrared spectroscopy FTIR. Due to the small wavelengths of neutrons (some 2 Å) no diffraction problems occur in neutron radiography (the neutron wavelength is much smaller than the aperture diameter). However, apodization was tested for neutron radiography in order to minimize near zero zones in the MTF. The idea is to avoid zeros in the Fourier transform of the PSF that occur with extended single hole apertures (the PSF is a pill-box function for circular single hole apertures). As a Gauss function never becomes zero and its Fourier transform is also a Gauss function, the PSF of the neutron radiography station was shaped to a Gauss function. This was done by a lead filter. Lead was chosen because of its low gradient of neutron cross sections in dependency of energy in the region between 1 meV and 1 keV (Fig. 3.57). By this beam hardening effects are reduced. A desirable side effect of lead

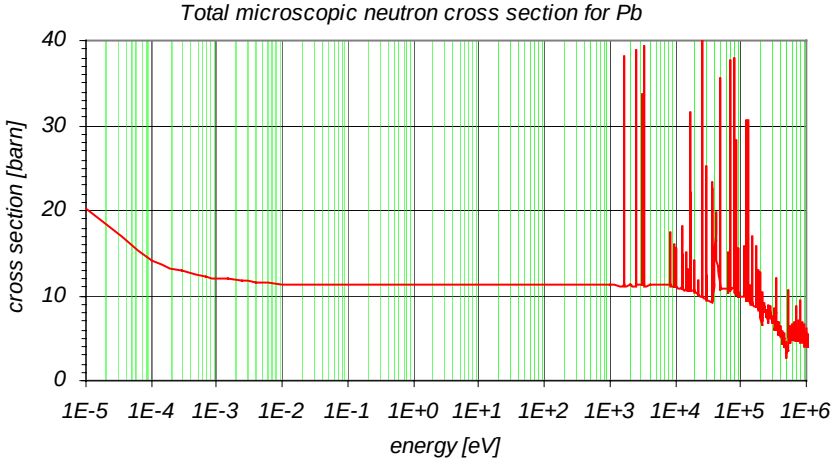

Fig. 3.57: Microscopic total neutron cross section for Pb (natural isotope composition, data from [12])

as filter material is the high gamma attenuation, i.e. background gamma radiation in the beam is also reduced. The lead filter is shown in Fig. 3.58. It is a lead cylinder with a diameter of 4 cm, a length of 12 cm, and a special inner shape. The transmission $T(R)$ of neutrons through the filter material in dependency of the distance R to the beam axis (transmission function) is given by Eq. 3.21. It considers the energy dependent attenuation of neutrons in aperture material as well as the energy dependency of neutron detection (here the ^{7}Li(n,α)^{3}H reaction). The transmission function $T(R)$ is adjusted by the thickness $t(R)$ of lead in dependency of the distance R to the filter axis:

$$T(R) = \frac{\int_0^\infty \Sigma_{Li}(E) \cdot \Phi(E) \cdot e^{-\Sigma_{Pb}(E) \cdot t(R)} dE}{\int_0^\infty \Sigma_{Li}(E) \cdot \Phi(E) dE} \quad (3.21)$$

R : Distance from filter axis
$T(R)$: Transmission through filter at radius R
$t(R)$: Thickness of lead at radius R
Σ_{Li} : Macroscopic ^{7}Li(n,α)^{3}H cross section
Σ_{Pb} : Macroscopic total cross section of Pb
$\Phi(E)$: Neutron flux density at energy E.

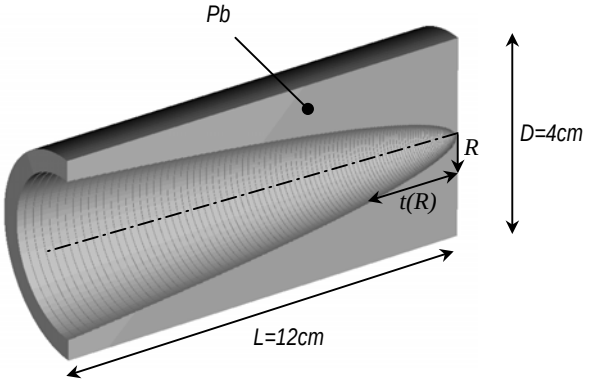

Fig. 3.58: Cut through the lead filter that shapes the PSF to a Gauss function

For big distances between filter and specimen the PSF obtained by the lead filter becomes:

$$PSF(r) = T(r \cdot L / d) \quad (3.22)$$

L : Distance filter-specimen
d : Distance specimen-detector
r : Distance from center of PSF

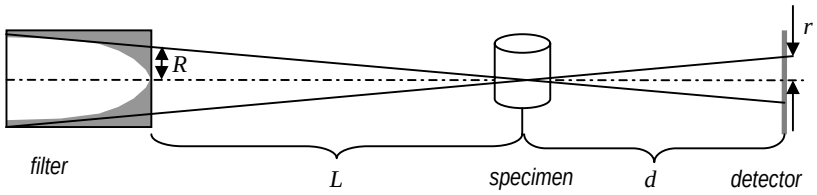

Fig. 3.59: Schematic overview of the arrangement with lead filter

In a strict sense Eq. 3.22 is only true for infinite distance between filter and specimen, but it is even a good approximation for the virtual radiography facility, where the distance between filter and specimen is only 1 m. The desired PSF for neutron radiography was a Gauss function as shown in Eq. 3.23, where ps is the pixel size (467 µm):

$$PSF(r) = \exp\left(-\left(\frac{r}{0.2 \cdot ps}\right)^2\right) \quad (3.23)$$

The inner shape of the aperture $t(R)$ was calculated according to Eqs. 3.21, 3.22 and 3.23. In principle a Gauss function never becomes zero, hence the lead filter must have an infinite diameter. On the other hand, the value of the PSF is below 2 % of the maximum of the PSF for distances of more than 4 mm from the center of the PSF (Fig. 3.60). Hence setting all values of the PSF to zero in this region is a satisfying approximation of the Gauss function for apodization purposes. The aperture radius can be limited to 2 cm.

A comparison between the desired PSF from Eq. 3.23 and the obtained PSF by the lead filter is displayed in Fig. 3.60.

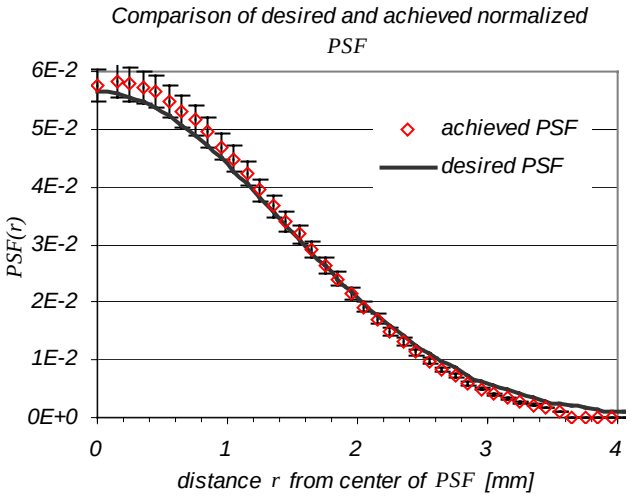

Fig. 3.60: Comparison of the desired PSF and the PSF obtained by the lead filter

For testing the lead aperture for radiography purposes, it was mounted inside the collimator of the virtual radiography station. The projection obtained with the lead filter is shown in Fig. 3.61 left hand

side. For comparison the projection obtained by the single pin hole arrangement with L/D =50 geometry is plotted in Fig. 3.61 right hand side. Transmission trough the lead filter and the single pin hole aperture is the same. Hence the signal to noise ratio in both projections is also the same. The image quality of the projection obtained by the single pin hole arrangement is superior to the quality of the projection obtained by the lead filter. The $MTFs$ for the lead filter arrangement and the single pin hole arrangement are shown in Fig. 3.62. Close to the origin of the Fourier domain (low frequencies), the MTF for the lead filter has higher values than the MTF for the single pin hole arrangement. The latter one shows even near zero zones for low frequencies. Hence for projections of specimen with wide structures the lead filter would be superior. For bigger distances from the origin (high frequencies), the MTF of the lead filter arrangement has smaller values than the MTF for the single pin hole (but no zero regions). Hence fine structured specimen (as the test specimen) can be projected with higher quality with the single pin hole arrangement. For most applications in neutron radiography apodization is therefore not beneficial. However the lead filter has an advantage compared to the single pin hole arrangement: Attenuation of gamma radiation by the Cd-plate with the single pin hole is negligible compared to the attenuation by the lead filter. For neutron beams with high contamination by gamma radiation the lead filter may be advantageous.

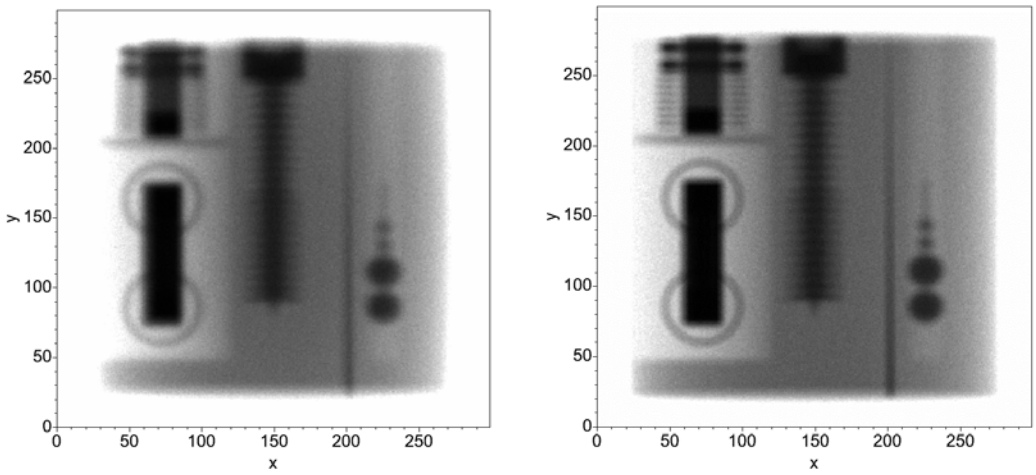

Fig. 3.61: Projections of the test specimen obtained by the lead filter (left hand side) and by a the single pin hole arrangement with L/D =50 ratio. Flux in the detector plane is the same for both projections. Hence the signal to noise ratio SNR is also the same.

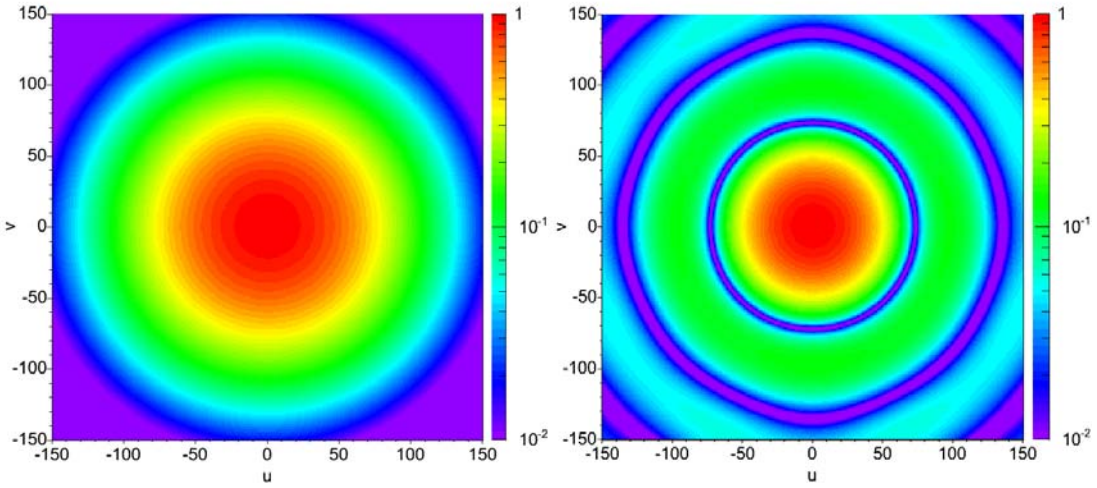

Fig. 3.62: $MTFs$ of the arrangement for apodization with lead filter (left hand side) and for the single pin hole arrangement with L/D =50 geometry (right hand side).

3.5.6 Limits of coded mask imaging

The quality of a reconstruction from a projection obtained by a coded mask is dependent on the specimen. There are certain structures that cannot be reconstructed correctly. This is demonstrated by a slightly modified version of the test specimen projected by the 10 hole NRA mask shown in Fig. 3.36. The wedge shaped gap of depth 1 cm filled with cadmium is replaced by a gap that tunnels through the whole specimen and that is not filled with any material. Drill holes of different diameter, heading in beam direction and also spanning through the whole object are placed between the screw and the iron balls. This new version of the test specimen is displayed in Fig. 3.63.

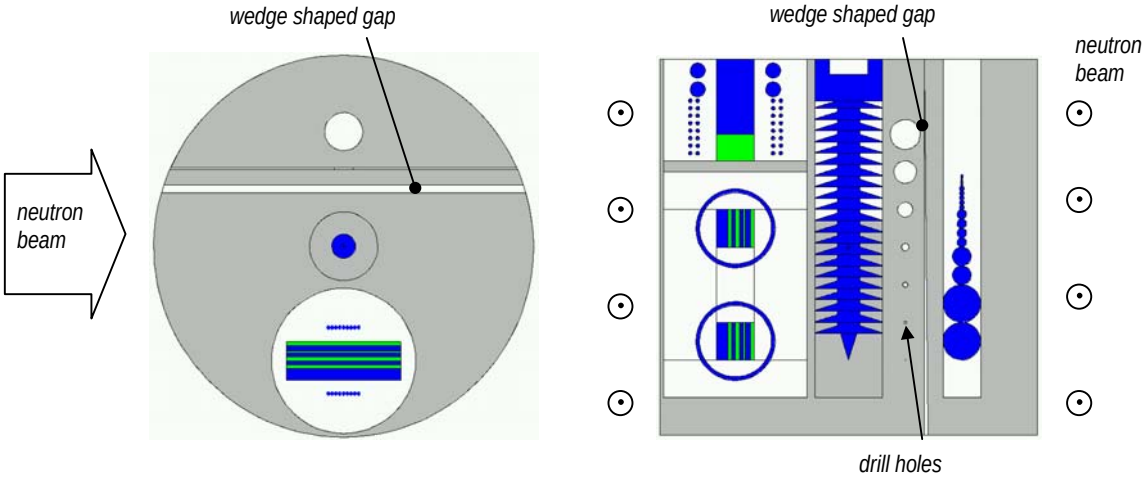

Fig. 3.63: Horizontal cut (left hand side) and vertical cut (right hand side) through the modified test specimen. An end-to-end gap and drill holes are added to the specimen in this version. The gap and the holes are not illuminated in the same way by all holes of the coded mask.

A reconstruction of a projection of the new specimen obtained by the 10 hole NRA as described above is shown in Fig. 3.64 (a Wiener filter was used for reconstruction): The new structure elements are not satisfactorily restored. Especially the wedge shaped gap is not resolved correctly. The reason is that the gap is not illuminated by all holes in the mask in the same way: Neutrons from holes located in gap direction can cross the specimen through the gap without any interaction. This is not the case for holes located not in gap direction. I.e. the signals caused by each hole are not identical and cannot be merged by deconvolution as described above.

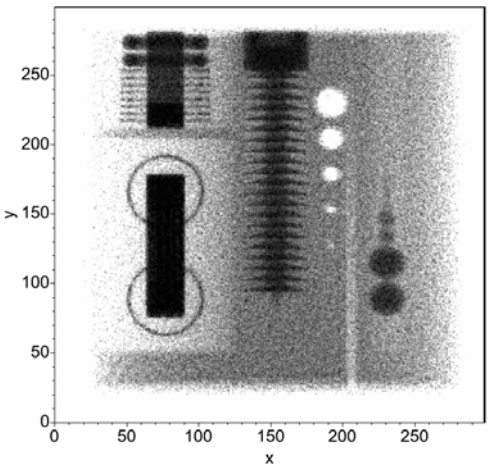

Fig. 3.64: Reconstruction of the modified specimen. Especially the end-to-end gap is not resolved properly, because it is not illuminated by all holes of the coded mask in the same way.

3.6 Experimental results

3.6.1 Image deconvolution

The application of image deconvolution algorithms in neutron radiography was tested for some of the first projections measured at the ANTARES facility. All data shown in this chapter were recorded at a reactor power of 20 MW and with the collimator with an aperture diameter of 2.1 cm (L/D=800 collimator). As detector the ANTARES standard detector was used (chapter 2.9.1 'ANTARES detector system'). Correction of image degradation by geometry effects from the neutron beam was performed as well as correction of detector blur.

3.6.1.1 Revision of image degradation by geometry effects

Revision of image degradation due to an extended aperture (effective neutron source of the neutron radiography station) was tested with an old electric temperature indicator as specimen. The device is shown in Fig. 3.65 and its high resolution radiography in Fig. 3.66.

Fig. 3.65: Temperature indicator that was used as specimen

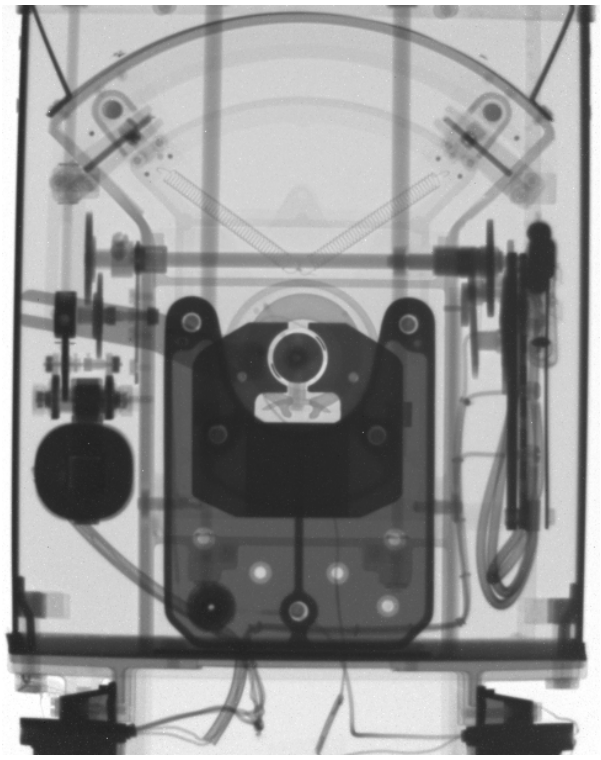

Fig. 3.66: High resolution projection of the temperature indicator

High resolution was obtained by placing the specimen at a distance of only 37 cm to the scintillator. Exposure time was 5 sec. The L/D ratio is 780 in this case. Even subtle details are recognizable. The point spread function PSF of the neutron beam is a pill-box function with a diameter of only 470 µm for this projection. The displayed data was preprocessed analog to the procedure described below for the blurred image. A blurred projection of the specimen was achieved by placing the specimen at a distance of 2 m to the scintillator. Exposure time was also 5 sec. Even though the L/D ratio is quite high (L/D=700), the PSF of the neutron beam is much more extended now, due to the big distance between specimen and detector. The diameter of the pill-box function is 2.9 mm for this projection. The unprocessed raw data obtained by this setup is shown in Fig. 3.67.

Preprocessing

Deviations in intensity are visible in the raw data; the intensity level at the margins of the projection is lower than in the center. This intensity deviation is not caused by the neutron beam, but by the detector system itself. The solid angle, under which the lens of the CCD camera is seen from a point on the scintillator surface, is smaller for points at the margins of the scintillator. Therefore less photons from the margins of the scintillator reach the lens of the CCD camera. This effect can be compensated by dividing the values in the raw data set I_{raw} by the values of an open beam image I_{ob}. An open beam image is obtained by performing the projection without specimen. Most detectors show non-zero pedestal values, even when they are not illuminated ('dark currents' and offset of the ADC in the CCD camera). As the values in each data set contain these dark current values I_{dc}, they have to be subtracted from the projection data and the open beam data before division. In the case of the ANTARES standard camera system, dark current values are obtained by data acquisition with not illuminated CCD chip. A mechanical shutter in front of the CCD chip can be closed for this purpose.

Mean values for the dark currents in dependency of integration time and temperature are shown in the chapter 2.9.1.1 ‘CCD camera’.

The result I_{pre} of the preprocessing procedure is given by:

$$I_{pre} = \frac{I_{raw} - I_{dc}}{I_{ob} - I_{dc}} \qquad (3.24)$$

Further preprocessing like e.g. gamma filtering was not necessary for this projection. The preprocessed data of the specimen is shown in Fig. 3.68.

Deblurring

For correction of the blur in the preprocessed data, caused by the extended aperture, a Wiener filter and the Richardson-Lucy maximum likelihood algorithm were applied. In order to demonstrate the improvement of resolution, a fine-structured section of the specimen is displayed below. The preprocessed projection is shown in Fig. 3.69. The result of a Wiener filter with c_{wiener}=0.5% of the maximum of the squared MTF is displayed in Fig. 3.70. The reconstruction shows more details than the blurred data but noise level is also increased: The SNR in the preprocessed data is 39.0 and the SNR in the reconstruction by a Wiener filter is 23.8. As already shown with the Monte Carlo data, the Richardson-Lucy maximum likelihood algorithm provides a higher SNR in the reconstruction: The result of 100 iterations is shown in Fig. 3.71. The SNR in this data set is 27.0.

For comparison, the same section of the temperature indicator in the preprocessed high resolution projection (distance between object and specimen: 37 cm) is shown in Fig. 3.72. The quality of this projection considering the spatial resolution as well as the signal to noise ratio (SNR=42) is not achieved by the reconstructions. This demonstrates that choosing an appropriate geometry for the projection (as there are: distance between aperture and specimen, distance between specimen and detector, and the diameter of the aperture) results in a higher signal quality than reconstructions from blurred projections. This holds whenever the neutron fluence in the projection is high. Examples for projections with low neutron fluence where image deconvolution is beneficial are shown below in the chapter “3.6.1.3 Image deconvolution in low intensity radiographs”.

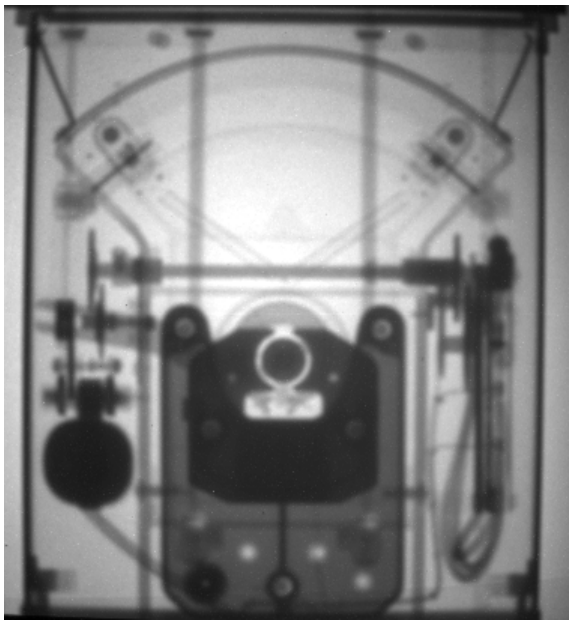

Fig. 3.67: Unprocessed raw data of the low resolution projection of the temperature indicator.

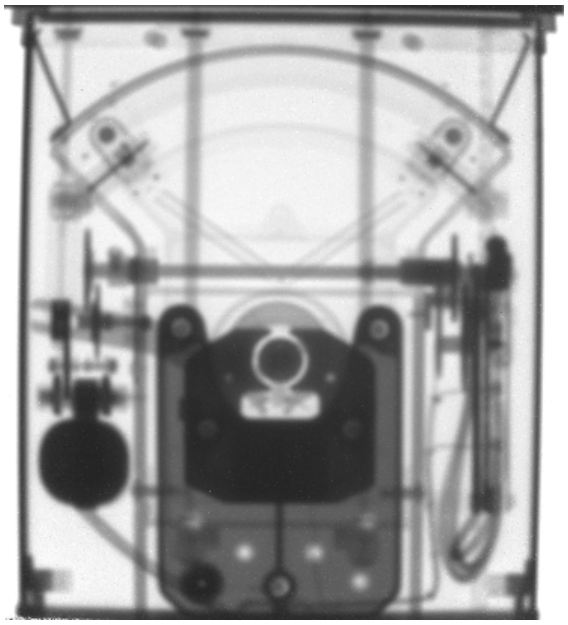

Fig. 3.68: Preprocessed data of the low resolution projection of the temperature indicator.

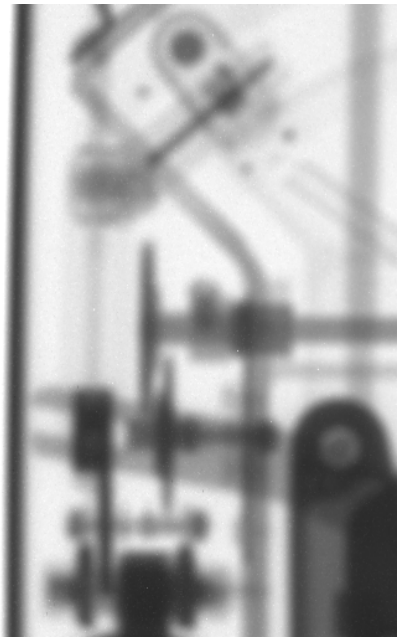

Fig. 3.69: Section of the preprocessed projection of the temperature indicator. The object was placed at a distance of 2 m from the detector. Exposure time for the projection was 5 sec. The SNR in the preprocessed data is 39.

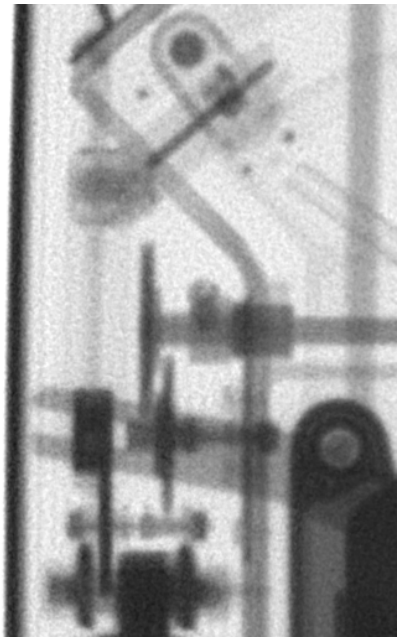

Fig. 3.70: Reconstruction of the preprocessed projection of the temperature indicator by a Wiener filter. The blur due to neutron beam geometry is corrected. The SNR in the reconstruction is 24.

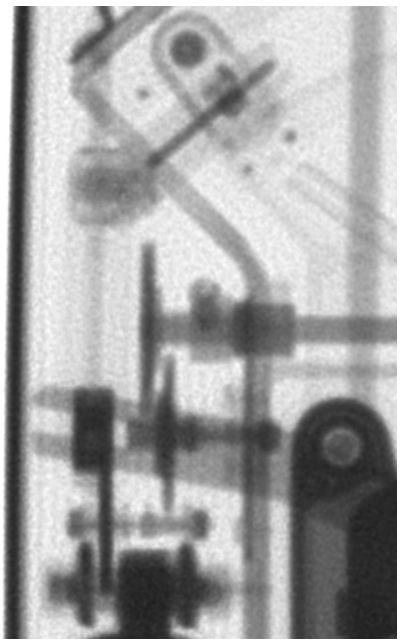

Fig. 3.71: Reconstruction of the preprocessed projection of the temperature indicator by 100 iterations of the Richardson-Lucy maximum likelihood algorithm. The blur due to neutron beam geometry is corrected. The SNR in the reconstruction is 27.

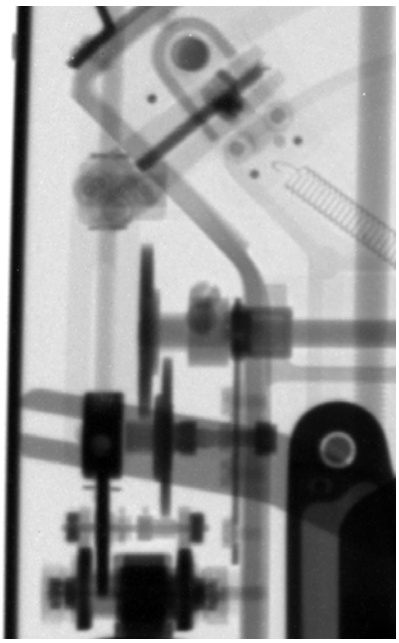

Fig. 3.72: Preprocessed projection of the temperature indicator for a distance of 37 cm between object and detector. Exposure time for the projection was 5 sec. The SNR in the preprocessed data is 42. The quality of this projection is not achieved by the reconstructions.

3.6.1.2 Revision of detector blur

At the ANTARES facility the width of the pill-box shaped PSF caused by the neutron beam geometry has a diameter of only 13 µm for a specimen placed at a distance of 1 cm to the scintillator and for application of the L/D =800 collimator. For standard applications the pixel size of the detector system is some 100 µm x 100 µm. I.e. the extension of the PSF due to the extended aperture is smaller than the pixel area of the detector system for such small distances between specimen and scintillator. The PSF due to the neutron beam geometry becomes a delta function in the discrete space of the detector. Image degradation is caused only by the detector system itself. In the case of the ANTARES standard detector system, reasons for degradation are the finite range of α-particles in the scintillator and blurring from the lens system of the CCD camera. For a distance of approx. 50 cm between CCD-camera and scintillator, blurring due to the lens system is dominant. In contrast to beam geometry effects, image degradation by the detector is independent from the distance between specimen and detector, i.e. the extension of the PSF is constant. This is an example where image deconvolution is very helpful, because elimination of limitations in resolution due to the detector system is difficult and time–consuming: Either the detector system has to be modified (e.g. implementation of another lens system for the CCD-camera) or has to be replaced by an other detector system (e.g. image plates).

Revision of the detector blur was tested with a mainboard of a PC (Fig. 3.73 left hand side) that was placed at a distance of 1 cm to the scintillator. The reactor power was 20 MW and the CCD chip was cooled down to –60 °C. Exposure time for the projection was 6 sec. The PSF of the detector system is a Gauss function with $fwhm$=320 µm. The unprocessed projection of the main board is shown in Fig. 3.74 right hand side. The SNR in this projection is 61.6.

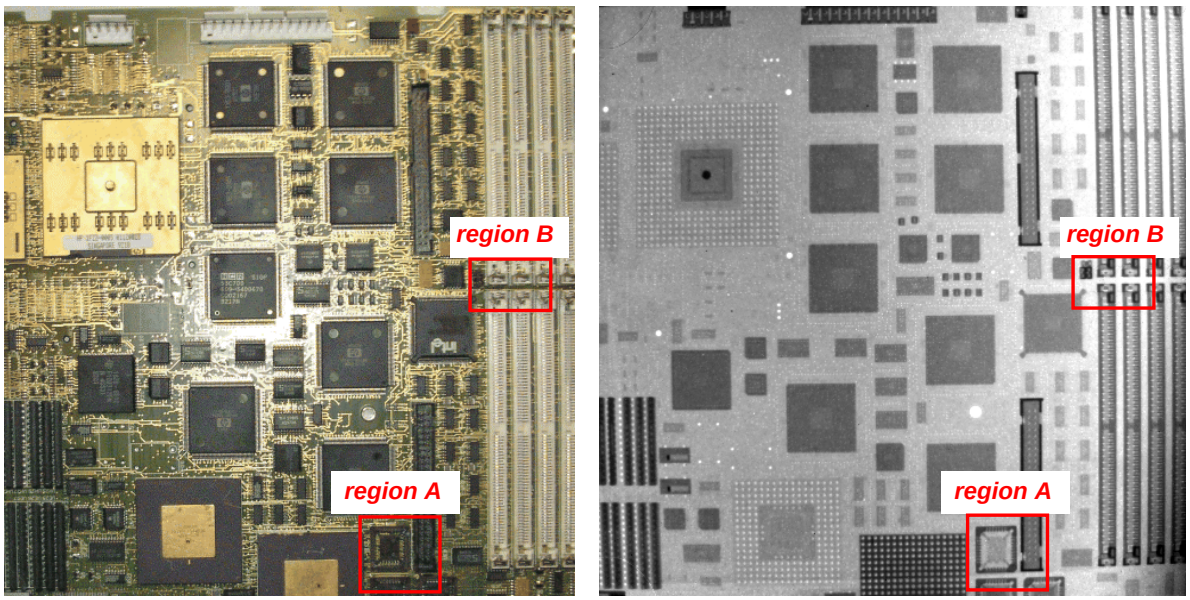

Fig. 3.73: A mainboard of a PC that was used as specimen (left) and its unprocessed projection (right)

At a first glance the projection in Fig. 3.73 right hand side seems to be very sharp. A closer look at small regions in this projection (region A and B in Fig. 3.73) reveals that some details are not resolved properly (Figs 3.74 and 3.77). A reconstruction of region A with Wiener filter (c_{wiener}=0.01% of $\max(MTF^2)$) is displayed in Fig. 3.75. Circuit points and holes in the circuit board that are barely recognizable in the raw data (Fig. 3.74) are clearly visible in the reconstruction. The SNR is decreased by the deconvolution to 40 % (SNR=25.3). A reconstruction with 200 iterations of Richardson-Lucy maximum likelihood algorithm is shown in Fig. 3.76. Here the SNR is only reduced to 55 % (SNR=34.0).

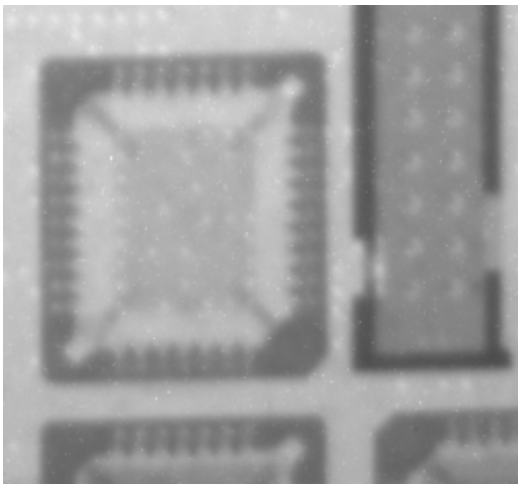

Fig. 3.74: Unprocessed raw data in region A of the projection of the mainboard.

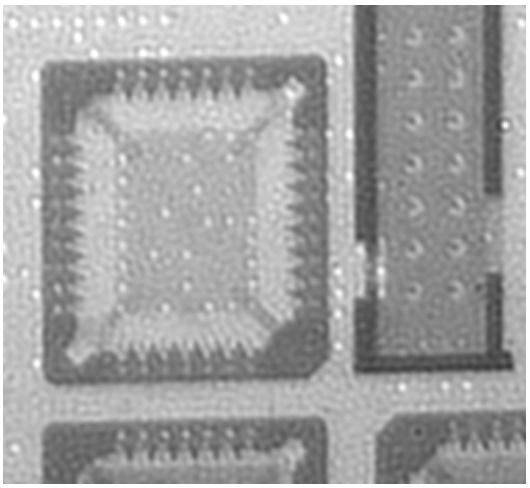

Fig. 3.75: Reconstruction of region A of the mainboard with a Wiener filter

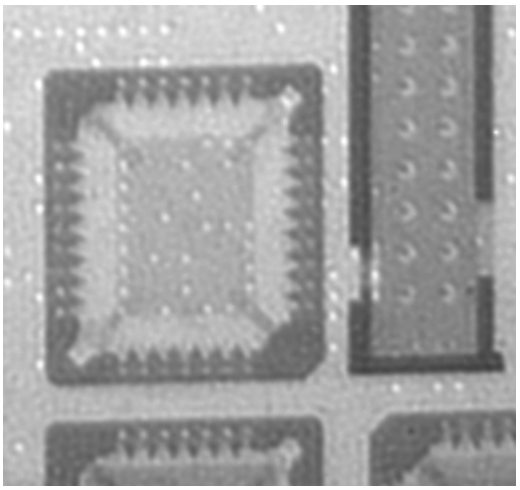

Fig. 3.76: Reconstruction of region A of the mainboard with 200 iterations of the Richardson-Lucy maximum likelihood algorithm.

The unprocessed raw data of region B is shown in Fig. 3.77 left hand side and the reconstruction by Wiener filter (c_{wiener}=0.01 % of $\max(MTF^2)$) on the right hand side. The reconstruction reveals many details that were not visible before, e.g. a small steel clip of 150 µm thickness (green arrow) for fixing plug-in modules in the socket is not recognizable in the raw data but clearly visible in the reconstruction.

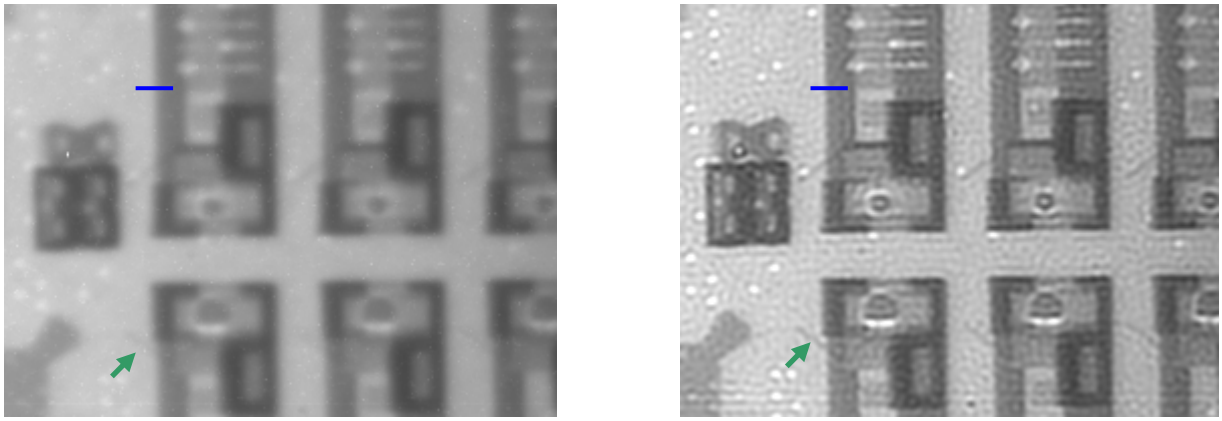

Fig. 3.77: Unprocessed raw data in region B (left hand side) and reconstruction with Wiener filter (right hand side)

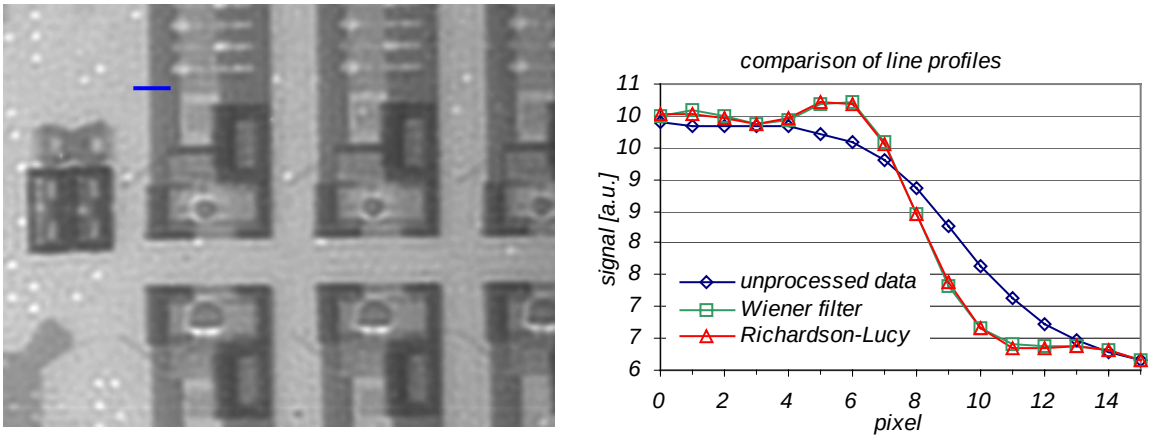

Fig. 3.78: Reconstruction of region B with 200 iterations of Richardson-Lucy maximum likelihood algorithm (left hand side) and comparison of line profiles along the blue line in the projection and reconstructions (right hand side).

The reconstruction of region B with 200 iterations of Richardson-Lucy maximum likelihood algorithm is shown in Fig. 3.78 left hand side. For comparison of resolutions in the unprocessed data and the reconstructions, line profiles along the blue lines in Figs. 3.77 and 3.78 at the edge of the plug-in socket are displayed in the diagram of Fig. 3.78 right hand side. The gradient at the edge is increased considerably by the Wiener filter and the Richardson-Lucy algorithm. Application of both methods provide in this case same gradients, but the SNR in the reconstruction with the Richardson-Lucy method is higher than that obtained with Wiener filtering.

3.6.1.3 Image deconvolution in low neutron fluence radiographs

In the previous chapters it was shown that increasing the spatial resolution by increasing the L/D ratio is superior to image deconvolution algorithms, whenever counter noise or quantum noise is the dominant contribution to noise.

When only a very low neutron fluence can be achieved in an experiment (e.g. due to small transmission through the aperture or limited exposure time), another contribution to noise is dominating: Detector noise like e.g. thermal noise in the CCD chip (see chapter 2.9.1 'ANTARES detector system'). This type of noise is independent from the neutron fluence in the measured projection, i.e. for high fluences fluctuations due to detector noise are negligible and for low fluences fluctuations may be even bigger than the measured signal itself.

Whenever the signal in a projection is not much bigger or even smaller than the fluctuations due to detector noise, image deconvolution may be useful. This is shown in the following. A projection of blossoms of a chestnut tree carried out with low neutron flux is shown in Fig. 3.79. For this projection a circular single hole aperture with 1 mm diameter was used. The distance between aperture and specimen is 12.8 m and the distance between specimen and detector is 2.5 m. The neutron flux in the detector plane is reduced to $6.9 \cdot 10^4$ $sec^{-1}cm^{-2}$ by this arrangement. The exposure time for this projection was 300 sec. The signal of the specimen is not much bigger than the fluctuations due to thermal noise from the CCD chip; the signal to noise ratio SNR is only 10.3. A projection of the same specimen using a circular single hole aperture with a diameter of 7 mm is shown in Fig. 3.80. The exposure time was also 300 sec. Due to the higher transmission of the aperture the signal is much higher than the detector noise (SNR=37.8). A reconstruction of this projection using a Wiener filter is shown in Fig. 3.81. The blur due to the neutron beam geometry as well as detector blur was corrected. Much more details are recognizable in the reconstruction. The SNR in the reconstruction (SNR=20.8) is higher than in the projection obtained by the aperture with smaller diameter.

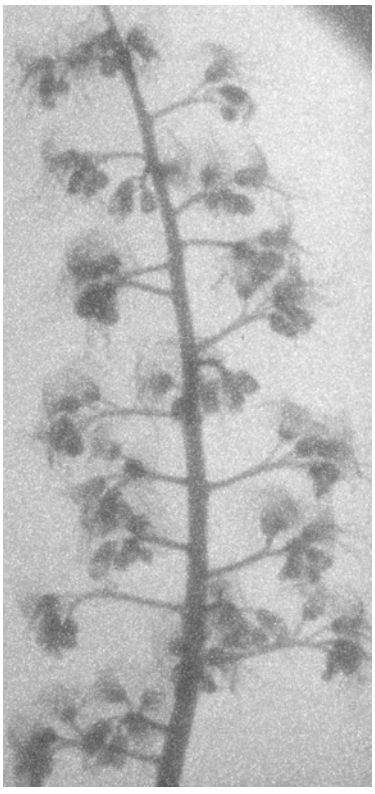

Fig. 3.79: Projection of blossoms of a chestnut tree. Exposure time was 300 sec and an aperture with a diameter of 1 mm was used. The SNR is 10.3.

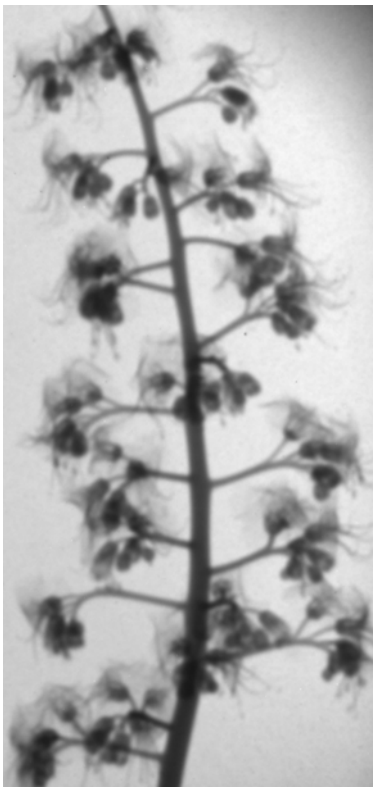

Fig. 3.80: Projection of blossoms of a chestnut tree. Exposure time was 300 sec and an aperture with a diameter of 7 mm was used. The SNR is 37.8.

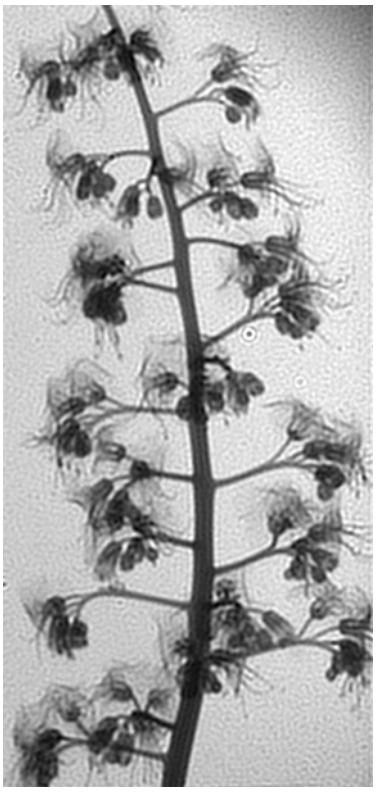

Fig. 3.81: Reconstruction of the projection shown in Fig. 3.80 by help of a Wiener filter. The blur due to the geometry of the neutron beam and detector blur is removed. The SNR is 20.8.

Noise from the detector system (e.g. thermal noise) is bothering especially when objects with a low contrast are investigated with low neutron fluence. Deviations in the signal due to the structure of the specimen may be far below the fluctuations due to detector noise. This is demonstrated with the projection of a leaf of a chestnut tree (Fig. 3.82; aperture diameter: 1 mm; exposure time: 300 sec). The experimental setup is the same as described above. The veins of the leaf are hardly recognizeable due to fluctuations caused by detector noise. The SNR in this projection is 9.1. A projection obtained by an aperture with a diameter of 7 mm is shown in Fig. 3.83 (SNR=31.5). The veins are much better recongizeable because their signal exceeds the fluctuations caused by detector noise, but the data is blurred. A reconstruction of the projection that corrects the blur from beam geometry and the detector blur is shown in Fig. 3.84. For reconstruction a Wiener filter was used. The SNR in the reconstruction is 20.6. It exceeds the SNR of the projection obtained by the smaller aperture diameter by more than a factor of two.

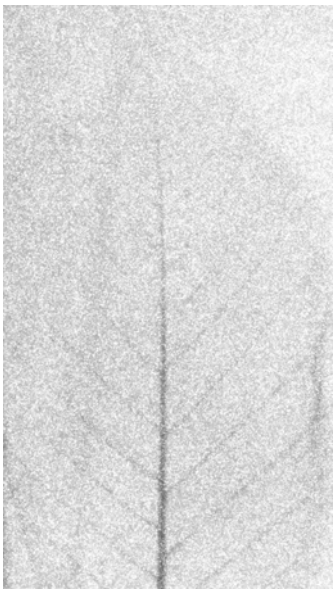

Fig. 3.82: Projection of a leaf of a chestnut tree. Exposure time was 300 sec and an aperture with a diameter of 1 mm was applied. The SNR is 9.1.

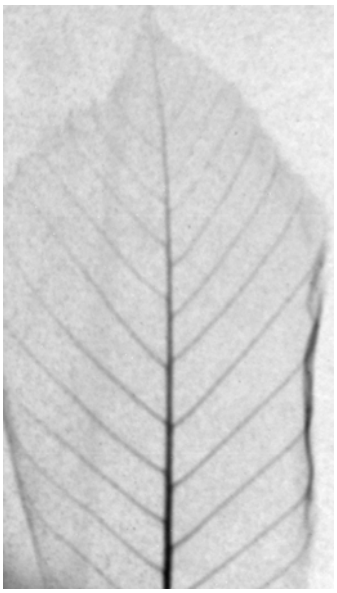

Fig. 3.83: Projection of a leaf of a chestnut tree. Exposure time was 300 sec and an aperture with a diameter of 7 mm was applied. The SNR is 31.5.

Fig. 3.84: Reconstruction of the projection shown in Fig. 3.83 by help of a Wiener filter. The blur due to the geometry of the neutron beam and detector blur is removed. The SNR is 20.6.

3.6.2 Coded masks in neutron radiography

3.6.2.1 Projection of monochromator crystals

The 10 hole NRA mask as described above (Fig. 3.36) was tested in an experiment at the powder diffractometer SPODI at FRM-II. At this facility, neutrons are guided from the biological shielding of the reactor to a monochromator by neutron guides. As monochromator, 17 Ge-crystalls (Fig. 3.85) are used that can be tilted for adjustment. In order to test for misalignments, it is helpful to map the reflected neutrons with spatial resolution, i.e. to carry out a 'reflection radiography' of the crystals. The coded mask (10 hole NRA) that was used in this experiment is shown in Fig. 3.86. It consists of a Cadmium plate of 1 mm thickness with an arrangement of holes as it was tested with the Monte Carlo method (Fig. 3.36). The holes are circular and have a diameter of 0.5 mm. Neutron attenuation of 1 mm Cadmium is sufficient for this experiment, because (in contrary to the spectrum used for Monte Carlo simulations) no epithermal and fast background neutron radiation exists at the powder diffractometer. The mask was placed at a distance of 5 m from the crystals. For spatially resolved neutron detection the ANTARES standard detector was located 3.3 m behind the coded mask. The experimental setup and a schematic overview are shown in Figs. 3.87 and 3.88. As the neutron count rate is extremely low for this setup, the CCD-chip was cooled down to –60 °C for reduction of thermal noise. Data acquisition was done in single steps, each with 6 minute integration time. In principle 6 minutes integration time is sufficient for detecting misalignments of the crystals. However, in order to get a brighter signal, a total exposure time of 138 min was chosen (23 projections). These projections were merged afterwards. Having several projections of a specimen enables for effective gamma filtering: A gamma event in a pixel causes a signal much higher than a neutron count. Therefore gamma events in a certain pixel can be found by comparing the gray value of this pixel in all projections: If one or a few pixel readings are much higher than the average value from all projections, the cause is most probably gamma interaction. For gamma suppression in the data, two different methods were tested:

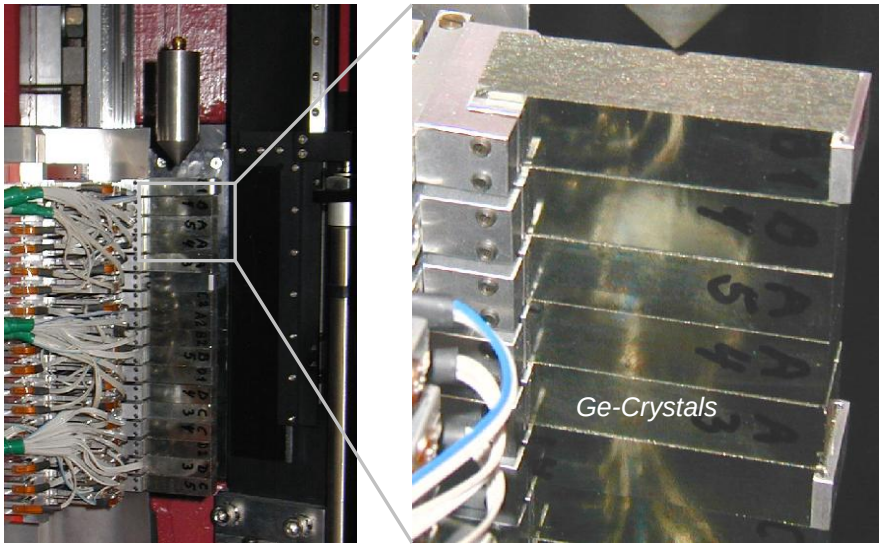

Fig. 3.85: The Ge-monochromator crystals

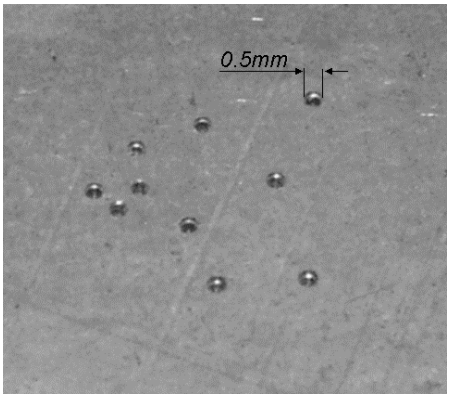

Fig. 3.86: 10 hole NRA mask used for the experiment

- The average value for each pixel and the standard deviation was calculated. Afterwards the mean value was calculated again, but all values outside of a confidence interval of one standard deviation from the mean value were omitted.
- A median filter [55] in time was used, i.e. for each pixel only the median value from all projections was used.

Both methods clean the data from gamma events effectively and provide similar results.

Exactly the same procedure (measurement and preprocessing) was repeated twice:

- With a single hole aperture of diameter 0.5 mm. The transmission area is as big as for one hole in the coded mask, hence transmission through the aperture is 10 times less.
- With a single hole aperture of diameter 1.2 mm. The transmission area is 57.6 % of the total transmission area of the coded mask.

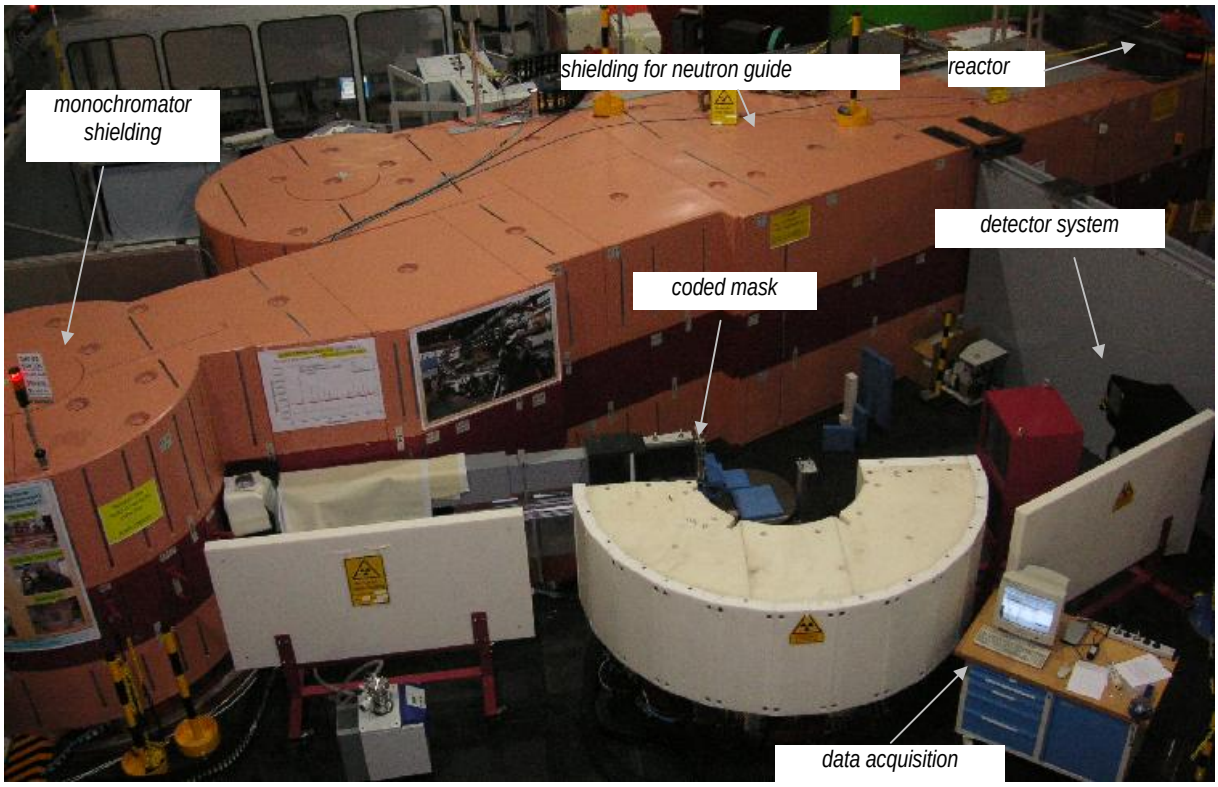

Fig. 3.87: The setup for testing the monochromator crystals at the powder diffractometer SPODI.

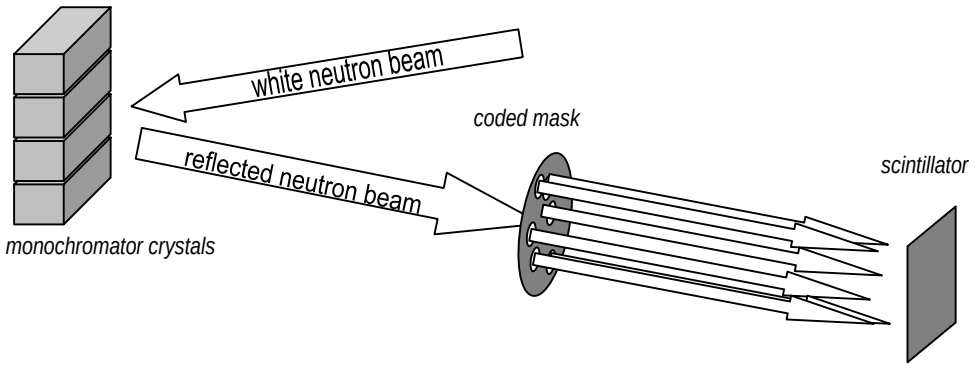

Fig. 3.88: Schematic overview of the setup for testing the monochromator crystals at the powder diffractometer SPODI.

The preprocessed projection (gamma filtered) obtained by the single pin hole aperture with a diameter of 0.5 mm is shown in Fig. 3.89 left hand side. The signals of most crystals do not rise much over the noise level and are barely recognizable. The signals from the crystals are much better recognizable in the reconstruction of the projection obtained by the 10 hole NRA mask (Fig. 3.89 right hand side). The signals are clearly separated from the background noise level. A crystal at around y=300 appears that was not visible in the single hole data.

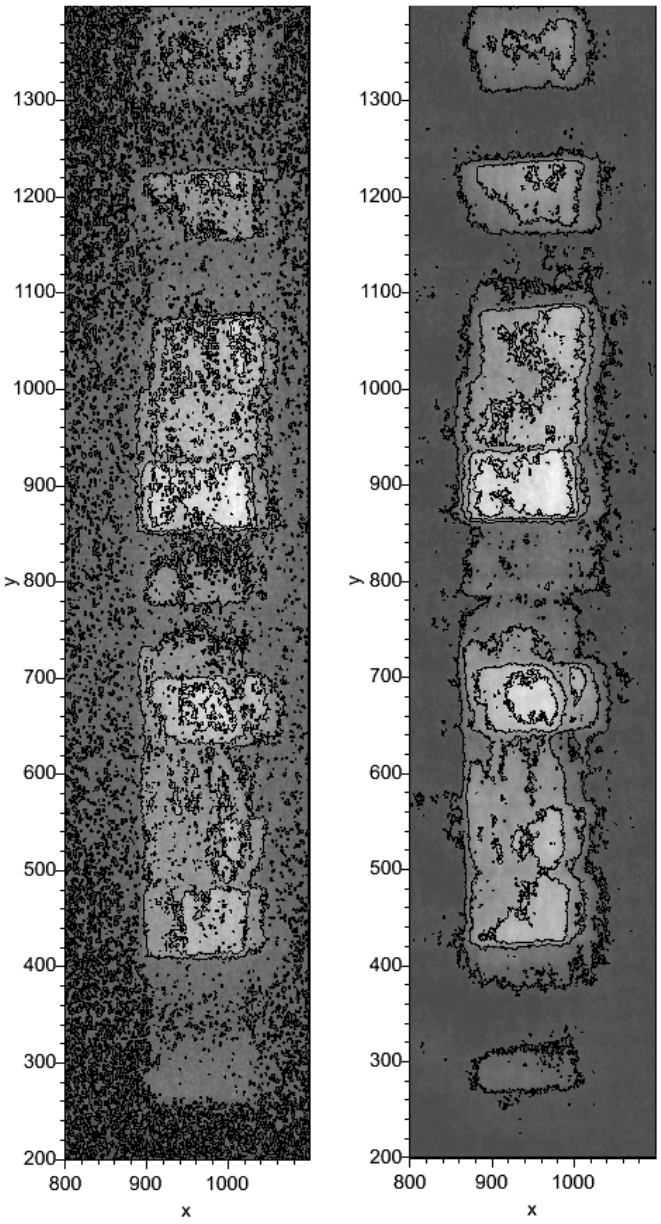

Fig. 3.89: Left hand side: Preprocessed (gamma filtered) projection of the monochromator crystals obtained by a single hole aperture with diameter 0.5 mm.

Right hand side: Reconstructed projection obtained by the 10 hole NRA mask (hole diameter 0.5 mm). Exposure time was 138 minutes in both cases.

The improvements due to the 10 hole NRA are also demonstrated with the line profiles through the signal of the brightest crystal at y=890 (here the data of projections with 6 minutes integration time are used): Fig. 3.90 left hand side shows the profile obtained by the single hole aperture of diameter 0.5 mm, Fig. 3.90 right hand side shows the profile in the reconstruction of the 10 hole NRA data and Fig. 3.91 left hand side shows the profile for the single hole aperture with 1.2 mm diameter. Noise in these profiles is much higher than in the projections of Fig. 3.89, because exposure time is only 1/23. Due to short exposure time even the signal of the brightest crystal at y=890, does not rise much above the background noise level when the small single hole aperture is applied (diameter 0.5 mm). In contrary, in the 10 hole NRA data (Fig. 3.90 right hand side) the signal of the crystal rises clearly above the background noise level. The desired effect of having 10 times more flux exceeds the unwanted effect of noise amplification by the deconvolution algorithm by far. However, the data do not achieve the SNR of the data obtained by the big single hole aperture (diameter 1.2 mm). On the other hand with the big single hole aperture resolution is decreased considerably compared to the small single hole aperture and the 10 hole NRA. This is demonstrated with the line profile across the gap between two crystals at y=930 (Fig. 3.91 right hand side). The width of the projected gap is the same in the data obtained by the small single hole aperture (diameter 0.5 mm) and by the 10 hole NRA. For the big single hole aperture (diameter 1.2 mm), the width of the projected gap is much bigger and resolution therefore considerably smaller.

The projections of the monochromator crystals revealed that some crystals are misaligned.

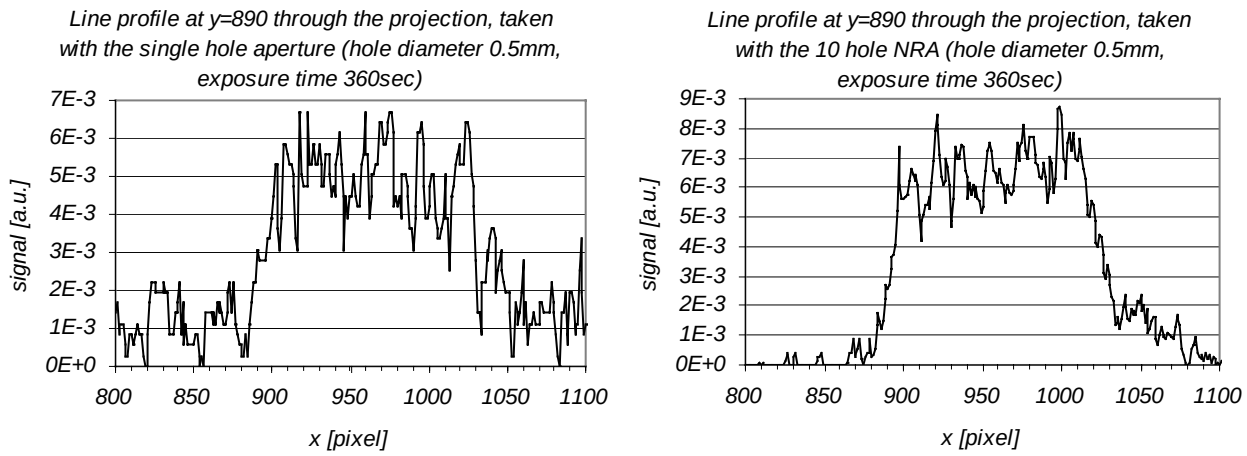

Fig. 3.90: Line profiles at y=890 through the signal of the brightest crystal. The left hand side shows the line profile obtained by the small single hole aperture (diameter 0.5 mm) and the right hand side shows the line profile in the reconstruction from the 10 hole NRA data. Exposure time was 6 minutes in both cases.

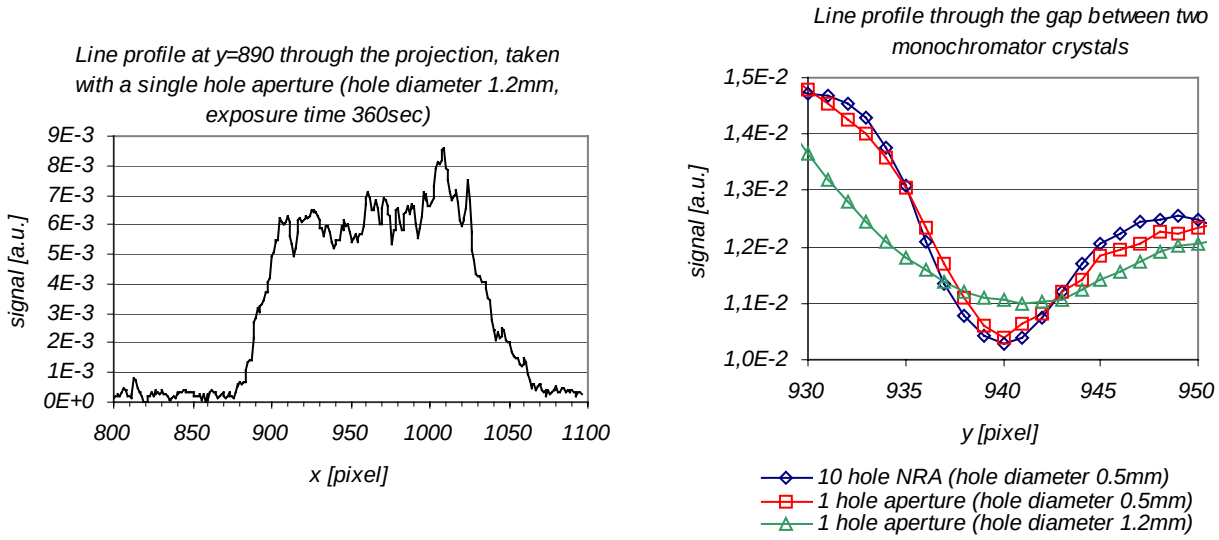

Fig. 3.91: Left hand side: Line profile at y=890 in the data obtained by the big single hole aperture (diameter 1.2 mm, exposure time 6 minutes).
Right hand side: Line profile across the gap between the two crystals at y=930

3.6.2.2 Coded masks in phase contrast radiography

When the phase of a plain wave front is shifted in the specimen e.g. due to another velocity of the wave in the specimen, diffraction occurs [21]. In the projection of the specimen a diffraction pattern is observable at the margins of the projected specimen in this case. The propagation velocity of the wave front in the specimen may differ from that around the specimen due another refractive index of the specimen. However for most materials the refractive index for neutrons is very close to one for most materials: $|n-1|$ is in the region between 10^{-7} and 10^{-5} [81]. In order to observe the phase contrast effect, the impact wave front must be as plain as possible. In neutron radiography this can be achieved by an aperture with a very small diameter and a big distance between aperture and specimen (high L/D ratio). In addition the phase contrast effect (diffraction pattern) is more distinct for big neutron wavelengths λ, i.e. for phase contrast imaging a big transversal coherence length $l_c = \lambda / \theta \approx \lambda \cdot L / D$ is necessary [88] (with θ=maximal angle between different neutron paths at the position of the specimen). As the neutron flux at the specimen is proportional to $(D/L)^2$, neutron phase contrast imaging suffers from a very low flux. Usually big exposure times (up to several days [85]) are necessary in order to get a satisfying signal to noise ratio (SNR).

A neutron radiography of a model air plane engine is shown in Fig. 3.92a. An enlarged section around the tappet of the engine is shown in Fig. 3.92b. For this projection an aperture with a diameter of 7 mm (Fig. 3.93 left hand side) was used. The distance between aperture and specimen was 12.8 m (L/D =1829) and the distance between specimen and detector was 2.5 m. No phase contrast effect in the projection is observable with this setup. The transversal coherence length of the neutron beam is too low. The exposure time was 120 sec. Due to the relative low L/D ratio a satisfying SNR of 55.8 is achieved in this projection.

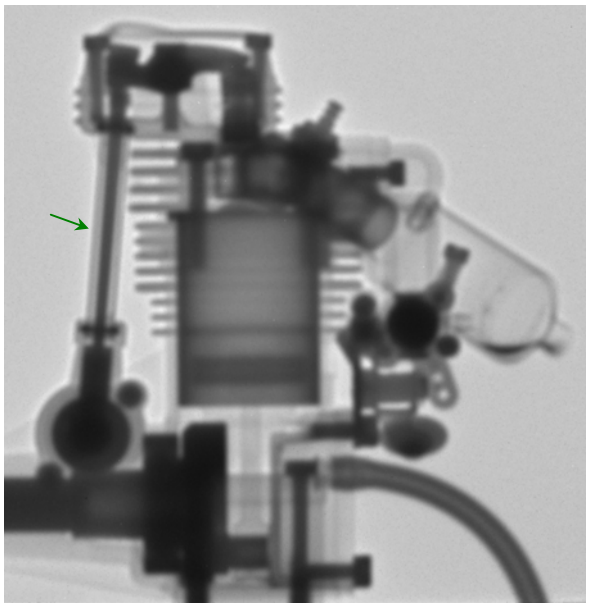

Fig. 3.92a: Projection of the model air plane engine using the aperture with a diameter of 7 mm. Exposure time for this projection was 120 sec. No phase contrast effect is visible. The SNR in the projection is 55.8

Fig. 3.94a shows a projection of the same model airplane engine obtained by an aperture with a diameter of 1 mm (L/D =12800; Fig. 3.93 middle). The distances between aperture and specimen and between specimen and detector are the same as for the projection in Fig. 3.92a. The phase contrast effect becomes visible in this projection especially at the Al-cover of the tappet of the engine (green arrow in Fig. 3.94a) due to the increased L/D ratio. Although the exposure time was 400 sec for this projection, the SNR is decreased considerably (SNR =7.3) compared to the projection obtained by the aperture with a diameter of 7 mm. An enlarged section around the tappet of the engine is shown in Fig. 3.94b. The margins of the tappet occur dark due to the phase contrast effect.

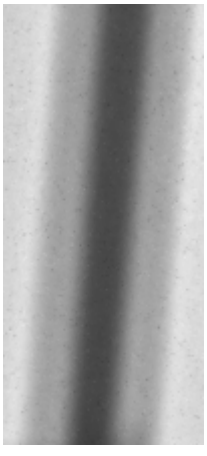

Fig. 3.92b: Section around the tappet (green arrow in Fig. 3.92a) in the projection shown in Fig. 3.92a obtained by the aperture with a diameter of 7 mm (exposure time 120 sec). The SNR in the projection is 55.8. No phase contrast effect is visible in this section.

A reconstruction of a projection of the model airplane engine obtained by a 10 hole NRA mask is shown in Fig. 3.95a. Each hole of the mask has a diameter of 0.8 mm. The arrangement of holes (Fig. 3.93 right hand side) is the same as used for the projection of the monochromator crystals (previous chapter; Fig. 3.86). The exposure time for the projection was also 400 sec. Considering one hole of the 10 hole mask, the L/D ratio (L/D =16000) and therefore the transversal coherence length is even higher compared to the setup using the single hole aperture with a diameter of 1 mm. The raw data obtained by the 10 hole mask is a superposition of 10 projections with distinct phase contrast effect. The neutron fluence is increased by

a factor 6.4 compared to the single pin hole projection using a diameter of 1 mm. The data was reconstructed by help of a Wiener filter (c_{wiener}=5% of $\max(MTF^2)$). The SNR in the reconstruction is 10.5. An enlarged section around the tappet of the engine is shown in Fig. 3.95b. The margins of the projected tappet occur dark due to the phase contrast effect. This measurement shows, that it is possible to increase the SNR in a phase contrast projection by a coded mask and a reconstruction algorithm without decrease of the phase contrast effect.

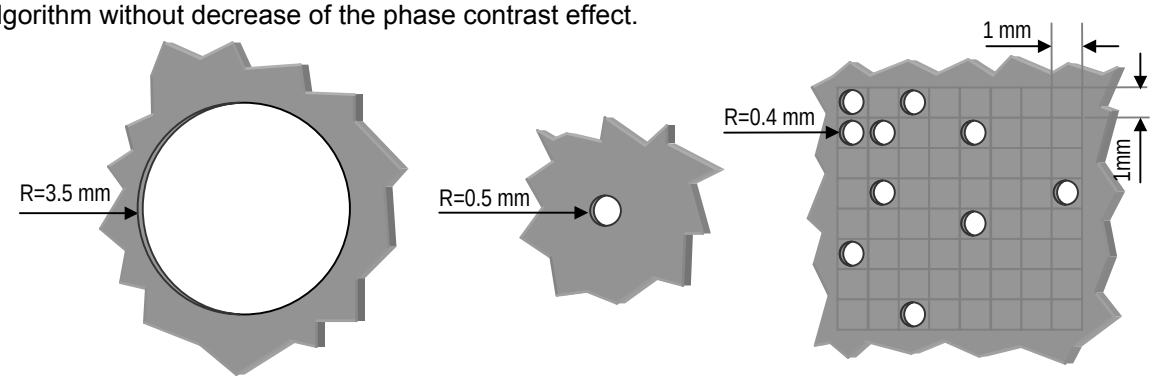

Fig. 3.93: The apertures used for the projections (scale 4:1). Left hand side: Single pin hole aperture with a diameter of 7 mm. Middle: Single pin hole aperture with a diameter of 1 mm. Right hand side: 10 hole NRA mask (each hole has a diameter of 0.8 mm). All apertures consist of a 2 mm Cd layer and a 1 mm Gd layer.

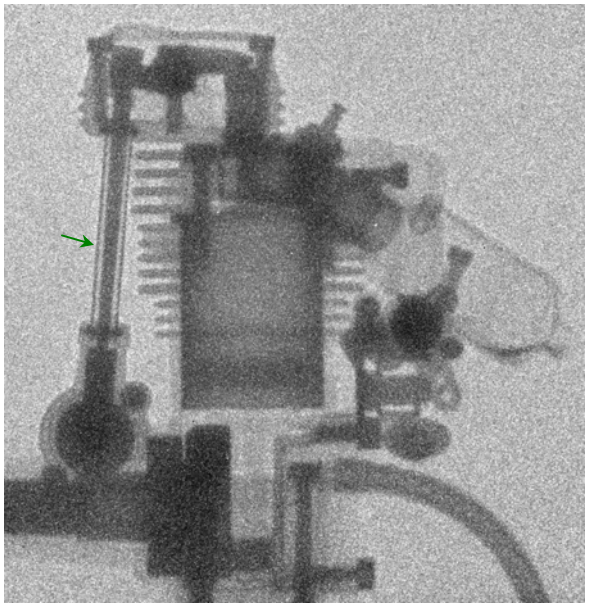

Fig. 3.94a: Projection of the model air plane engine using the aperture with a diameter of 1 mm. Exposure time for the projection was 400 sec. The phase contrast effect is visible at the tappet of the engine (green arrow). The SNR in the projection is 7.3.

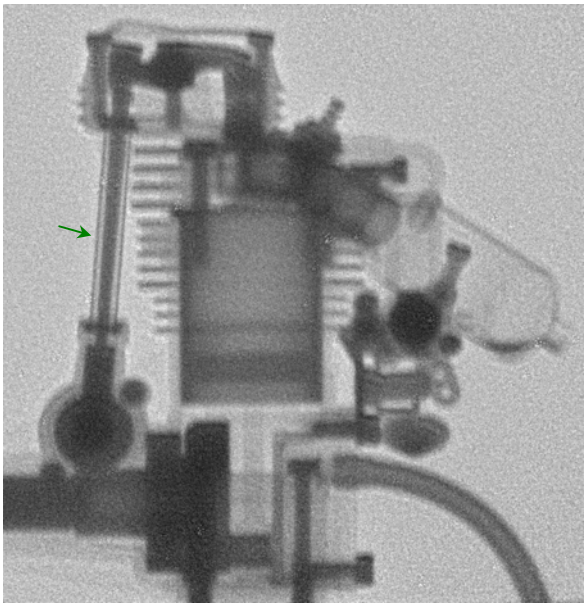

Fig. 3.95a: Reconstructed projection of the model air plane engine using the NRA mask with 10 holes. Each hole has a diameter of 0.8 mm. Exposure time for the projection was 400 sec. The phase contrast effect is visible at the tappet of the engine (green arrow). The SNR in the reconstruction is 10.5.

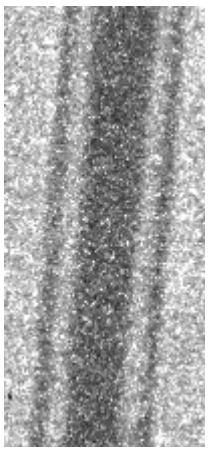

Fig. 3.94b: Section around the tappet (green arrow in Fig. 3.94a) in the projection shown in Fig. 3.94a obtained by the aperture with a diameter of 1 mm (exposure time 400 sec). The SNR in the projection is 7.3. The phase contrast effect is visible at the margins of the tappet of the engine.

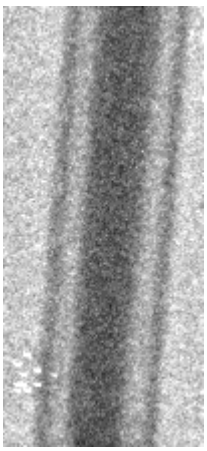

Fig. 3.95b: Section around the tappet (green arrow in Fig. 3.95a) in the reconstruction shown in Fig. 3.95a (reconstructed projection obtained by the 10 hole NRA mask (exposure time 400 sec). The SNR in the reconstruction is 10.5. The phase contrast effect is visible at the margins of the tappet of the engine.

3.7 Conclusion

- Deconvolution algorithms
  - The spatial resolution in a projection can be increased by the application of image deconvolution algorithms. Best results are obtained with the Richardson-Lucy maximum likelihood algorithm. Whenever a high fluence is achieved in a projection, so that quantum noise is the dominating contribution to noise, the quality of reconstructions do not reach the quality of a projection obtained with a higher L/D ratio. Reconstructions suffer from noise amplification by deconvolution algorithms. When only a small fluence can be obtained within reasonable exposure times, the signal from the specimen does not exceed the noise level from the detector system (e.g. thermal noise of the CCD chip). In these cases an increase of fluence by choosing a lower L/D ratio and application of reconstruction algorithms for resolution enhancement improves the quality of a projection considerably.

- Advanced apertures
  - Most coded masks as proposed e.g. in X-ray astronomy are less applicable in neutron radiography. Fine textures of extended specimen cannot be developed to a satisfying image quality. The detection of fine structures inside of specimen is the main field of applications of neutron radiography (unlike in astronomy, where distinct objects are investigated).
  - Multiple pin hole apertures are useful, when a single pin hole aperture for a given resolution (i.e. L/D ratio) would provide a fluence for which the signal to noise ratio is too weak. The obtained raw data is the superposition of projections which have the desired resolution. The quality of a reconstruction using deconvolution techniques depends on the arrangement of holes. Best results are obtained with a non redundant arrangement (non redundant array mask). An application of this technique is e.g. phase contrast radiography where only a small fluence can be obtained due to the necessary very high L/D ratio. Similar to other coded masks it is originally proposed to perform reconstruction by a correlation technique. For extended fine structured specimen, this technique causes a high noise level (inherent noise). The implementation of this method is therefore restricted to a subset of neutron radiography applications.
  - Apodization with filters is not beneficial in neutron radiography. The quality of projections obtained by a single pin hole aperture is not reached.

A Appendix

A.1 Collimator geometry

In chapter 2.35 ‘Collimators’ a beam adjusted collimator geometry is described that attenuates undesired radiation components as close to the source as possible and that maximizes path lengths of undesired radiation components through collimator material. The lower half of the collimator shape is shown in Fig. A.1. For machining such a collimator, a mathematical description of the inner shape of the collimator is necessary. The volume to be carved out of the shielding material is derived in the following:

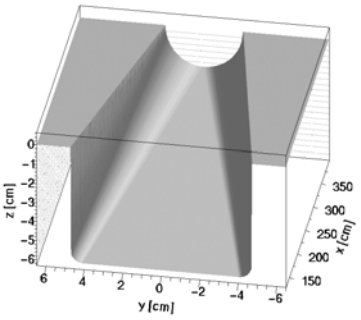

Fig. A.1: Lower half of the inner shape for a beam adjusted collimator

The somehow complicated inner shape of the collimator (Fig. A.1) can be represented by the union of simpler volumes as shown in Fig. A.2.

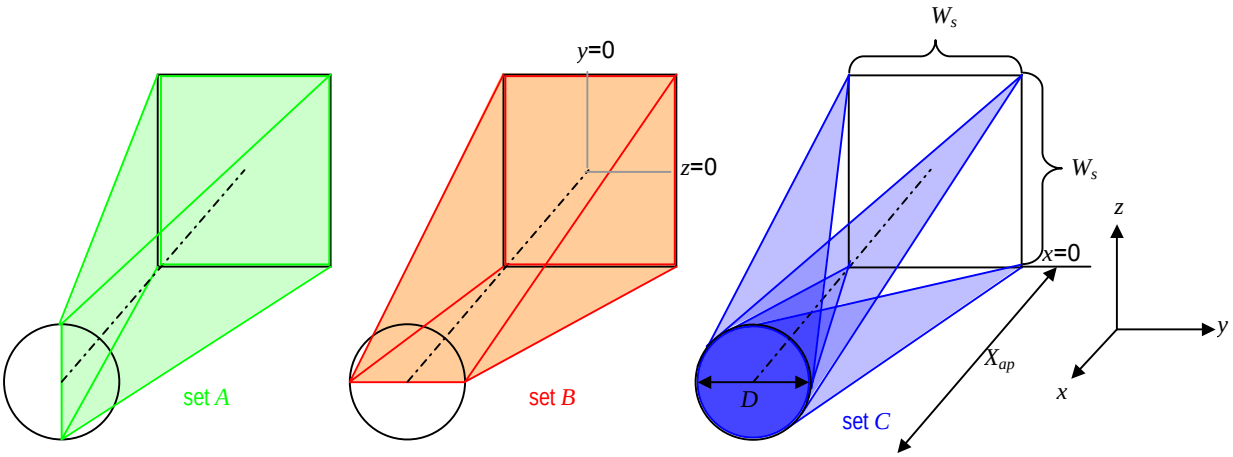

Fig: A.2: The inner transmitting volume of the beam adjusted collimator can be represented by the union of these three simpler volumes

All points inside the volume bordered by the structure shown on the left hand side of Fig. A.2 are enclosed by five planes (green). The same is true for the point set within the red structure in the middle of Fig. A.2. In order to get the desired inner volume for the collimator, the point set within the four blue cones on the right hand side in Fig. A.2 has to be included into the set union. In the following, the source area is at x=0 and the aperture is located at x=X_{ap}.

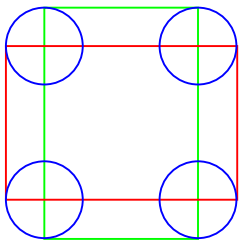

Fig. A.3: Vertical cut (x=const) through the volumes of Fig. A.2 between the source area and the aperture

The space enclosed by the structure shown on the left hand side of Fig. A.2 is defined by the set A of points (x,y,z) that fulfill:

A:

$$\left\{y(x) \geq \frac{W_s}{2 \cdot X_{ap}} \cdot x - \frac{W_s}{2}\right\} \cap \left\{y(x) \leq \frac{-W_s}{2 \cdot X_{ap}} \cdot x + \frac{W_s}{2}\right\} \cap$$

$$\left\{z(x) \geq \frac{-D+W_s}{2 \cdot X_{ap}} \cdot x - \frac{W_s}{2}\right\} \cap \left\{z(x) \leq \frac{D-W_s}{2 \cdot X_{ap}} \cdot x + \frac{W_s}{2}\right\} \cap$$

$$\{x \geq 0\} \cap \{x \leq X_{ap}\} \qquad \text{(A.1)}$$

Where '$\cap$' denotes intersection. The space enclosed by the structure shown in the middle of Fig. A.2 is given by replacing y by z and z by y in Eq. A.1. The resulting point set is set B:

B:

$$\left\{y(x) \geq \frac{-D+W_s}{2 \cdot X_{ap}} \cdot x - \frac{W_s}{2}\right\} \cap \left\{y(x) \leq \frac{D-W_s}{2 \cdot X_{ap}} \cdot x + \frac{W_s}{2}\right\} \cap$$

$$\left\{z(x) \geq \frac{W_s}{2 \cdot X_{ap}} \cdot x - \frac{W_s}{2}\right\} \cap \left\{z(x) \leq \frac{-W_s}{2 \cdot X_{ap}} \cdot x + \frac{W_s}{2}\right\} \cap$$

$$\{x \geq 0\} \cap \{x \leq X_{ap}\} \qquad \text{(A.2)}$$

Representative for all elliptical cones of the structure shown on the right hand side in Fig. A.2, the point set inside the upper left cone (in beam direction) is derived in the following: The axis of this cone (blue dotted line in Fig. A.4) is given by:

$$y_c(x) = -\frac{W_s}{2 \cdot X_{ap}} \cdot x + \frac{W_s}{2} \cap z_c(x) = -\frac{W_s}{2 \cdot X_{ap}} \cdot x + \frac{W_s}{2} \qquad \text{(A.3)}$$

All cross sections of the cone in planes parallel to the y-z-plane are circles with radius $r_c(x)$. This radius is proportional to the distance x from the source area (see Fig. A.4):

$$r_c(x) = \frac{D}{2} \cdot \frac{x}{X_{ap}} \qquad \text{(A.4)}$$

Considering an y-z plane at location x, all points inside the cone have smaller distances to the cone axis than $r_c(x)$:

$$\sqrt{(y - y_c(x))^2 + (z - z_c(x))^2} \leq r_c(x) \qquad \text{(A.5)}$$

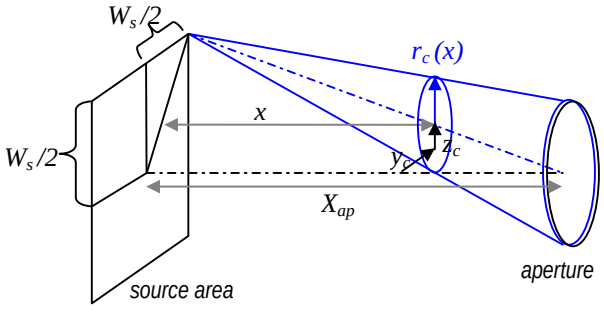

Fig. A.4: Upper left cone (in beam direction) from Fig. A.2

Under consideration of Eqs. A.3, A.4 and constraint A.5, the latter becomes:

$$\sqrt{\left(y + \frac{W_s}{2 \cdot X_{ap}} \cdot x - \frac{W_s}{2}\right)^2 + \left(z + \frac{W_s}{2 \cdot X_{ap}} \cdot x - \frac{W_s}{2}\right)^2} \leq \frac{D}{2} \cdot \frac{x}{X_{ap}} \qquad \text{(A.6)}$$

The point sets within the other cones of the blue structure on the right hand side in Fig. A.2 can be derived in an analog way: Just the algebraic signs in Eq. (A.6) have to be adjusted. The complete inner volume of the blue structure is given by the point set C:

C:

$$\left\{\sqrt{(y+H\cdot x-G)^2+(z+H\cdot x-G)^2}\le r_c(x)\right\}\quad\cup$$

$$\left\{\sqrt{(y-H\cdot x+G)^2+(z+H\cdot x-G)^2}\le r_c(x)\right\}\quad\cup$$

$$\left\{\sqrt{(y+H\cdot x-G)^2+(z-H\cdot x+G)^2}\le r_c(x)\right\}\quad\cup$$

$$\left\{\sqrt{(y-H\cdot x+G)^2+(z-H\cdot x+G)^2}\le r_c(x)\right\}\qquad\text{(A.7)}$$

with the substitutions $H=\frac{W_s}{2\cdot X_{ap}}$ and $G=\frac{W_s}{2\cdot}$

For construction of the inner collimator, the volume that has to be carved out of the collimator material can be found by the union set of point sets A, B, C.

A.2 Optimal adjustment of the L/D=800 and L/D=400 collimators

When the L/D =800 collimator is moved into the neutron beam, the fixed part of the L/D =400 collimator in the biological shielding should not hamper desired neutron paths. On the other side, it should confine all desired neutron paths as close as possible. There is an optimal solution for adjustment: The diagonal in vertical cross sections through an imaginary extended L/D =800 collimator (extended into the biological shielding) must have the same size as the diagonal in the real fixed L/D =400 collimator part for all distances x from the source area. This imaginary extension of the collimator is demonstrated in Fig. A.5.

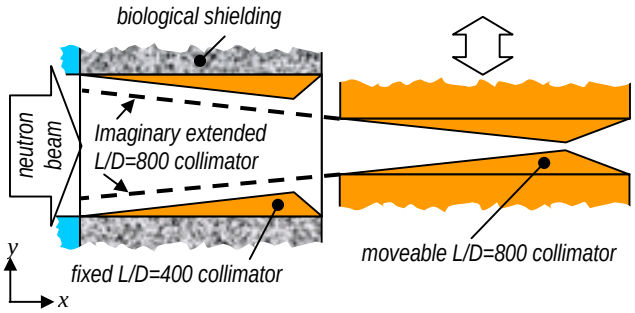

Fig. A.5: Illustration of the imaginary extended collimator

The case of same diagonals in vertical cross sections for both collimator geometries is displayed in Fig. A.7 (green line). This solution is obtained, as shown in Fig. A.6, when the diameter D_{400} of the desired L/D =400 aperture and the distance X_{ap400} between source area and the L/D =400 aperture fullfills:

$$D_{400} = \frac{D_{800} - \sqrt{2W_s^{\,2}}}{X_{ap800}} \cdot X_{ap400} + \sqrt{2W_s^{\,2}} \qquad \text{(A.8)}$$

where D_{800} is the diameter of the desired L/D =800 aperture, and X_{ap800} is the distance between source area and L/D =800 aperture. Diameter and location of the L/D =800 aperture was already determined in the chapter 1.3.4 'Location of aperture' by the desired width of fully illuminated area in the detector plane: X_{ap800} =430 cm and D_{800} =2.1 cm.

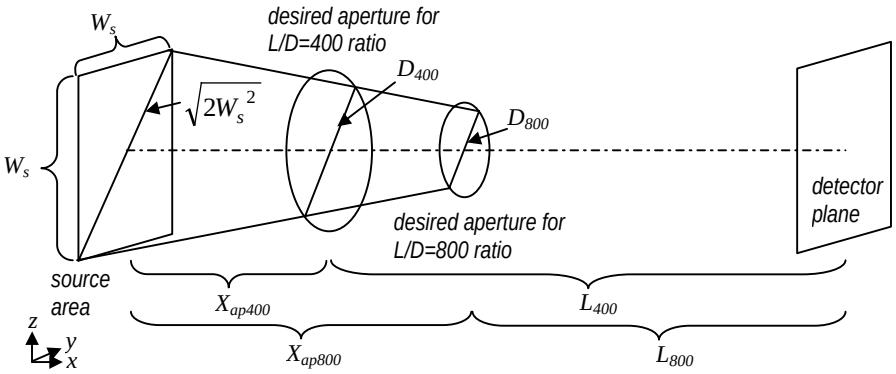

Fig. A.6: Geometry for optimal collimator adjustment. The diagonals in vertical cross sections of both collimators have same size for each distance x from the source area

The desired L/D =400 geometry has to fullfill the following constraints:

- Given by the layout of the reactor hall, the distance between source area and detector plane is 2100 cm, hence $X_{ap400} + L_{400} = 2100cm$ (A.9)
- The desired L/D ratio of 400 must be obtained: $L_{400} / D_{400} = 400$ (A.10)

Combination of both boundary conditions in Eqs. A.8 and A.8 results in:

$$D_{400} = \frac{2100cm - X_{ap400}}{400} \qquad \text{(A.11)}$$

Solutions of Eqs. A.8 and A.11 are displayed in Fig. A.8. Both equations are solved simultanously for

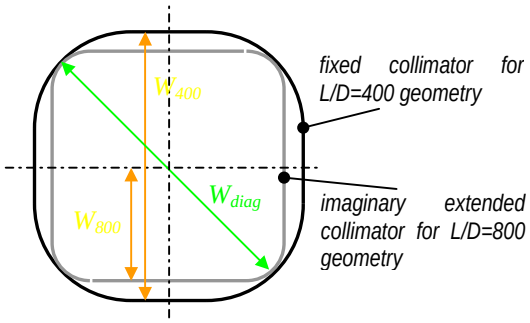

Fig. A.7: Vertical cross sections through the fixed L/D=400 collimator and the imaginary extended L/D=800 collimator. An optimal solution for adjustment of collimators is obtained when the diagonals W_{diag} have same size.

a diameter D_{400} of 4.3 cm and a distance between source area and aperture X_{ap400} of 365.3 cm. This is the optimal solution in a mathematical sense. From a practical point of view it is difficult to move the L/D =800 collimator as precise that both collimators axes coincide exactly in one line. The L/D =400 collimator should not hamper desired neutron paths for the L/D =800 geometry even if the moveable collimator is missaligned to a small degree. For this reason the aperture location X_{ap400} was shifted to a distance of 370 cm from the source area. The resulting diagonals and widths in vertical cross sections through the collimator geometries as function of the distance x to the source area are plotted in Fig. A.9. The maximum difference in diagonal extension is 0.6 mm and the maximum difference in vertical extension (W_{400}-W_{800}, see Fig. A.9) is 4 mm. Maximum tolerances appear at the narrowest part of the fixed collimator (x=370 cm). For smaller distances x to the cold source, both geometries fit even better. Hence the fixed L/D =400 collimator part in the biological shielding is very close to the desired geometry for the L/D =800 beam adjusted collimator.

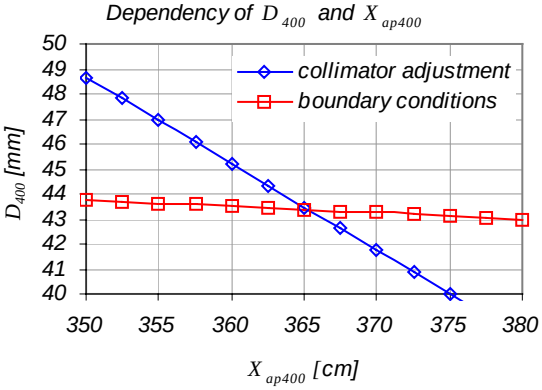

Fig. A.8: Solutions for D_{400} and X_{ap400} for collimator adjustment (Eq. A.8) and boundary conditions (Eq. A.11)

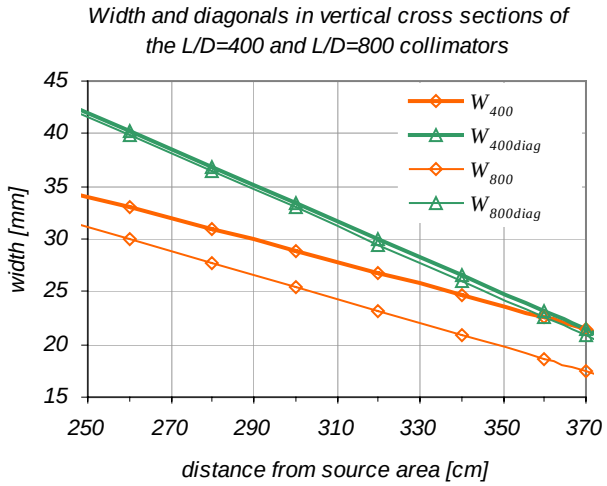

Fig. A.9: Diagonal and vertical extensions of collimator cross sections as function of the distance x to the cold source (source area). W_{400} is the vertical extension of the L/D=400 collimator and W_{800} is the vertical extension of the L/D=800 collimator. The vertical extensions are equal to the horizontal extensions. $W_{400diag}$ is the diagonal extension of the L/D=400 collimator and $W_{800diag}$ is the diagonal extension of the L/D=800 collimator.

A.3 Analysis of Au-foil measurement

As described in the chapter 2.8.2 “Measurement of total flux and Cd ratio at position of the specimen”, the flux and the Cd-ratio at position of the specimen were measured by gold-foil activation. The derivation of the total flux Φ_{total} from the activity of the Au-foil is described in the following.

Gold is activated by the reaction ^{197}Au(n,γ)^{198}Au [31] (in natural isotope composition only the isotope ^{197}Au is found [32]).

During neutron exposure, the creation rate of ^{198}Au nuclei in the foil is given by:

$$C_{^{198}Au} = \int_0^\infty N_{^{197}Au} \cdot \sigma_{^{197}Au}(E) \cdot \Phi(E) \cdot V \cdot dE \qquad \text{(A.12)}$$

with

$C_{^{198}Au}$: Creation rate of ^{198}Au nuclei

$N_{^{197}Au}$: Density of ^{197}Au nuclei

$\sigma_{^{197}Au}(E)$: microscopic neutron absorption cross section of ^{197}Au

$\Phi(E)$: spectral neutron flux density

V: Volume of Au-foil

In Eq. A.12 it is assumed that the foil is thin, hence no shielding effects exist (constant neutron flux within the whole volume of the foil).

During the exposure of Au-foil, some of the created ^{198}Au decay. The decay rate (activity) of ^{198}Au is given by:

$$D_{^{198}Au} = \lambda n_{^{198}Au} \qquad \text{(A.13)}$$

with

$D_{^{198}Au}$: decay rate of ^{198}Au nuclei

λ: decay constant of ^{198}Au ($\lambda = 1.79 \cdot 10^{-4}\ \mathrm{min}^{-1}$)

$n_{^{198}Au}$: number of ^{198}Au nuclei

The time derivation of the number of ^{198}Au nuclei is given by the difference of production rate and decay rate:

$$\frac{dn_{^{198}Au}}{dt} = C_{^{198}Au} - D_{^{198}Au} = C_{^{198}Au} - \lambda n_{^{198}Au} \qquad \text{(A.14)}$$

with

t: time

The solution for $n_{^{198}Au}$ of this equation is:

$$n_{^{198}Au}(t) = \frac{C_{^{198}Au}}{\lambda}\left(1 - e^{-\lambda t}\right) \qquad \text{(A.15)}$$

Hence, the activity of the gold foil at the end of neutron exposure is:

$$A = \lambda n_{^{198}Au}(T) = C_{^{198}Au}\left(1 - e^{-\lambda T}\right) \qquad \text{(A.16)}$$

with

T: exposure time

The Au-foil was exposed to the neutron beam for 90 min, hence the activity after exposure is:

$$A = C_{^{198}Au} \cdot 1.6 \cdot 10^{-2} \qquad \text{(A.17)}$$

Using Eq. A.17, Eq. A.16 becomes:

$$A = 1.6 \cdot 10^{-2} \cdot \int_0^{\infty} N_{^{197}Au} \cdot \sigma_{^{197}Au}(E) \cdot \Phi(E) \cdot V \cdot dE \quad \text{(A.18)}$$

No simple analytic expression exits for the Au cross section $\sigma_{^{197}Au}(E)$ (in the literature often the approximation is used that the cross section is indirect proportional to neutron velocity, but by this approximation the resonances are not considered; Fig. A.10). Same is true for the spectral neutron flux density. Hence, Eq. A.18 was solved in a numerical way. The cross section values are known from literature. The normalized spectral flux density $\Phi(E)/\Phi_{total}$ is known from the TOF measurement and from Monte Carlo calculations (of course, from Monte Carlo the total flux is also known, but it is not used here, as one aim of the Au-foil activation measurement is to verify the Monte Carlo data).

For numerical solution of Eq. A.18, the activity A^* of the gold foil caused by a total neutron flux Φ^* of 1 $cm^{-2}sec^{-1}$ was calculated by help of the normalized spectral flux density:

$$A^* = 1.6 \cdot 10^{-2} \cdot \int_0^{\infty} N_{^{197}Au} \cdot \sigma_{^{197}Au}(E) \cdot \Phi(E)/\Phi_{total} \cdot \Phi^* \cdot V \cdot dE \quad \text{(A.19)}$$

The real total neutron flux is given by multiplication of Φ^* with the ratio of the measured activity to the activity A^*:

$$\Phi_{total} = \Phi^* \cdot \frac{A}{A^*}$$

The analysis of the Au-foil activation with Cd cover is analog, but the energy dependent neutron attenuation of Cd has to be considered in Eq. A.12:

$$C_{^{198}Au} = \int_0^{\infty} e^{-\sigma_{Cd} \cdot N_{cd} \cdot d} \cdot N_{^{197}Au} \cdot \sigma_{^{197}Au}(E) \cdot \Phi(E) \cdot V \cdot dE \quad \text{(A.12*)}$$

with

σ_{Cd}	microscopic absorption cross section of Cd
N_{Cd}	particle density of Cd
d	thickness of Cd cover

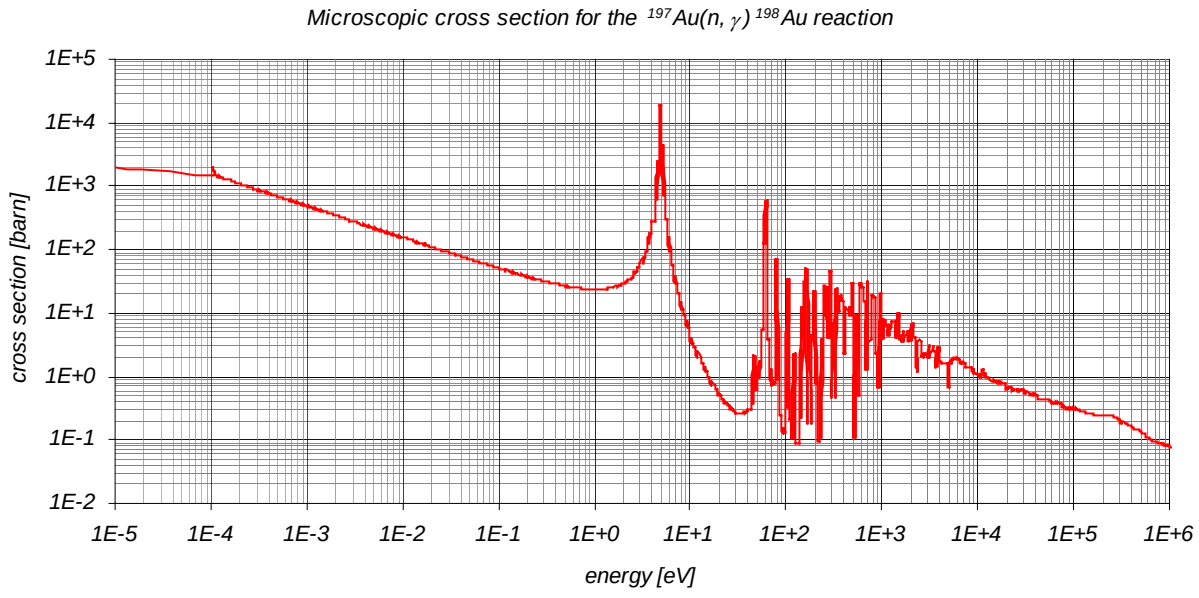

A.10: Microscopic cross section for the reaction $^{197}Au(n,\gamma)^{198}Au$

A.4 Activation in the experimental chamber

If the experimental chamber is opened immediately after an irradiation time of several hours, three structures show a significant activation (beside the specimen itself):

- The casing of the beam catcher (made from Al; dose rate on surface: approximately 30 µSv/h)
- The manipulator for the specimen (made from Al; when irradiated during tomographies dose rates on the surface of up to 100 µSv/h occur)
- The mirror of the detector system (made from glass)

The activity of the casing of the beam catcher and the manipulator descends down to 1 % (less than 1 µSv/h) within 15 minutes; the measured half-life time is about 2 minutes. Both structures consist of aluminum. Neutron activation of aluminum is done by the reaction $^{27}Al(n,\gamma)^{28}Al$. ^{28}Al is a β-emitter with a half-life time of $t_{1/2}$=2.246 minutes [32]. The β-decay generates an excited ^{28}Si-Nuclei that transmits gamma radiation with an energy of 1.78 MeV [40] ($t_{1/2}$=0.5 ps).

As the activity of the aluminum structures decreases very fast, it is not disturbing the experimental activities. Experimenters have only to wait a few minutes before a save access to the experimental chamber is possible.

The activity of the mirror descends much slower. The measurement of the half-life time ($t_{1/2}$=15 h) clearly showed that activation is dominated by the sodium content of the mirror. The crucial reaction is $^{23}Na\ (n,\gamma)\ ^{24}Na$. The accumulated ^{24}Na-Nucleus is a β-emitter with a half-life time of $t_{1/2}$=14.96 h. From the β-decay an excited ^{24}Mg-Nucleus is created, that transmits gamma radiation with energies of 1.37 MeV and 2.75 MeV [40].

However the activation of the mirror is not disturbing the experimental activities, because the dose rate is below 5 µSv/h at a distance of 0.5 m. Experimenters has just to keep distance from the mirror.

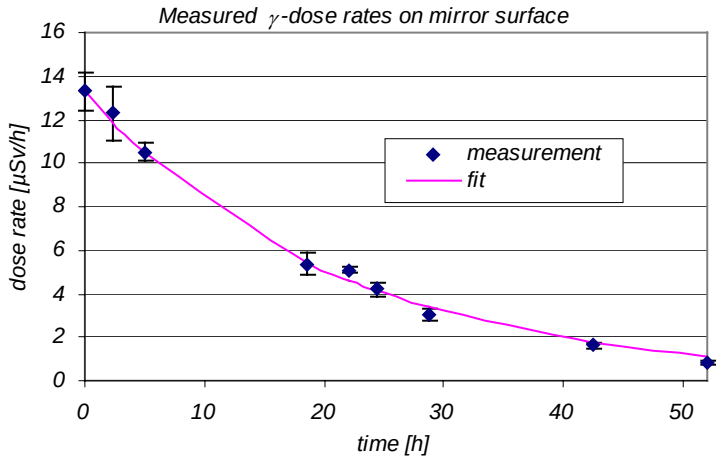

Fig. A.11: Comparison of theoretical decrease of ^{24}Na dose rate and measured decrease of dose rate from the activated mirror of the ANTARES standard detector system

A.5 Mounting the roof elements for the radiation shielding of the flight tube

Two platforms for the positron experiment are mounted above the ANTARES facility. The regions below the platforms are not accessible by the hall crane [98]. The elements of the side walls of the shielding of the flight tube can be moved by air cushions to their positions below the platforms. This holds not for the roof elements of the shielding. For them, a rail system on top of the side walls of the shielding had to be installed. For this rail system the shielding thickness of the side walls had to be increased at one position (see chapter 2.10.5.3 'Radiation shielding for the flight tube').

The whole region with distances less than 8 m from the cold source is not accessible by the hall crane, due to platform 1 (Fig. A.13) of the positron experiment. Same holds for the region more than 15 m distant from the cold source, where a second platform (platform 2 in illustration Fig. A.13) of the positron experiment is mounted. The region with a distance from 8.2 m to 15 m from the cold source is accessible by the hall crane. All roof elements for positions below the platforms are positioned here and are driven to their final position by help of the rail system. The gauge of the rail system for the region below platform 1 (gauge 1 in Fig. A.13) is limited by the shielding for the UCN (ultra cold neutrons) experiment (Figs. A.12, A.13) and is smaller than gauge 2 below platform 2. The rail system is supported by the side walls of the shielding. Due to the smaller gauge of rail system 1, the inner width of the shielding had to be reduced between distances of 8.2 m and 10.3 m from the cold source, leading to a shielding thickness of 80 cm.

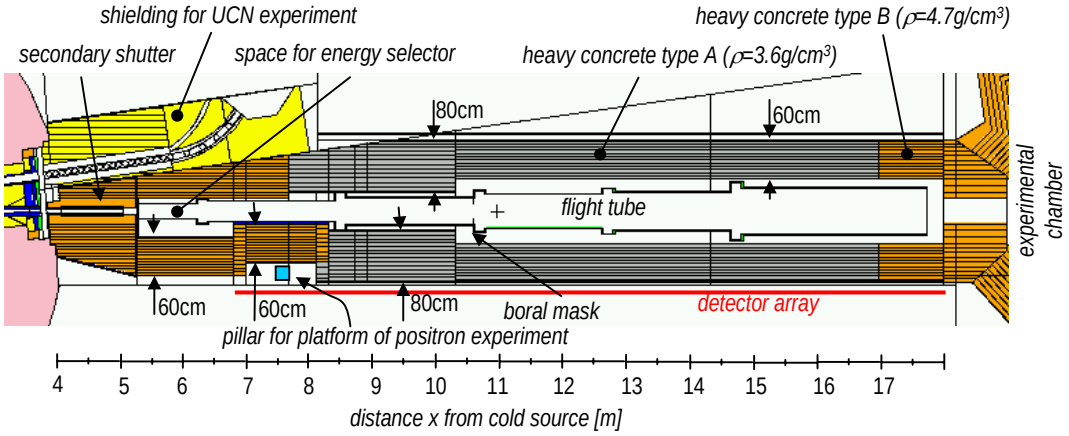

Fig. A.12: Horizontal cut along beam axis through the Monte Carlo model of the shielding for the flight tube.

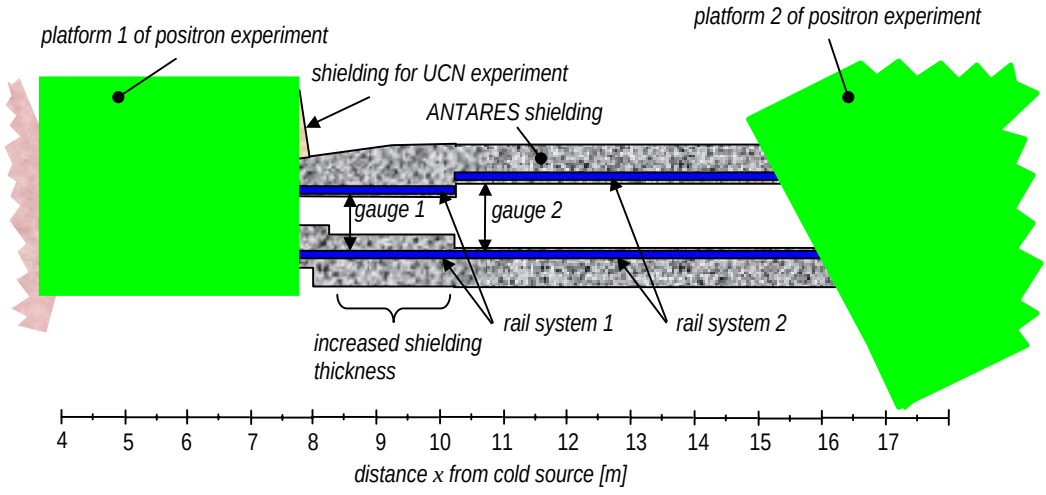

Fig. A.13: Schematic overview of the rail systems on top of the side walls of the ANTARES shielding for mounting the roof elements below the platforms of the positron experiment.

A.6 Test of coded masks with a low textured specimen

The results of the investigations about coded masks combined with correlation techniques showed that they are not applicable in neutron radiography of structured objects. Investigations were also carried out whether the methods are advantageous for minor textured specimen. The specimen used here is an iron plate of 2 cm thickness with spherical voids of different diameters. The practical background is the detection of cavities, e.g. in steel. A vertical cut through the specimen is shown in Fig. A.14. The radii r of the voids are in the range from 0.1 mm to 3.0 mm. The projections were carried out by the virtual radiography station as described above. The distance between aperture (or coded mask) and the specimen is 1 m, the distance between specimen and detector plane is 20 cm. For all projections $2 \cdot 10^9$ particle histories were calculated. The projections and reconstructions are shown in Fig. A.15 to Fig. A.18. The gray scales are inverted, hence darker regions indicate lower attenuation. The minimum and maximum of displayed gray values are adjusted for each projection in a way that highest contrast between voids and surrounding material is obtained. Line profiles through the projections of the biggest void (r=3 mm; void at the upper left corner of the projection) are shown in Fig. A.19 and Fig. A.20 for the data obtained by the different methods. The projection obtained by a quadratic single hole aperture of 5.4 mm^2 transmission area is shown in Fig. A.15. The aperture is the same as used in chapter 3.5.3 (displayed in Fig. 3.32). Just the two biggest voids are recognizable, those with radii of 3.0 mm and 2.0 mm. The signals of all other voids do not stick out of the noise. Fig. A.16 shows a projection obtained by a circular single hole aperture with a transmission area, that is 10 times bigger (54 mm^2, radius 4.16 mm). Due to the higher transmission, the SNR is higher in this projection and more voids can be recognized. However the signal of voids is still close to the noise level, even for big voids (see line profile through the signal of the biggest void in Fig. A.19 right hand side). Situation is improved considerably by the 10 hole NRA mask, as described in chapter 3.5.3 (Fig.3.33). For reconstruction the correlation technique was used (see chapter 3.5.3). The result is shown in Fig. A.17. Although this mask has the same transmission area (54 mm^2), as the circular single hole aperture, big voids are displayed with a much

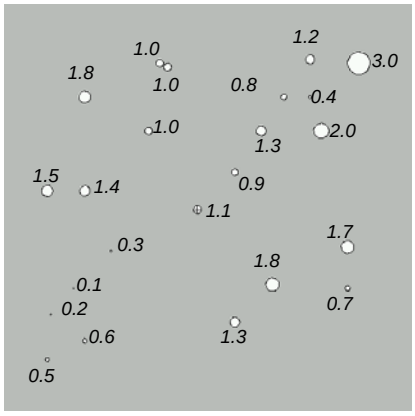

Fig. A.14: Vertical cut through the specimen (iron plate with spheric voids). The numbers are the radii of the voids.

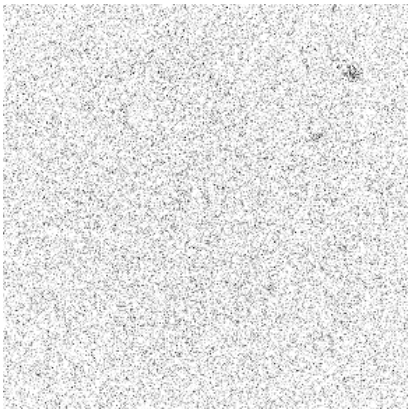

Fig. A.15: Unprocessed projection of the Iron plate with voids, obtained by a single hole aperture with a quadratic transmission area of 5.4 mm^2.

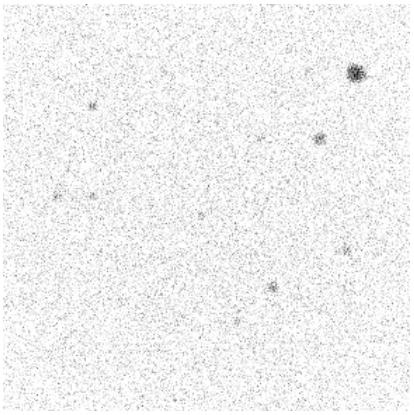

Fig. A.16: Unprocessed projection of the Iron plate with voids, obtained by a single hole mask with transmission area of 54 mm^2 (same transmission area as the 10 hole NRA mask)

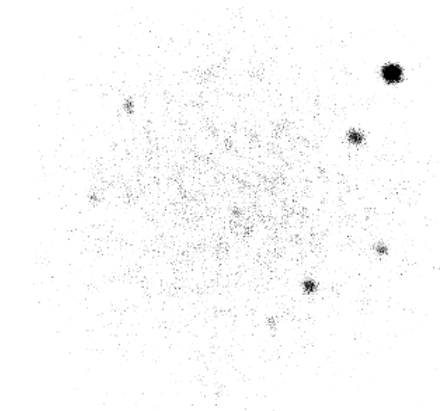

Fig. A.17: Reconstruction by correlation technique of a projection of the Iron plate with voids, obtained by a 10 hole NRA mask. Each hole of the mask has a transmission area of 5.4 mm^2.

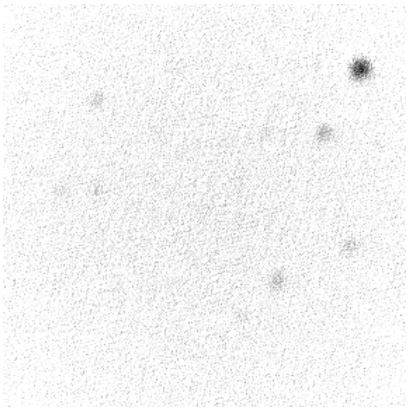

Fig. A.18: Reconstruction by correlation technique of a projection of the Iron plate with voids, obtained by a random array mask. Each hole of the mask has a transmission area of 5.4 mm^2.

higher contrast to the noise level. A disadvantage of this technique is also visible in this example. Some small voids disappeared completely: When statistical fluctuations completely exceed the signal of the projected mask pattern presenting one point in the object, this point is not reconstructed at all.

The random array described in chapter 3.5.2 was also tested, but results are not satisfying (Fig. A.18). Due to the small number of holes, inherent noise is too big for this mask. The projected voids are spread to big regions, hence contrast is rather low. The same is true for the ring aperture. Results for the ring aperture are therefore not presented here.

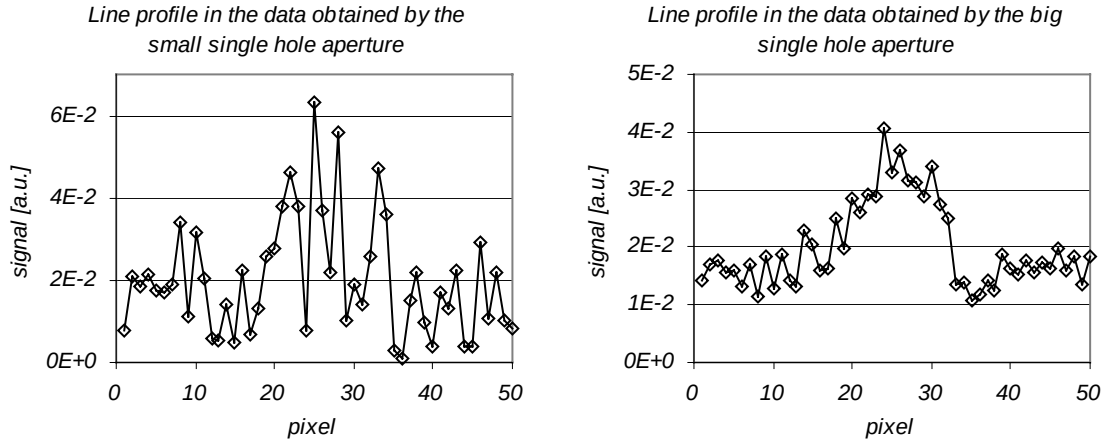

Fig. A.19: Left hand side: Line profile through the projection of the biggest void (r=3 mm) in the unprocessed data obtained by the quadratic single hole aperture with a transmission area of 5.4 mm^2.
Right hand side: Line profile through the projection of the biggest void (r=3 mm) in the unprocessed data obtained by the circular single hole aperture with a transmission area of 54 mm^2.

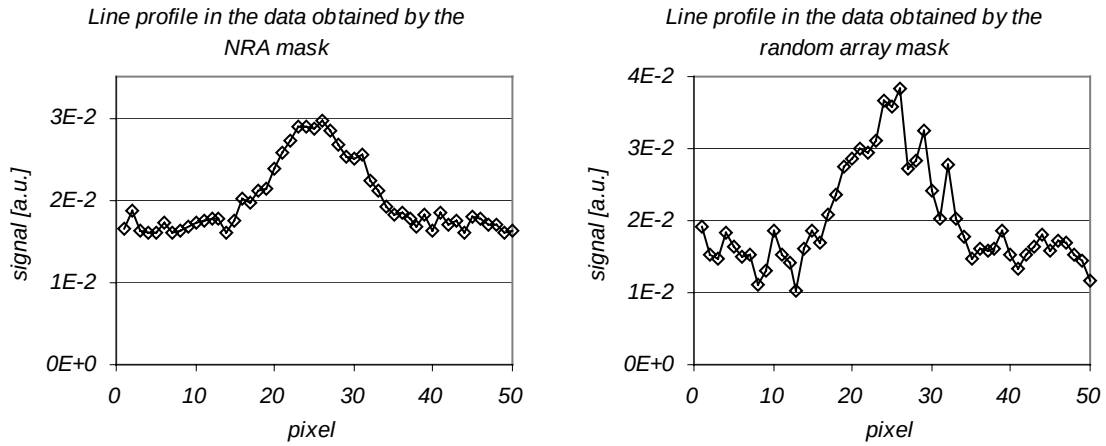

Fig. A.20: Left hand side: Line profile through the projection of the biggest void (r=3 mm) in the reconstructed data obtained by the 10 hole NRA mask (transmission area 54 mm^2).
Right hand side: Line profile through the projection of the biggest void (r=3 mm) in the reconstructed data obtained by the random array mask.

A.7 Response function of a neutron detector for radiation protection purposes

At FRM-II commercially available neutron detectors are used for radiation monitoring and protection (Biorem FHT 750 [51]). This type of neutron dosimeter consist of a BF_3 counter tube that is arranged in a cylindrical polyethylene volume with 10.2 cm radius. The polyethylene is used as neutron moderator, because detection probability for epithermal and fast neutrons in BF_3 tubes is much lower compared to thermal neutrons. For neutron dose rate detectors it is desired that the count rate is as proportional as possible to the dose rate, hence fast neutrons should cause a higher count rate as thermal neutrons. For this purpose borated polyethylene (Figs. A.22, A.23), arranged on a cylinder, is included in the polyethylene moderator. Fast and epithermal neutrons cross borated polyethylene with higher probability than thermal neutrons. Thermal neutrons can cross the borated polyethylene cylinder only at certain locations, where gaps in the cylinder exist. By this, the response function is adjusted to neutron energy.

Fig. A.21: Neutron dose rate detector

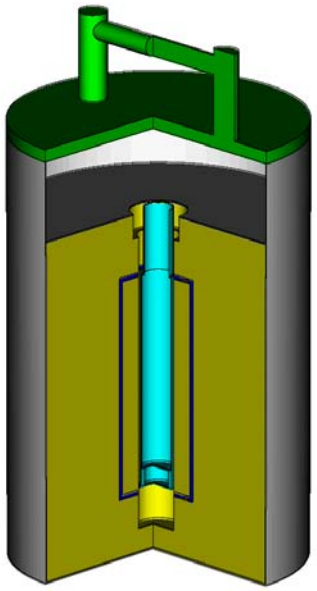

Fig. A.22: Cut through the Monte Carlo model of the neutron dose rate detector

This type of detector is approved in the energy range of thermal to fast neutrons and for irradiation of the whole dosimeter arrangement. Contrary to usual applications of neutron dosimetry (e.g. reactor halls), a major contribution of cold neutrons has to be expected in the neutron-guide hall of FRM-II. It had to be examined whether this detector is suitable for cold spectra and if so, what calibration and security factors have to be applied under these special conditions.
Beside spectral effects, the dependency of the incidence angle of the neutron beam with regard to the detector axis had to be examined, since in contrast to 'standard applications', the detector will be illuminated only from one side in some cases at FRM-II. For calculation an homogeneous, monoenergetic and monodirectional beam was used. The beam fully illuminates the whole detector. The response to different angles of

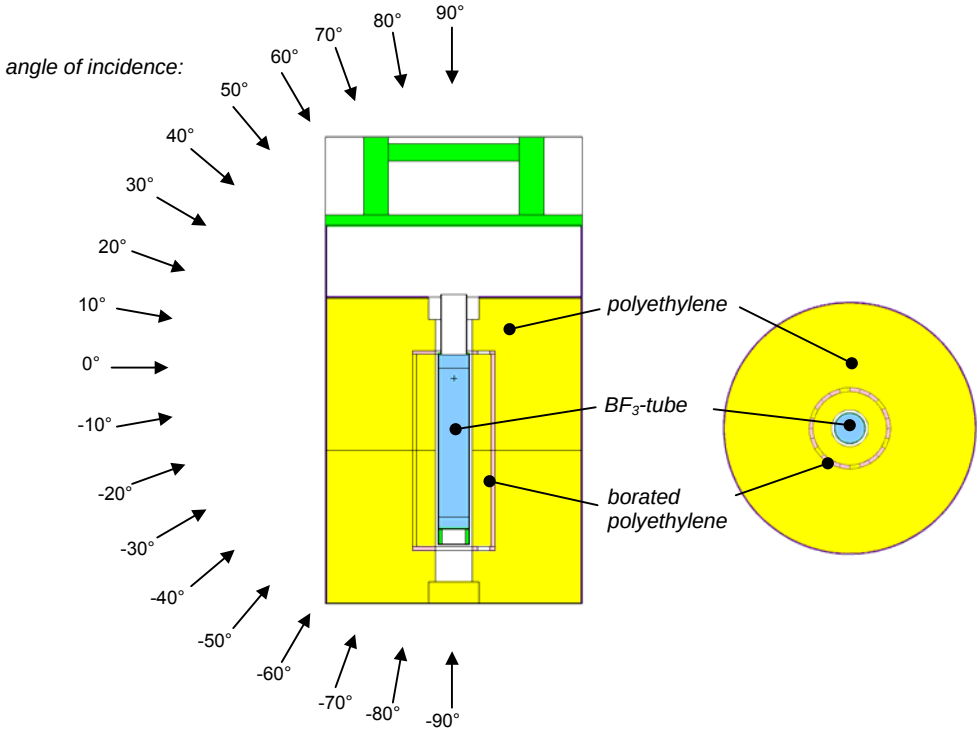

Fig. A.23: Vertical (left hand side) and horizontal (right hand side) cut through the Monte Carlo model of the neutron dosimeter

incidence was investigated by rotation of the detector in the beam. The angles are displayed in Fig. A.23 left hand side. For each angle the number of $^{10}B(n,\alpha)^{7}Li$ reactions in the counter tube was calculated. These calculations were repeated for different neutron energies of the incident beam. Fig. A.24 shows the count rate of the detector related to the real, undisturbed neutron flux. The undisturbed neutron flux in this context is the flux if the whole dosimeter were removed. For an incidence angle of 0° (illumination from the side; black line in Fig. A.24) the count rate increases monotonically with increasing neutron energy. This is not the case for all incidence directions: An extreme case is illumination from the top (90°). Thermal neutrons cause the biggest response. Neutrons impinging on the top of the detector can reach the counter tube through a hole in the polyethylene moderator (Figs. A.22, A.23). The hole is intended for the feed lines for the counter tube.

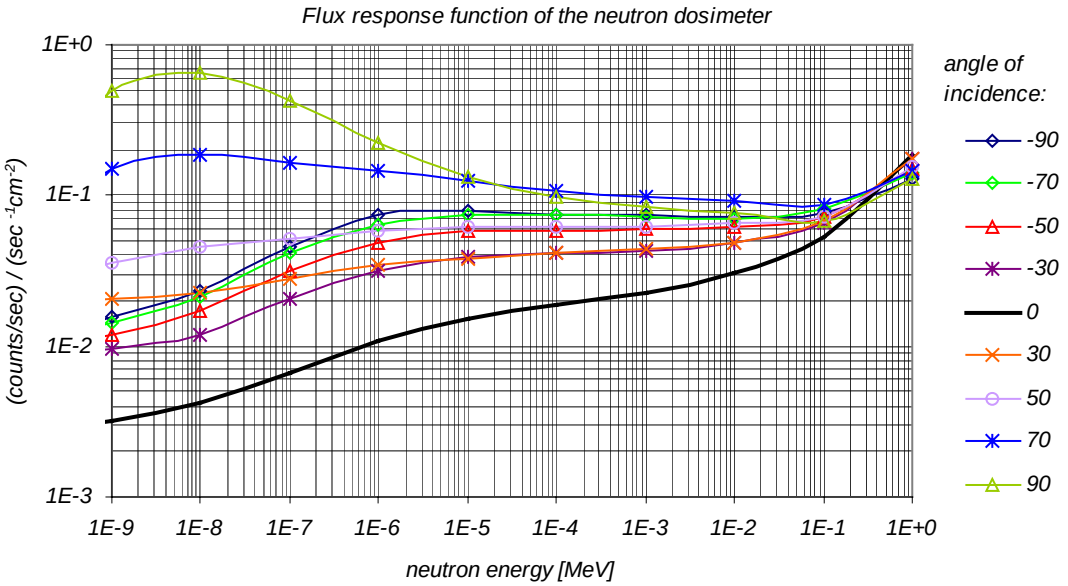

Fig. A.24: Response function of the neutron dosimeter relating to undisturbed neutron flux. The whole dosimeter is exposed to the homogeneous parallel neutron beam

The number of $^{10}B(n,\alpha)^{7}Li$ reactions related to the undisturbed neutron dose rate is shown in Fig. A.25. The undisturbed dose rate is the dose rate if the dosimeter were removed. Neutron dose was calculated according to ICRP 74 [67][68][69].

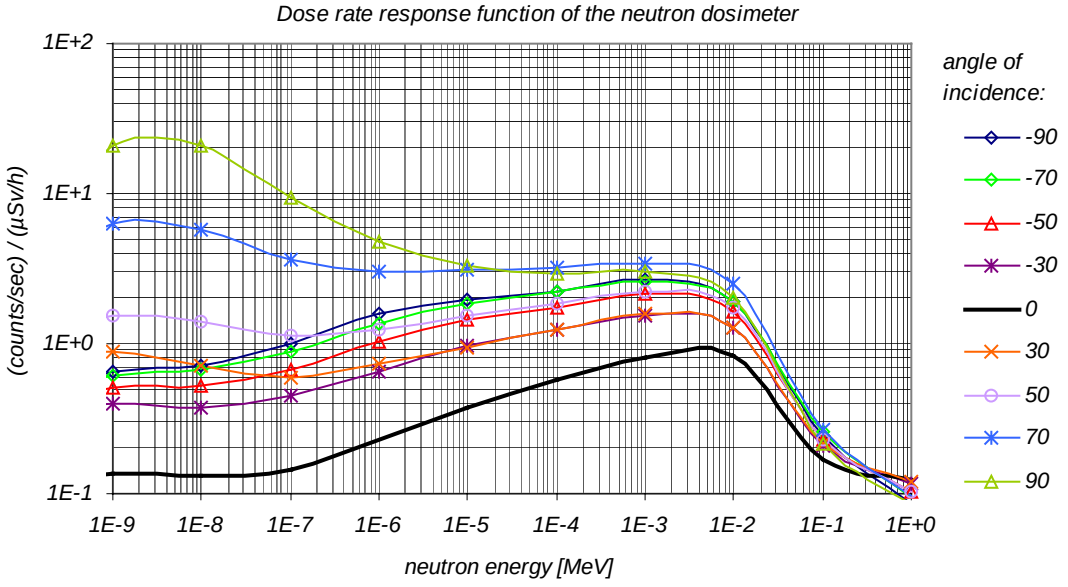

Fig. A.25: Response function of the neutron dosimeter relating to undisturbed neutron dose rate. The whole dosimeter is exposed to the homogeneous, parallel neutron beam

For illumination from the side (black curve in Fig. A.25, 0°), the biggest response appears for epithermal neutrons (5 keV). For higher neutron energies the response decreases due to the steep increase of fluence-to-dose conversion factors with neutron energy (see Fig. A.28 in the next chapter). The count rate itself increases, as shown in Fig. A.24, but not as fast as the conversion factors, hence count rate per dose rate decreases. For thermal neutrons under an incidence angle of 0° the response is smaller than for epithermal neutrons. A comparison of response for thermal neutrons (around 25 meV) and cold neutrons (around 2 meV) shows that the detector behaves similar for both energies. Under illumination from the top, the detector shows higher sensitivity for thermal neutrons due to the feed line hole in the polyethylene moderator. The response is even bigger than for epithermal neutrons. However, the difference between cold and thermal neutrons is also low. The dependency of angle of incidence is much higher than the dependency on neutron energy for this detector, hence no problem arises from using it for cold neutron spectra. The manufacturer of the dosimeter specifies the 'typical neutron response' as 1 cps at 1.8 µSv/h [51].

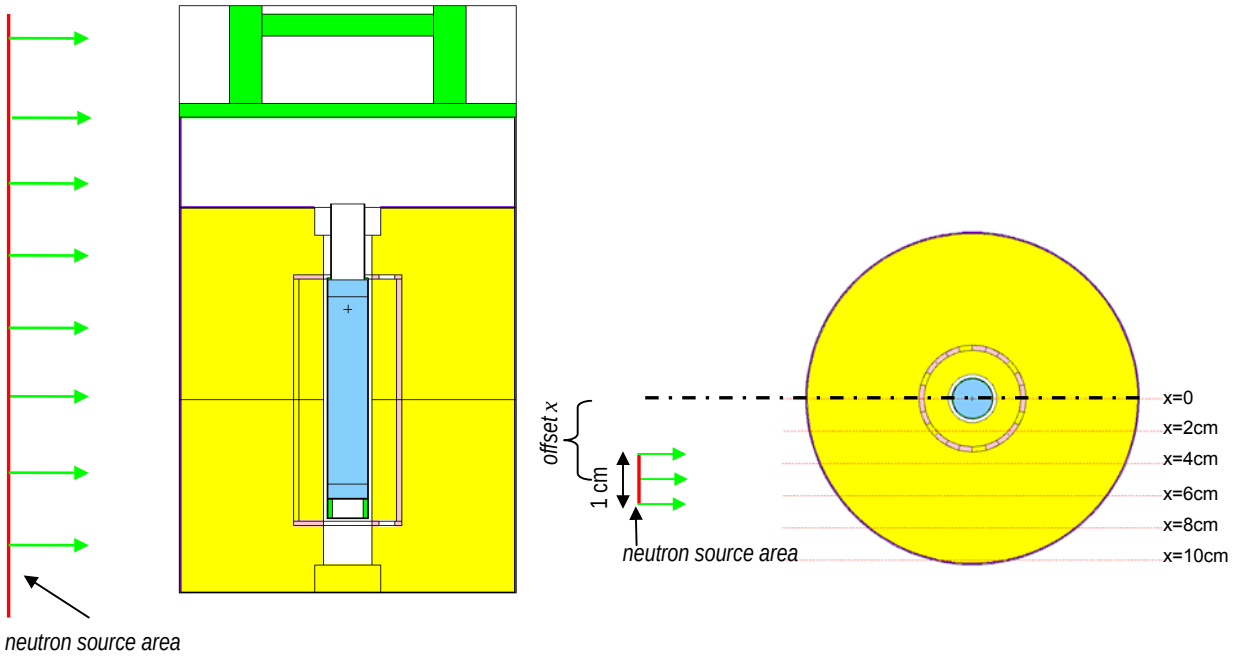

Fig. A.26: Vertical cut through the Monte Carlo model for investigation of the influence of partial illumination of the dosimeter (left hand side) and horizontal cut (right hand side). The neutron beam is displayed as green arrows.

In special applications, radiation fields have to be measured that are smaller than the detector itself, e.g. areas with gaps in radiation shieldings or with low attenuating shielding material. Therefore the dependency of detector response for partial illumination was also investigated: An homogeneous, monoenergetic and parallel neutron beam of 1 cm width illuminates the detector. The height of the beam is bigger than the detector. Hence the detector is fully illuminated in vertical direction. The detector response was calculated for different offsets x between detector axis and neutron beam (Fig. A.26).

The ratio of detector response for partial illumination to full illumination is displayed in Fig. A.27. For an

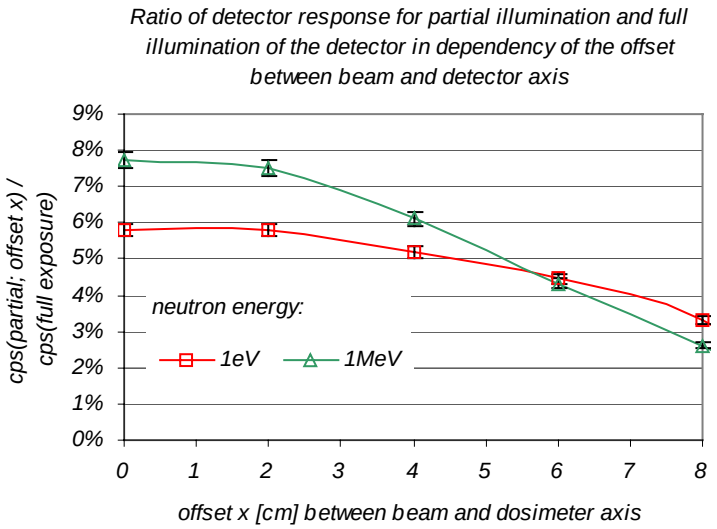

Fig. A.27: Ratios of counts per second (cps) for partial and full illumination as function of the offset x between beam axis and detector axis.

offset of x=0, the response for partial neutron illumination with an energy of 1 eV is 5.8 % of the response for full illumination. This is very close to the ratios of exposed detector areas for partial and full illumination. The differences in the detector response for different offsets x are rather small. Even for an offset of x=8 cm the response is 3.3 % of the response under full illumination. Neutrons in the thermal energy region experience many scatter events even in small distances, hence the direction distribution of neutron flight paths is nearly isotropic in the moderator. The probability to reach the counter tube is therefore not decreased too much for big offsets between beam axis and detector center. This is not the case for fast neutrons (1 MeV): Neutrons in this energy region are scattered with lower probability in the moderator, mean free paths are larger. A fast neutron impinging perpendicular to the moderator surface has to face a longer path through the moderator than a neutron impinging tangential at the margin of the moderator surface. Differences in detector response related to the offset between beam and detector axis are therefore higher as for thermal neutrons. The detector response for fast neutrons decreases faster with increasing offset x.

A.8 Fluence to dose conversion factors

All results for dose equivalent values in this thesis are calculated according to ICRP74 [67, 68]. Energy deposition by radiation is not a field property in a mathematical sense like e.g. flux. It depends on the material, on the size of the considered volume, etc. For consistent indication of energy deposition in tissue, the ambient dose equivalent $H^*(10)$ is defined in [67]. It is the dose in 10 mm depth in a sphere with a diameter of 30 cm that consists of ICRU-tissue (Weight fractions: 10.1% H; 11.1% C; 76.2% O; 2.6% N [68]). With this definition, energy dependent conversion factors $h^*(10)(E)$ between fluence and dose can be specified. For a given fluence Φ, the ambient dose equivalent $H^*(10)$ is:

$$H^*(10) = \int_0^\infty h^*(10)(E) \cdot \phi(E) dE \quad \text{(A.20)}$$

The conversion factors for neutron radiation are shown in Fig. A.28. For comparison former conversion factors according to ICRP 21 are also displayed. The values for gamma radiation are shown in Fig. A.29.

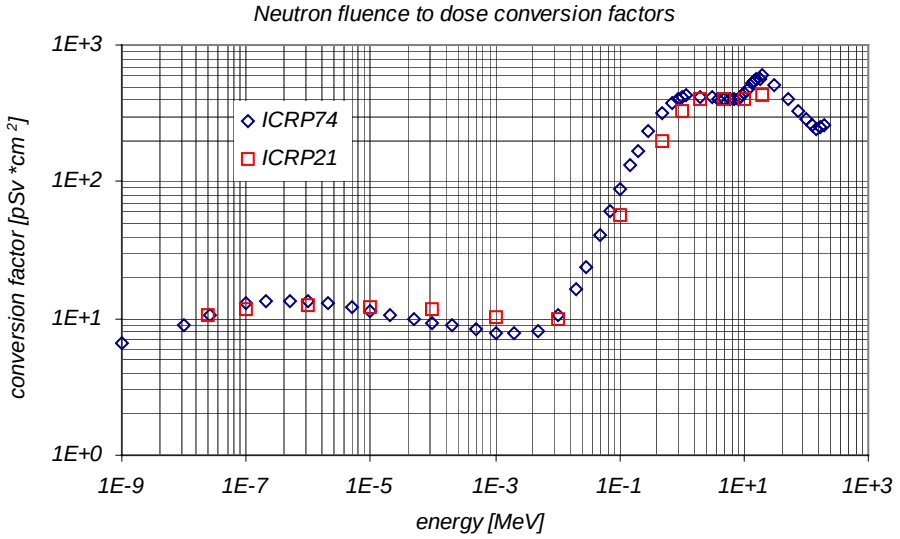

Fig. A.28: Neutron fluence to dose conversion factors $h^*(10)$ according to ICRP74 and the former values according to ICRP21

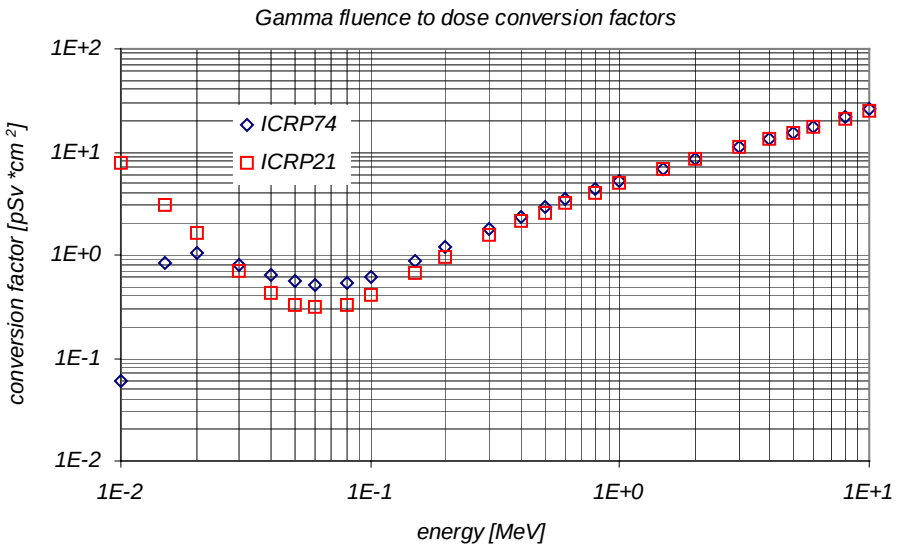

Fig. A.29: Photon fluence to dose conversion factors $h^*(10)$ according to ICRP74 and the former values according to ICRP2

As in former literature dose values are specified according to ICRP21 and even today sometimes ICRP21 dose to fluence conversion factors are used, comparison of dose values is difficult. Hence the

question arises how big the influence of different conversion factors is on the result of typical shielding calculations. This was investigated by the sphere (R=80 cm) for testing shielding materials as described in chapter 2.10.3.1 'Calculation model for testing shielding materials'. The sphere is filled with heavy concrete type B ρ=4.7 g/cm^3 (chapter 2.10.3.1 'Concrete as shielding material'). The spectrum of the neutron source is that of the ANTARES facility. The neutron dose per source neutron outside the sphere was calculated according to ICRP74 and ICRP21. The results are shown in Fig. A.30 left hand side. The values according to ICRP21 are 77 % of the values according to ICRP74.

The dose of generated gamma radiation per source neutron outside the sphere according to ICRP74 and ICRP2 are displayed in Fig. A.30 right hand side. The difference is smaller compared to neutrons. ICRP2 results are 96.4 % of the value obtained by ICRP74.

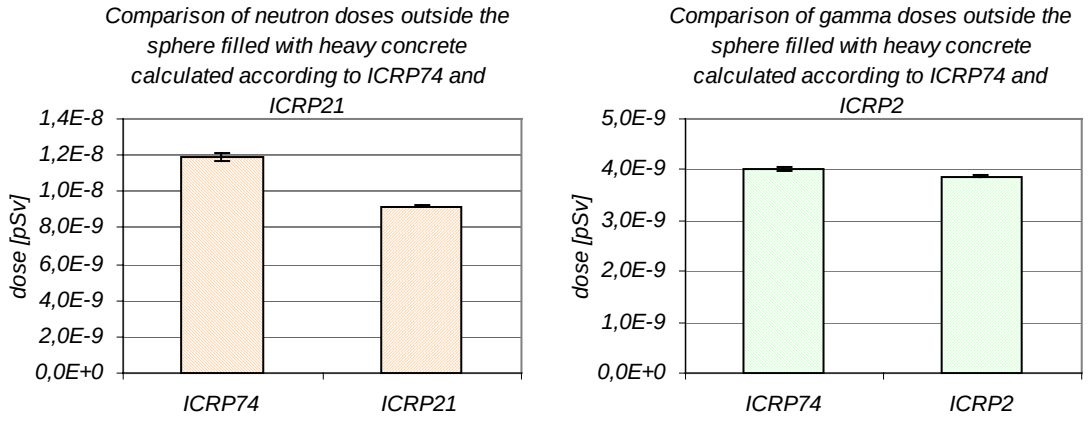

Fig. A.30: Left hand side: Comparison of neutron dose per source neutron outside the sphere (R=80 cm) filled with heavy concrete type B (ρ=4.7 g/cm^3, see chapter 2.10.3.1 'Concrete as shielding material') according to ICRP74 and ICRP21

Right hand side: Comparison of generated gamma dose per source neutron outside the sphere filled with heavy concrete type B (ρ=4.7 g/cm^3, see chapter 2.10.3.1 'Concrete as shielding material') according ICRP74 and ICRP2

A.9 Influence of fast and epithermal neutron scattering in neutron guides

Some of the experiments at FRM-II are not located in the experimental hall around the biological shielding of the reactor, but in the adjacent 'neutron guide hall' (Fig. A.31 top). In order to minimize the loss of neutron flux due to the big distance from the neutron source, neutrons are guided to the instruments by help of neutron guides, in which cold neutrons are totally reflected [7]. The neutron guides have linear and curved parts. By the curved parts the background radiation of fast and epithermal neutrons and gamma radiation that is not totally reflected is minimized in the neutron guide hall. All neutron guides are directed to the cold source, hence all instruments in the neutron guide hall are provided with a cold neutron spectrum. For the ANTARES facility it was shown that a flight tube has a big impact on the dose distribution due to scattering of fast and epithermal neutrons in the tube wall material. Similar to the flight tube of the ANTARES facility, the incident angles of neutron flight path on the neutron guide walls are rather small. From this the question arises how big is the influence of scattering of fast neutrons and epithermal neutrons in the neutron guide walls. Scattering of thermal and cold neutrons inside the guide wall material (borated glass) is negligible due to its high absorption cross section. The neutron guides cross two walls between the reactor and the neutron guide hall (wall A and B; see Fig. A.31 top).

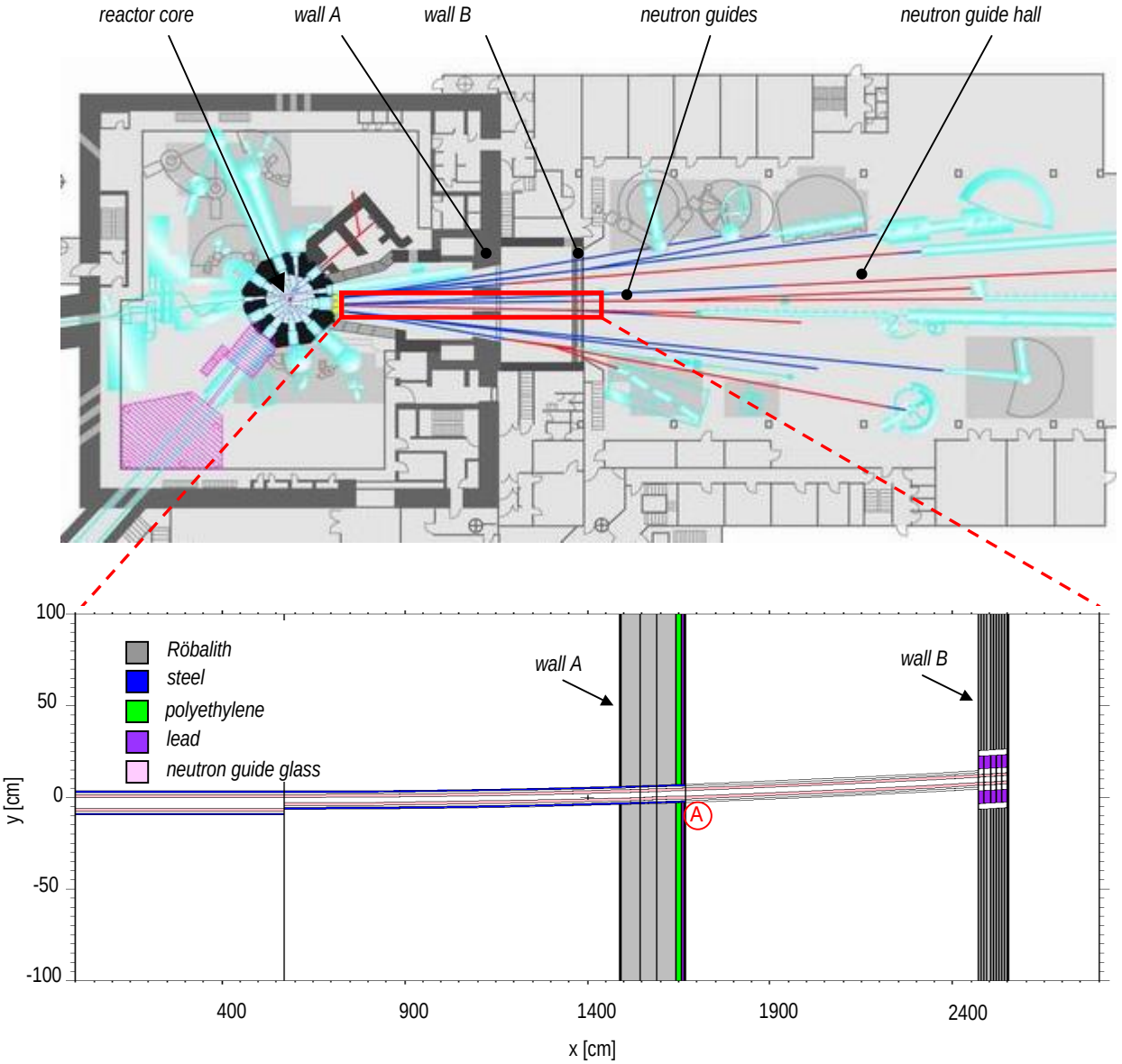

Fig. A.31: Top: Horizontal cut through the reactor, the experimental hall, and neutron guide hall. Neutrons are guided by neutron guides (red and blue lines) to the instruments.
Bottom: Horizontal cut through the Monte Carlo model of the neutron guide NL5. The neutron dose distribution was calculated for this plane. The marker A indicates the position for which the dose rate was measured.

The main task of the walls is to shield all radiation components that are not totally reflected and leave the guides. As materials for wall A Röbalith, polyethylene and lead were intended, arranged in three layers of each material. In beam direction the layers are: 148 cm Röbalith, 16 cm polyethylene and 10 cm lead. The layers are arranged between steel liners (thickness 3 cm). Röbalith is a barite concrete. Its composition is shown in chapter 2.10.3.3 'Concrete as shielding material'.

As shown in chapter 2.10.3.3, Röbalith is not the optimal solution for shielding fast neutrons, due to a low hydrogen content, no iron content and no absorbers that prevent production of high energetic gamma radiation. From this the question arises whether the radiation level in the room between walls A and B can be minimized by replacing Röbalith by other shielding materials like e.g. heavy concrete or steel and polyethylene layers. The Monte Carlo model of neutron guide NL5 is shown in Fig. A.31 bottom. The radius of curvature for this neutron guide is 1.64 km; the resulting end of direct sight to the cold source is achieved in the room between wall A and wall B. The guide walls consist of borated glass (wall thickness at the sides 1.6 cm, wall thickness at top and bottom: 1 cm). The inner guide cross section is 2.9 cm (width) x 17 cm (height). For evacuation of the neutron guide, it is surrounded by a steel casing in the region before wall A and within wall A. Fig. A.32 shows a vertical cut through the Monte Carlo model of this arrangement. The dose rates around the neutron guide in a horizontal plane are shown in Figs. A.33 to A.36 for different energy groups above 1 eV. The data refers to a reactor power of 20 MW. The setup of wall A is that described above (Röbalith, polyethylene and lead layers). The spatial resolution for the calculation is 10 cm in beam direction and 5 cm perpendicular to beam direction. The calculations show that the neutron guide itself becomes a secondary 'line source' for fast and epithermal neutrons within the range of direct sight to the cold source. Neutrons in lower energy groups (below 1eV) are totally reflected or absorbed in the boron content of the guide glass. Several calculations showed that the dose rate between wall A and B remains constant when Röbalith is replaced by other shielding materials. The dose is dominated by scattering of fast neutrons in the guide glass between the walls (Figs. A.33 to A.36). Transmission through wall A yields a minor contribution. Hence for effective reduction of the dose rate, a shielding around the guide is necessary (that was realized after first measurements confirmed the results of the calculations).

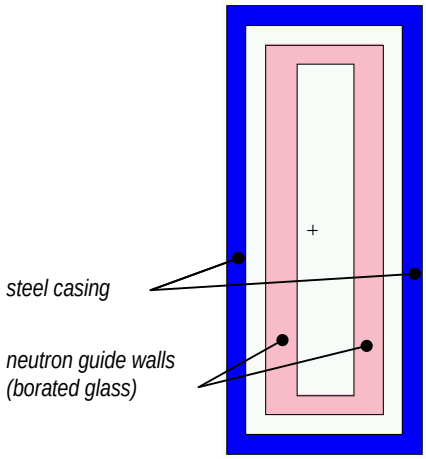

Fig. A.32: Vertical cut through the Monte Carlo model of the neutron guide NL5

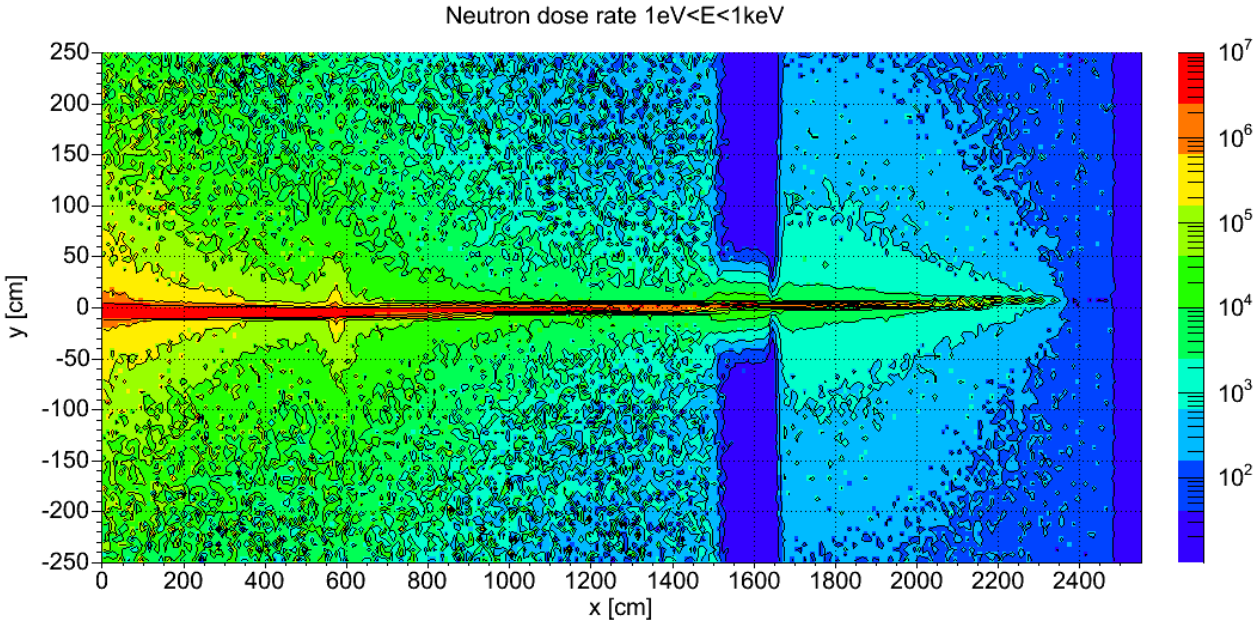

Fig. A.33: Neutron dose rate [µSv/h] in the energy range between 1 eV and 1 keV in a horizontal plane around the neutron guide. Values above 10^7 µSv/h are set to 10^7 µSv/h (red regions) in this plot in order to visualize lower dose rates between wall A and B more clearly.

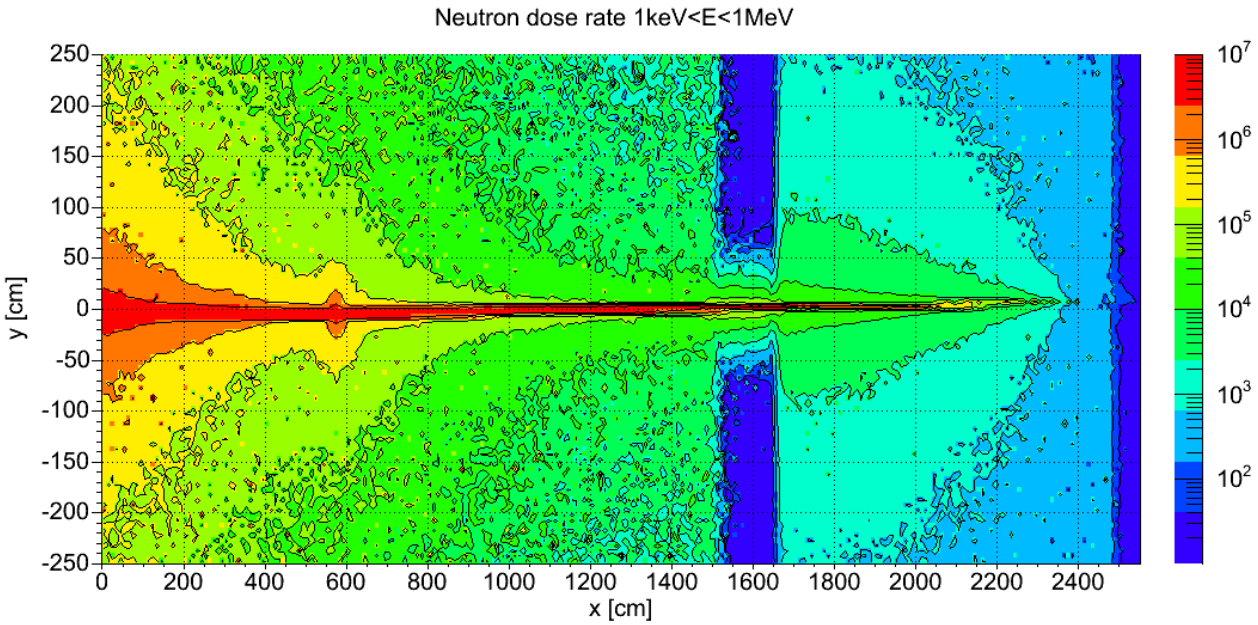

Fig. A.34: Neutron dose rate [µSv/h] in the energy range between 1 keV and 1 MeV in a horizontal plane around the neutron guide. Values above 10^7 µSv/h are set to 10^7 µSv/h (red regions) in this plot in order to visualize lower dose rates between wall A and B more clearly.

On the one hand borated glass shows no outstanding cross sections for fast and epithermal neutrons, on the other hand the neutron paths through the material are quite long due to flat angles of incidence. The angle of incidence for a neutron entering the guide material in wall A is about 0.2 °, resulting in a path length of about 4 m through the guide wall (when no scatter event takes place).

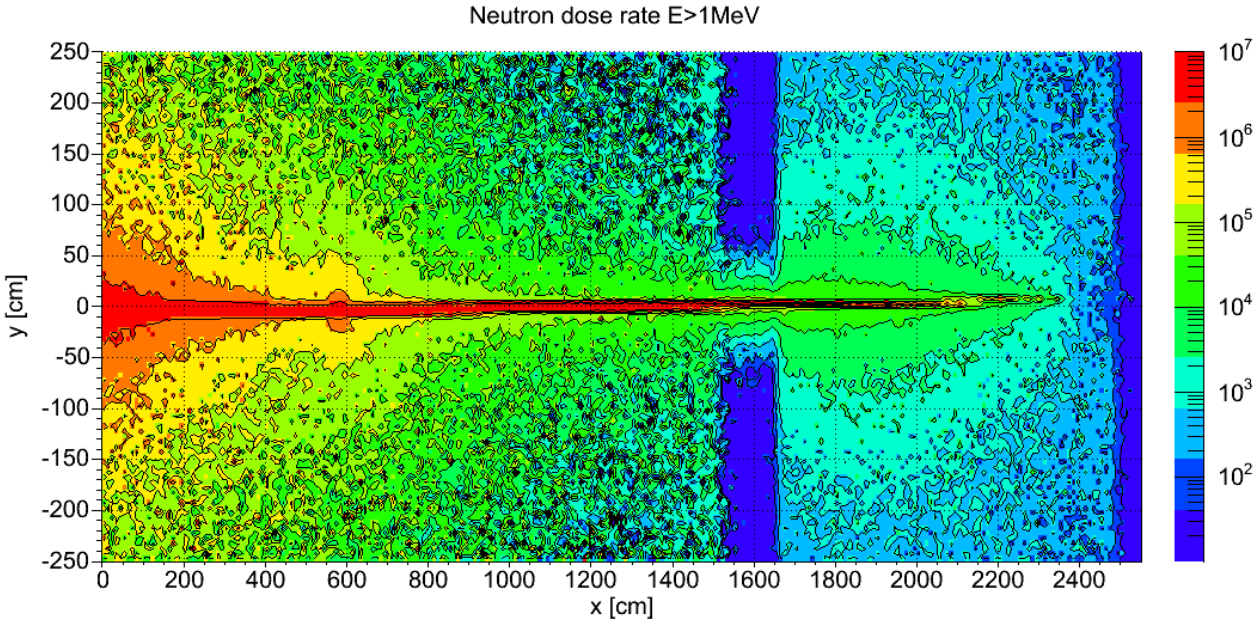

Fig. A.35: Neutron dose rate [µSv/h] in the energy range above 1 MeV in a horizontal plane around the neutron guide. Values above 10^7 µSv/h are set to 10^7 µSv/h (red regions) in this plot in order to visualize lower dose rates between wall A and B more clearly.

The calculated dose rates were verified by measurement. The neutron dose rate behind wall A at a distance of approximately 30 cm to the guide axis of NL5 was measured with a dosimeter. The position is indicated in Figs. A.31 and A.36 by the marker **A**. The calculated total neutron dose rate at this position is 20 mSv/h and the measured neutron dose rate is 19.2 mSv/h. Results of measurement and caclulation are in good accordance. The measurement was performed during a reactor power of 250 kW; results of the measurement were scaled to a reactor power of 20 MW.

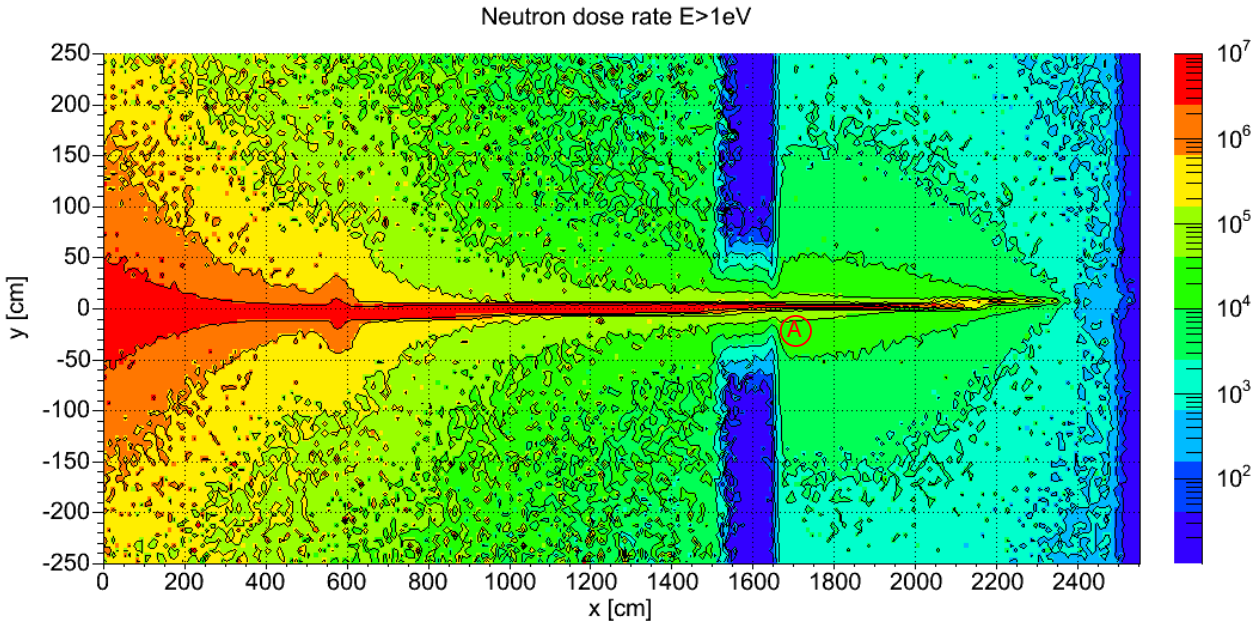

Fig. A.36: Neutron dose rate [µSv/h] in the energy range above 1 eV (sum of the values displayed in Fig. A.33 to Fig. A.35) in a horizontal plane around the neutron guide. Values above 10^7 µSv/h are set to 10^7 µSv/h (red regions) in this plot in order to visualize lower dose rates between wall A and B more clearly. The marker A indicates the position for which the dose rate was measured.

For experiments, the level of background radiation behind wall B in the neutron guide hall is of much more importance. The dose rate should be as low as possible for radiation protection purposes and background radiation - especially from thermal neutrons – is bothering for experiments. The second point is even a harder restriction than the first one. Measurements with a few neutron counts per minute are only possible when the background neutron count rate is far below. Wall B has a thickness of 80 cm and Röbalith was intended as shielding material. The question arises whether another shielding material would be beneficial for reduction of radiation level in the neutron guide hall. A horizontal cut through the Monte Carlo model at wall B is shown in Fig. A.37. Inside the wall the neutron guide is surrounded by a lead shielding. The neutron dose was calculated directly on the surface of wall B in the neutron guide hall in dependency of distance to the neutron guide. The results are shown in Fig. A.38. The red line in Fig. A.38 is achieved by the setup using Röbalith as shielding material. For distances smaller than 35 cm from the middle of the guide, the dose rate decreases with increasing distance. This effect is caused by the recess for the guide through the wall and by the gap system around the guide and the lead shielding. For distances between 35 cm and 85 cm from the guide middle, the dose rate remains nearly constant at a level of 1 µSv/h, because it is

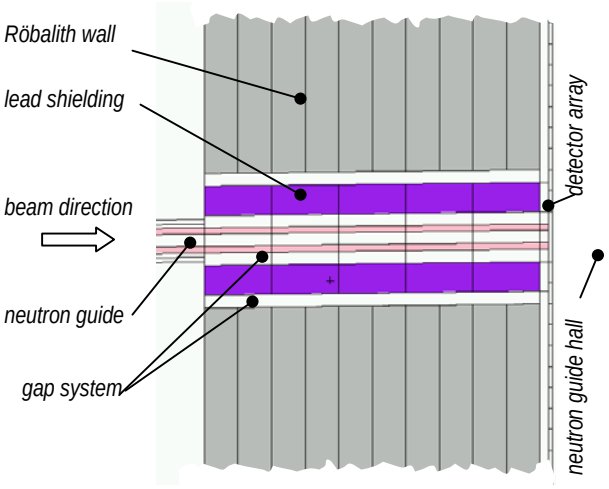

Fig. A.37: Horizontal cut through the Monte Carlo model of wall B at the recess for the neutron guide

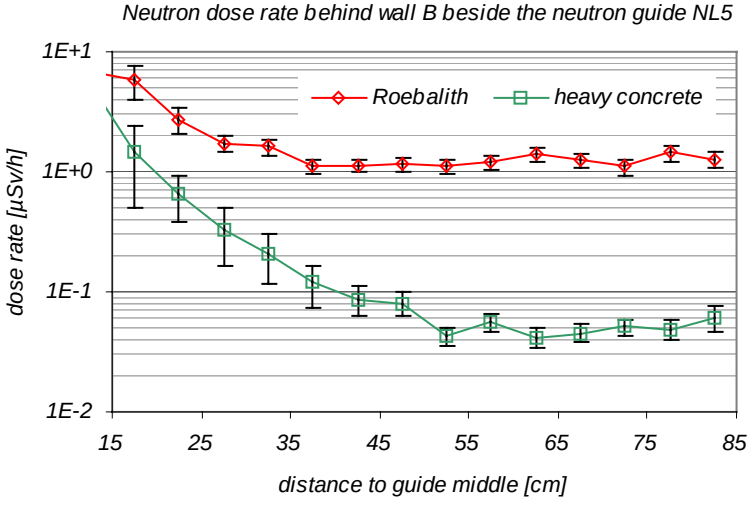

Fig. A.38: Neutron dose rate behind wall B in the neutron guide hall beside NL5.

dominated by direct transmission through the wall. The limit for radiation protection of 2.5 µSv/h is not reached by this single neutron guide except in a small region of 25 cm around the neutron guide. Under consideration, of all 6 neutron guides (some with even bigger cross sections) it is hardly possible not to exceed the desired dose rate threshold. In a further calculation Röbalith was replaced by heavy concrete type B of density ρ=4.7 g/cm^3 (see chapter 2.10.3.3 'Concrete as shielding material') as shielding material. In this case also a decrease of dose rate with increasing distance from the guide can be observed in a region of up to 50 cm to the guide. For bigger distances the dose level becomes constant at a level of 0.05 µSv/h. I.e. the dose rate is decreased by a factor of 20 compared to Röbalith, hence the radiation protection limit is not exceeded even if all neutron guides are considered.

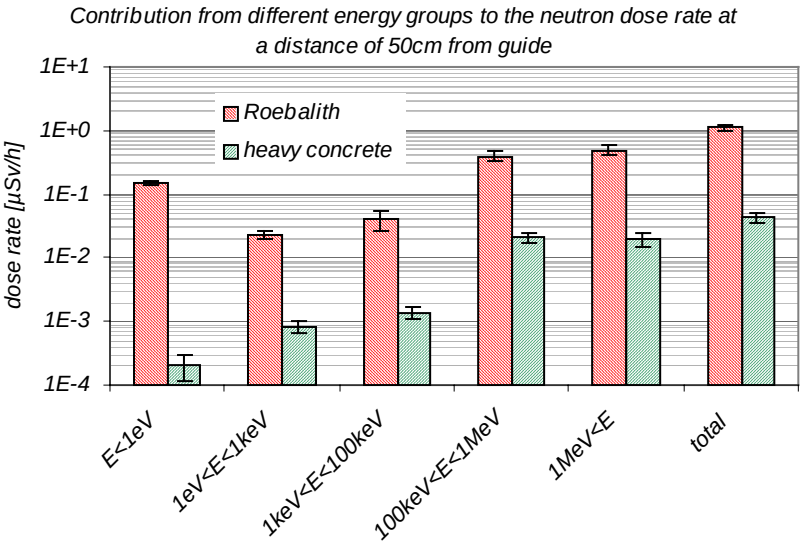

Fig. A.39: Contributions from different energy groups to the neutron dose rate behind wall B at a distance of 50 cm to the guide middle

From the point of view of experiments, advantages of heavy concrete compared to Röbalith are even more significant: As Röbalith has no boron content (in contrast to heavy concrete type B), the contribution of thermal neutrons caused by moderation of fast neutrons in the shielding material is quite high. It is 3 orders of magnitude bigger compared to heavy concrete. The contributions from different energy groups at a distance of 50 cm to the guide middle are displayed in Fig. A.39. Beside the higher neutron attenuation of heavy concrete type B, a lower generated gamma dose rate level is obtained (see chapter 2.10.3.1 'Concrete as shielding material). Replacing Röbalith by heavy concrete as shielding material in wall B is therefore a very effective means for reduction of the background radiation level in the neutron guide hall.

A.10 Fluence and dose in shielding materials

In the chapter ‘shielding materials’ the dose of neutron and gamma radiation after 80 cm of different concrete types and iron polyethylene mixtures as shielding material are shown. A sphere with a radius of 80 cm is used as calculation model (see chapter 2.10.3.1 ‘Calculation model for testing shielding materials’). The neutron source is located in the center of the sphere and has the energy spectrum of the ANTARES neutron beam. The distribution of neutron emission direction is isotropic. For estimation of shielding thicknesses it is useful to know the dose as function of shielding thickness. Therefore fluence and dose distributions on concentric spheres with different radii (centered around the neutron source) are shown in Figs. A.40 to A.63.

A.10.1 Ordinary concrete

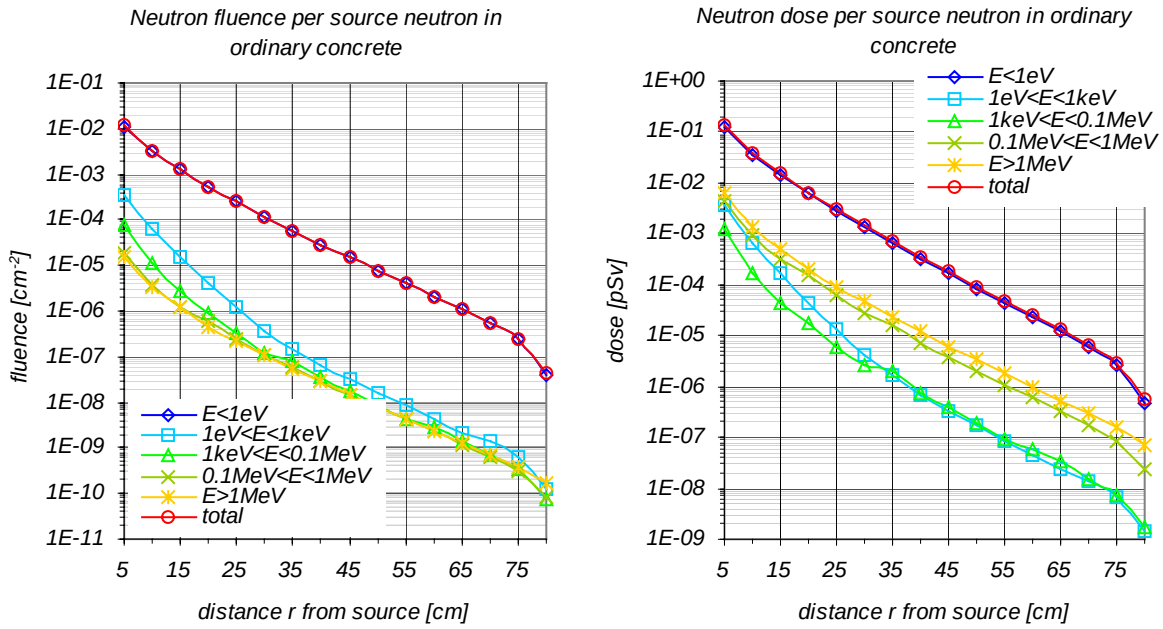

Fig. A.40: Fluence (left hand side) and dose (right hand side) of neutron radiation per source neutron as function of the distance to the source for the sphere filled with ordinary concrete as shielding material.

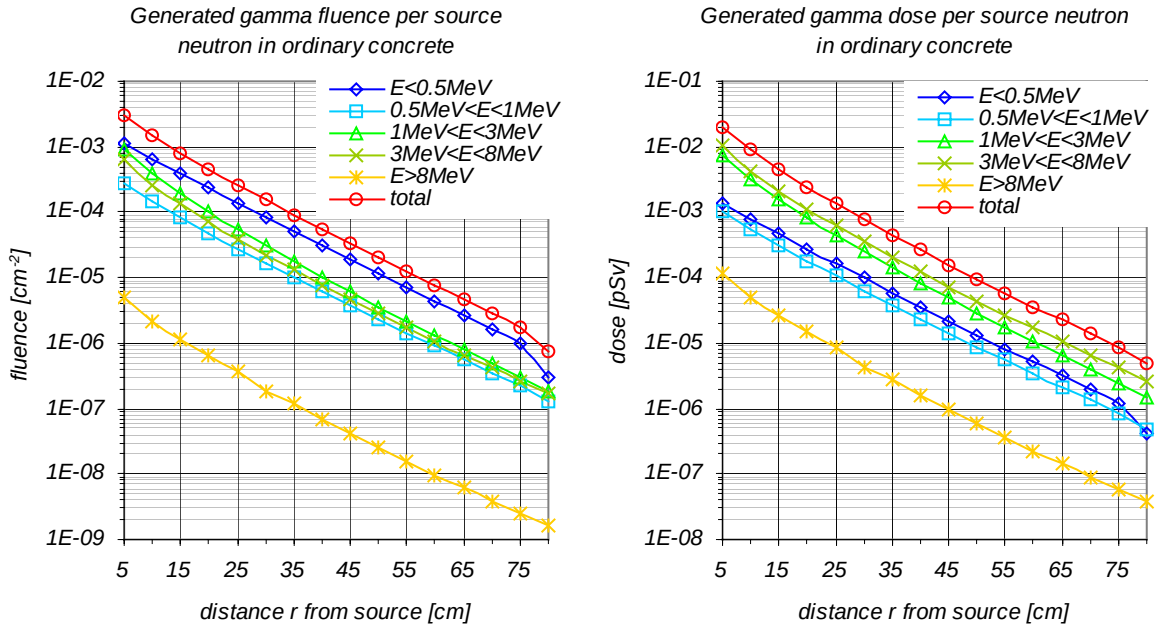

Fig. A.41: Fluence (left hand side) and dose (right hand side) of generated gamma radiation per source neutron as function of the distance to the source for the sphere filled with ordinary concrete as shielding material.

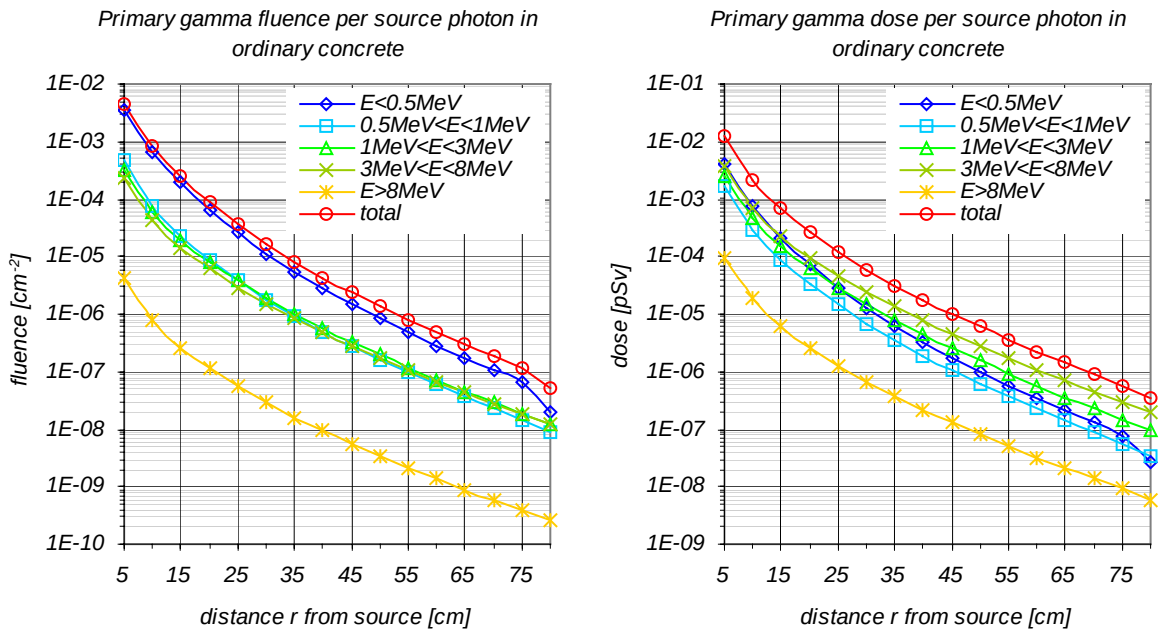

Fig. A.42: Fluence (left hand side) and dose (right hand side) of primary gamma radiation per source photon as function of the distance to the source for the sphere filled with ordinary concrete as shielding material.

A.10.2 Homogeneous iron-polyethylene mixture

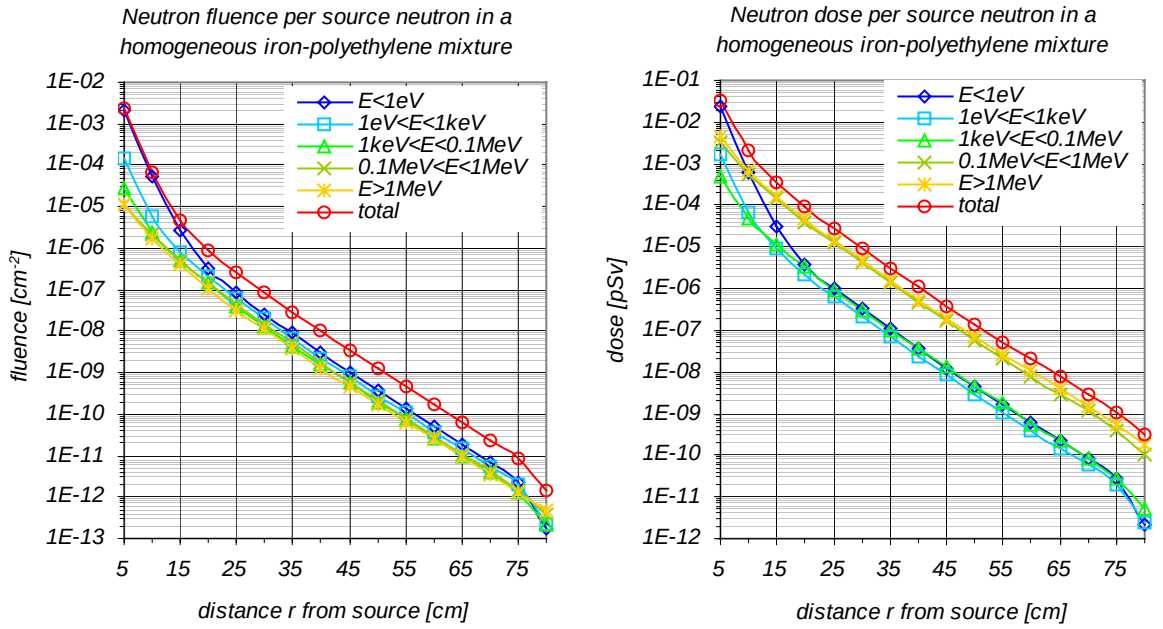

Fig. A.43: Fluence (left hand side) and dose (right hand side) of neutron radiation per source neutron as function of the distance to the source for the sphere filled with an homogeneous iron-polyethylene mixture (partial mass density of iron: ρ(Fe)=4.5 g/cm^3).

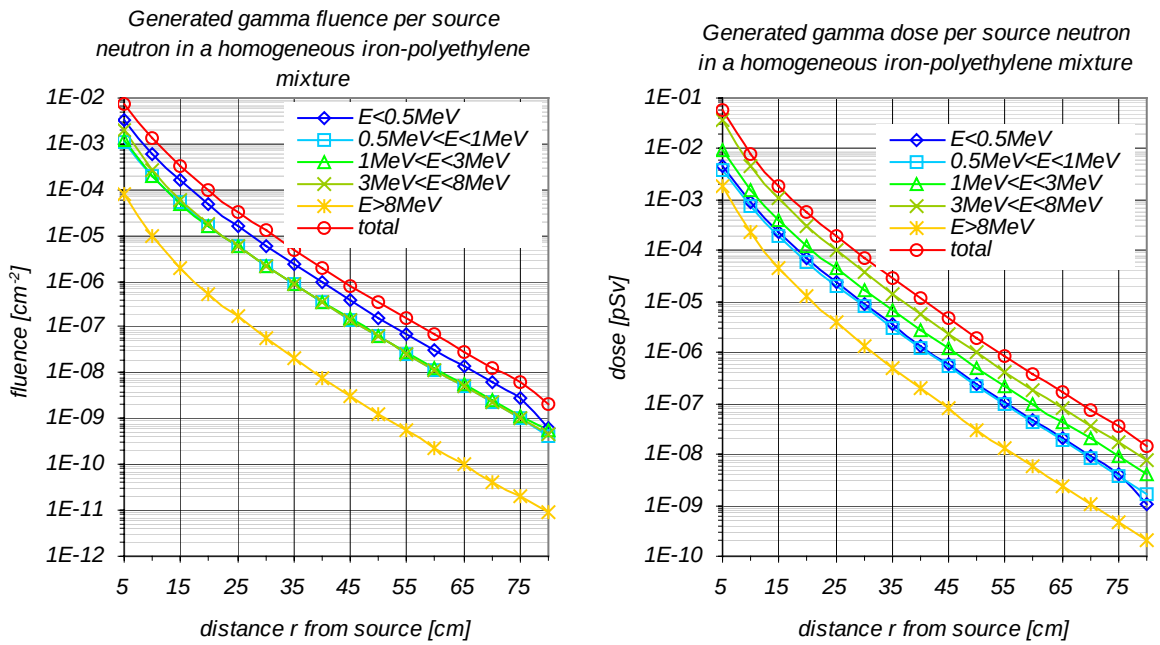

Fig. A.44: Fluence (left hand side) and dose (right hand side) of generated gamma radiation per source neutron as function of the distance to the source for the sphere filled with an homogeneous iron-polyethylene mixture (partial mass density of iron: ρ(Fe)=4.5 g/cm^3).

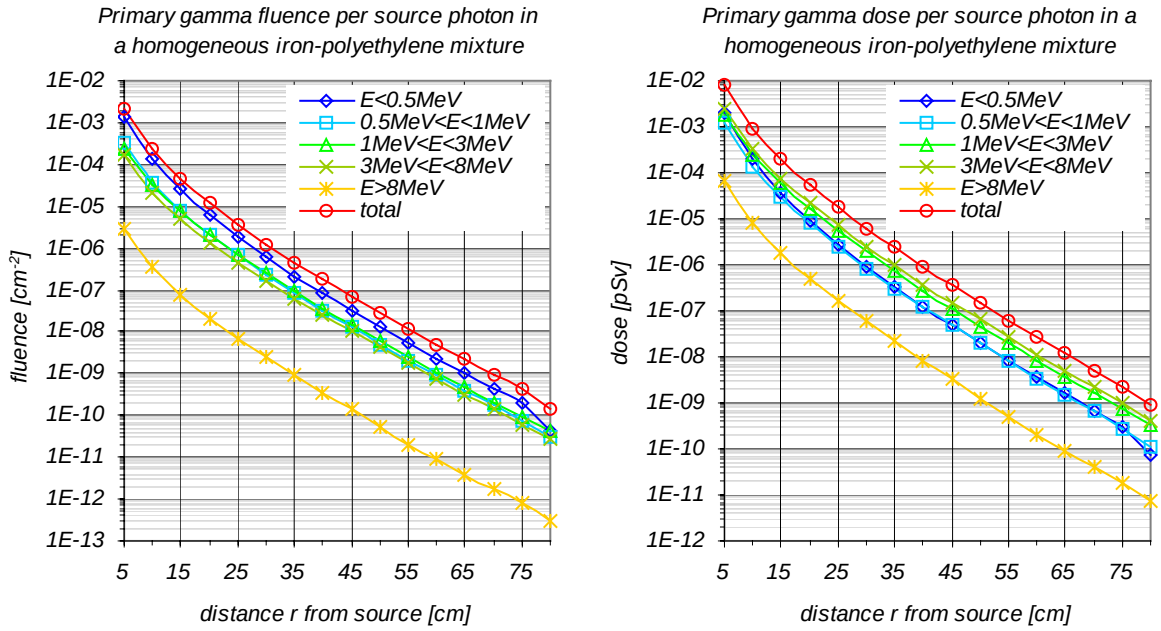

Fig. A.45: Fluence (left hand side) and dose (right hand side) of primary gamma radiation per source photon as function of the distance to the source for the sphere filled with an homogeneous iron-polyethylene mixture (partial mass density of iron: ρ(Fe)=4.5 g/cm^3).

A.10.3 Heavy concrete type A

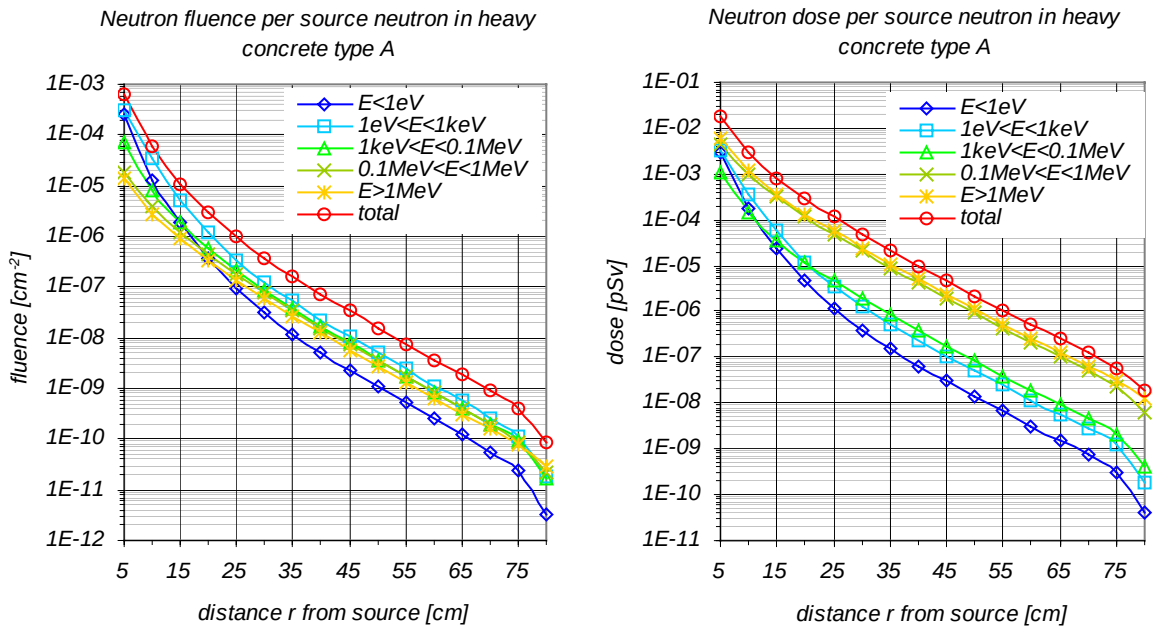

Fig. A.46: Fluence (left hand side) and dose (right hand side) of neutron radiation per source neutron as function of the distance to the source for the sphere filled with heavy concrete type A as shielding material.

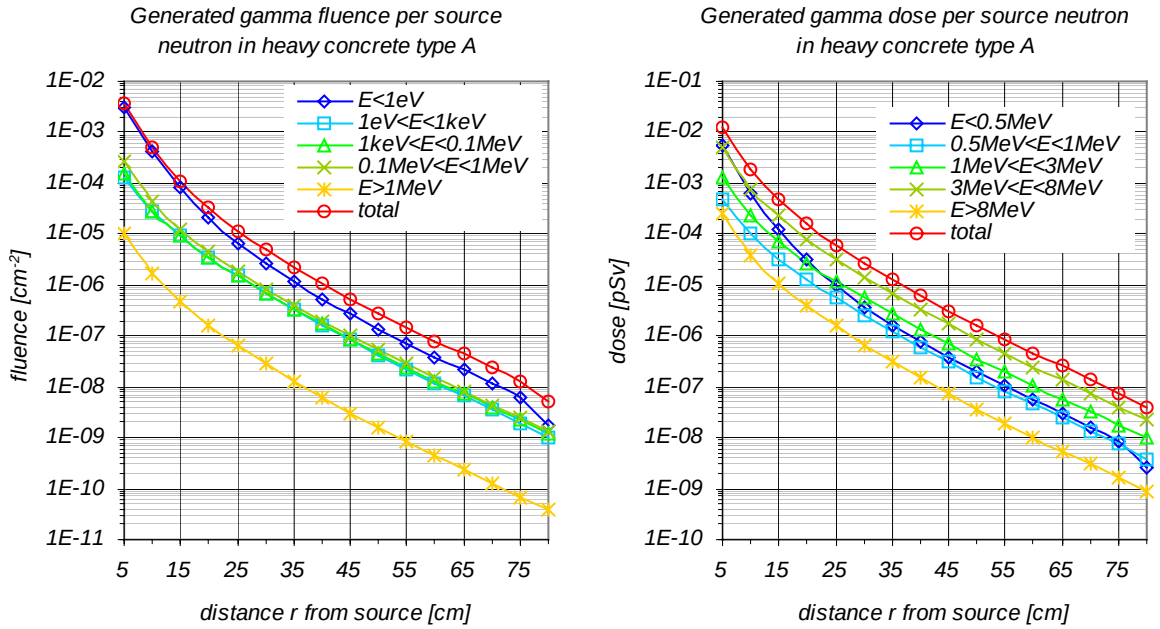

Fig. A.47: Fluence (left hand side) and dose (right hand side) of generated gamma radiation per source neutron as function of the distance to the source for the sphere filled with heavy concrete type A as shielding material.

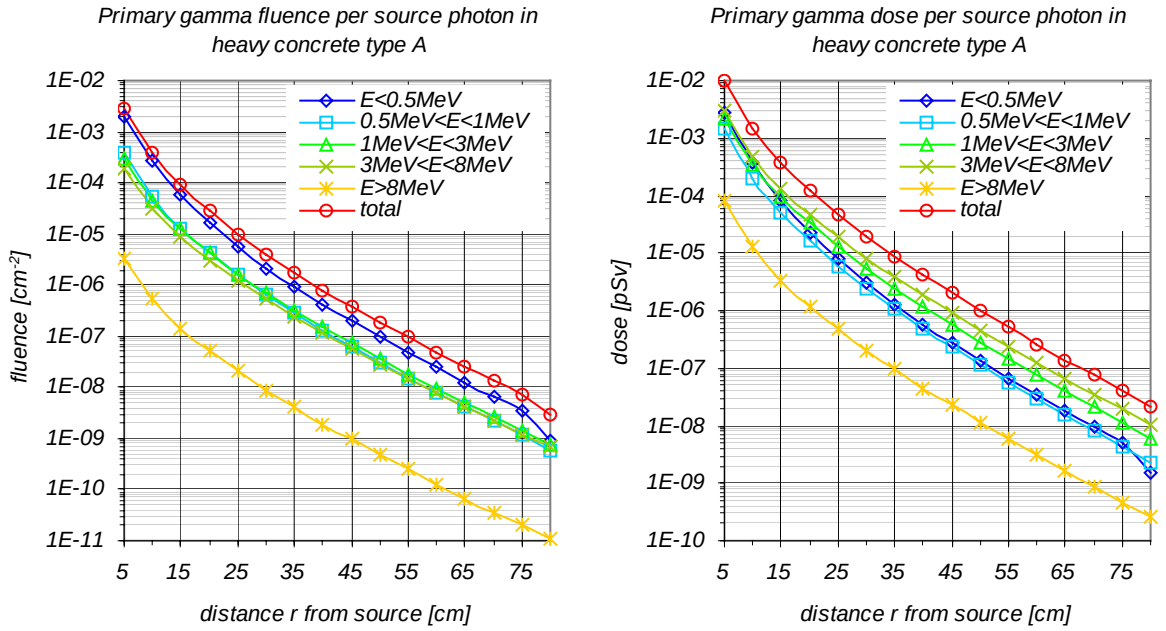

Fig. A.48: Fluence (left hand side) and dose (right hand side) of primary gamma radiation per source photon as function of the distance to the source for the sphere filled with heavy concrete type A as shielding material.

A.10.4 Heavy concrete type B

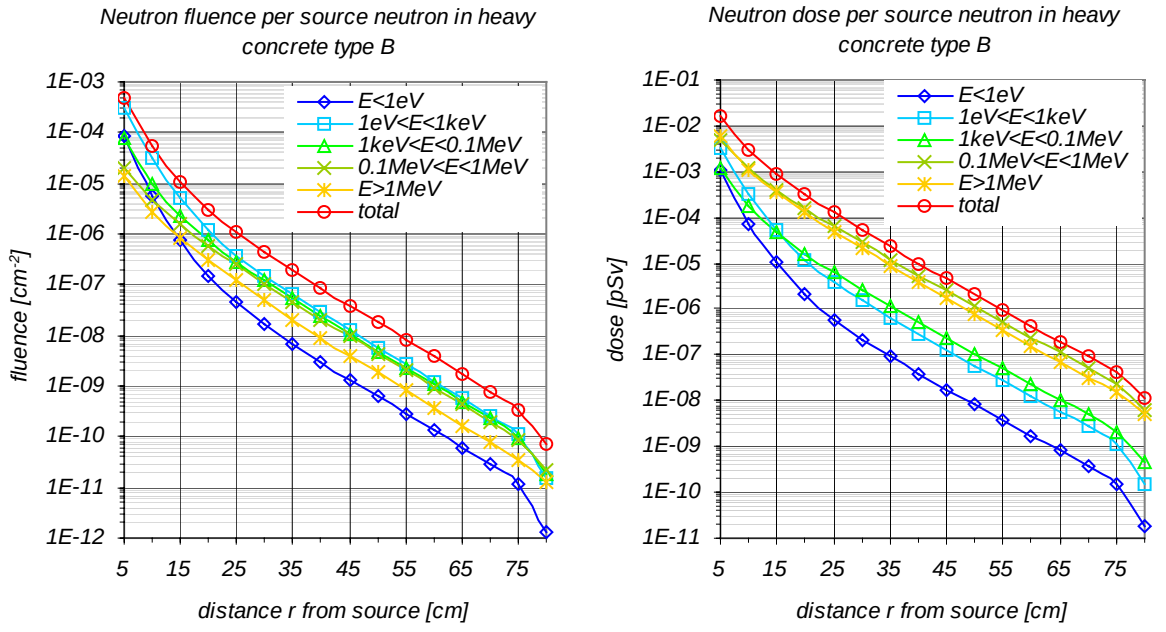

Fig. A.49: Fluence (left hand side) and dose (right hand side) of neutron radiation per source neutron as function of the distance to the source for the sphere filled with heavy concrete type B as shielding material.

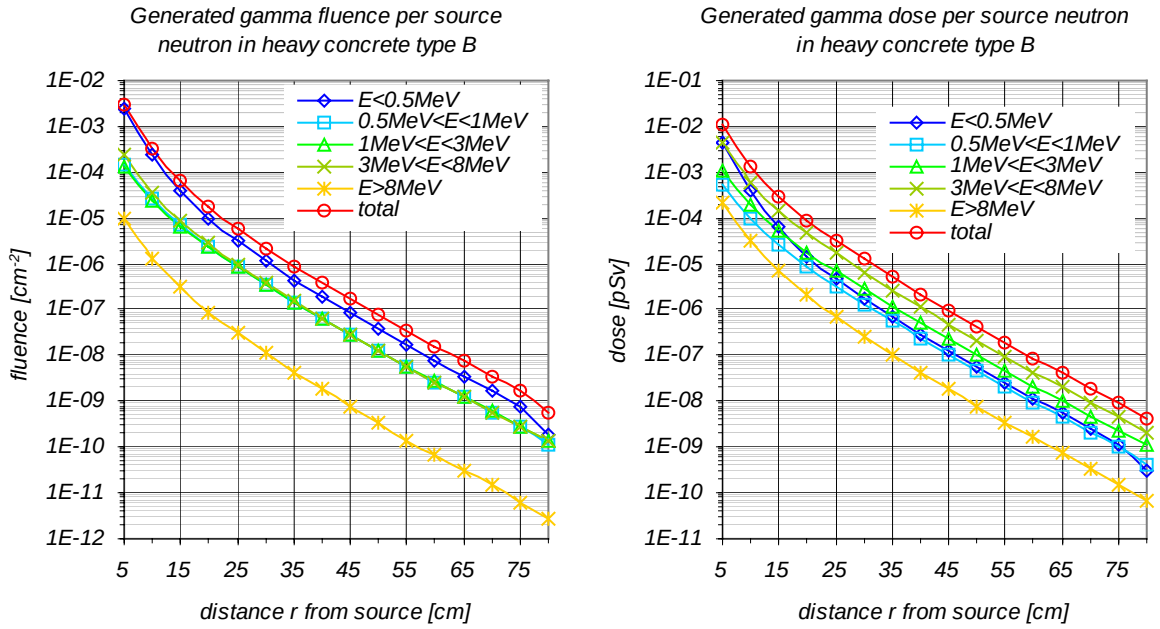

Fig. A.50: Fluence (left hand side) and dose (right hand side) of generated gamma radiation per source neutron as function of the distance to the source for the sphere filled with heavy concrete type B as shielding material.

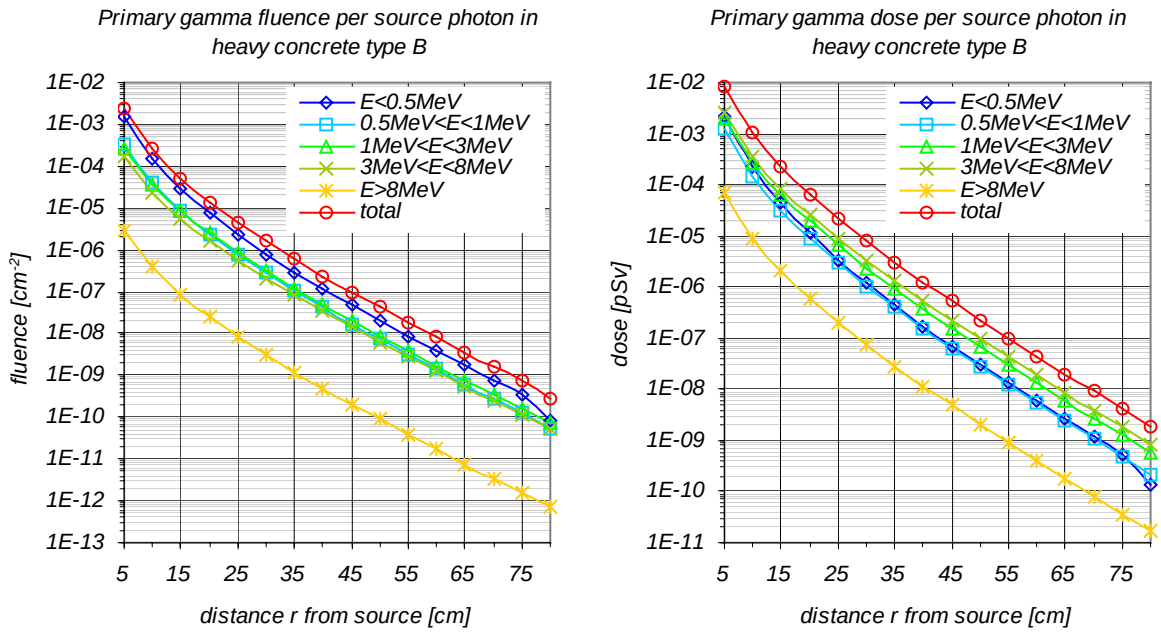

Fig. A.51: Fluence (left hand side) and dose (right hand side) of primary gamma radiation per source photon as function of the distance to the source for the sphere filled with heavy concrete type B as shielding material.

A.10.5 Heavy concrete type C

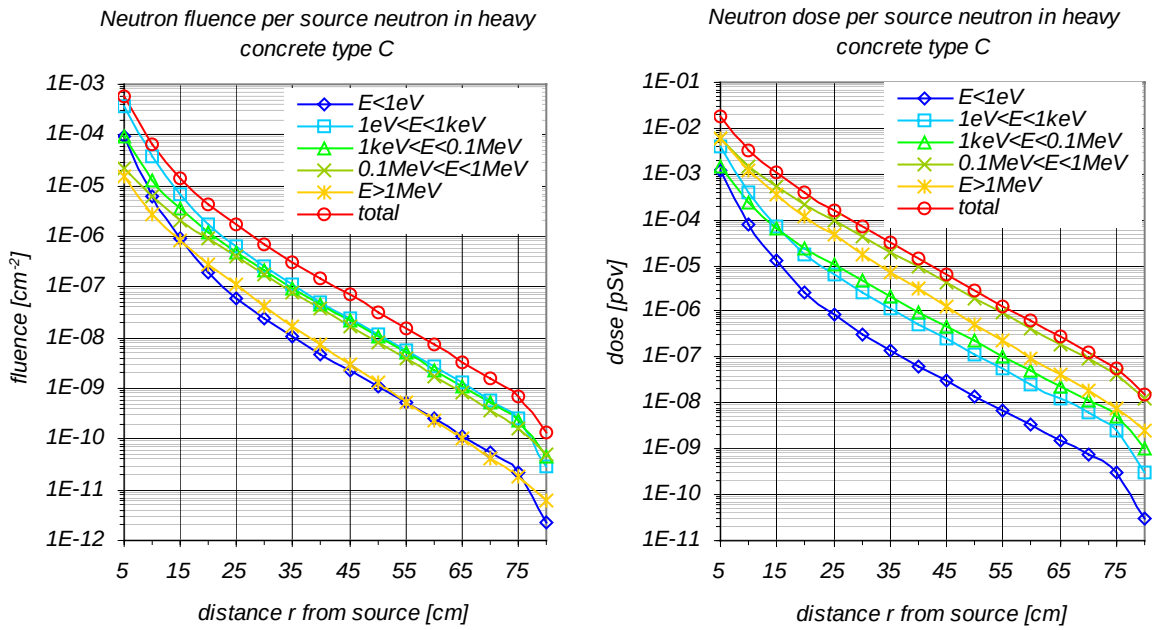

Fig. A.52: Fluence (left hand side) and dose (right hand side) of neutron radiation per source neutron as function of the distance to the source for the sphere filled with heavy concrete type C as shielding material.

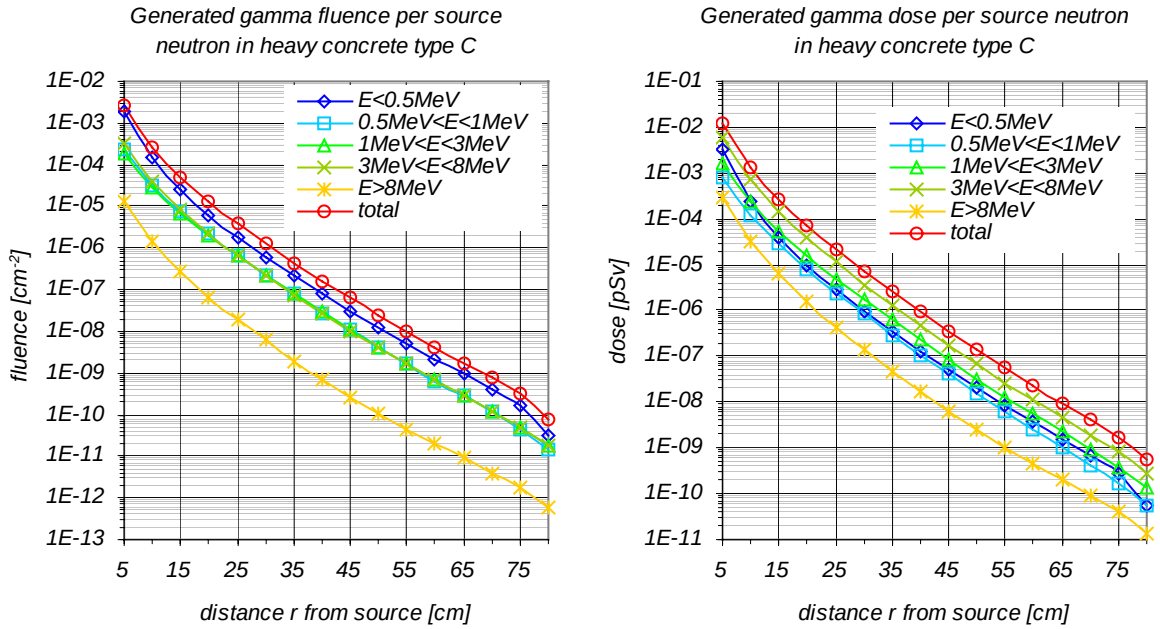

Fig. A.53: Fluence (left hand side) and dose (right hand side) of generated gamma radiation per source neutron as function of the distance to the source for the sphere filled with heavy concrete type C as shielding material.

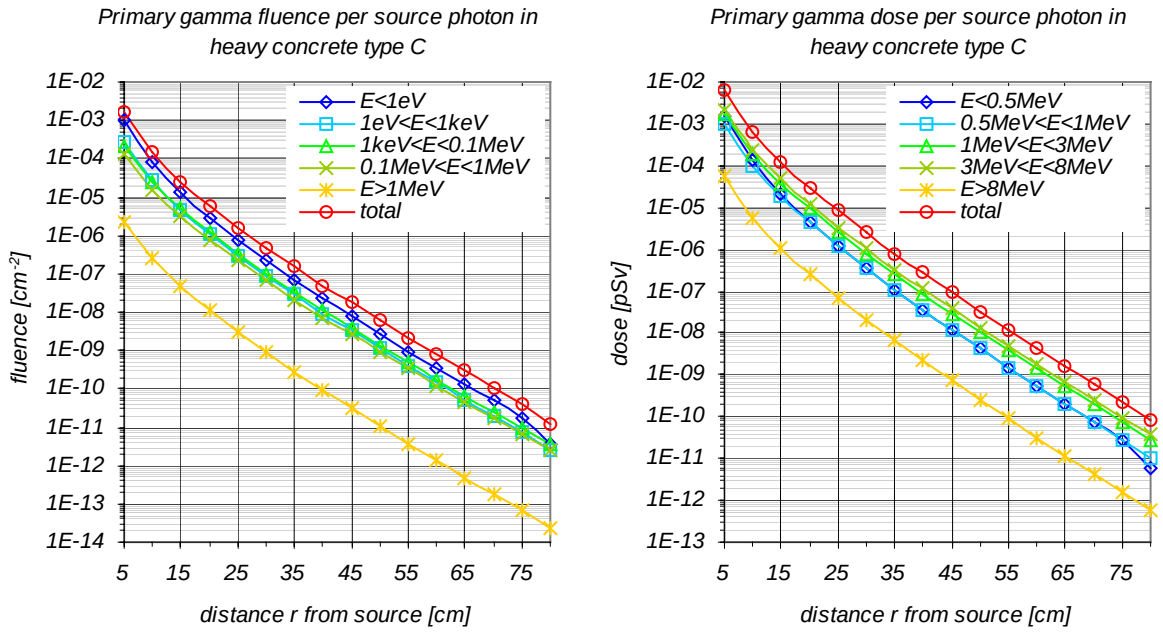

Fig. A.54: Fluence (left hand side) and dose (right hand side) of primary gamma radiation per source photon as function of the distance to the source for the sphere filled with heavy concrete type C as shielding material.

A.10.6 Heavy concrete type D

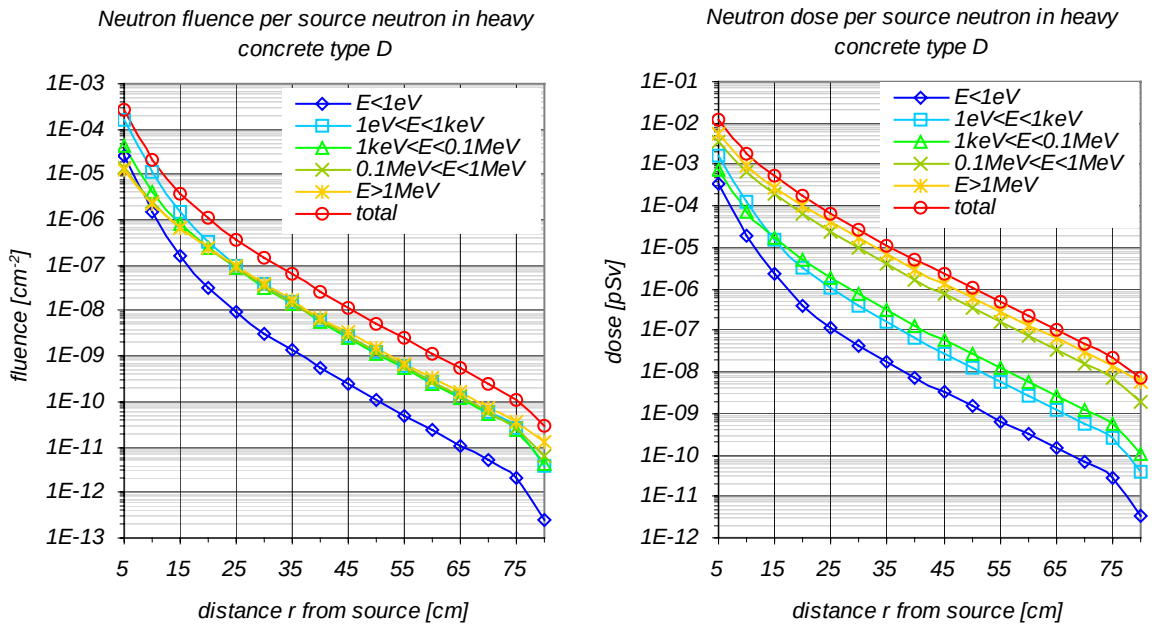

Fig. A.55: Fluence (left hand side) and dose (right hand side) of neutron radiation per source neutron as function of the distance to the source for the sphere filled with heavy concrete type D as shielding material.

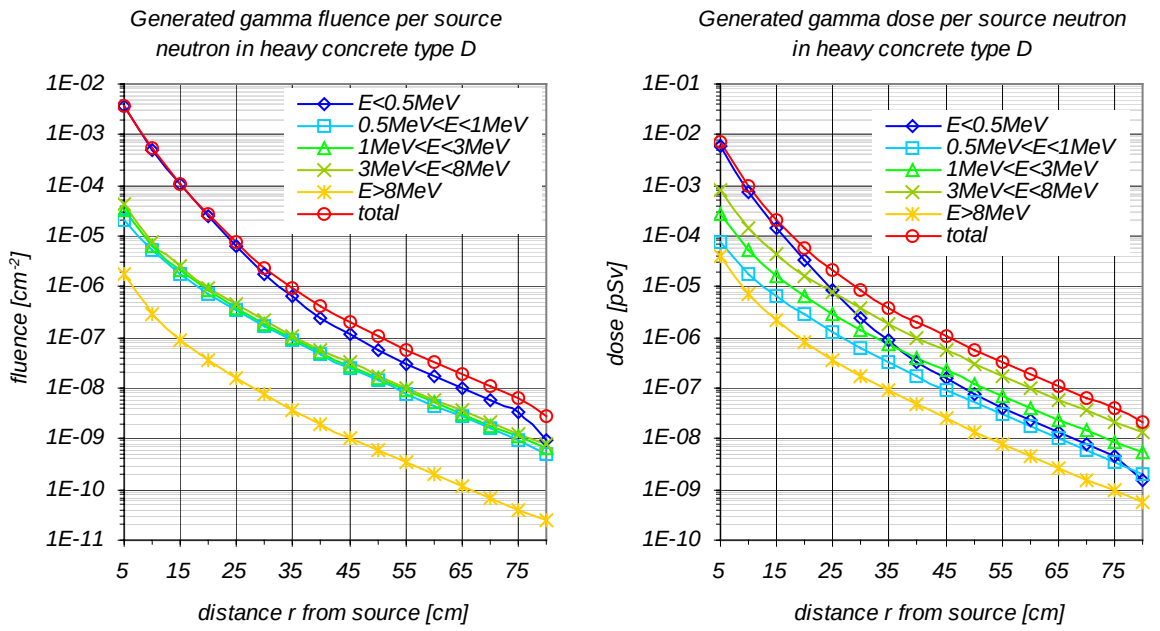

Fig. A.56: Fluence (left hand side) and dose (right hand side) of generated gamma radiation per source neutron as function of the distance to the source for the sphere filled with heavy concrete type D as shielding material.

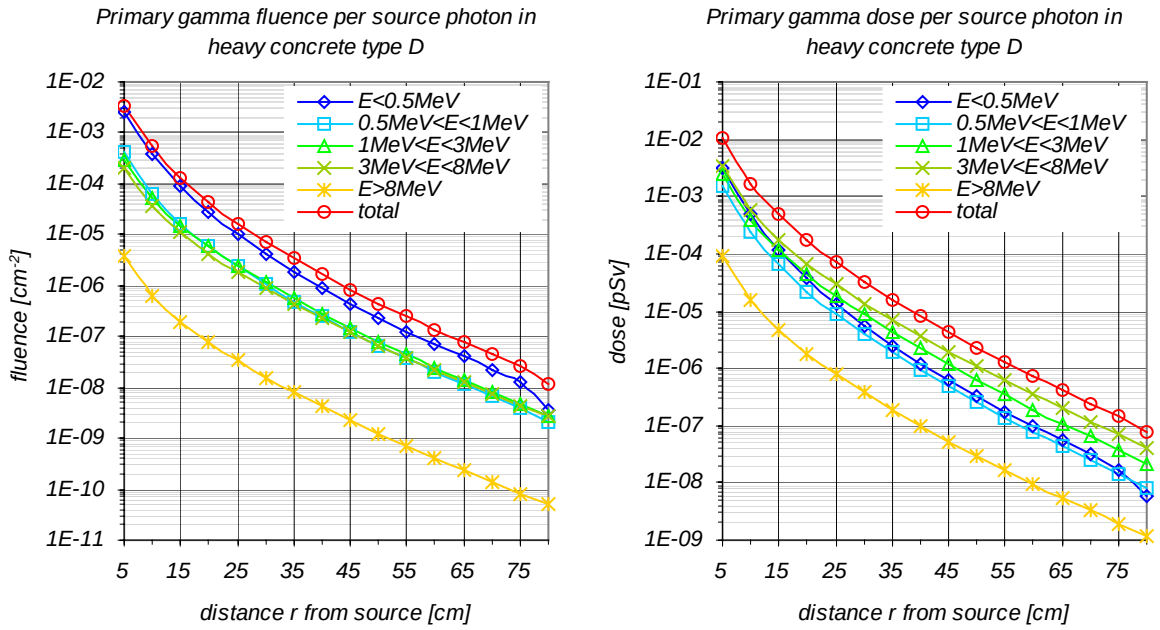

Fig. A.57: Fluence (left hand side) and dose (right hand side) of primary gamma radiation per source photon as function of the distance to the source for the sphere filled with heavy concrete type D as shielding material.

A.10.7 Heavy concrete type E

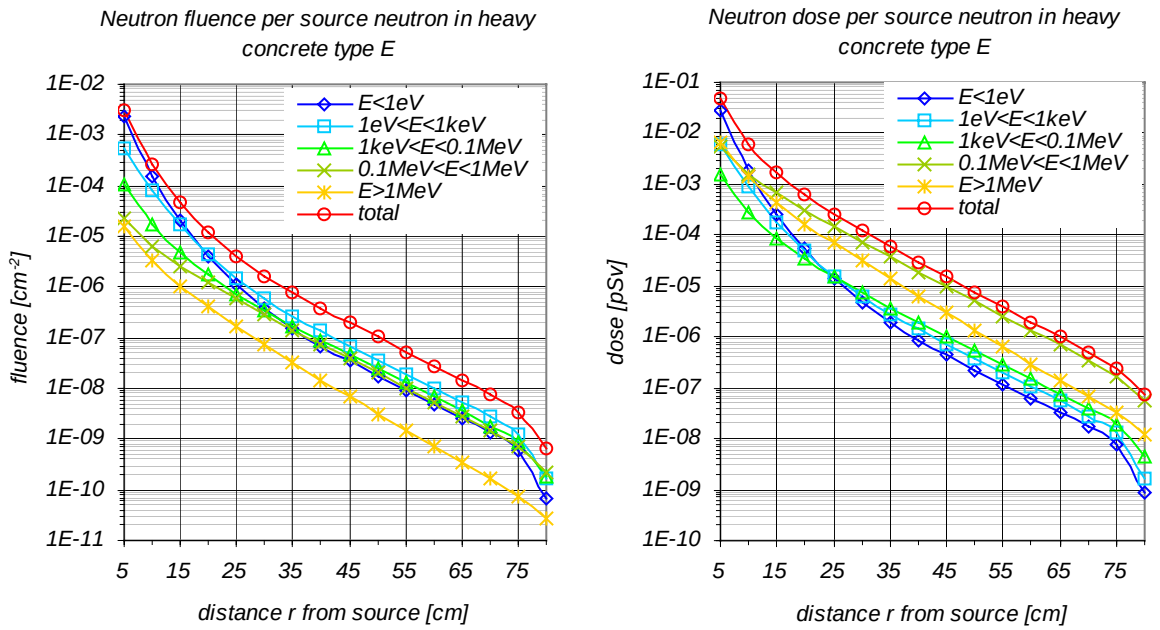

Fig. A.58: Fluence (left hand side) and dose (right hand side) of neutron radiation per source neutron as function of the distance to the source for the sphere filled with heavy concrete type E as shielding material.

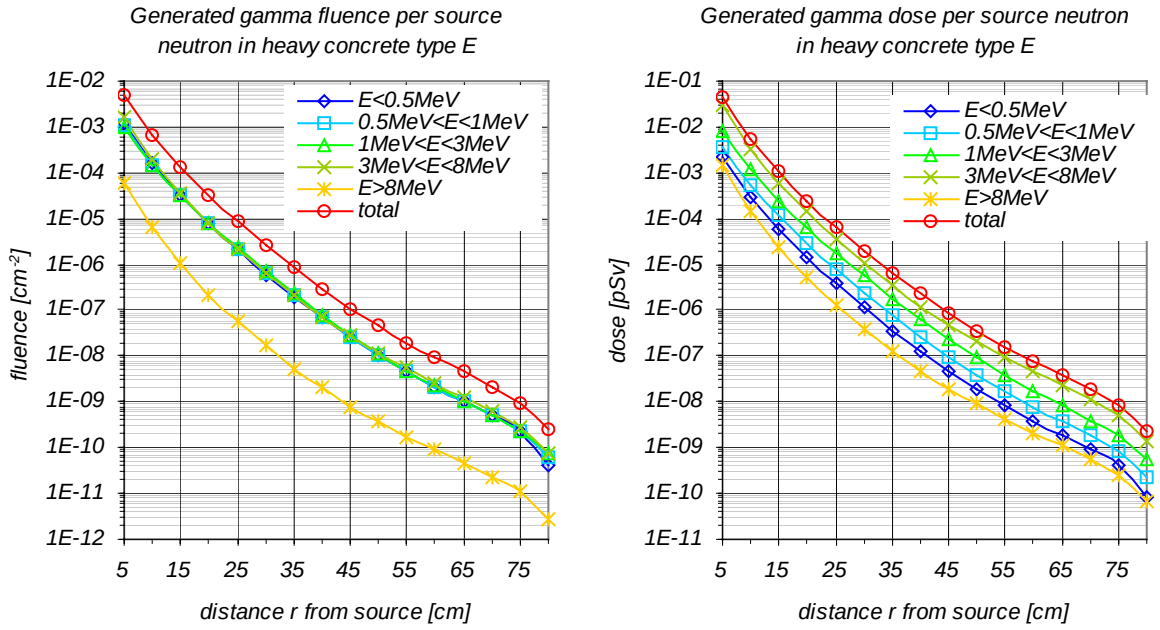

Fig. A.59: Fluence (left hand side) and dose (right hand side) of generated gamma radiation per source neutron as function of the distance to the source for the sphere filled with heavy concrete type E as shielding material.

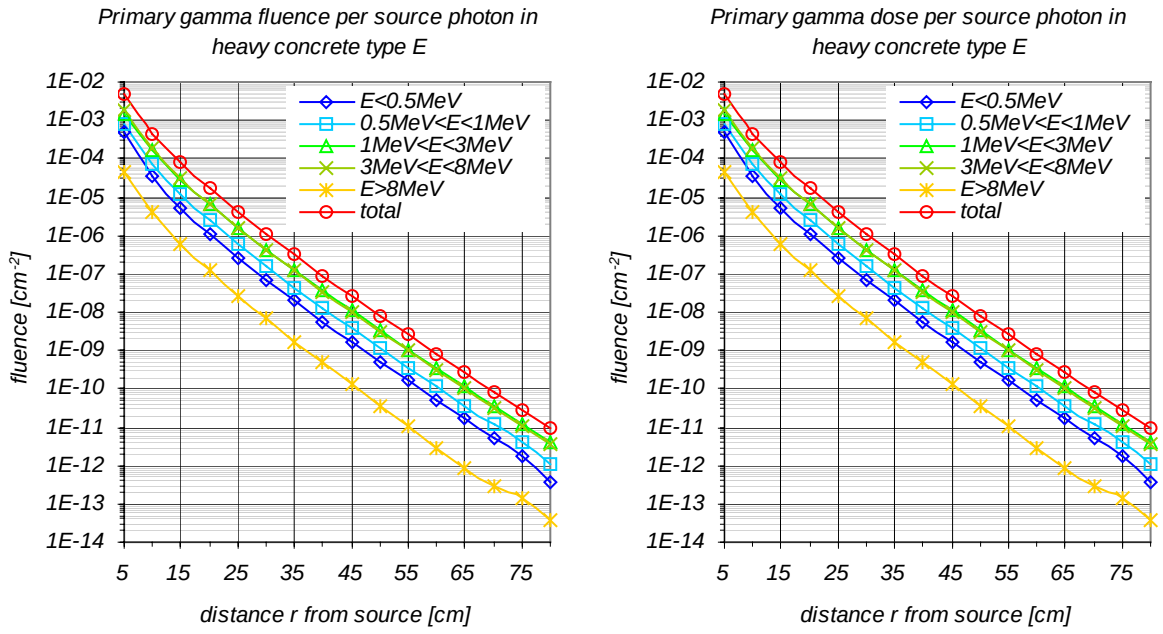

Fig. A.60: Fluence (left hand side) and dose (right hand side) of primary gamma radiation per source photon as function of the distance to the source for the sphere filled with heavy concrete type E as shielding material.

A.10.8 Heavy concrete type F

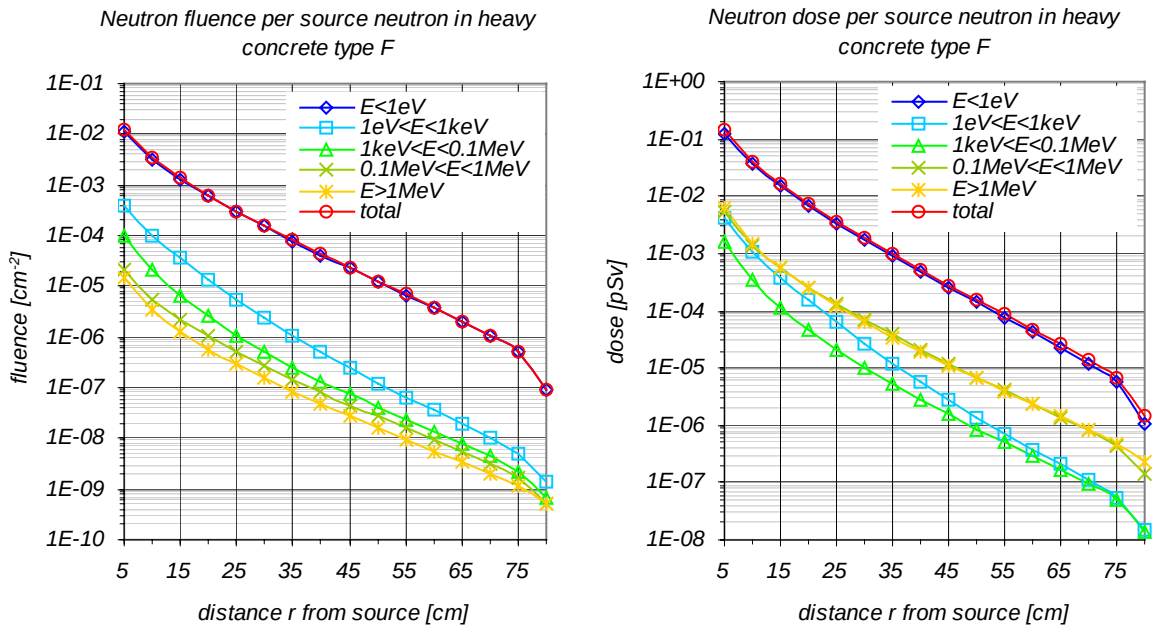

Fig. A.61: Fluence (left hand side) and dose (right hand side) of neutron radiation per source neutron as function of the distance to the source for the sphere filled with heavy concrete type F as shielding material.

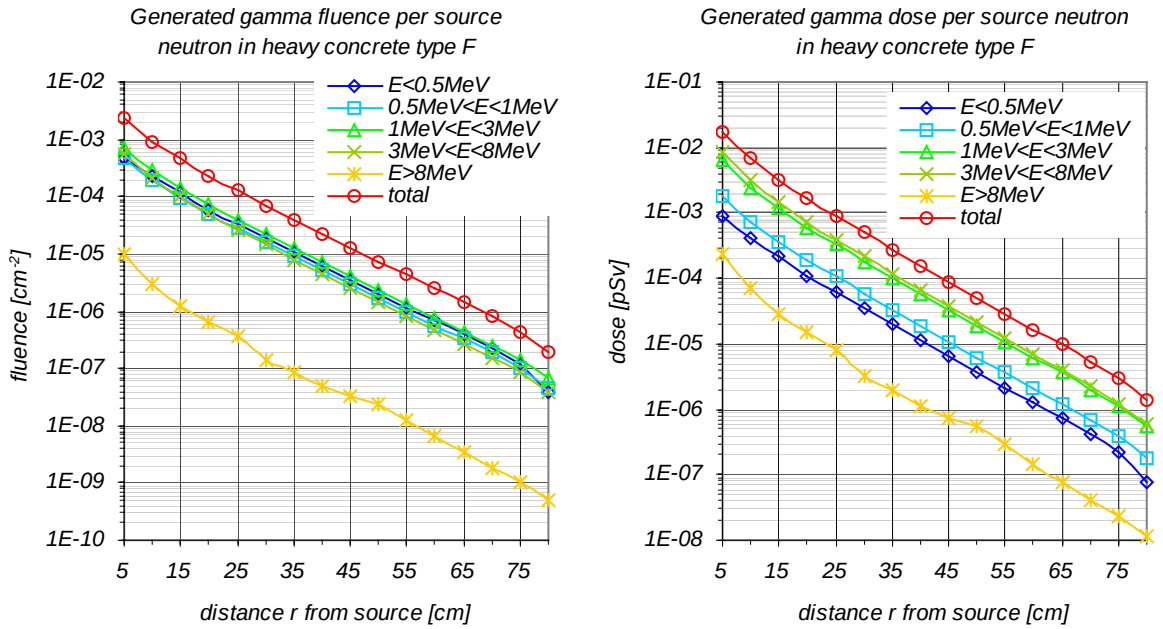

Fig. A.62: Fluence (left hand side) and dose (right hand side) of generated gamma radiation per source neutron as function of the distance to the source for the sphere filled with heavy concrete type F as shielding material.

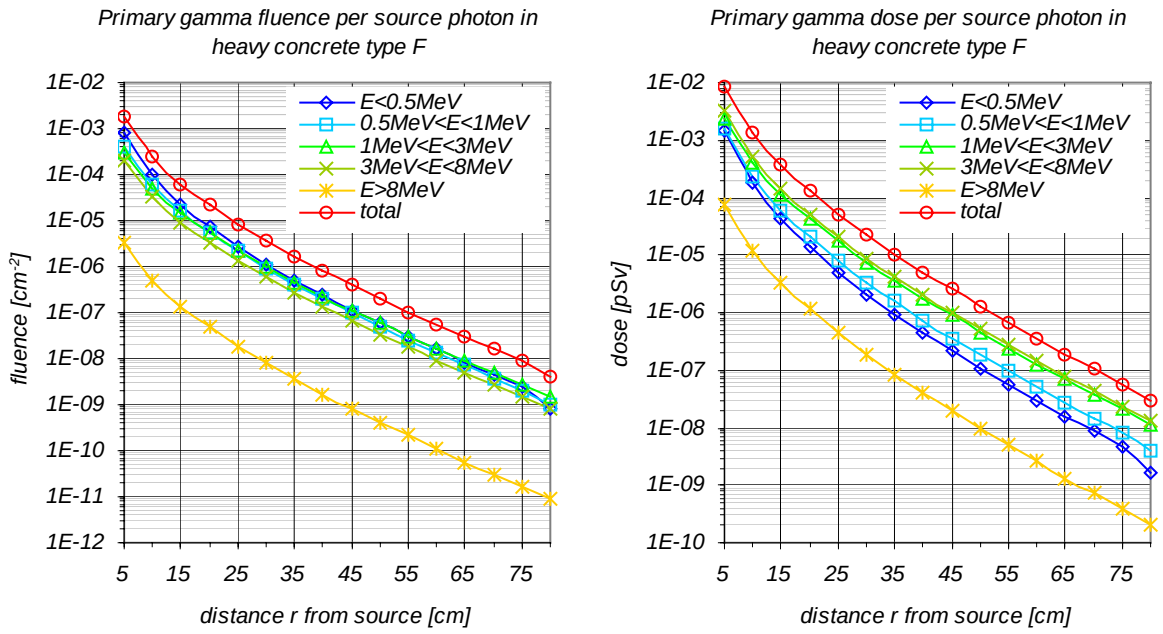

Fig. A.63: Fluence (left hand side) and dose (right hand side) of primary gamma radiation per source photon as function of the distance to the source for the sphere filled with heavy concrete type F as shielding material.

A.11 Comparison of neutron and X-ray cross sections

The cross section for X-rays is increasing with increasing atomic number. Light elements like e.g. hydrogen have low X-ray cross sections. The contrast between close-by elements in X-ray radiographies is low. X-ray cross sections are displayed in Fig. A.65. Contrary some light elements have relatively high neutron cross sections (e.g. hydrogen, lithium and boron). Even the cross sections of different isotopes of one element differ several orders of magnitude in some cases (e.g. $\sigma(^{10}B)$=3840 barn; $\sigma(^{11}B)$=0.005 barn). Neutron cross sections are shown in Fig. A.64. The cross sections correspond to natural isotope composition.

Due to the different cross sections for neutrons and X-rays of the elements, Neutron and X-ray radiography are an ideal supplement of each other. A comparison of neutron radiography and X-ray radiography is shown in [93].

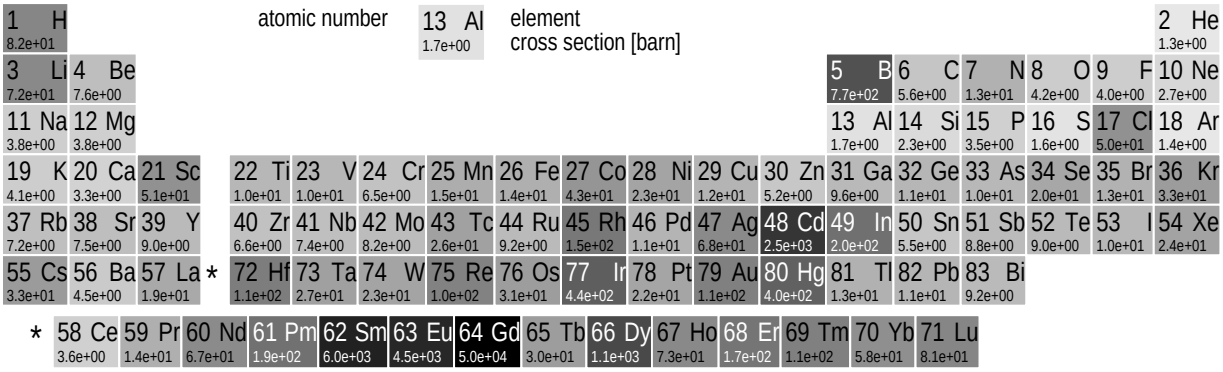

Fig. A.64: Total microscopic cross section σ [barn] for neutrons with an energy of 25 meV [94]. The displayed gray value is proportional to $\log_{10}(\sigma)$.

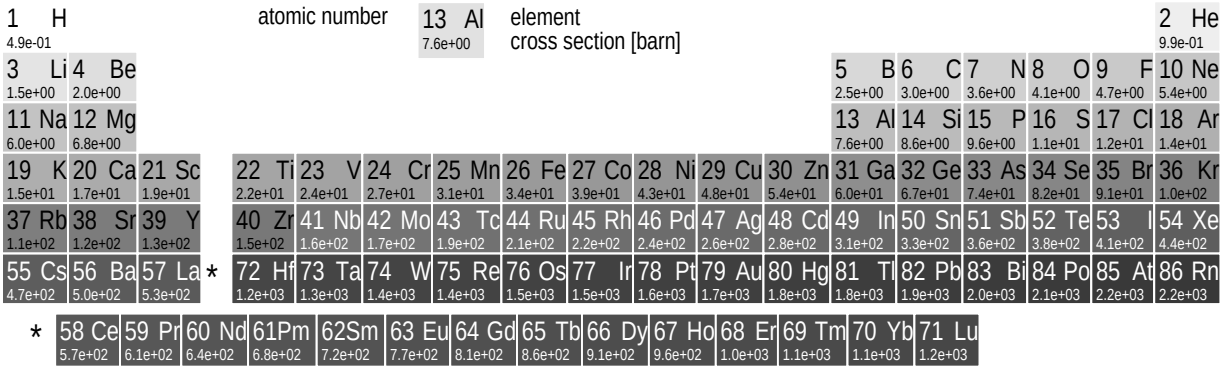

Fig. A.65: Total microscopic cross section σ [barn] for photons with an energy of 100 keV [8]. The displayed gray value is proportional to $\log_{10}(\sigma)$.

A.12 References

[1] Röntgen, C. R., *On a New Kind of Rays,* Nature 53, 274 (1896)

[2] Kallman, H., Research 1 (1947-48), 254

[3] Chadwick, F.R.S., *The Existence of a Neutron*, Proc. Roy. Soc., A, 136, p. 692-708

[4] Radon, J., *On the determination of functions from their integrals along certain manifolds*, Ber. Saechsische Akad. Wiss. 29, 1917, 262-279.

[5] Rosenfeld, A.; Kak A., *Digital Picture Processing*, second edition, Academic Press, New York London Paris, 1982

[6] Altschuler M.D., *Image Reconstruction from Projections*, Springer, Berlin Heidelberg New York, 1979

[7] P. Böni, *Novel Concepts in Neutron Instrumentation*, Physica B 276-278, 6-11, 2003

[8] W. Petry, *Advanced neutron instrumentation at FRM-II*, atw48 5, 315-318, 2003 online available under: http://www-igorr.cea.fr/proceedings/igorr9/papers/nfu_14.pdf

[9] Böning, K, FRM-II: Neutron source, *Experimental facilities at FRM-II*, TU München, 2001

[10] www.frm2.tum.de

[11] McDonald Jr., T.E. et al, *Time-gated energy-selected cold neutron radiography*. Nucl. Instr. Methods A 424, 1999, 235-241.

[12] Allman, B.E., et al, *Phase radiography with neutrons*, Nature, London, 408, 158-159

[13] Gaubatz, W., *Rechnerische Optimierung der sekundären Neutronenquellen des neuen Münchner Forschungsreaktors FRM-II*, Ph.D. thesis, TU München, 1998

[14] Emendörfer, D., Höcker, K.H., *Theorie der Kernreaktoren*, Bibliographisches Institut AG, Mannheim, 1969

[15] Briesmeister, J.F. (Ed), *MCNP – A general Monte Carlo N-Particle Transport Code*, Radiation Safety Information Computational Center (RSICC), Oak Ridge, 1977

[16] Von der Hardt, P., Röttger, H., *Neutron Radiography Handbook*, D. Reidel Publishing Company, Dordrecht Boston London, 1981

[17] Ziegler, A., *Lehrbuch der Reaktortechnik*, Springer, Berlin Heidelberg New York Tokyo, 1983

[18] Harms, A.A., Wyman, D. R., *Mathematics and Physics of Neutron Radiography*, D. Reidel, Dordrecht Boston Lancaster Tokyo, 1986

[19] http://www.appscintech.com

[20] Domanus, J.C., *Collimators for thermal neutron radiography*, D. Reidel, Dordrecht Boston Lancaster Tokyo, 1987

[21] Hecht, E., *Optik*, Addison-Wesley, Bonn München,1989

[22] Keepin, G. R., *Physics of Nuclear Kinetics*, Addison-Wesley, Reading Palo Alto London, 1965

[23] Grünauer, F., et al, *Optimization of the beam geometry for the cold neutron tomography facility at the new neutron source in Munich*, Applied Radiation and Isotopes 61, Elsevier, 479-485, 2004

[24] Bilge, A.N., Turgul, B., *Nuclear Applications with the TRIGA Reactor of Istanbul Technical University*, Proceedings of an international symposium on the utilization of multipurpose research reactors Grenoble 1987, IAEA 1988, 587-595

[25] Rosa, R., Burgio, N., *Monte Carlo design for a new neutron collimator at the ENEA Casaccia TRIGA reactor*, Applied Radiation and Isotopes 61, Elsevier, 663-666, 2004

[26] Jaeger, R.G., et al, *Engineering Compendium on Radiation Shielding Vol. I*, Springer, Berlin Heidelberg New York, 1975

[27] Jaeger, R.G., et al, *Engineering Compendium on Radiation Shielding Vol. II*, Springer, Berlin Heidelberg New York, 1975

[28] Information from Eagle-Picher Technologies GmbH

[29] Grünauer, F., *Berechnung der Neutronen- und γ-Flüsse in einem Strahlrohr und in einer Abschirmburg des FRM-II*, Diploma thesis, Technische Universität München, 1999

[30] Gutsmiedel, E., Gobrecht, K., *Kalte Quelle*, Experimentier- und Forschungseinrichtungen am FRM-II, TU München, 2001

[31] Baumgärtner, F., *Table of Neutron Activation Constants*, Karl Thiemig, München, 1967

[32] Pfennig, G., et al., *Chart of the nuclides*, 6th Edition 1995, Druckhaus Haberbeck, Lage, 1998

[33] private communication with E. Calzada

[34] Zimmermann, H., Weigert, A., *Lexikon der Astronomie*, Spektrum Akademischer Verlag, Heidelberg Berlin, 1999

[35] Spowart, A. R., *Measurement of the absolute scintillation efficiency of granular and glass neutron scintillators*, Nuclear Instruments and Methods 75, 35-42, 1969

[36] Fujine, S., et al., *Statistical image analysis of high-sensitivity neutron images obtained by cooled CCD systems*, Applied Radiation and Isotopes 61, Elsevier, 465-470, 2004

[37] Thoms, M., et al., *Spatial correlation and photostimulability of defect centers in the X-ray storage phosphor BaFBr:Eu2+*, Phys. Rev. B 44(17), 9240, 1991

[38] Schillinger, B. et al., *A new fast and large area neutron detector using a novel image plate readout technique*, Applied Radiation and Isotopes 61, Elsevier, 451-454, 2004

[39] Blizard, P. E., Abbott, S. L., *Reactor Handbook Volume III Part B*, Interscience Publishers, John Wiley & Sons, New York London, 1962

[40] Lederer, C. M., Hollander, J. M., *Table of Isotopes*, Sixth Edition, John Wiley & Sons, New York London Sydney, 1968

[41] private communication with T. Keller

[42] Zinth, W., Körner, H.-J., *Physik III Optik*, Quantenphänomene und Aufbau der Atome, R.Oldenbourg, München Wien, 1994

[43] http://www-nds.iaea.org/oldwallet/tnc/capgam.shtml

[44] Bos, A. J. J., et al., *Optimization of Shielding outside the biological shield of a nuclear reator*, Proceedings of the annual meeting on nuclear technology 1998, München 1998, Inforum, Bonn, 1998

[45] Holleman, A. F., Wiberg, E., *Lehrbuch der anorganischen Chemie*, De Gruyter, Berlin, 1964

[46] http://www.a-m.de/index.html

[47] Information from Schielein Kies + Beton GmbH & Co. KG

[48] Information from Wayss & Freytag Ingenieurbau AG

[49] Information from Seitz + Kerler GmbH & Co. KG

[50] Information from automess Automation und Messtechnik GmbH

[51] http://www.esm-online.de/sm/product/group1/FHT750.htm

[52] Rosenfeld, A., Kak, A. C., *Digital Picture Processing*, Second edition, Volume 1, Academic Press, New York London Paris San Francisco Sao Paulo Sydney Tokyo Tornto, 1982

[53] Meyberg, K., Vachenauer, P., *Höhere Mathematik 1*, Springer, Berlin Heidelberg New York London Paris Tokyo Hong Kong, 1990

[54] Meyberg, K., Vachenauer, P., *Höhere Mathematik 2*, Springer, Berlin Heidelberg New York London Paris Tokyo Hong Kong, 1991

[55] Russ, J.C., *The image processing handbook*, CRC Press, Boca Raton Ann Arbor London Tokyo, 1995

[56] Cittert, van P. H., Z. Physik, Vol. 69, p. 298, 1931

[57] Lucy, L. B., AJ, 79, 1974, 745

[58] Richardson, B.H., J. Opt. Soc. Am, 62, 1972, 55

[59] Pruksch, M., Fleischmann F., *Postive Iterative Deconvolution in Comprison to Richardson-Lucy like Algorithms*, Astronomical Data Analysis Software and Systems VII, ASP Conference series, Vol. 145, 1998

[60] Fenimore,E. E., Cannon, T. M., *Coded aperture imaging with uniformly redundant arrays*, Applied Optics, Vol. 17 No. 3, 1973

[61] Mertz, L. & Young, N., *Fresnel Transformations of Images*, Proc. Int'l Conf. on Optical Instruments and Techniques, Ed. K. J. Habell, p. 305, Chapman & Hall, London, 1961.

[62] Grindlay, J. E.; Hong, J., *Optimizing wide-field coded aperture imaging: radial mask holes and scanning*, Optics for EUV, X-Ray, and Gamma-Ray Astronomy. Edited by Citterio, Oberto; O'Dell, Stephen L. Proceedings of the SPIE, Volume 5168, pp. 402-410 (2004), online available under: http://hea-www.harvard.edu/EXIST/documents/imaging-spie03.pdf

[63] Willmore, A.P., et al., *A coded mask telescope for the Spacelab 2 Mission*, Nuclear Instruments and Methods in Physics research 221, 1984, 284-287

[64] Wouters, A., *Direct Method of decoding Multiple Images*, Applied Optics, Vol. 12, No. 8, 1973

[65] Chang, L.T.; MacDonald, B.; Perez-Mendez, V.; Shiraishi, L., *Coded aperture imaging of gamma-rays using multiple pinhole arrays and multiwire proportional chamber detector*, IEEE Transactions on Nuclear Science, Vol.NS-22, 1975

[66] Harris, F. J., *On the use of windows for harmonic analysis with discrete fourier transform*; Proceedings of the IEEE, 66(1978)51

[67] ICRP 74: *Conversion Coefficients for Use in Radiological Protection against External Radiation*, Annals of the ICRP 26, 3-4, New York, 1996

[68] DIN 6802-2, *Neutronendosimetrie, Teil 2: Konversionsfaktoren zur Berechnung der Orts- und Personendosis aus der Neutronenfluenz und Korrektionsfaktoren für Strahlenschutzdosimeter*, November 1999

[69] Burgkhardt, B., et al., *The neutron fluence and H*(10) response of the new LB6411 rem counter*, Radiation Protection Dosimetry, Vol 70. Nos. 1-4, 361-364, Nuclear Technology Publishing, 1997

[70] http://imagine.gsfc.nasa.gov/docs/features/exhibit/current.html

[71] private communication with B. Schillinger

[72] http://www.ill.fr/ (Institute Laue-Langevin)

[73] Phosphor/Scintillator Data Sheet 40, Applied Scintillation Technologies Inc.

[74] http://pollux.uv.es/integral/Masks/integralhome.htm

[75] Goldwurm A. et al., *Gamma-ray imaging with the coded maks IBIS telescope*, astro-ph/0102386 online available under: http://arxiv.org/PS_cache/astro-ph/pdf/0102/0102386.pdf

[76] Calabro, D., Wolf, J. .K., Inform. Control 11, 537, 1968

[77] Lanza, C. R., *Optimal coded aperture patterns for improved SNR in nuclear medicine imaging*, Nuclear Instruments and Methods in Physics Research A 474, 273-284, 2001

[78] Skinner, G. K., *Imaging with coded-aperture masks*, Nuclear Instruments and Methods in Physics Research 221, 33-40, 1984

[79] Accorsi, R., *Design of near field aperture cameras for high-resolution medical and industrial gamma ray imaging*, Ph. D. thesis, Massachusetts Institute of Technology, 2001

[80] http://www.radiochemie.de/main/instr/nectar/nectar.html

[81] Dubus, F., et al., *First phase contrast tomography with thermal neutrons*, Proceedings of the seventh world conference on neutron radiography, September 15-21, ENEA, 2002

[82] Grünauer, F., *Image deconvolution and coded masks in neutron radiography*, Nuclear Instruments and Methods in Physics Research A 542, 342-352, 2005

[83] Grünauer, F., *Shielding aspects for the neutron tomography facility at FRM-II*, Proceedings of the seventh world conference on neutron radiography, September 15-21, ENEA, 2002

[84] Calzada, E., Grünauer, F., Schillinger, B., *Engineering solutions for the new radiography and tomography facility at FRM-II*, Proceedings of the seventh world conference on neutron radiography, Rome September 15-21 2002, ENEA, 2005

[85] Jacobsen, D.L., et al., *Thermal and cold neutron phase-contrast radiography*, Applied Radiation and Isotopes 61, 547-550, 2004

[86] Schillinger, B., Calzada, E., Grünauer, F., Steichele, E., *The design of the neutron radiography and tomography facility at the new research reactor FRM-II at Technical University Munich*, Applied Radiation and Isotopes 61, Elsevier, 653-657, 2004

[87] Bücherl, T., et al., *The NECTAR facility at FRM-II*, Proceedings of the seventh world conference on neutron radiography, Rome September 15-21 2002, ENEA, 2005

[88] http://www.esrf.fr/exp_facilities/ID18/pages/technique/nfs/tech_nfs7.html

[89] Gallmeier, F. X., *Neutronenphysikalische Optimierung von experimentellen Einbauten am Forschungsreaktor FRM-II mit Monte Carlo Methoden*, Ph. D. thesis, Technische Universität München, 1993

[90] Hammersley, J. M., Handscomb, D. C., *Monte Carlo Methods*, Methuen, London, 1964

[91] Lindackers, K.-H., *Praktische Durchführung von Abschirmberechnungen*, Karl Thiemig, München, 1964

[92] Wiener, N. *Extrapolation, Interpolation, and Smoothing of Stationary Time Series*, Wiley, New York, 1949

[93] Bennett, L. G. I., Chalovich, T. R., Lewis, W. J., *Comparison of neutron radiography with other non-destructive techniques for the inspection of CF188 flight control surfaces*, IEEE Transactions on nuclear science, Vol. 52, No. 1, February 2005 online available under: http://ieeexplore.ieee.org/iel5/23/30668/01417161.pdf?arnumber=1417161

[94] http://www-nds.iaea.org/exfor/endf00.htm

[95] http://physics.nist.gov/PhysRefData/XrayMassCoef/cover.html

[96] http://lheawww.gsfc.nasa.gov/docs/cai/coded.html

[97] http://www.ph.tn.tudelft.nl/Courses/FIP/noframes/fip.html

[98] Calzada, E., Schillinger, B., Grünauer, F., *Construction and assembly of the neutron radiography and tomography facility ANTARES at FRM-II*, Nuclear Instruments and Methods in Physics Research A 542, 38-44, 2005

[99] Schillinger, B., et al., *Detection systems for short-time stroboscopic neutron imaging and measurements on a rotating engine*, Nuclear Instruments and Methods in Physics Research A 542, 142-147, 2005

[100] private communication with H. Zeising (radiation protection group at FRM-II)

Acknowledgements

I thank all those who have supported me during the creation of this work.

In particular I would like to thank Prof. Dr. P. Böni for giving me the opportunity to work on this interesting and exciting topic at his chair. I am grateful for his constant support and the chance to present and discuss my results at several conferences.

Many thanks to my direct supervisor Dr. B. Schillinger for his support, for giving me the opportunity to visit several conferences, and the great atmosphere in his group.

For many intersting discussions, the assistance during the construction of the ANTARES facility, and the comradeship in the ANTARES group I would like to thank J. Brunner, E. Calzada, K. Lorenz, M. Mühlbauer and M. Schulz.

For his help during the construction of the ANTARES facility and many interesting discussions I would like to thank Dr. T. Keller.

I am grateful for many interesting discussions with Dr. E. Steichele.

For the support during the TOF-measurement of the spectral neutron flux density I would like to thank Dr. K. Zeitelhack.

I would like to thank M. Ullrich for his support during the construction of the ANTARES facility.

Many thanks to all members of the work shop of the reactor station for their excellent and fast work.

Many thanks to J. Pulz, J. Beckmann and F. Zöbisch for the excellent maintenance of the computer network at FRM-II. They guaranteed a top stability of the network.